

Guanosine 5'-Monophosphate as a Small Biomolecule Hydrogelator to Form Supramolecular Hydrogels with Metal-oxo Nanoclusters, Metal Complex, and Small Organic Molecule: Synthesis, Characterization, and Applications

Ph.D. Thesis

By

AMRITA CHAKRABORTY



DEPARTMENT OF CHEMISTRY
INDIAN INSTITUTE OF TECHNOLOGY INDORE
JANUARY 2025

Guanosine 5'-Monophosphate as a Small Biomolecule Hydrogelator to Form Supramolecular Hydrogels with Metal-oxo Nanoclusters, Metal Complex, and Small Organic Molecule: Synthesis, Characterization, and Applications

A THESIS

Submitted in partial fulfillment of the requirements for the award of the degree

of

DOCTOR OF PHILOSOPHY

By

AMRITA CHAKRABORTY



**DEPARTMENT OF CHEMISTRY
INDIAN INSTITUTE OF TECHNOLOGY INDORE**

JANUARY 2025



INDIAN INSTITUTE OF TECHNOLOGY INDORE

I hereby certify that the work which is being presented in the thesis entitled '**Guanosine 5'-Monophosphate as a Small Biomolecule Hydrogelator to Form Supramolecular Hydrogels with Metal-oxo Nanoclusters, Metal Complex, and Small Organic Molecule: Synthesis, Characterization, and Applications**' in the partial fulfillment of the requirements for the award of the degree of **DOCTOR OF PHILOSOPHY** and submitted in the **DEPARTMENT OF CHEMISTRY, Indian Institute of Technology Indore**, is an authentic record of my own work carried out during the time period from **JULY 2019** to **JANUARY 2025** under the supervision of **DR. TRIDIB KUMAR SARMA**, Professor, Department of Chemistry, Indian Institute of Technology Indore.

The matter presented in this thesis has not been submitted by me for the award of any other degree of this or any other institute.

AMRITA CHAKRABORTY

This is to certify that the above statement made by the candidate is correct to the best of my knowledge.

Dr. TRIDIB KUMAR SARMA

AMRITA CHAKRABORTY has successfully given his/her Ph.D. Oral Examination held on 27th May, 2025

Dr. TRIDIB KUMAR SARMA

Acknowledgments

A thesis, like any meaningful journey, is never an individual effort, it's the support and guidance of a whole tribe that makes it possible. This thesis would not have been possible without the guidance and encouragement of several individuals who generously offered their valuable assistance. I am deeply grateful to all who contributed and helped make this work a reality.

I am deeply grateful to my supervisor Dr. Tridib Kumar Sarma for his constant support, guidance, and patience throughout this process. Without his understanding and generosity, this would not have been possible. I am grateful for always believing in and supporting my research ideas and letting them flourish. I am also very thankful for his help and empathy in my hard times. My research growth in this journey would not have been possible without his deep expertise, exceptional mastery of the subject, invaluable guidance, and unwavering enthusiasm.

I am also thankful to my PSPC members, Dr. Anjan Chakraborty and Dr. Dipak Kumar Roy for their invaluable suggestions and guidance. Their gentle feedback and support have immensely helped me throughout my journey. I also express my sincere gratitude towards Dr. Deepa Dey for her kind support and compassion.

I would like to express my gratitude to Prof. Tushar Kanti Mukherjee, Head of the Department of Chemistry at IIT Indore, Professor Suhas Joshi, Director of IIT Indore, and all the faculty members of the Department of Chemistry for their guidance and invaluable insights regarding my thesis work. I am thankful to the Ministry of Human Resource and Development (MHRD), New Delhi for the fellowship. I am also thankful to the Sophisticated Instrument Centre (SIC) at the Indian Institute of Technology Indore for providing the necessary in-house research equipment. I would also take the opportunity to mention SAPTARSHI IIT Jammu for the XPS facility, CRF IIT Delhi, SAIF IIT Bombay, and NEHU Shillong for extending their help with the TEM facility.

I also express my sincere gratitude to Mr. Kinny Pandey, Dr. Ravinder Kumar, Mr. Ghanshyam Bhavsar, Mr. Nitin Upadhyay, Mr. Mayur Dhake for their technical support and Mr. Tapesih Parihar, Mr. Manish Kushwaha, Mrs. Vinita Kothari, Mr. Rameshwar Dauhare, Mr. Souvik, for their official support, which was crucial for the continuation of my work. Additionally, I acknowledge the support and service provided by all the technical and non-technical staff of IIT Indore.

The research endeavor would not have been possible without my collaborators. I sincerely thank Dr. Debasis Nayak, Dr. Rajesh Kumar, Dr. Hem Chandra Jha, Ms. Sashwati Dash, Dr. Tanushree Ghosh, and Dr. Annu Rani for their help in biological and physics-related studies. I would also like to mention Dr. Indrasen Singh and Mr. Arun Singh for helping us with the UTM instrument.

I would also like to thank my seniors Dr. Neha Thakur, Dr. Siddarth Jain, Dr. Daisy Sarma, and Dr. Abhiram Panigrahi for warmly welcoming and guiding me on this journey. I am also thankful to Dr. Soumya Kanti De for his support and guidance. I am also grateful to M.Sc. alumni Barsha Deori and Nitin Kumar for always being so helpful and nice. There is no greater fortune at any workplace than having your colleagues become your friends. I would like to mention my lab juniors Aditya Prasun, Ravindra Vishwakarma, Suryakamal Sarma, and Tarun Kumar Sahu. In the last four years, we have grown together and I have learned so much from them. I am grateful for their constant support and humor. Also, a special thanks to Anjali Singh, Huma Tabassum, Priyanka Nath, Naveen Kumar, Suman, Shaurya, Reetik Chib, Sheetal Leva, Yoshita, and Soniya for their constant support and for keeping the environment always positive and cheery. I would especially like to mention some names here who have been a part of my journey from beginning to end. Vidhi Agarwal for her constant selfless support and for always pushing me to be a better person. I can never thank her enough for the impact she has made in my professional as well as personal life. Debanjan Bagchi for all the insightful discussions, honesty, and for making the environment always cheery. I am grateful for his patience and

compassion during my difficult times. Avijit Maity for being there since the beginning and making me comfortable in the new environment. I am sincerely thankful for all his help and support especially when I was too shy to ask.

I was grateful for all the wonderful people I have met and friends I have made in the last few years at IIT Indore aside from my lab who had played such a crucial part in my growth. I am thankful to my wonderful batchmates and friends Dr. Shivendu Mishra, Dr. Sayantan Sarkar, Dr. Argha Chakraborty, and Dr. Shivendra Singh for all the positivity and support. I am grateful to Ms. Moupia Mukherjee, for all the insightful scientific discussions that helped me expand my research knowledge. Then I was blessed to have the best roommates and would like to have a special mention for them. Jyoti Tiwari for her calming presence and always lending her listening ears whenever in need, Achena Saha for always being so selflessly caring and supportive like a mother outside of the home, Ekta Yadav for all the fun times and our special morning songs, and finally Dr. Vaishnavi Kulkarni, my partner in crime in late night teas/coffees and Sunday morning breakfasts.

Most importantly I would not have reached here without my parents. I am grateful to my mother Mrs. Namrata Chakraborty and my father Mr. Ashis Chakraborty for everything they have done for me. I can never express in words how thankful I am to them for being supportive, accepting, and broad-minded in every aspect of my life. Last but not least I am grateful to Anil Giri for playing such a pivotal role in helping me complete this journey. I most definitely could not have done this without his selfless support and encouragement. I am grateful to him for believing in me even in times I could not. I am indebted to him for his tremendous empathy and positivity throughout. A great number of people have been involved, whether directly or indirectly, in making this journey a success. Although I wish I could thank every one of them, time and space require me to stop here.

Amrita Chakraborty

**DEDICATED TO MY PARENTS,
ANIL, AND LATE
GRANDPARENTS**

SYNOPSIS

1. Introduction

Supramolecular chemistry forms the foundation of self-assembly, where the structural motifs of individual molecules encode instructions for assembling into larger entities. Molecular self-assembly is the spontaneous organization of molecules into ordered hierarchical structures directed by noncovalent interactions such as hydrogen bonding, π - π stacking, electrostatic interactions, Van-der-Waal forces, and hydrophobic interactions etc. Self-assembly is a widespread phenomenon in nature, where a high degree of sophistication is achieved through the ensemble of the various components into a well-defined pattern, such as in protein folding, lipid bilayer formation, and hybridization of the DNA double helix etc.^{1,2} Gels are distinguished soft colloidal states of matter embraced with viscoelastic properties which comprised of a continuous 3D cross-linked network with entrapped solvent inside. The formation of the highly entangled fibril network is a direct consequence of the self-assembly process, where macro or small molecules are integrated into well-defined fibrillar structures through noncovalent interactions. If the solvent trapped inside the fibrillar matrix is water, they are termed as hydrogels, which are ubiquitous soft solids laying foundation of a living organism.³ The extracellular matrix (ECM) of most soft tissues in our body such as cartilage, cornea, heart vessels, and skin tissue are essentially fibrous hydrogel composites.⁴ Given that hydrogel is the basic functional material in nature, it is vital to continue exploring the development of hydrogels for the creation of smart materials for various applications.

The self-organization of small biomolecules, such as amino acids, nucleic acids, and monosaccharides, serves as the foundation of life. These building blocks self-assemble and integrate into complex superstructures like proteins, DNA, and carbohydrates. Their inherent ability to self-assemble and high biocompatibility make small biomolecules excellent candidates for the formation of low molecular weight gels (LMWG). In water, the self-assembly of these fundamental

biological units forms a basis for mimicking the structural and functional characteristics of biomacromolecules. The straightforward self-assembly process eliminates the need for complex synthetic routes while preserving the essential properties of the precursors in their pristine form. The reversible non-covalent crosslinking responds to external energy making them stimuli-responsive materials. Furthermore, LMWGs offer consistency and avoid the batch-to-batch variations commonly associated with polymeric gels. Owing to their advantages, self-assembled small biomolecule hydrogels have found a broad field of applications such as in water purification and other industrial applications, controlled drug delivery, cell culture, tissue engineering, sensing, green catalysis, optoelectronic devices, etc. Nucleotides are gaining recognition as precursors for low molecular weight gels (LMWGs) due to their numerous sites for non-covalent interactions. The aromatic base groups in nucleotides provide π - π stacking and hydrophobic interaction sites, while the nitrogen, oxygen, and ribose moieties facilitate hydrogen bonding. Additionally, the phosphate groups enable further crosslinking, resulting in the formation of entangled fiber networks. Nucleotides are highly water soluble, allowing them to form hydrogels without requiring further derivatization. Among nucleotides, guanosine monophosphate (GMP) is of particular interest as a low molecular weight gelator (LMWG) due to its ability to form various types of supramolecular assemblies such as G-Quartets, dimers, ribbons, and sheets, owing to the presence of a higher number of hydrogen-bonding sites in guanine as compared to other nucleobases.⁵⁻⁹

In this thesis, we focused on the development of mechanically robust hydrogels using low-cost, commercially available, and highly biocompatible GMP as a low molecular weight gelator. A range of multifunctional properties, such as self-healing, self-supporting, injectable, stimuli-responsive, biomimetic, and ion-conducting abilities were demonstrated by the hydrogels. We aimed to establish a straightforward, efficient, and environmentally sustainable synthetic approach for developing supramolecular hydrogels of GMP with varied

moieties to tailor specific characteristics. We examined the interactions driving the growth of the fibrillar network to gain deeper insights into the biological self-assembly of biomolecules. Finally, we explored the wide-ranging potential of these self-assembled hydrogels for applications in enzyme mimetics, optoelectronics, drug delivery, and biomineralization.

2. Summary of the Thesis

The thesis comprises of total 6 chapters and the contents of each chapter included in the thesis are discussed in brief as follows:

2.1 Chapter 1. General Introduction and Background

The first chapter of the thesis is devoted to the general background and introduction to the supramolecular self-assembled gel. It addresses the basic understanding of gels and their classifications. Self-assembled hydrogels of biomolecules are also grazed on, to move on to the studies on the development of guanosine monophosphate hydrogels. We discuss the factors leading to their gelation, and also their functional properties further used for various applications, and their recent advancements.

2.2. Chapter 2. Polyoxometalate-Guanosine Monophosphate Hydrogel with Haloperoxidase-like Activity for Antibacterial Performance

In this chapter, we fabricated two supramolecular hydrogels through a simple self-assembly strategy by mixing polyoxometalates (POM), phosphotungstic acid (PTA), and silicotungstic acid (STA) with guanosine monophosphate (GMP) as a low molecular-weight hydrogelator. The hydrogels were stimuli-responsive, mechanically robust, thixotropic, and showed enhanced biocompatibility compared to bare POM. Intrinsic haloperoxidase activity of the POMs was retained in the hydrogel, with PTA showing much higher activity than STA. Kinetic studies for the haloperoxidase activities showed that the hydrogel was more specific towards the oxidation of iodide than bromide, thus showing specific iodoperoxidase activity. The iodoperoxidase activity of the PTA-GMP gel was further exploited as an antifouling agent towards both

gram-positive and gram-negative bacteria by disrupting the quorum sensing process, where the HOI formed during iodoperoxidase process catalyzes the oxidative iodination of bacterial signaling molecules such as homoserine lactones (HSL) leading to its inactivation. The ability of the PTA-GMP hydrogel to form a uniform film on the surface resulted in better antibacterial activity in comparison to only PTA solution, thus making it more suitable to be used as paint or coating compared to bare POM. The polyoxometalate-GMP hydrogel with haloperoxidase mimicking activity can be a biocompatible, sustainable, and easy approach to substitute conventional toxic antifouling coatings or expensive and inconvenient enzyme-embedded systems.

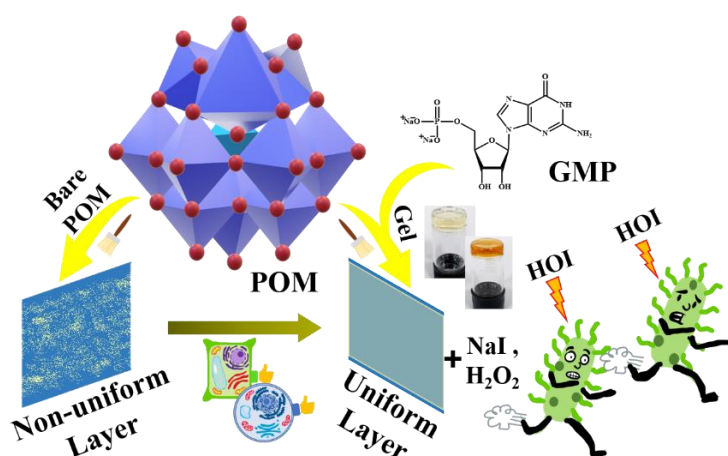


Figure 1. Schematic representation of POM-GMP hydrogel formation exhibiting haloperoxidase activity further employed for antibacterial purposes.

2.3. Chapter 3. A multi-stimuli responsive polyoxometalate-guanosine monophosphate hybrid chromogenic smart hydrogel

In Chapter 3, we discuss about developing a chromogenic supramolecular hydrogel system, developed via a simple self-assembly of Keggin-structured polyoxometalate, phosphomolybdic acid with guanosine monophosphate in an aqueous medium. The mechanically robust, flexible, and thermo-reversible hydrogel not only exhibited a stimuli-triggered visible change in its optical property, from yellow to blue upon exposure to multiple stimuli, such as visible light, stress, electricity, temperature, and metals but also showed enhanced stimuli

responsiveness as compared to its bare counterpart. The hydrogel also exhibits chemochromism towards biologically relevant thiols, such as cysteine and glutathione along with iodide selectively among all halides. Further, phosphomolybdic acid induced self-assembly of the guanosine monophosphate molecules into a G-Quartet structure makes the hydrogel conductive owing to the ion-conducting property of the supramolecular assembly. This enables in designing of a 2-layered electrochromic device (ECD) as a simpler alternative to the traditional 5-layered setup. The simplicity of fabrication of the hydrogel, biocompatibility, and responsiveness to multi-stimuli make it highly appealing for smart device applications.

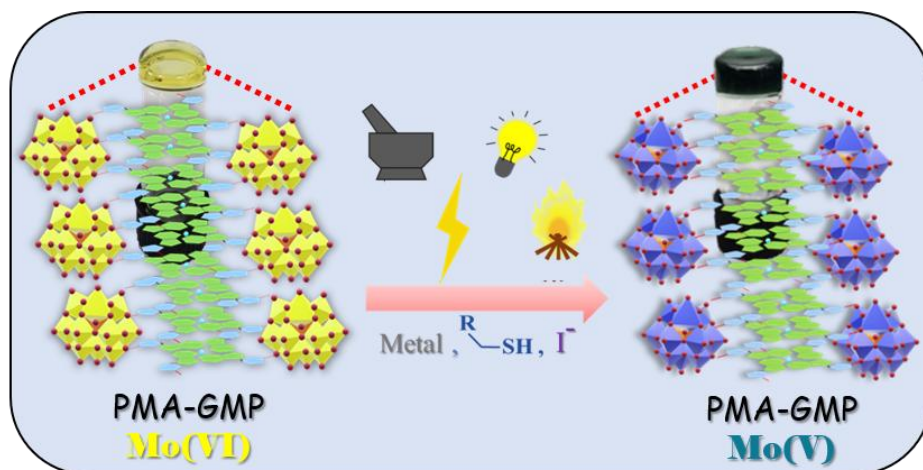


Figure 2. Schematic representation of POM-GMP hydrogel displaying multi-stimuli responsive chromism.

2.4 Chapter 4. A supramolecular approach to structurally mimic carbonic anhydrase enzyme

In Chapter 4, we designed a hydrogel that could structurally mimic the active site of the natural carbonic anhydrase enzyme by applying a simple self-assembly strategy of the small molecule precursors. The fibrillar structure of GMP provides a crowded environment similar to the protein chain in enzymes leading to the stability of the tetrahedral $Zn(His)_3H_2O$ complex. The Zn-His-GMP hydrogel also functionally mimicked the carbonic anhydrase enzyme, which was confirmed by studying the

kinetics of the esterase and CO₂ hydration activity. The hydrogel showed excellent enzymatic activity and better affinity towards the substrate than the natural enzyme. CO₂ sequestration was performed via biomineralization with different metals which provided us with interesting complex architectural structures. Biomineralization of calcium in phosphate buffer resulted in the formation of carbonated hydroxyapatite which is a very crucial mineral from the biological point of view since it's close to the chemical composition of bone and shows better resorption than pure hydroxyapatite making it suitable for bone tissue engineering. The biomineralization technique was further applied for the removal of heavy toxic metal ions such as Pb²⁺ and Cd²⁺. While the structural replication of the natural enzyme generally requires a tedious synthetic route, this simple self-assembly technique provided us with a very facile strategy to structurally and functionally mimic natural enzymes thus providing a significant step towards the direction of synthesizing various artificial enzymes.

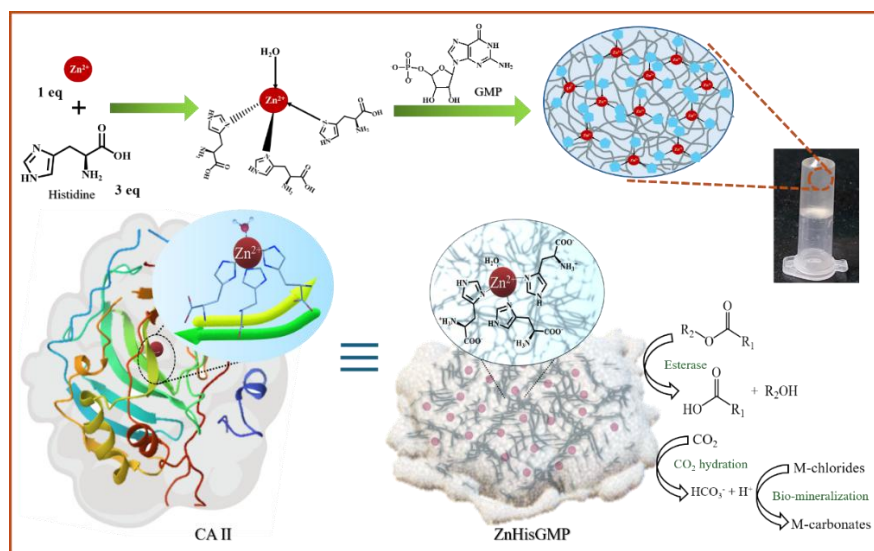


Figure 3. Schematic illustration of Zn-Histidine-GMP hydrogel formation that structurally and functionally mimics carbonic anhydrase enzyme. The hydrogel was further exploited for biomineralization of metals.

2.5 Chapter 5. Guanosine-monophosphate Induced Solubilization of Folic Acid Leading to Hydrogel Formation for Targeted Delivery of Hydrophilic and Hydrophobic Drugs

In Chapter 5, we proposed a straightforward method for preparing a hydrogel of highly water-insoluble folic acid, by enhancing its solubility through self-assembly with amphiphilic LMWG guanosine monophosphate (GMP) for targeted drug delivery. The gelation process was spontaneous and the FA-GMP hydrogel was thermoreversible, injectable, thixotropic, self-healing, self-adhesive, and highly biocompatible. The FA-GMP hydrogel was then employed as a drug carrier that could encapsulate and show sustained release for both hydrophilic (Dox) and hydrophobic (curcumin) drugs. Both the drugs showed elevated cytotoxicity and cellular uptake in the MCF-7 cancer cells when loaded in the FA-GMP hydrogel than its free form. Hydrogel-encapsulated drugs demonstrated improved therapeutic efficacy compared to free drugs by significantly upregulating the expression of tumor suppressor and apoptotic genes, while also inhibiting cell proliferation markers to a greater extent than free drugs. Loading Dox and curcumin in FA-GMP hydrogel demonstrated improved targeted delivery and overall anticancer activity. Thus, the folic acid hydrogel with GMP represents a simple, economical, and biocompatible approach that can be an effective drug carrier for targeted delivery, aiding in the fight against cancer.

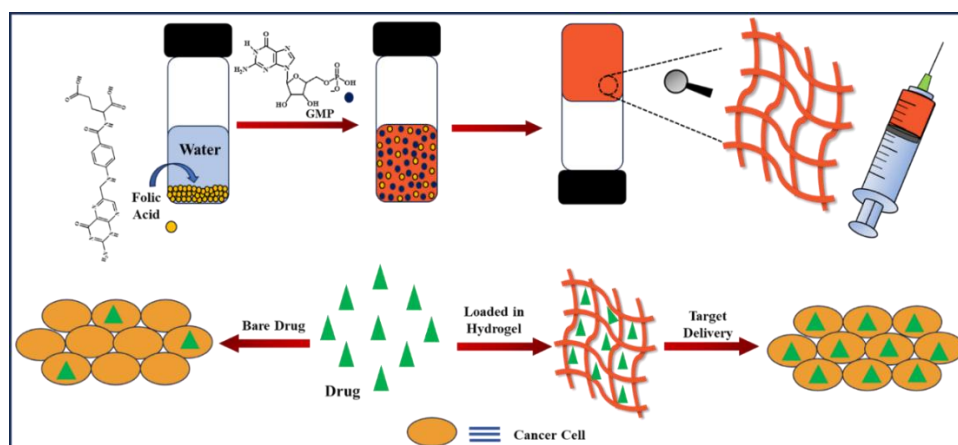


Figure 4. Schematic illustration of GMP-induced solubilization of folic acid through self-assembly ultimately leading to hydrogel formation. The hydrogel is further used for targeted drug delivery to cancer cells.

2.6. Chapter 6. Conclusion and Future Outlook

The final chapter highlights the significance of the research presented in this thesis and explores its potential for future applications. The studies primarily focus on the synthesis and applications of nucleotide-based supramolecular hybrid hydrogels of guanosine monophosphate across various fields. These investigations reveal exceptional self-assembly properties, forming self-assembled fibrillar structures of guanosine monophosphate in the presence of different crosslinkers, whether it is inorganic materials such as polyoxometalates, and Zn-Histidine complex or an insoluble organic molecule such as folic acid. The different properties of the hydrogels obtained based on the precursors used have been further utilized to develop enzyme mimetic systems, chromogenic material, biocompatible systems for controlled drug release, and structural mimics of enzymes. Looking ahead, these advancements are anticipated to open new avenues for nucleotide-based nanohybrid hydrogels in multifunctional applications.

References

1. Rajbhandary A., Nilsson B.L. (2016), Self-Assembling Hydrogels. In Gels Handbook (World Scientific), pp. 219–250. (DOI: 10.1142/9789813140370_0009)
2. Mendes A. C., Baran E. T., Reis R. L., Azevedo H. S. (2013), Self-assembly in nature: using the principles of nature to create complex nanobiomaterials. Wiley Interdiscip. Rev. Nanomed. Nanobiotechnol. 5, 582–612. (DOI: 10.1002/wnan.1238)
3. Du X., Zhou J., Shi J., Xu B. (2015), Supramolecular Hydrogelators and Hydrogels: From Soft Matter to Molecular Biomaterials. Chem. Rev. 115, 13165–13307. (DOI: 10.1021/acs.chemrev.5b00299)

4. Islam M. R., Oyen M. L. (2022), 1 - Mechanical characterization of hydrogels. In *The Mechanics of Hydrogels Elsevier Series in Mechanics of Advanced Materials.*, H. Li and V. Silberschmidt, eds. (Woodhead Publishing), pp. 1–24. (DOI: 10.1016/B978-0-08-102862-9.00014-2)
5. Vázquez-González M., Willner I. (2020), Stimuli-Responsive Biomolecule-Based Hydrogels and Their Applications. *Angew. Chem. Int. Ed.* 59, 15342–15377. (DOI: 10.1002/anie.201907670)
6. Raeburn J., Cardoso A.Z., J. Adams D. (2013), The Importance of the Self-Assembly Process to Control Mechanical Properties of Low Molecular Weight Hydrogels. *Chem. Soc. Rev.* 42, 5143–5156. (DOI: 10.1039/C3CS60030K)
7. Draper E. R., Adams D. J. (2017), Low-Molecular-Weight Gels: The State of the Art. *Chem* 3, 390–410. (DOI: 10.1016/j.chempr.2017.07.012)
8. Peters G. M., Davis J. T. (2016), Supramolecular gels made from nucleobase, nucleoside and nucleotide analogs. *Chem. Soc. Rev.* 45, 3188–3206. (DOI: 10.1039/C6CS00183A)
9. Chen M., Lin W., Hong L., Ji N., and Zhao H. (2019), The Development and Lifetime Stability Improvement of Guanosine-Based Supramolecular Hydrogels through Optimized Structure. *BioMed Res. Int.* 2019, 6258248. (DOI: 10.1155/2019/6258248)

Table of Contents

List of Figures	xxiii-xxxi
List of Tables	xxxii
Acronyms	xxxiii-xxxiv
Nomenclature	xxxv
Chapter 1: General Introduction and Background	1-52
1.1. Gels: An Introduction.....	1
1.1.1 Classification of gels.....	2
1.2. Hydrogels.....	3
1.3. Supramolecular hydrogel.....	4
1.3.1. Self-Assembly Inspiration from Nature.....	4
1.3.2. Low Molecular Weight Gelator (LMWG).....	6
1.3.3. Properties of Supramolecular Hydrogels.....	9
1.3.3.1. Self-Healing.....	9
1.3.3.2. Stimuli-Responsive Behaviour.....	10
1.3.3.3. Facile Synthetic Process.....	11
1.3.4. Hybrid Organic-Inorganic Hydrogels.....	12
1.4. Small Biomolecules as LMWG.....	13
1.4.1. Nucleobases, Nucleosides, and Nucleotides as LMWG.....	15
1.5. Supramolecular Assembly of Guanosine and Derivatives.....	17
1.5.1. History of Guanosine-Based Assembly.....	18
1.5.2. Characterization of G-Quartet Motif.....	19
1.5.3. Recent Advances in G-Assembly-Based Hydrogels.....	23
1.6. Thesis Objective.....	27

1.7. Organization of the Thesis.....	28
1.8. References.....	29
Chapter 2: Polyoxometalate-Guanosine Monophosphate Hydrogel with Haloperoxidase-like Activity for Antibacterial Performance.....	53-98
2.1. Introduction.....	53
2.2. Results and Discussion.....	56
2.2.1. Synthesis of the hydrogels.....	56
2.2.2. Morphological Evaluation.....	59
2.2.3. Spectroscopic Characterization.....	60
2.2.4. Rheological Studies.....	66
2.2.5. Haloperoxidase Activity.....	68
2.2.6. Biocompatibility Assay.....	76
2.2.7. Antibacterial Activity.....	78
2.3. Conclusion.....	81
2.4. Experimental Section.....	82
2.4.1. Materials.....	82
2.4.2. Synthesis of Hydrogels.....	82
2.4.3. Instrumentation.....	82
2.4.4. Characterization Methods.....	83
2.4.5. Haloperoxidase Activity.....	84
2.4.6. MTT Assay.....	85
2.4.7. Antibacterial Activity.....	86
2.4.8. Crystal violet assay for Biofilm Quantification.....	86
2.5. References.....	87

Chapter 3: A multi-stimuli responsive polyoxometalate-guanosine monophosphate hybrid chromogenic smart hydrogel..... 99-130

3.1. Introduction.....	99
3.2. Results and Discussion.....	101
3.2.1. Synthesis of PMA-GMP Hydrogel.....	101
3.2.2. Morphological Evaluation.....	102
3.2.3. Spectroscopic Characterization.....	103
3.2.4. Mechanical Strength.....	107
3.2.5. Chromogenic response to physical stimuli.....	109
Designing 2-layered Electrochromic device.....	111
3.2.6. Chromogenic response to chemical stimuli.....	112
3.2.7. Reversibility Cycle.....	115
3.2.8. Reduction of Mo ^{VI} to Mo ^V	115
3.3. Conclusion.....	116
3.4. Experimental Section.....	117
3.4.1. Materials.....	117
3.4.2. Synthesis of Hydrogel.....	117
3.4.3. Instrumentation.....	117
3.4.4. Characterization method.....	118
3.4.5. UV-visible studies for chromism.....	119
3.4.6. Cyclic Voltammetry.....	120
3.4.7. Conductivity Measurement.....	120
3.4.8. X-ray photoelectron spectroscopy (XPS).....	120
3.5. References.....	121

Chapter 4: Zinc-histidine complex hydrogel with GMP, a supramolecular approach to structurally mimic carbonic anhydrase enzyme..... 131-168

4.1. Introduction.....	131
4.2. Results and Discussion.....	134
4.2.1. Synthesis of Hydrogel.....	134
4.2.2. Morphological Evaluation.....	135
4.2.3. Spectroscopic Characterization.....	135
4.2.4. Rheological Studies.....	143
4.2.5. Esterase Activity.....	144
4.2.6. CO ₂ hydration activity.....	147
4.2.7. Biomineralization for CO ₂ sequestration.....	148
4.3. Conclusion.....	155
4.4. Experimental Section.....	156
4.4.1. Materials and Reagents.....	156
4.4.2. Preparation of Hydrogel.....	157
4.4.3. Characterization method.....	157
4.4.4. Esterase Assay.....	158
4.4.5. CO ₂ Hydration and pH Studies.....	160
4.4.6. Biomineralization of Metal Carbonates.....	160
4.5. References.....	161

Chapter 5: Guanosine-monophosphate Induced Solubilization of Folic Acid Leading to Hydrogel Formation for Targeted Delivery of Hydrophilic and Hydrophobic Drugs..... 169-206

5.1 Introduction.....	169
5.2. Results and Discussion.....	172

5.2.1. Fabrication of Hydrogel.....	172
5.2.2. Morphological Evaluation.....	174
5.2.3. Spectroscopic Characterization.....	175
5.2.4. Rheological Studies.....	179
5.2.5. Drug Encapsulation and Release.....	179
5.2.6. Biocompatible of Hydrogel.....	182
5.2.7. Cytotoxicity Against Cancer Cells.....	183
5.2.8. Cellular Uptake.....	184
5.2.9. Anticancer Properties of Compounds.....	186
5.3. Conclusion.....	188
5.4. Experimental Section.....	189
5.4.1. Materials.....	189
5.4.2. Instrument.....	190
5.4.3. Synthesis of Hydrogel.....	190
5.4.4. Characterization.....	191
5.4.5. Drug Encapsulation and Release.....	192
5.4.6. Cell Culture.....	193
5.4.7. Cell Cytotoxicity through MTT Assay.....	193
5.4.8. Cellular Uptake.....	193
5.4.9. Quantitative real-time polymerase chain reaction.....	194
5.4.10. Cell Proliferation Assay.....	194
5.4.11. Statistical Analysis.....	194
5.5. References.....	195

Chapter 6: Conclusion and Future Scope.....	207-209
6.1. Conclusion.....	207
6.2. Future Prospect.....	208
List of Publications.....	211-212

List of Figures

Figure 1.1. Representation of a gel and the constituent fibrillar network.....	1
Figure 1.2. Classification of gels.....	2
Figure 1.3. Hydrogels in living organisms.....	3
Figure 1.4. Non-covalent interactions involved in self-assembled systems.....	5
Figure 1.5. (a) molecular aggregation with three possibilities: (i) crystal, (ii) amorphous precipitate, and (iii) gel and (b) different stages of self-assembly leading to gelation.....	8
Figure 1.6. Characterization techniques to understand the mechanism of supramolecular hydrogel formation.....	9
Figure 1.7. Digital images displaying the self-healing property of supramolecular hydrogels.....	10
Figure 1.8. Digital images displaying the stimuli-responsive nature of supramolecular hydrogels.....	11
Figure 1.9. Illustration showing biomolecules as low molecular weight hydrogelator.....	15
Figure 1.10. Sites for non-covalent interactions in nucleobases, nucleotides, and nucleosides	16
Figure 1.11. Figure depicting different sites and faces for hydrogen bonding in guanine further lead to the formation of G-quartet and Ribbon assemblies.....	18
Figure 1.12. Figure showing the crystal structure of DHX36 Bound to the c-Myc G-quartet.....	19
Figure 1.13. Various characterization techniques for G-quadruplex structure (a) PXRD, (b) ThT assay, (c) CD, (d) Proton NMR, and (e) Sodium NMR.....	21

Figure 1.14. Recent research works using G-assembly in the biomedical field.....	24
Figure 2.1. Formation of polyoxometalate (POM), phosphotungstic acid (PTA), and silicotungstic acid (STA) hydrogels with GMP.....	57
Figure 2.2. Digital images of POM-GMP system with different concentrations (a, b) varying the concentration of GMP with respect to POMs, (c, d) varying the concentration of POMs with respect to GMP.....	58
Figure 2.3. Digital images displaying (a,b) thermoreversible property of the hydrogels (c,d) gel molded into different shapes, (e,f) Stimuli-responsive behavior of the hydrogel, (g-l) the hydrogels dried to thin films.....	59
Figure 2.4. (a,b) SEM and (c,d) TEM images of the hydrogels.....	60
Figure 2.5. (a, b) UV-vis spectra of GMP, POMs, and GMP-POM hydrogels, (c,e) UV spectra upon addition of an equimolar solution of GMP to PTA and STA solutions respectively at different ratios, (d, f) their respective Job's plot.....	61
Figure 2.6. (a, b) CD spectra of POM, GMP, and POM-GMP hydrogels Circular dichroism spectra of the hydrogels recorded with decreasing mole fraction of GMP respectively.....	62
Figure 2.7. (a,b) FTIR spectra of PTA and STA xerogels, and (c) Digital image of PTA-IMP system showing the inability of POM to form a hydrogel with IMP.....	64
Figure 2.8. (a) ^1H and (b) ^{31}P NMR spectra of GMP, PTA-GMP, and STA-GMP.....	65
Figure 2.9. A schematic representation for the proposed self-assembly of the POM (PTA, STA) and GMP leading to a hydrogel.....	66

Figure 2.10. (a, c) Dynamic strain sweep hydrogels respectively, (b, d) Frequency sweep measurements and (e, f) Thixotropic loop measurements for PTA GMP and STA-GMP hydrogels.....	67
Figure 2.11. Digital images showing (a) rigidity and mechanical robustness of the hydrogels where it can hold weight and (b) injectability of the hydrogels.....	68
Figure 2.12. (a) Thymol blue (TB) and Phenol red (PR) colorimetric assay for haloperoxidase activity, (b) Haloperoxidase activity comparison of PTA and STA hydrogels, and (c) Control experiments.....	69
Figure 2.13. Time-dependent UV-visible spectra of (a) Iodination and (b) bromination of thymol blue (TB) respectively, and (c) Iodination and (d) Bromination of phenol red (PR) respectively using PTA-GMP as the catalyst.....	70
Figure 2.14. Effect of (a) pH and (b) temperature on haloperoxidase activity.....	71
Figure 2.15. Michaelis-Menten curve to calculate kinetic parameters with respect to I^- and H_2O_2 in TB and PR assay.....	72
Figure 2.16. Michaelis-Menten curve to calculate kinetic parameters with respect to Br^- and H_2O_2 in TB and PR assay.....	73
Figure 2.17. UV-vis spectra of oxidative iodination of thymol blue in the presence of natural anti-oxidants (a) ascorbic acid and (b) cysteine.....	74
Figure 2.18. A probable mechanism for the iodoperoxidase reaction of PTA-GMP.....	75
Figure 2.19. Measurement of the amount of oxygen released for: i) H_2O_2 + catalyst, ii) $NaI + H_2O_2$, iii) $NaI + H_2O_2 + PTA-GMP$ hydrogel iv) $TB + NaI + H_2O_2 + PTA-GMP$ hydrogel system.....	76
Figure 2.20. (a) Cell viability % of HeK cells after treatment with bare POM solutions (PTA and STA) and their hydrogels (PTA-GMP and STA-	

GMP) (b) Cell viability % of HeK cells after treatment with (i) Untreated (ii) PTA-GMP hydrogel, (iii) only H₂O₂, (iv) H₂O₂ + NaI, and (iv) PTA-GMP + NaI + H₂O₂ system..... 77

Figure 2.21. Antibacterial activity of the hydrogel in the presence of NaI and H₂O₂..... 79

Figure 2.22. Digital image showing the difference in an inhomogeneous aggregation of bare PTA and the uniform coating of PTA-GMP hydrogel..... 80

Figure 2.23. Biofilm inhibition activity of the hydrogel in the presence of NaI and H₂O₂..... 81

Figure 3.1. (a) Schematic representation of the formation of PMA-GMP hydrogel and its thermoreversible property, (b) Digital images depicting the shape molding ability of PMA-GMP hydrogel owing to its thermoreversible property, and (c) Concentration-dependent studies of PMA-GMP system..... 102

Figure 3.2. (a) FESEM image of PMA-GMP hydrogel showing highly tangled fibrillar morphology, (b) HRTEM image of the fibril strands, and (c) AFM image of the hydrogel..... 103

Figure 3.3. (a) CD spectra and (b) ¹H NMR spectra of GMP and PMA-GMP hydrogel..... 104

Figure 3.4. (a) UV-visible spectra of GMP, PMA, and PMA-GMP solution, (b, c) UV-vis and circular dichroism spectra of PMA-GMP recorded with decreasing mole fraction of GMP..... 105

Figure 3.5. (a) ³¹P NMR of GMP, PMA, and PMA-GMP hydrogel, (b) FTIR spectra of GMP, PMA, and PMA-GMP hydrogel, and (c) PXRD of PMA and PMA-GMP hydrogel..... 106

Figure 3.6. Schematic representation for the proposed self-assembly of the PMA and GMP leading to fibrillar morphology resulting in gelation..... 107

Figure 3.7. Measurement of (a) Dynamic strain-sweep, (b) Frequency sweep, (c) Thixotropic loop, and (d) Tensile stress vs tensile strain curve of PMA-GMP hydrogel.....	108
Figure 3.8. Digital images showing (a) the mechanical strength, (b) the injectability of the hydrogel, and (c) the hydrogel stretched in the universal testing machine.....	109
Figure 3.9. (a) Digital image of PMA-GMP hydrogel before and after exposure to electricity, visible light, temperature, and mechanical stress, (b) UV-visible spectra of the hydrogel and after triggered by stimuli, (c) i) PMA-GMP hydrogel and bare PMA solution on heating, ii) PMA-GMP hydrogel and bare PMA solution after exposure to light.....	110
Figure 3.10. (a) UV-vis absorbance spectra of the hydrogel heated at different temperatures (inset: digital images), (b) Time-dependent UV-visible spectra of PMA-GMP hydrogel exposed to heat, and (c) Time-dependent UV-vis spectra of the hydrogel after exposure to light.....	111
Figure 3.11. (a) Cyclic voltammogram of bare PMA solution and PMA-GMP hydrogel, (b) Electrochemical impedance spectroscopy (Nyquist plot) of the PMA-GMP hydrogel, (c) i) traditional electrochromic device with five layers, and ii) proposed electrochromic device with two layers, and (d) digital image of the electrochromic device.....	112
Figure 3.12. (a) Absorbance spectra of the hydrogel after exposure to various metals, (b) UV-visible spectra of the hydrogel in response to glutathione, cysteine, 2,3 – dimercaptosuccinic acid, (c) UV-vis spectra of the hydrogel in response to iodide	113
Figure 3.13. Concentration-dependent absorbance spectra of the hydrogel when treated with varying concentrations of (a) GSH, (b) cysteine, (c) 2,3-DMSA, and (d) Iodide respectively, and their digital images.....	114

Figure 3.14. Halochromic behavior as well as sol-gel transition of PMA-GMP hydrogel with pH change.....	115
Figure 3.15. Reversibility cycle for chromism induced by various stimuli (a) mechanical stress, (b) visible light, (c) electricity, (d) temperature, and (e) metal (Fe).....	115
Figure 3.16. Deconvoluted XPS spectra of PMA-GMP xerogel (a) Before exposure to stimuli, (b) after exposure to mechanical stress, (c) after exposure to visible light, (d) after exposure to elevated temperature, (e) after exposure to electricity, and (f) after exposed to metal.....	116
Figure 4.1. (a) Schematic representation of the formation of ZnHG Hydrogel through the intermediate step of ZnH complex, (b-d) Digital image of ZnHG system varying the component ratio (Zn:His:GMP).....	134
Figure 4.2. (a-c) SEM images of ZnHG supramolecular system for day 2, day 7, and day 14 respectively, (d) TEM image of ZnHG hydrogel, (e) AFM image of the hydrogel.....	135
Figure 4.3. (a) UV-visible spectra of ZnSO ₄ , histidine, GMP, ZnH complex, and ZnHG hydrogel, (b) UV-vis spectra upon addition of GMP to ZnH solution at variable concentration ratio, and (c) Job's plot calculated.....	137
Figure 4.4. (a) ¹ H NMR of histidine and Zn-histidine complex, (b, c) Deconvoluted N 1s XPS spectra for histidine and Zn-histidine complex.....	138
Figure 4.5. (a) ThT assay for ZnHG system, (b) Comparison of ThT+ZnHG emission with different reported assemblies, (c) Temperature-dependent emission spectra of ThT+ZnHG system, and (d) PXRD data of ZnH complex and ZnHG hydrogel.....	139
Figure 4.6. (a) FTIR of GMP and ZnHG xerogel and (b) ³¹ P NMR of GMP and ZnHG hydrogel.....	140

Figure 4.7. LCMS spectra of (a) ZnH complex and (b) ZnHG Hydrogel.....	141
Figure 4.8. Deconvoluted Zn 2p xps spectra of (a) ZnH complex and (b) ZnHG xerogel.....	142
Figure 4.9. A schematic representation of the plausible building mechanism of the ZnHG Hydrogel.....	143
Figure 4.10. (a) Dynamic strain sweep, (b) Frequency sweep measurements, (c) Thixotropic loop measurements, and (d) Viscosity measurement as a function of shear rate for ZnHG hydrogel.....	144
Figure 4.11. (a,b) Esterase activity of ZnHG Xerogel hydrolyzing pNPA to pNP (c) Time-dependent UV-visible spectra of pNPA hydrolysis reaction for 30 minutes, (d) the control experiment to compare esterase activity of precursors, bare ZnH complex, and ZnHG xerogel, and (e) Hydrolysis rate for different nitrophenyl esters.....	145
Figure 4.12. Steady-state kinetic assay for pNPA, (f,g) effect of pH and temperature in reaction rate respectively, and (h) Recyclability study for ZnHG xerogel.....	146
Figure 4.13. (a) Change in pH value under CO ₂ bubbling condition in absence and in presence of ZnHG xerogel, (b) change in UV-visible absorbance of PR in the presence of CO ₂ before and after addition of ZnHG xerogel, (c) Michaelis Menten curve fitting for CO ₂ hydration by varying CO ₂ concentration, (d) recyclability of the ZnHG xerogel.....	148
Figure 4.14. (a) SEM image, (b,c) SEM-EDS analysis, (d-f) EDS elemental mapping of the C, O, and P respectively, (g) FTIR, and (h) PXRD of CO ₃ Ap.....	149
Figure 4.15. (a) SEM image, (b,c) SEM-EDS analysis (d-f) EDS elemental mapping of the Ca, O, and C respectively, (g) FTIR, and (h) PXRD of CaCO ₃	150

Figure 4.16. (a,b) SEM image (c,d) SEM-EDS analysis (e-h) EDS elemental mapping of the O, Ba, C, and P respectively, (j) FTIR, and (i) PXRD of silicate biomorph implying BaCO ₃	152
Figure 4.17. (a) SEM image (b,c) SEM-EDS analysis, (d-f) EDS elemental mapping of the O, Ba, and C respectively, (g) FTIR, and (h) PXRD of BaCO ₃	153
Figure 4.18. (a) SEM image, (b,c) SEM-EDS analysis, (d-f) EDS elemental mapping of the O, Pb, and C respectively, (g) FTIR, and (h) PXRD of PbCO ₃	154
Figure 4.19. (a) SEM image (d,e) SEM-EDS analysis of CdCO ₃ , (f-h) EDS elemental mapping of the O, Cd, and C respectively, (i) FTIR, and (j) PXRD of CdCO ₃	155
Figure 5.1. Formation of FA-GMP hydrogel and its thermoreversible property.....	172
Figure 5.2. Digital images demonstrating (a) Concentration-dependent gelation process, (b) solubility comparison of bare FA and FA-GMP, (c) self-adhesive property of the FA-GMP hydrogel, (d) flexibility of the hydrogel where it can be compressed and stretched to a thin line, and (e) the self-healing property of the hydrogel.....	173
Figure 5.3. (a) SEM, (b) TEM, and (c) AFM images of the FA-GMP hydrogel showing highly tangled fibrillar morphology.....	174
Figure 5.4. (a) UV-visible spectra of FA, GMP, and FA-GMP hydrogel, (b) PXRD of FA-GMP xerogel, (c) ²³ Na NMR spectra for GMP and FA-GMP hydrogel, (d) ThT assay for FA-GMP hydrogel.....	176
Figure 5.5. (a) ³¹ P NMR of GMP and FA-GMP hydrogel and (b) FTIR of FA, GMP, and FA-GMP xerogel.....	177
Figure 5.6. Schematic representation for the proposed self-assembly mechanism of FA and GMP leading to hydrogel formation.....	178

Figure 5.7. (a) Dynamic strain-sweep analysis, (b) Frequency sweep measurement, (c) Thixotropic loop measurements, and (d) digital images showing injectability of FA-GMP hydrogel.....	179
Figure 5.8. (a) Structure of (i) hydrophilic drug: Doxorubicin hydrochloride and (ii) hydrophobic drug: curcumin, (b) Digital images of FA-GMP hydrogel, Dox-loaded FA-GMP hydrogel, and curcumin-loaded FA-GMP hydrogel and their amplitude strain sweep analysis, and (c) Digital image of bare curcumin and curcumin loaded on FA-GMP hydrogel.....	180
Figure 5.9. (a, c) Calibration curve of Dox and curcumin, and (b, d) Absorbance spectra of initial concentration to drug and supernatant obtained after washing drug-loaded hydrogels.....	181
Figure 5.10. The cumulative release profile of (a) Doxorubicin and (b) Curcumin from FA-GMP hydrogel.....	182
Figure 5.11. Biocompatibility experiment by assessment of HEK293T cells viability after treatment with a) FA, b) GMP, and c) FA-GMP.....	182
Figure 5.12. Cell viability of MCF-7 cells after treatment with (a) Dox, (b) Dox-FAGMP, (c) Cur, and (d) Cur-FA-GMP.....	183
Figure 5.13. CLSM images to study cellular uptake of (a) bare Dox and Dox loaded in the hydrogel, and (b) bare curcumin and curcumin loaded in the hydrogel in MCF7 cells.....	185-186
Figure 5.14. Investigating the markers related to cancer properties: a) Tumour suppressor genes, (b) apoptotic markers, and (c) cell cycle regulator genes after treatment with Dox, Dox-FA-GMP, Cur, and Cur-FA-GMP.....	187
Figure 5.15. Cell proliferation assay.....	188

List of Tables

Table 2.1. K_m and V_{max} values with respect to I^- , and H_2O_2 73

Table 2.2. K_m and V_{max} values with respect to Br^- , and H_2O_2 74

Acronyms

3D	Three Dimensional
LWMG	Low Molecular Weight Gelator
pH	The negative logarithm of hydronium-ion concentration ($-\log_{10} [\text{H}_3\text{O}^+]$)
DNA	Deoxyribonucleic acid
RNA	Ribonucleic acid
5'-GMP	Guanosine monophosphate
POM	Polyoxometalate
PTA	Phosphotungstic acid
STA	Silicotungstic acid
PMA	Phosphomolybdic acid
A	Adenine
G	Guanine
C	Cytosine
T	Thymine
U	Uracil
UV-vis	Ultraviolet-visible
CD	Circular dichroism
SEM	Scanning electron microscopy
TEM	Transmission electron microscopy

AFM	Atomic force microscopy
FTIR	Fourier Transform Infrared
NMR	Nuclear magnetic resonance
CLSM	Confocal laser scan microscopy
Asp	Aspartic acid
His	Histidine
Cys	Cysteine
2,3-DMSA	2,3-Dimercaptosuccinic acid
EDS	Energy dispersive X-ray spectroscopy
Dox	Doxorubicin
Cur	Curcumin
FA	Folic Acid
LMCT	Ligand to metal charge transfer
XPS	X-ray Photoelectron Spectroscopy
G'	Storage Modulus
G''	Loss Modulus
EIS	Electrochemical impedance study
ECD	Electrochromic device
FL	Fluorescence
AS	Amplitude Sweep
FS	Frequency Sweep

Nomenclature

λ Wavelength

π Pi

nm Nanometre

eV Electron volt

\AA Armstrong

θ Theta

ϵ Extinction coefficient

s Seconds

M Molar concentration

μM Micromolar

mV Millivolt

mS Milli Siemens

Hz Hertz

σ Sigma

μl Microlitre

$^{\circ}\text{C}$ Degree Centigrade

a.u. Arbitrary Unit

mg Milligram

Chapter 1

Introduction and General Background

1.1 Gels: An Introduction

Gels are quasi-solid materials comprising three-dimensional crosslinked networks and can immobilize large amounts of solvent in their matrix. According to the IUPAC Gold Book, a gel is defined as a non-fluid colloidal or polymer network that is expanded throughout its whole volume by a fluid.¹⁻³ An elementary identification test to determine the formation of a gel is an “inversion test”, i.e., when a vial containing gel matrix is inverted upside down it does not flow under the gravitational pull (Figure 1.1). The gel matrix arises from the coexistence of two distinct phases: an abundant 'liquid-like' phase and a 'solid-like' network thus making it a viscoelastic material where the elastic property is dominant over the viscous property.⁴⁻⁶ A gelator is the basic unit of a gel that forms a three-dimensional network and sometimes there may be more than one type of gelator component in a gel that can be either covalently crosslinked (chemical gels) or non-covalently crosslinked (physical gels) to each other.⁷ Gels, such as cosmetic creams, toothpaste, facewash, jam jelly, etc., have become an integral part of our daily lives.⁸

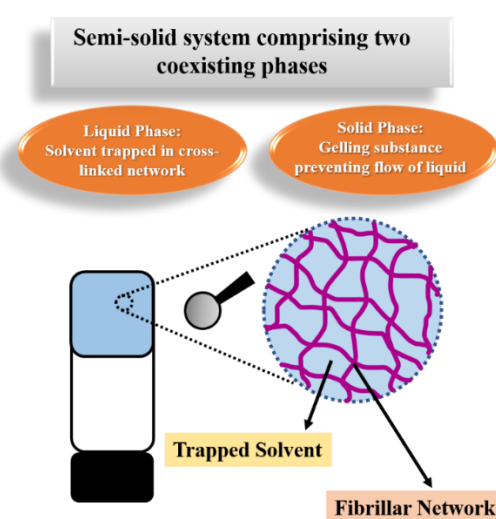


Figure 1.1. Representation of a gel and the presence of two phases within the gel

1.1.1 Classification of gels

Gels can be categorized in various ways based on their composition, the type of cross-linking that forms their 3D structure, and the solvent medium (Figure 1.2). They are classified into macromolecular (polymer) gels and supramolecular gels, with the latter originating from small molecule precursors. If the gelation process involves permanent covalent cross-linking, the gel is considered a chemical gel. In contrast, physical gels are formed through dynamic non-covalent interactions. The gelation of macromolecular compounds can occur through either chemical cross-linking or physical interactions. Gels are classified as hydrogels when the solvent is water and organogels when an organic solvent is used.^{7,9,10}

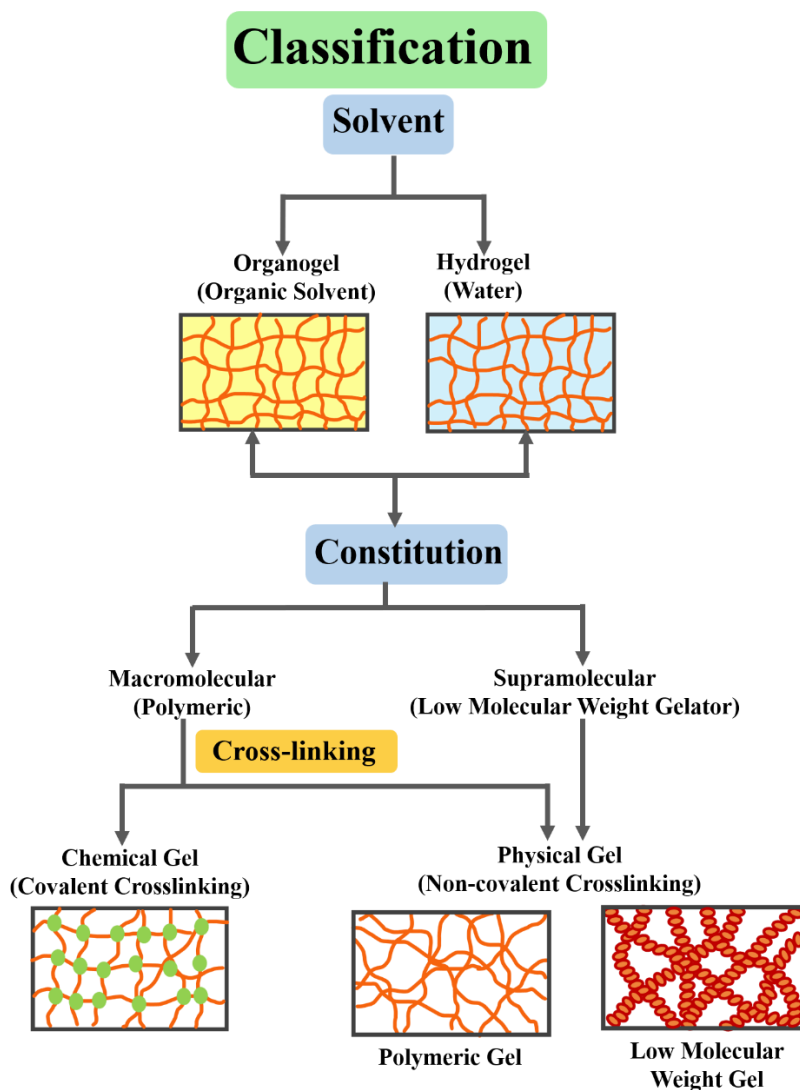


Figure 1.2. Classification of gels.

Gels derived from low molecular weight gelator (LMWG) compounds are strictly considered supramolecular, as they are formed through the self-aggregation of small gelator molecules. This process creates entangled self-assembled fibrillar networks (SAFINs) via a combination of non-covalent interactions such as hydrogen bonding, π - π stacking, metal coordination, solvophobic forces (or hydrophobic forces in water-based gels), and van der Waals interactions.^{7,11}

1.2. Hydrogel

Hydrogels are integral to the structure and function of living organisms (Figure 1.3). The cytoplasm, the gelatinous fluid that fills the cellular matrix, is a hydrogel.^{12,13} Likewise, the extracellular matrix (ECM) of many soft tissues - such as cartilage, the cornea, blood vessels, and skin is made up of fibrous hydrogel composites. Vitreous humor in eyes is a hydrogel with a viscous gelatinous consistency.¹⁴ These composites comprise a hydrated proteoglycan gel reinforced with biopolymer fibers, such as collagen or elastin. Yuk *et al.* developed a hydrogel that could perform as joints for mechanical and robotic structures. The group later stated that '*the human body is a hydrogel soft robot*'.¹⁵ Gelatin, agar, collagen, chitosan, and alginate are some naturally occurring biopolymers that comprise most of the hydrogels in nature.^{16,17}

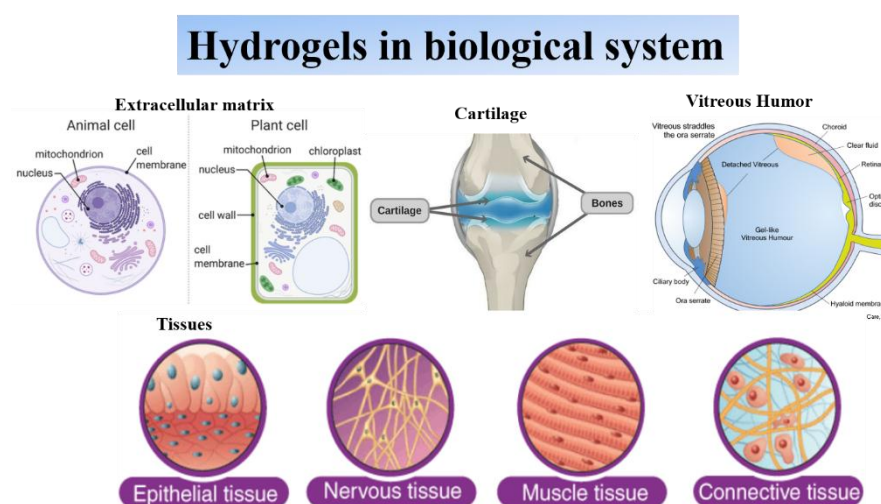


Figure 1.3. Hydrogels in biological systems.

As hydrogels serve as a fundamental functional material in nature, it is essential to continue advancing their development and understanding their self-assembled mechanism. Their high water-retention, soft tissue-like properties, biocompatibility, and biodegradability make hydrogels particularly well-suited for creating biomimetic materials.^{18–20} They play a crucial role in various biomedical applications, including contact lenses,^{21,22} drug delivery systems,^{23–25} tissue engineering^{26–29}, wound care and closure,^{30–33} and tumor treatment,³⁴ etc. Consequently, hydrogels hold significant promise, surpassing organogels, which face limitations in biomedical fields. It is important to note that early research about hydrogels addressed polymer-based gels such as poly (ethylene glycol) diacrylate, poly (acryl amide), poly (vinyl alcohol) as synthetic polymers, and gelatin, agar, chitosan, and alginate as natural polymers. These are still the most commonly found in commercial use and supermarkets. However, since the 1990s, an essential and highly encouraging field of research has developed, emphasizing the use of low molecular weight gelators (LMWG) for creating gels guided by supramolecular protocols.³⁵

1.3. Supramolecular Hydrogel

1.3.1. Self-Assembly Inspiration from Nature

Supramolecular chemistry forms the foundation of self-assembly, where the structural motifs of individual molecules encode instructions for assembling into larger entities.³⁶ This is a spontaneous process occurring with the help of several non-covalent interactions such as hydrogen bonding, hydrophobic effect, stacking interactions, Van der Waals force, electrostatic interactions, etc. Self-assembly is a widespread phenomenon in nature that is crucial for the emergence, sustenance, and evolution of life.^{37,38} Through the self-assembly of small molecules, a higher degree of sophistication is achieved through the ensemble of the various components into a well-defined pattern. Some examples of naturally occurring self-assemblies found in biological systems are the lipid bilayer membrane of cells,³⁹ RNA⁴⁰, and DNA complexes.⁴¹ These

organized assemblies are crucial for important physiological roles and life functions, such as amyloid fibril formation⁴², chromatin organization⁴³, antigen-antibody recognition^{44,45}, and membrane construction.⁴⁶ Since these self-assembled structures are also indicators of several diseases, such as amyloid fibrillation in the case of Alzheimer's or Parkinson's, understanding the pathway for self-assembly in the bio-world is crucial for diagnosis and therapeutics.⁴⁷

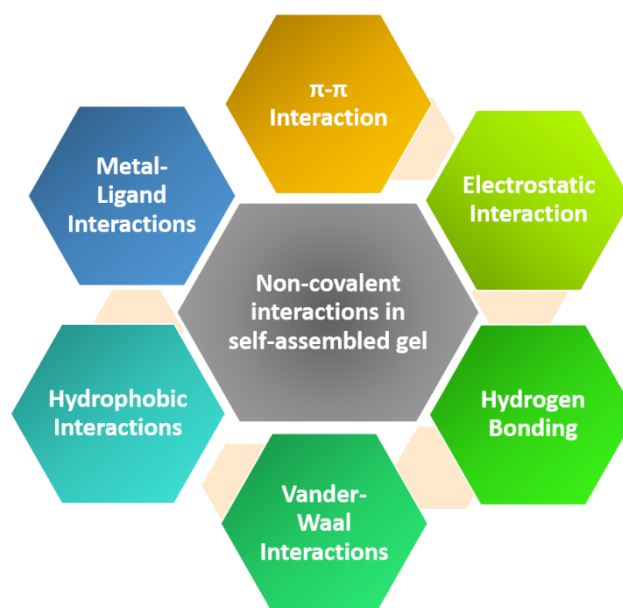


Figure 1.4. Non-covalent interactions are involved in a self-assembled system.

These nature-inspired architectures have served as a blueprint for the development of innovative synthetic and strategic counterparts, designed to mimic their organization and functionality. Since the formation of gel is one of the common consequences of self-assembly, this approach has paved the way for the creation of a new generation of porous, intelligent, and adaptive materials for a wide range of applications such as in the biomedical field⁴⁸, optics⁴⁹, energy field^{50,51}, catalysis⁵², electronic materials,^{53,54} etc.

1.3.2. Low Molecular Weight Gelator (LMWG)

Low molecular weight gelators (LMWG) are small compounds with a molecular weight of ≤ 3000 Daltons.⁵⁵ The formation of gels occurs as small molecules self-assemble into long, anisotropic structures, usually fibers. At higher concentrations of the gelator, sometimes in the presence of a trigger, these fibers interconnect or cross-link, creating a network that traps the solvent.^{55,56} During the 1930s, the first molecular gelators were introduced, serving as thickeners in lubricants, printing inks, and napalm. However, research in this area remained at a standstill for decades until it was revived in the mid-1990s, by Hanabusa, Shinkai, Hamilton, van Eshch, and a few other groups.⁵⁷ Hanabusa, a Japanese researcher and his coworkers, accidentally discovered that while synthesizing amphiphilic amino acid derivatives, gelation of methanol or cyclohexane took place in the presence of a small quantity (less than 1% by weight) of N-benzyloxycarbonyl-L-alanine 4-hexadecanoyl-2-nitrophenyl ester was present.⁵⁷ Since then, a wide range of low molecular weight (LMW) structures has been identified as capable of forming gels. Initially, many of these discoveries were made by chance. With a deeper understanding of structural motifs that encourage aggregation, deliberate design approaches have become more achievable. As noted by Du et al., “One can (almost) make any small molecule a supramolecular hydrogelator, providing proper derivatization.”¹¹ Despite this progress, one cannot certainly predict whether a specific molecule will gel based solely on its structure. LMWGs that lead to the formation of hydrogels usually consist of hydrophilic components, which ensure compatibility with water, and hydrophobic components that promote the self-assembly of the LMWG in water.⁵⁸ Supramolecular hydrogels formed from LMWG tend to have different properties to those of polymeric gels which endow the supramolecular gels with an upper hand in some aspects.⁵⁹ Since the crosslinking occurs via dynamic non-covalent interactions in LMWG, they often show stimuli-responsive reversible gel-to-solution transition. This dynamic nature of interaction also renders the hydrogel with self-healing properties.^{55,60} The absence of covalent interactions keeps the precursors in their original form

without any modification, thereby preserving their properties. Furthermore, LMWGs offer consistency and avoid the batch-to-batch variations commonly associated with polymeric gels. The connection between self-assembly and hydrogel formation is not yet fully understood. Not all substances that self-assemble in water contribute to the gelation of the medium. Some self-assembled materials form fibers that simply precipitate out of the solution, likely due to suboptimal interactions between the supramolecular fiber network and water. In cases where self-assembled materials do promote hydrogelation, the rate of assembly does not always correspond directly with the development of hydrogel properties. Hydrogels of low molecular mass gelators are generally fabricated by dissolving the gelator in water through heating, followed by cooling the isotropic supersaturated solution to room temperature. Upon cooling, the molecules begin to condense, which can lead to three possible outcomes: (1) orderly aggregation that forms crystals, known as crystallization, (2) disordered aggregation producing an amorphous precipitate, or (3) an intermediate aggregation process that results in the formation of a gel (Figure 1.5 a).⁷ For gelation to occur, a network of fibers must be formed. This process involves multiple levels of hierarchical assembly, from individual molecules to the overall network (Figure 1.5 b). As previously mentioned, molecular interactions are essential for driving self-assembly, which in turn governs the formation of the nanostructures. This nanostructure must favor the formation of one-dimensional fibers rather than other possible configurations. The self-assembly of these one-dimensional structures, as opposed to crystallization, is influenced by a balance of forces. Non-covalent interactions, such as hydrogen bonding and π -stacking, facilitate the assembly. In an aqueous environment, hydrophobic forces are the primary drivers of assembly. The mechanical properties of a hydrogel are influenced by factors such as the average thickness and mechanical properties of the fibers, the degree of branching (i.e., the spacing between cross-linking points), the type of cross-link, and the microstructure (i.e., the arrangement of fibers at a larger scale).⁶¹ These characteristics are, to some extent, determined by the molecular structure, as the primary

assembly is driven by the intermolecular interactions encoded within the molecules.

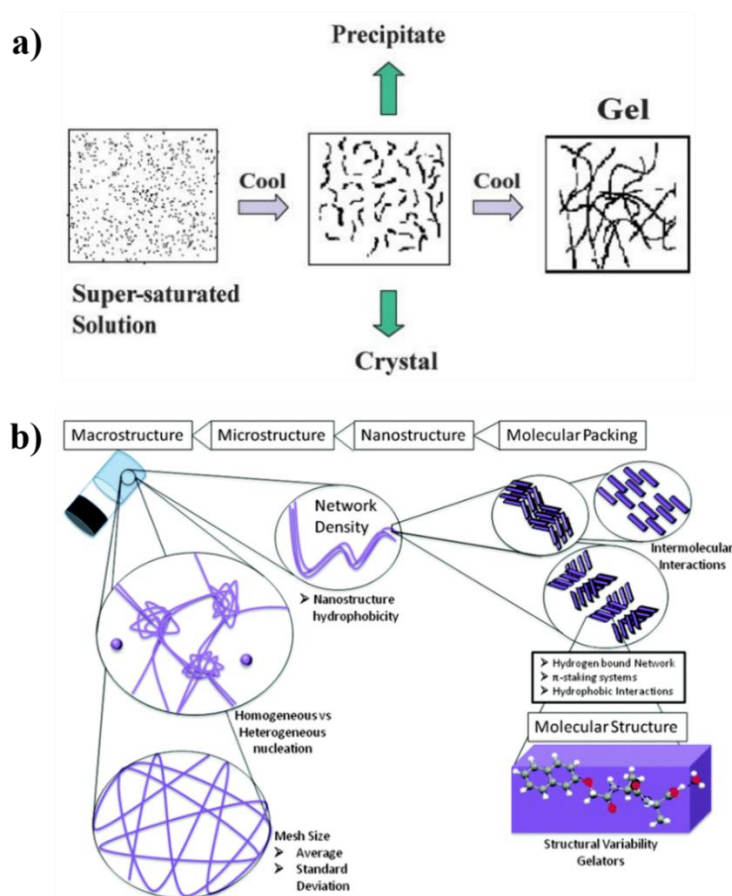


Figure 1.5. Schematic representation of (a) molecular aggregation with three possibilities of product: (i) crystal, (ii) amorphous precipitate, and (iii) gel,[7] (copyright 2005 RSC) (b) different stages of self-assembly leading to gelation.[59] (copyright 2013 RSC)

The formation of a supramolecular hydrogel is a multi-step process involving different interactive sites for various non-covalent interactions and to explore the process of hydrogelation, a diverse range of skills and instrumentation techniques is necessary (Figure 1.6). Understanding the supramolecular interactions and molecular self-assembly/packing involves employing several spectroscopic methods, such as Fourier Transform Infrared Spectroscopy (FTIR), Nuclear Magnetic Resonance (NMR), Circular Dichroism (CD), X-ray Diffraction, and Fluorescence Spectroscopy. The viscoelastic property and the mechanical strength of the hydrogel are determined by

rheological studies where elastic modulus (G') is dominant over the viscous modulus (G'').^{62,63}

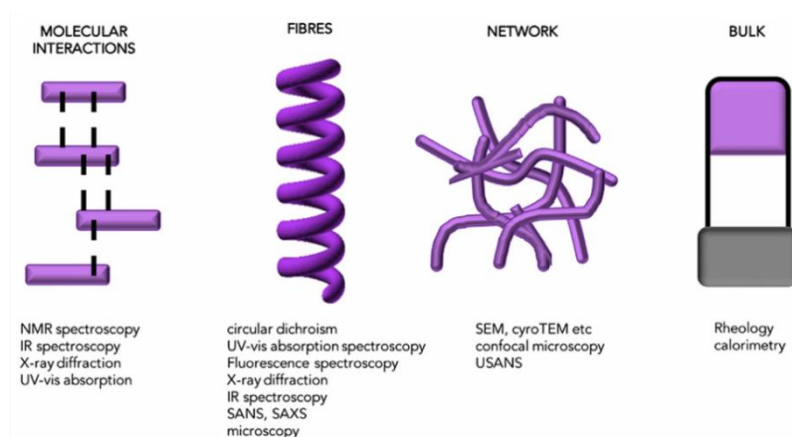


Figure 1.6. Various characterization techniques to understand the mechanism of supramolecular hydrogel formation [55] (Copyright 2017 Elsevier)

1.3.3. Properties of Supramolecular Hydrogel

1.3.3.1. Self-Healing

One of the standout characteristics of biological tissues is their capacity to heal and regenerate after physical injury. The similarity between supramolecular hydrogels and biological tissues has driven significant scientific advancements in creating smart hydrogels with distinctive self-healing capabilities. In these hydrogels, self-healing involves the reformation of broken bonds within the network owing to the dynamic and reversible nature of the noncovalent interactions.^{64,65} It is a process by which they regain their gel state after facing external disturbances such as mechanical force, cutting, heat, or other interactions.⁶⁶ The recovery from sol to gel state under mechanical stress is called thixotropic behavior, whereas recovery from heat stress is termed thermoreversible. Sarma and his coworkers reported several works on supramolecular hydrogel with self-healing, thermoreversible, thixotropic, and shape-sustaining properties.⁶⁷ Self-healing properties enable the hydrogels to be used in a plethora of applications such as in tissue engineering⁶⁸, the thixotropic property is associated with the injectability of the material, and thermoreversible property aids in the encapsulation of drugs thus making them ideal for drug delivery.⁶⁹ The

thermoreversible nature of the hydrogel can also be utilized to mold the hydrogel into different shapes.⁷⁰

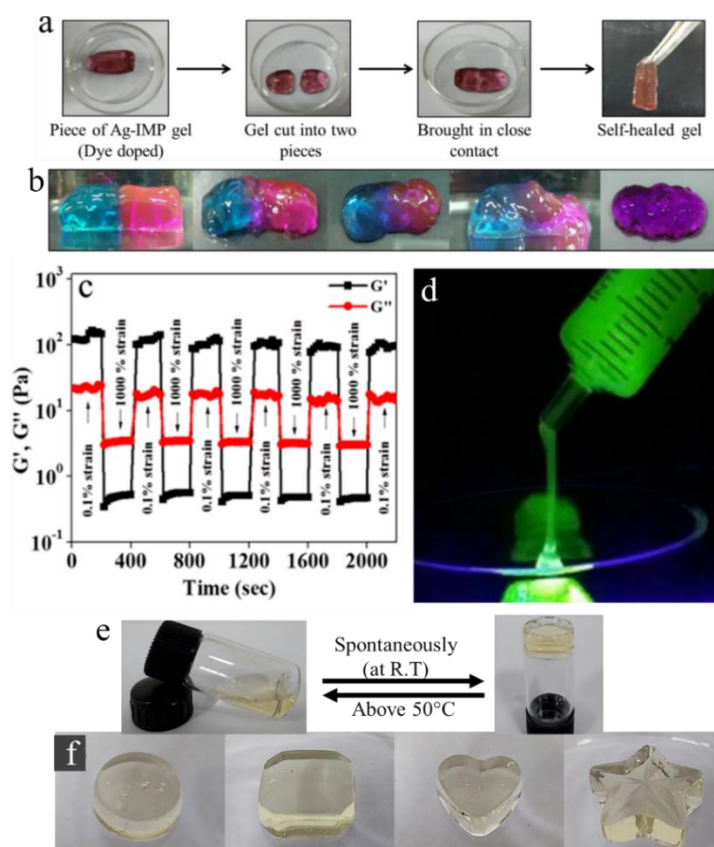


Figure 1.7. (a) self-healing property of the hydrogel, (b) images showing the dynamic nature of the hydrogel where two dye-loaded pieces of hydrogel when kept close to each other, exchange dye molecules across the fusion interface upon self-healing, (c,d) thixotropy and injectability of the hydrogel, [67] (Copyright 2018 ACS) (e) thermoreversible property of the hydrogel, and (f) thermoreversible nature of the hydrogel exploited to mold it into different shapes[70] (Copyright 2024 ACS).

1.3.3.2. Stimuli-responsive behavior

Supramolecular hydrogels possess stimuli-responsive characteristics, enabling them to undergo reversible transitions between gel and sol states in response to various external triggers due to the dynamic nature of their intermolecular forces.^{71,72} Physical stimuli such as temperature,^{73–75} electromagnetic fields,^{76,77} light,^{78–81} and mechanical forces,^{82,83} as well as chemical stimuli including pH changes,^{84–86} small molecules, redox agents, enzymes, and ions, can prompt phase transitions in these hydrogels.^{67,87–90} Their versatility makes them suitable for numerous applications, such as drug delivery, cell culture, tissue

engineering, sensing, and optical devices.^{91–94} For example, hydrogels derived from low-molecular-weight gelators can release therapeutic agents at specific sites, responding to physiological stimuli like pH or redox shifts. Saha *et al.* synthesized Zn²⁺ - amino acid hydrogel with multi-stimuli responsive properties.⁹⁵

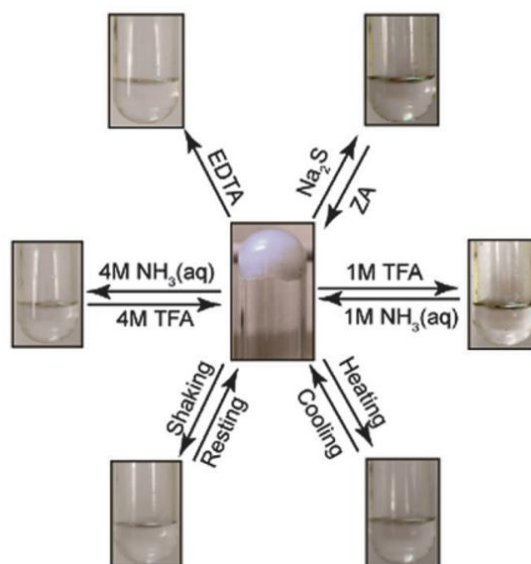


Figure 1.8. Thermal, mechanical, pH, and chemical stimuli-triggered gel-to-sol transitions of the ZAVP hydrogel. ZA = zinc acetate dihydrate [95] (Copyright 2014 RSC)

1.3.3.3. Facile Synthetic Process

Covalent crosslinking in chemical gels often alters the characteristic properties of the gelator.^{96,97} Since supramolecular hydrogels are obtained via non-covalent interactions between the gelator molecules, the precursors remain in their unmodified pristine form thus preserving the original characteristic of the gelator. Another added advantage of supramolecular hydrogel is the straightforward fabrication process.

- With a correctly chosen gelator or combination of gelators and crosslinkers, a hydrogel can be obtained through a one-pot synthesis method simply by mixing the precursors in a solvent. This approach eliminates the need for a lengthy synthetic process,

thereby conserving resources and energy, and serves as an eco-friendly method for synthesizing smart materials.^{98–100}

- Besides, the LMWHs do not possess the batch-to-batch variations that are generally found in polymeric hydrogel systems. This discrepancy in polymeric hydrogels could be attributed to the fact that they are highly influenced by polymerization conditions, highlighting the necessity of strict oversight of the preparation procedure, particularly regarding temperature and environmental factors.¹⁰¹ Despite the intricate molecular interactions in LMWG supramolecular hydrogels, the synthesis process is straightforward, requiring minimal maintenance and no stringent reaction conditions.

This aspect is also one of the primary focal points in this thesis work where we proposed a facile synthetic approach to fabricate smart supramolecular hydrogels.

Hydrogels without metal exhibit applications in areas such as sensing, drug delivery, and medicinal therapy.^{102,103} However, incorporating metal ions into the gel matrix enhances these soft materials, expanding their potential into advanced fields like catalysis, redox optoelectronics, magnetism, sensing, drug delivery, nanoparticle synthesis, stabilization, and environmental remediation.^{67,104–111}

1.3.4. Hybrid Organic-Inorganic Hydrogels

Organic small-molecule gelators can also interact with metal ions^{112,113} or other inorganic moieties such as metal clusters,^{114–116} nanoparticles,^{117,118} or metal-organic frameworks (MOF)¹¹⁹ to form hybrid organic-inorganic supramolecular hydrogels. Additionally, the diverse metal-ligand interactions within the supramolecular gel matrix can result in intriguing features, including color, redox responsiveness, and electronic, optical, and magnetic properties. These hybrid hydrogels provide a simple pathway to combine the properties of inorganic moiety with the benefits of the supramolecular hydrogel. Contemplating all the discussed properties of hydrogel along with the scope of synthesizing a

wide range of materials, it's gaining popularity in various fields of applications such as catalysis, biomimetics, enzyme mimetic, tissue engineering, drug delivery, sensing, actuators, conductive materials, photoluminescence, gas adsorption, etc.^{120–127}

If the gelator is directly crosslinked to the metal ions through various non-covalent interactions such as electrostatic interaction and weak coordinate bonds, they are classified as metallogels. Coordination polymer hydrogel is a subset of metallogel, where metal ions act as nodes and LMWGs act as linkers. Contrary to its name, coordination polymer hydrogels are LMW gels. In other words, they can be described as polymeric strands crosslinked through coordination bonds between metal centers and gelator molecules, forming various structures where the fibers or helices are composed of interconnected coordination linkages.^{128,129}

However, when the hydrogel formation takes place via the interaction of the organic gelator with other inorganic moieties such as nanoparticles, metaloxo clusters, or inorganic complexes, they are given an umbrella term of hybrid organic-inorganic hydrogels. Based on the interaction between the organic molecule gelator with the inorganic moiety, hybrid materials are classified into two categories:¹³⁰

- ***Class I hybrid hydrogel*** – In this category, the organic molecule interacts with inorganic moiety through reversible non-covalent interactions to develop the crosslinked fibrillar network. This is a purely self-assembled system.
- ***Class II hybrid hydrogel*** – The organic gelator covalently links with the inorganic moiety to form a discrete gelator. The discrete gelator can further self-assemble to form hydrogels.¹³¹

1.4 Small Biomolecules as LMWG

In the quest for biocompatible and bioavailable low molecular weight gelators with ample non-covalent interaction sites, researchers have taken a keen interest in fundamental biological building blocks to create hydrogels.^{132,133} Biological systems often utilize the self-assembly

of three main types of biomolecules: nucleic acids, proteins, and polysaccharides, building blocks, that self-assemble and integrate into complex superstructures such as proteins, DNA, and carbohydrates, with functions that form the basis of life to carry out various functions (Figure 1.9).

Amino acids, peptides, and nucleic acids possess functional groups such as amines, thiols, carboxyl, hydroxyl, and phosphates, which serve as effective sites for hydrogel bonding accompanied by the occasional presence of aromatic groups promoting π - π stacking and synergy of these non-covalent interactions ultimately leading to the formation of supramolecular hydrogels.¹³⁴⁻¹³⁸ Furthermore, they can also coordinate with metal ions to produce functional metalloids.^{139,140} Mimicking this natural process, the self-assembly of small molecules derived from fundamental biological building blocks in aqueous environments provides a promising approach for replicating the structures and functions of biomacromolecules.

The inherent self-assembly characteristics of these biomolecules give rise to larger ordered and functional structures with remarkable attributes, such as adjustable conformations, precise recognition capabilities, diverse sequencing, biocompatibility, regulated biodegradability, binding, and catalytic enhancements. The easy and natural accessibility of these biomolecules at a low cost makes them suitable for large-scale synthesis. As a result, supramolecular hydrogel networks composed of fundamental biological motifs could eventually lead to the development of soft materials with either intentional or novel biological functions.

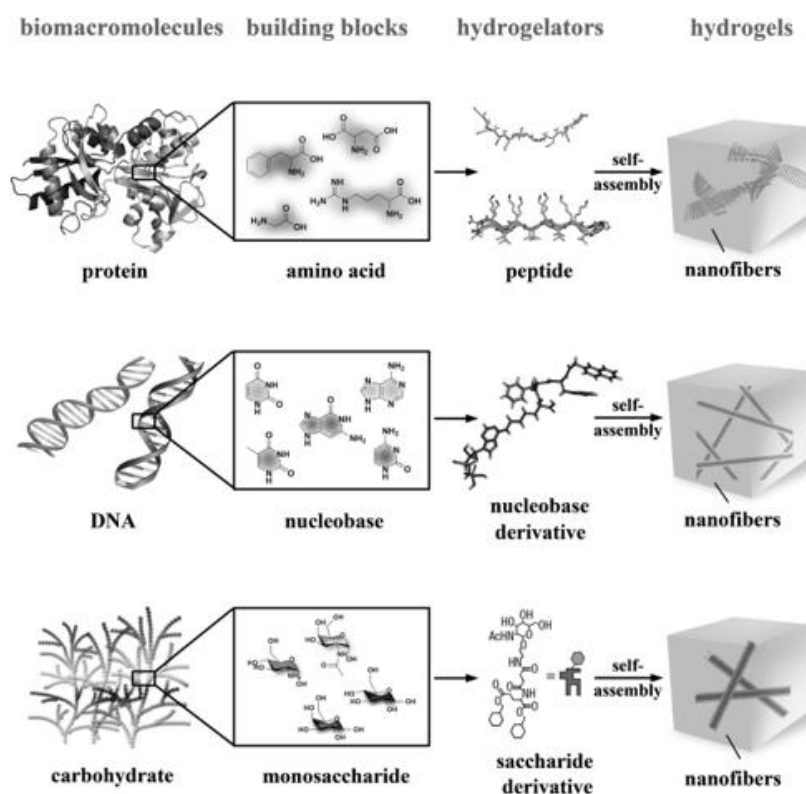


Figure 1.9. Small biomolecules and their self-assembled macrostructure in nature. [133] (Copyright 2014 Wiley)

1.4.1 Nucleobases, Nucleosides, and Nucleotides as LMWG

Nucleobases are the basic units of nucleosides, nucleotides, and nucleic acids that further self-assemble to form RNA/DNA. The nucleobases are nitrogen-containing heterocycles that are classified into two categories: purines (adenine A and guanine G) and pyrimidines (uracil U, thymine T, and cytosine C).^{141,142} The helical structures of DNA and RNA are formed when these five nucleobases (ATGC in DNA and AUGC in RNA) pair through hydrogen bonds, with their aromatic rings also stacking on top of one another via π - π interactions. While the pyrimidine ring features a single edge with three hydrogen bond donors and acceptors, the purine's bicyclic structure offers multiple faces for hydrogen bonding. While a pyrimidine ring has a single edge of three hydrogen bond donors and acceptors, the purine's bicyclic structure results in multiple faces for hydrogen bonding interactions. The most significant of these noncovalent interactions is Watson-Crick base pairing, a key motif in double-stranded nucleic acids. In this

arrangement, complementary base pairs - adenine with uracil (or thymine in DNA) and guanine with cytosine - form two and three hydrogen bonds along the Watson-Crick edge. While this hydrogen bonding pattern is the most well-known, it is not the only possible configuration. Other hydrogen bonding patterns include reverse Hoogsteen and alternate Watson-Crick base pairs.

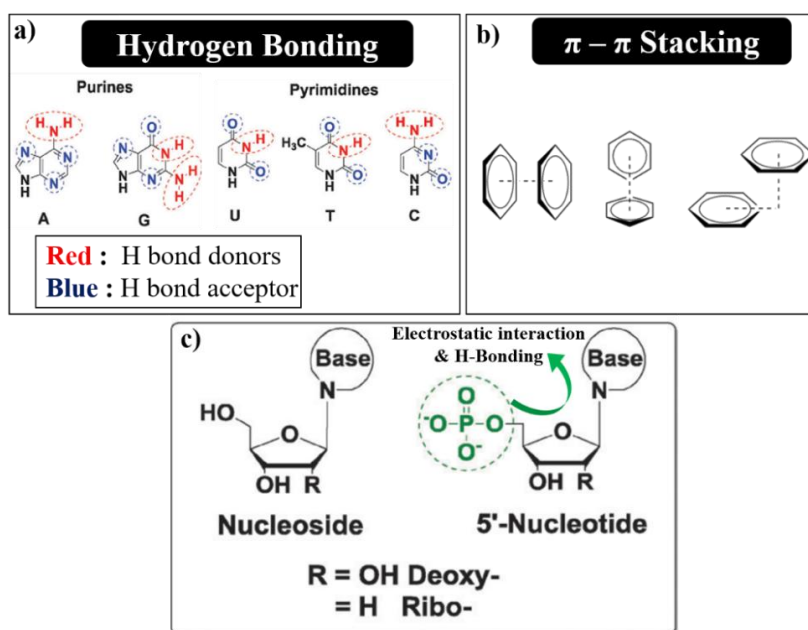


Figure 1.10. (a) H-bonding sites in nucleobases, (b) π - π stacking of nucleobases, and (c) additional non-covalent interactions in nucleosides and nucleotides.[143] (Copyright 2016 RSC)

Nucleosides are created when a nucleobase covalently attaches to a ribose via an N-glycosidic bond, and this ribose ring becomes phosphorylated in a nucleotide. The anionic phosphate group of the nucleotide contributes to electrostatic interactions and acts as a hydrogen bond acceptor. At acidic pH, the phosphate group can protonate from PO_3^{2-} to PO_3H^- , allowing it to function also as a hydrogen bond donor, which further facilitates the cross-linking process.¹⁴³

1.5 Supramolecular Assembly of Guanosine and Derivatives

As we can see in Figure 1.10a, guanosine has three H-bond acceptor groups (N3, N7, and O6) and two hydrogen bond donor groups (N1 amide and N2 amino), which is higher compared to other nucleobases. This provides guanosine with an upper hand to self-assemble into unique architectural aggregates through both Watson-Crick and Hoogsteen faces.^{143,144} When both faces are involved, the supramolecular assembly is influenced by the experimental conditions. In the presence of cations such as Na⁺, K⁺, Li⁺, Ca²⁺, or Pb²⁺, etc., the formation of guanosine (G) quartets is favored. This occurs because alkali metals can neutralize the electrostatic repulsion between the carbonyl groups of guanine base that point inward within the quartet's inner cavity. The stability of the macrocyclic structure is therefore due to a combination of eight hydrogen bonds, cation-mediated electronic stabilization, and the delocalization of nucleobase electrons (resonance), which can involve either π -electrons, σ -electrons, or both.¹⁴⁴⁻¹⁴⁶ Even though the G-quartet is the most commonly observed assembly of guanosine, however, various other G-assemblies such as G-ribbons,¹⁴⁷ duplexes,¹³¹ planar sheets,¹⁴⁸ etc. are also known (Figure 1.11). The G-quadruplex structure of guanosine and its derivatives plays vital biological roles *in vivo* and serves as a flexible and versatile template for creating ordered functional materials. Due to its inherent biocompatibility and biodegradability, the self-assembly of small-molecule guanine has garnered significant interest in biomedical applications, nanotechnology, material sciences, and supramolecular chemistry.¹⁴⁶

The ribose sugar in guanosine can also play a vital role in supporting the supramolecular structure and function. Many scientists working in this field have exploited the *cis*-1,2-diols of the sugar group in guanosine to covalently react with B(OH)₃ or B(OH)₄⁻ to form guanosine-borate (GB) esters. The formation of the GB esters aids in dissolving guanosine which is typically water-insoluble, leading to the

creation of GB hydrogels with improved stability.^{149,150} However, guanosine 5' monophosphate (GMP) is the natural phosphorylated derivative of guanosine that is water-soluble in its pristine form. Also, additional electrostatic and non-covalent interactions from the phosphate group enable them to stabilize hydrogels without the need for any further modification.^{151,152}

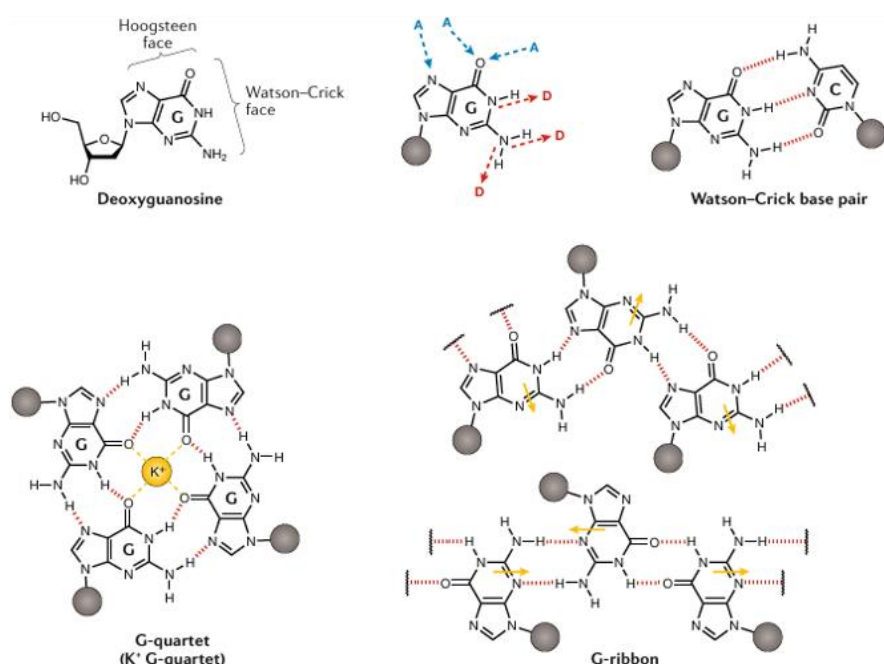


Figure 1.11. Guanine, along with its related compounds guanosine and deoxyguanosine, exhibits hydrogen bond donating and accepting capabilities through three acceptor (A) sites and three donor (D) sites. This allows both the Watson-Crick and Hoogsteen faces to participate in the formation of a wide variety of hydrogen-bonded networks, including the well-known guanine/cytosine ($G \equiv C$) base pair, the formation of G-quartet structures in the presence of cations, and the development of G-ribbons. [146]

1.5.1 History of Guanosine-Based Assembly

The first report on G-assembly based hydrogel was reported by Ivar Christain Bang. He observed that at lower pH, guanylic acid can form a hydrogel at higher concentrations.¹⁵³ About fifty years in 1962, Martin Gellert et al. followed up on this work and published the first structure of a G-tetrad that we know today.¹⁵⁴ They examined the x-ray fiber diffraction pattern for 5'-Guanosine monophosphate (5'-GMP) gel, which suggested four guanine molecules in proximity stabilized by

hydrogen bonds, where the N1-H and N2-H donor atoms of one guanine molecule pair with the N7 and O6 atoms of adjacent guanine molecules. They also observed that the spatial distance between stacked G-quartets was found to be 0.33 nm and it formed a helix pattern. However, at that time, guanosine tetramer was considered to be an *in vitro* process so research in the area of DNA-G4 was not much prioritized for a long time. However, in the late 1980s, an increasing amount of evidence has demonstrated that G4 DNA structures are highly prevalent, evolutionarily conserved, and appear to play significant roles in the processing of genetic information. Subsequently, biophysical studies of G4-rich DNA were focused upon (Figure 1.12b). Thereafter several research on G-tetramers in nature have been reported by scientists. Drawing inspiration from nature, the ease of *in vitro* hydrogel formation has motivated contemporary researchers to harness these spontaneously self-assembled systems for the development of smart materials. ^{155,156}

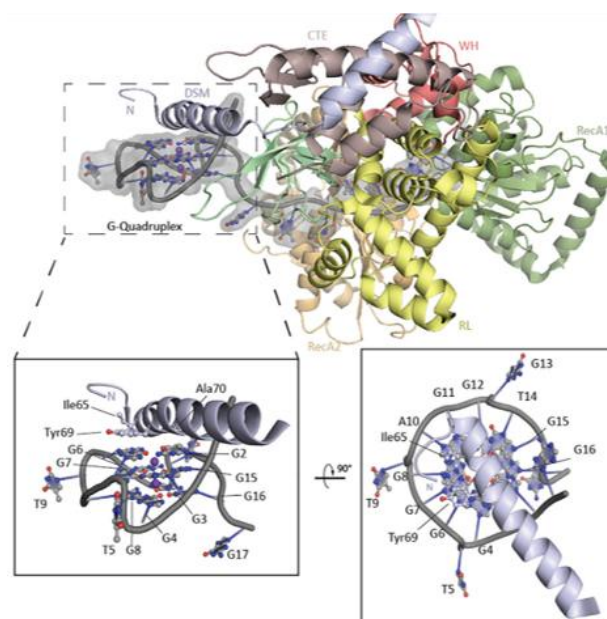


Figure 1.12. Crystal Structure of DHX36 Bound to the *c-Myc* G4 [156] (Copyright 2020 Elsevier)

1.5.2. Characterization of G-Quartet Motif

G-quartet formation occurs through the self-assembly of four guanosine or GMP molecules via Watson-Crick and Hoogsteen hydrogen bonding, creating a stable cation-rich G-quartet structure. These quartets

further stack over each other to form quadruplex fibrils, that crosslink to form a dense fibril network ultimately forming a gel. Gelation is driven by hierarchical multi-step nucleation, physical crosslinking, branching, and aggregation processes. When exposed to suitable external stimuli, the gel network can be easily broken down due to the disruption of molecular hydrogen-bonded assemblies. The reversible nature of G-quadruplex-based hydrogels has made them attractive as smart biomaterials, owing to their stimuli-responsive properties. The mechanistic understanding of gelation and the remarkable properties of G-quadruplex-based hydrogels have been elucidated through various spectroscopic characterization techniques.

X-ray diffraction

Powder X-ray diffraction (PXRD) investigation aids in characterizing the presence of G-quartet and further supramolecular architecture formation through π - π stacking of G-quartets to form the fibrillar strand. The peaks observed at $2\theta \sim 4.5^\circ$ correspond to the lattice spacing (d) of 2.2 nm which is the diameter of a Quartet. Another peak is observed at $2\theta \sim 27^\circ$ corresponding to the lattice spacing of 0.33 nm which is the interplanar distance between two layers of G-quartets stacked together due to π - π stacking (Figure 1.13a).¹⁵⁷

Thioflavin T (ThT) Assay

G-quartet formation could also be analyzed by loading thioflavin T into the hydrogel matrix. ThT is a fluorogenic dye that shows multifold enhancement in emission intensity at around 490 nm when trapped in between the G-quartet fibrils. The binding of ThT to G-assembly restricts the intermolecular rotation which causes the increment in the emission, which otherwise shows quenching in bare form (Figure 1.13b).¹⁵⁸⁻¹⁶⁰

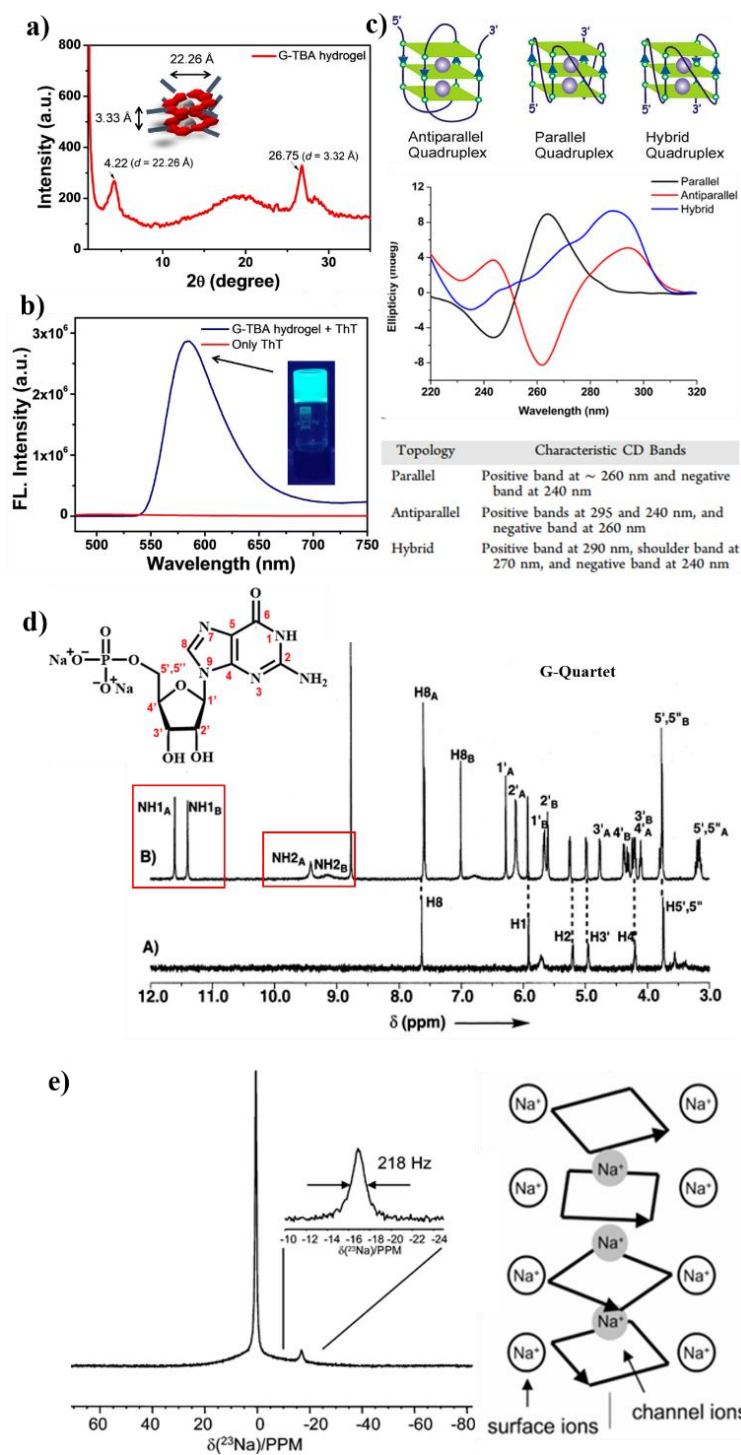


Figure 1.13. The characterization for G-quadruplex (a) PXRD spectra showing G-quartet assembly,[157] (b) ThT assay for G-quartet-based hydrogel,[157] (Copyright 2021 ACS) (c) CD spectra for three different conformations of G-quadruplex assembly: parallel, anti-parallel, and hybrid,[161] (Copyright 2017 ACS) (d) ^1H NMR of a G-quartet assembly,[162] (Copyright 2000 ACS) and (e) ^{23}Na NMR showing sodium ions present in two different environments: free or surface sodium ion and sodium ion trapped in the channel of G-quartet.[165] (Copyright 2007 RSC)

Circular Dichroism (CD)

Circular dichroism (CD) spectroscopy is essential for understanding the stereostructure and self-assembly behavior of supramolecular formations in a G-quadruplex hydrogel matrix. In the CD spectrum, the peaks between 250-320 nm reflect the stacking patterns of cation-stabilized G4-quartets in a helical arrangement, with positive peaks indicating head-to-tail stacking and negative peaks indicating head-to-head stacking. G-quadruplex structures are classified as parallel, antiparallel, or hybrid, based on the orientation of the nucleic acid strands that compose the G4 motif. The CD spectrum of an antiparallel G4 structure shows a strong positive peak at 290-295 nm and a weaker negative peak at 260-265 nm. In contrast, the parallel G4 conformation exhibits a positive peak at 260-265 nm and a negative peak at 240-245 nm. The hybrid conformation displays a positive peak at 290 nm, a shoulder at 270 nm, and a negative peak around 240 nm (Figure 1.13c).¹⁶¹

Nuclear Magnetic Resonance (NMR) Spectroscopy

(i) Proton (^1H) NMR

^1H NMR for supramolecular G-assembly may show an overall downfield shift due to H-bonding. The emergence of a peak near 9.5 ppm is the characteristic sign of G-quartet formation. This peak corresponds to the H of the amine group that participates in the quartet formation. The appearance of more than one peak at that position suggests the presence of more than two G-quartet layers, where one peak refers to the outer layer and the other refers to the inner layer. If both the peaks are of equal intensity then it indicates the presence of 4 G-quartet layers, that is G-hexadecamer (G16)

Similarly, new peaks emerge in the region of 11-13 ppm that correspond to the N1H proton participating in the G-quartet formation. (Figure 1.13d)^{162,163}

(ii) Sodium (^{23}Na) NMR

In ^{23}Na NMR, for a G-quartet system, two peaks are generally observed. One at near 0 ppm corresponding to the free/surface sodium ions that are bound to the phosphate group and a low intense peak near -17 ppm which is due to the sodium ions inside the G-quadruplex channel. (Figure 1.13e)^{164,165}

1.5.3. Recent Advances in G-Assembly-Based Hydrogels

Even though G-assembly based supramolecular hydrogels are turning the eyes of many researchers, it's still relatively a new field. It holds vast potential in the field of biocompatible and biomimetic smart materials, moreover, it can also interact with inorganic moiety to harness their properties into a soft hybrid material for a wide range of applications.

G-quadruplex in Biomedical Field

G-assembly based hydrogel is highly desirable in the biomedical field. Cheng *et al.* recently developed a guanosine 5'-monophosphate (GMP) G-quartet-based hydrogel with the antibacterial drug tobramycin (TOB) which is used in the clinical treatment of keratitis (Figure 1.14a). Gelation of TOB with GMP rendered it with biocompatibility, injectability, transparency, and sustained drug release. On treating mice with pristine drug, an opaque layer was observed on the cornea but not for the hydrogel, thus the hydrogel enhanced the therapeutic efficacy of the drug.¹⁶⁶ Li and his co-workers developed Ag-isoguanosine (Ag-isoG) hydrogel with outstanding antibacterial activity, saline-clearable characteristics, and high-temperature resistance (Figure 1.14b). Its strong antibacterial effectiveness against *E. faecalis* and low cytotoxicity highlight its significant potential as an alternative intracanal disinfectant for effective root canal therapy.¹⁶⁷ Multicomponent G-quadruplex of guanosine (Guo) and GMP has been shown to form stable hydrogels and has gained popularity in bio applications. Gallardo *et al.* reported a Guo/GMP system for tissue reconstruction and wound healing by 3D

bioprinting (Figure 1.14c). They combined Guo and GMP with boronic acid (BA) and K^+ ions, where the cross-association between Guo and GMP in the presence of K^+ and BA enhanced hydrogel formation and stability. This approach improved the printability while supporting cell survival and preserving cell functionality.¹⁶⁸

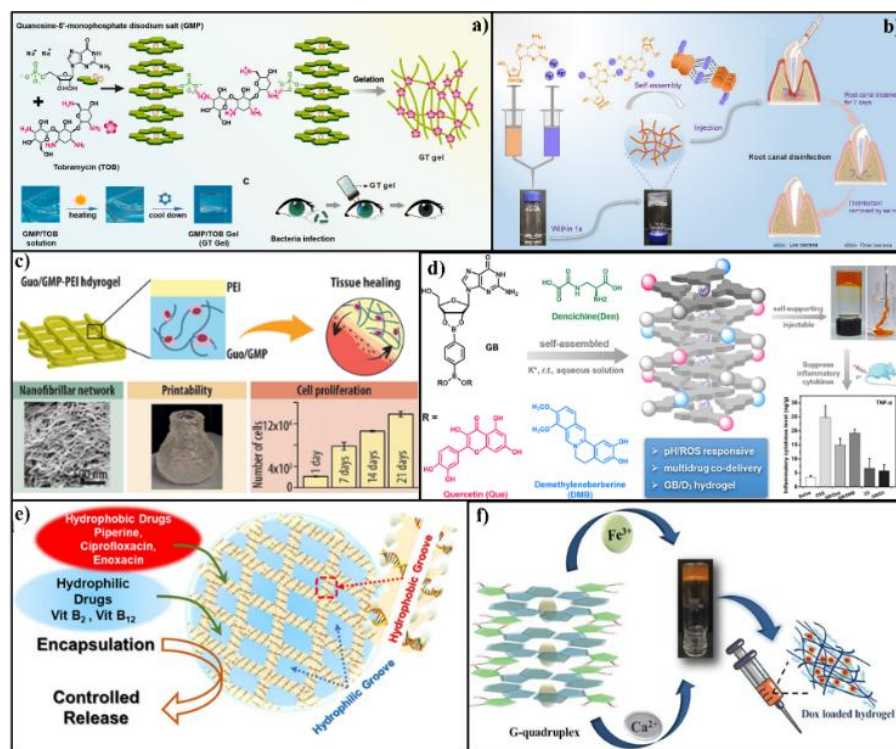


Figure 1.14. (a) GMP-TOB hydrogel used for the treatment of keratitis^[166], (b) Ag-IsoG hydrogel with antibacterial property to be used as a disinfectant in root canal therapy.^[167] (Copyright 2023 ACS) (c) Guo/GMP hydrogel for tissue healing through bioprinting.^[168] (Copyright 2023 ACS) (d) Guanosine Boronic acid hydrogel for sustained release of anti-inflammatory natural products(Quercetin, DMB, and Denon),^[169] (Copyright 2024 ACS) (e) DNA-GMP bio-condensate led hydrogel as hydrotropic carrier for both hydrophilic and hydrotropic drugs,^[170] and (f) Bimetal crosslinked 5'-GMP self-assembled hydrogel demonstrating pH-responsive zero-order drug release.^[171] (Copyright 2019 ACS)

The G-quadruplex systems are used in the field of drug delivery due to their stimuli-responsive reversible sol-gel transition. Hydrogels can entrap drugs in their fibrillar matrix and release them by transitioning into sol in response to various stimuli such as pH, enzymes, etc. Gao *et al.* synthesized a simple guanosine and boronic acid-based G-quartet GB hydrogel which was used to co-deliver three natural products quercetin

(Que), demethyleneberberine (DMB), and dencichine (Den) with anti-inflammatory property for the treatment of irritable bowel syndrome (Figure 1.14d).¹⁶⁹ Sarma *et al.* recently reported a DNA-GMP biocondensation led G-quadruplex hydrogel (Figure 1.14e).¹⁷⁰ The hydrogel functioned as a hydrotropic drug delivery vehicle and could release both hydrophobic and hydrophilic drugs. Thakur *et al.* proposed a bimetallic Ca-Fe-GMP hydrogel (Figure 1.14f). Crosslinking F-GMP hydrogel with Ca²⁺ enhanced their biocompatibility and mechanical strength and it exhibited a pH-responsive zero-order release of drug.¹⁷¹

G-quadruplex Systems in Catalysis

Catalysis of organic reactions is still not a very explored field for guanosine hydrogels, but hydrophobic pockets in G-assembly can facilitate organic reactions in water. Bai *et al.* developed guanosine diester hydrogel in the presence of borate anion (GBG) and this gave enantioselective Friedel-Craft alkylation in water medium in the presence of Cu²⁺.¹⁷² Recently Chen *et al.* also reported another guanosine borate hydrogel that enantioselectively catalyzes aldol reaction in water.¹⁷³ Lala *et al.* macrocyclic ligand within the G-quadruplex hydrogel matrix by click reaction of bisalkyne and bisazide. This study highlights G-quadruplex hydrogel as a versatile platform for complex reactions such as macrocyclization by bringing reactive fragments into proximity. The hydrogel's high viscosity reduces the mobility of the reactive fragments thus facilitating the reaction by aligning them in proximity.¹⁷⁴

G-Assembly Motif in Enzyme Mimetic Activity

Enzymes are the most specific and efficient biocatalysts for several chemical reactions in living organisms. However, they show significant drawbacks in *in vitro* conditions, such as the high cost of synthesis or isolation, thermal instability, and sensitivity to the environment limiting its application outside physiological conditions. Thus, we need to design enzyme mimetic systems that can mimic the enzyme activity but are also more economical and stable to external stimuli. Like protein macrostructure, guanosine supramolecular

assembly is also an amphiphilic system, it can be explored in the field of enzyme mimic activity. Chakraborty *et al.* recently reported a GMP-based hydrogel with an inorganic metal cluster (polyoxometalate). The hydrogel showed haloperoxidase-like activity which was further exploited for antibacterial activity by disrupting the quorum-sensing process of bacteria.⁷⁰ Hu *et al.* synthesized iron-tetra (4-carboxyphenyl) porphine (Fe-TCPP) based MOF and it was trapped in the hydrogel matrix of GMP. The Fe-TCPP complex showed peroxidase activity which was used for glucose sensing. The hydrogel matrix rendered the system with efficient portability and shape molding ability.¹⁷⁵ Dash and colleagues developed a supramolecular hydrogel through G-quartet-like self-assembly, involving phenyl-boronic acid crosslinking the diol functional group of guanosine in the presence of K^+ and Pb^{2+} ions. The K^+ -stabilized hydrogel successfully incorporated Fe(III)-hemin, demonstrating peroxidase-like activity, whereas the Pb^{2+} stabilized hydrogel failed to bind hemin and did not exhibit activity. These findings led to the creation of a molecular logic gate for sensing toxic Pb^{2+} ions.¹⁷⁶

Conductivity of G-Quadruplex System

G-quadruplex hydrogels are also known to conduct cations within the quartet channel. This endows the G-quadruplex hydrogel with ion-conductivity. Thakur *et al.* proposed a self-healing hydrogel of GMP with phytic acid through G-quadruplex formation. The hydrogel showed a high conductivity of 46.4 mScm^{-1} .¹⁷⁷ Li *et al.* also reported a conductive hydrogel of guanosine with pyridine-4-boronic acid (PyB) in the presence of KCl with conductivity of 43.2 mS cm^{-1} .¹⁷⁸ Taking advantage of the conductivity of G-quadruplex assembly, Chakraborty and her co-workers recently designed a 2-layered electrochromic device (ECD) compared to the traditional 5-layered device.¹⁶³ The GMP hydrogel with phosphomolybdic acid showed electrochromic properties and was used as the replacement for the electrode.

Collectively, these studies underscore the functional diversity of G-quadruplex hydrogels, emphasizing their potential as innovative soft

biomaterials. This opens the door to developing a variety of supramolecular hybrid nanostructured hydrogels by leveraging the stable self-assemblies formed by fundamental biological units upon interaction with metal ions or other biological/chemical agents. These hydrogels exhibit appealing biological and biochemical properties, including self-healing and responsiveness to stimuli.

1.6. Thesis Objective

The primary objective of this thesis is to propose a facile strategy for developing smart hydrogel materials with diverse applications. We proposed hydrogel formation simply by one-pot mixing of precursors in their pristine form, without requiring covalent modifications or tedious synthetic routes. In this thesis work, guanosine monophosphate (5'-GMP) was explored as the LMWG. GMP has an additional interactive site than guanosine, the phosphate group. Unlike guanine or guanosine, GMP is water-soluble in its native form. Additionally, the electrostatic interactions and hydrogen bonding facilitated by the phosphate group allow GMP to form a hydrogel in its unmodified state, unlike guanosine which usually requires some form of derivatization. In this thesis, we developed functional GMP hydrogels by physically crosslinking them with various materials. These included inorganic moieties like polyoxometalates for haloperoxidase-induced antibacterial and chromogenic activities, metal-amino acid complexes to structurally and functionally mimic the carbonic anhydrase enzyme and the water-insoluble organic molecule folic acid for targeted drug delivery.

1.7. Organization of The Thesis

This thesis work is divided into two categories:

Category 1: In the first three working chapters, GMP forms Class I hybrid organic-inorganic hydrogel. Class I hybrid materials are when the organic material interacts with the inorganic moiety through only non-covalent interactions. In the first two working chapters, GMP forms hydrogel with metal oxo clusters, polyoxometalates (POM), and in the third working chapter GMP forms hydrogel by interacting with an inorganic metal complex.

Category 2: In the fourth working chapter, GMP hydrogel formation occurs by self-assembling with another small molecule, folic acid.

The following sections provide a brief discussion of the thesis contents:

Chapter 2. discusses the synthesis of two supramolecular hydrogels of GMP with polyoxometalates (POMs), phosphotungstic acid (PTA), and silicotungstic acid (STA). These hydrogels are mechanically robust, stimuli-responsive, and more biocompatible than bare POMs. They showed haloperoxidase activity, with PTA-GMP hydrogel showing higher activity. The PTA-GMP hydrogel demonstrated specific iodoperoxidase activity, which was harnessed for antibacterial activity by disrupting bacterial quorum sensing

In **Chapter 3**, we discuss the development of chromogenic hydrogel by self-assembly of a POM, phosphomolybdic acid (PMA), and GMP. The hydrogel is mechanically strong, thermo-reversible, and changes color from yellow to blue under physical (light, electricity, stress, heat) and chemical (metal, thiols, iodide) stimuli. It features ion conductivity, enabling its use in a simplified electrochromic device, highlighting its potential for smart devices.

In **Chapter 4**, we design a hydrogel mimicking the active site of carbonic anhydrase through simple self-assembly of small molecules. The GMP fibrillar structure provides a similar hydrophobic environment to the protein chain and also stabilizes the $Zn(His)_3H_2O$ complex, enabling the

hydrogel to replicate enzyme functions, showing high esterase and CO₂ hydration activity. The hydrogel also facilitated biomineralization, producing carbonated hydroxyapatite for bone tissue engineering and removing toxic metals like Pb²⁺ and Cd²⁺.

Chapter 5. proposes a simple method to prepare a hydrogel from water-insoluble folic acid by enhancing its solubility through self-assembly with amphiphilic GMP for targeted drug delivery. The thermoreversible, injectable, thixotropic, and biocompatible FA-GMP hydrogel effectively encapsulated and sustained the release of both hydrophilic (Dox) and hydrophobic (curcumin) drugs. These hydrogel-encapsulated drugs showed higher cytotoxicity and cellular uptake in MCF-7 cancer cells, improving therapeutic efficacy by enhancing tumor suppressor gene expression and inhibiting proliferation markers. The FA-GMP hydrogel offers a simple, cost-effective, and biocompatible solution for targeted anticancer drug delivery.

Chapter 6 is the last, and it summarizes the significance of overall research works included in the thesis with the future scope of the developed hydrogel materials.

1.8. References

1. 'gel' in IUPAC Compendium of Chemical Terminology, 3rd ed. International Union of Pure and Applied Chemistry; 2006. Online version 3.0.1, 2019. (DOI: 10.1351/goldbook.G026002)
2. Malo de Molina, P., & Gradzielski, M. (2017). Gels Obtained by Colloidal Self-Assembly of Amphiphilic Molecules. *Gels*, 3(3), 30. (DOI: 10.3390/gels3030030)
3. Kuzina M.A., Kartsev D.D., Stratonovich A.V., et al. (2023), Organogels versus Hydrogels: Advantages, Challenges, and Applications, *Adv. Funct. Mater.* 33, 2301421 (DOI: 10.1002/adfm.202301421)

4. Li Z.-Y., Li T.-Y., Yang H.-C., et al. (2024), Design and Fabrication of Viscoelastic Hydrogels as Extracellular Matrix Mimicry for Cell Engineering, *Chem Bio Eng.* 1, 916–933 (DOI: 10.1021/cbe.4c00129)
5. Estroff L.A., Hamilton A.D. (2004), Water Gelation by Small Organic Molecules, *Chem. Rev.* 104, 1201–1218 (DOI: 10.1021/cr0302049)
6. Wang G.K., Yang Y.M., Jia D. (2024), Programming viscoelastic properties in a complexation gel composite by utilizing entropy-driven topologically frustrated dynamical state, *Nat. Commun.* 15, 3569 (DOI: 10.1038/s41467-024-47969-z)
7. Sangeetha N.M., Maitra U. (2005), Supramolecular gels: Functions and uses, *Chem. Soc. Rev.* 34, 821–836 (DOI: 10.1039/B417081B)
8. Wang Y., de Kruijff R.M., Lovrak M., et al. (2019), Access to Metastable Gel States Using Seeded Self-Assembly of Low-Molecular-Weight Gelators, *Angew. Chem. Int. Ed.* 58, 3800–3803 (DOI: 10.1002/anie.201812412)
9. Izadi R., Mahinroosta M., Mohammadzadeh K., et al. (2023), An inclusive review on inorganic gels: classifications, synthesis methods and applications, *J. Iran. Chem. Soc.* 20, 1757–1779 (DOI: 10.1007/s13738-023-02818-6)
10. Tripathy D., Gadtya A.S., Moharana S. (2023), Supramolecular Gel, Its classification, preparation, properties, and applications: A review, *Polym.-Plast. Technol. Mater.* 62, 306–326 (DOI: 10.1080/25740881.2022.2113892)
11. Du X., Zhou J., Shi J., et al. (2015), Supramolecular Hydrogelators and Hydrogels: From Soft Matter to Molecular Biomaterials, *Chem. Rev.* 115, 13165–13307 (DOI: 10.1021/acs.chemrev.5b00299)
12. Pollack G.H. (2003), Cells, gels and the engines of life: (A new, unifying approach to cell function) 1st edn, *Annals of Botany* 91, 404–405 (DOI: 10.1093/aob/mcg030)

13. Trevors J.T., Pollack G.H. (2005), Hypothesis: the origin of life in a hydrogel environment, *Prog. Biophys. Mol. Biol.* 89, 1–8. (DOI: 10.1016/j.pbiomolbio.2004.07.003)
14. Islam M.R., Oyen M.L. (2022), 1 - Mechanical characterization of hydrogels, *The Mechanics of Hydrogels*, 1–24 (DOI: 10.1016/B978-0-08-102862-9.00014-2)
15. Yuk H., Zhang T., Lin S., et al. (2016), Tough bonding of hydrogels to diverse non-porous surfaces, *Nat. Mater.* 15, 190–196 (DOI: 10.1038/nmat4463)
16. Zhao L., Zhou Y., Zhang J., et al. (2023), Natural Polymer-Based Hydrogels: From Polymer to Biomedical Applications, *Pharmaceutics* 15, 2514 (DOI: 10.3390/pharmaceutics15102514)
17. Tariq Z., Najaf Iqbal D., Rizwan M., et al. (2023), Significance of biopolymer-based hydrogels and their applications in agriculture: a review in perspective of synthesis and their degree of swelling for water holding, *RSC Adv.* 13, 24731–24754 (DOI: 10.1039/D3RA03472K)
18. Ciulla M.G., Massironi A., Sugni M., et al. (2023), Recent Advances in the Development of Biomimetic Materials, *Gels* 9, 833 (DOI: 10.3390/gels9100833)
19. Gao Y., Zhang X., Zhou H. (2023), Biomimetic Hydrogel Applications and Challenges in Bone, Cartilage, and Nerve Repair, *Pharmaceutics* 15, 2405 (DOI: 10.3390/pharmaceutics15102405)
20. Prince E., Kumacheva E. (2019), Design and applications of man-made biomimetic fibrillar hydrogels, *Nat. Rev. Mater.* 4, 99–115 (DOI: 10.1038/s41578-018-0077-9)
21. Ishihara K., Shi X., Fukazawa K., et al. (2023), Biomimetic-Engineered Silicone Hydrogel Contact Lens Materials, *ACS Appl. Bio Mater.* 6, 3600–3616. (DOI: 10.1021/acsabm.3c00296)

22. Filipecki J., Sitarz M., Kocela A., et al. (2014), Studying functional properties of hydrogel and silicone–hydrogel contact lenses with PALS, MIR and Raman spectroscopy. *Spectrochim, Acta. A. Mol. Biomol. Spectrosc.* 131, 686–690 (DOI: 10.1016/j.saa.2014.04.144)
23. Li J., Mooney D.J. (2016), Designing hydrogels for controlled drug delivery, *Nat. Rev. Mater.* 1, 1–17 (DOI: 10.1038/natrevmats.2016.71)
24. Vigata M., Meinert C., Hutmacher D.W., et al. (2020), Hydrogels as Drug Delivery Systems: A Review of Current Characterization and Evaluation Techniques, *Pharmaceutics* 12, 1188 (DOI: 10.3390/pharmaceutics12121188)
25. Buwalda S.J., Vermonden T., Hennink W.E. (2017), Hydrogels for Therapeutic Delivery: Current Developments and Future Directions, *Biomacromolecules* 18, 316–330 (DOI: 10.1021/acs.biomac.6b01604)
26. Lee K.Y., Mooney D.J. (2001), Hydrogels for Tissue Engineering, *Chem. Rev.* 101, 1869–1880 (DOI: 10.1021/cr000108x)
27. Khan M.U.A., Stojanović G.M., Abdullah M.F.B., et al. (2024), Fundamental properties of smart hydrogels for tissue engineering applications: A review, *Int. J. Biol. Macromol.* 254, 127882 (DOI: 10.1016/j.ijbiomac.2023.127882)
28. Kasai R.D., Radhika D., Archana S., et al. (2023), A review on hydrogels classification and recent developments in biomedical applications, *Int. J. Polym. Mater. Polym. Biomater.* 72, 1059–1069. (DOI: 10.1080/00914037.2022.2075872)
29. Hu S., Zeng C., Jiang Y., et al. (2024), Macrostructure and Microenvironment Biomimetic Hydrogel: Design, Properties, and Tissue Engineering Application, *Chem. Mater.* 36, 1054–1087 (DOI: 10.1021/acs.chemmater.3c02098).

30. Liang Y., He J., Guo B. (2021), Functional Hydrogels as Wound Dressing to Enhance Wound Healing, *ACS Nano* 15, 12687-12722 (DOI: 10.1021/acsnano.1c04206)
31. Pranantyo D., Yeo C.K., Wu Y., et al. (2024), Hydrogel dressings with intrinsic antibiofilm and antioxidative dual functionalities accelerate infected diabetic wound healing, *Nat. Commun.* 15, 954 (DOI: 10.1038/s41467-024-44968-y)
32. Qiao L., Liang Y., Chen J., et al. (2023), Antibacterial conductive self-healing hydrogel wound dressing with dual dynamic bonds promotes infected wound healing, *Bioact. Mater.* 30, 129–141. (DOI: 10.1016/j.bioactmat.2023.07.015)
33. Fan F., Saha S., Hanjaya-Putra D. (2021), Biomimetic Hydrogels to Promote Wound Healing, *Front. Bioeng. Biotechnol.* 9, 718377 (DOI: 10.3389/fbioe.2021.718377)
34. Fan D., Tian Y., Liu Z. (2019), Injectable Hydrogels for Localized Cancer Therapy, *Front. Chem.* 7, 675 (DOI: 10.3389/fchem.2019.00675)
35. Triboni E.R. (2019), 1 - Introduction, *Nano Design for Smart Gels*, 1–14 (DOI: 10.1016/B978-0-12-814825-9.00001-1)
36. Boncheva M., Whitesides G.M. (2005), Making Things by Self-Assembly, *MRS Bull.* 30, 736–742 (DOI: 10.1557/mrs2005.208)
37. Mendes A.C., Baran E.T., Reis R.L., et al. (2013), Self-assembly in nature: using the principles of nature to create complex nanobiomaterials, *WIREs Nanomedicine Nanobiotechnology* 5, 582–612 (DOI: 10.1002/wnan.1238)
38. Mendes, A.C., Baran, E.T., Reis, R.L., and Azevedo, H.S. (2013). Self-assembly in nature: using the principles of nature to create complex nanobiomaterials. *WIREs Nanomedicine Nanobiotechnology* 5, 582–612. <https://doi.org/10.1002/wnan.1238>.

39. Ng C.C., Cheng Y.-L., Pennefather P.S. (2004), Properties of a Self-Assembled Phospholipid Membrane Supported on Lipobeads, *Biophys. J.* 87, 323–331 (DOI: 10.1529/biophysj.103.030627)
40. Nasalean L., Baudrey S., Leontis N.B., et al. (2006), Controlling RNA self-assembly to form filaments, *Nucleic Acids Res.* 34, 1381–1392 (DOI: 10.1093/nar/gkl008)
41. Won J., Chae S.K., Kim J.H., et al. (2005), Self-assembled DNA composite membranes, *J. Membr. Sci.* 249, 113–117 (DOI: 10.1016/j.memsci.2004.08.031)
42. Chiti F., Dobson C.M. (2017), Protein Misfolding, Amyloid Formation, and Human Disease: A Summary of Progress Over the Last Decade, *Annu. Rev. Biochem.* 86, 27–68 (DOI: 10.1146/annurev-biochem-061516-045115)
43. Tyler J.K. (2002), Chromatin assembly, *Eur. J. Biochem.* 269, 2268–2274 (DOI: 10.1046/j.1432-1033.2002.02890.x)
44. Froimchuk E., Carey S.T., Edwards C., et al. (2020), Self-Assembly as a Molecular Strategy to Improve Immunotherapy, *Acc. Chem. Res.* 53, 2534–2545 (DOI: 10.1021/acs.accounts.0c00438)
45. Kominami H., Kobayashi K., Ido S., et al. (2018), Immunoactivity of self-assembled antibodies investigated by atomic force microscopy, *RSC Adv.* 8, 29378–29384 (DOI: 10.1039/C8RA05423A)
46. Monnard P.-A., Deamer D.W. (2002), Membrane self-assembly processes: Steps toward the first cellular life, *Anat. Rec.* 268, 196–207 (DOI: 10.1002/ar.10154)
47. Salahuddin P., Fatima M.T., Uversky V.N., et al. (2021), The role of amyloids in Alzheimer’s and Parkinson’s diseases, *Int. J. Biol. Macromol.* 190, 44–55 (DOI: 10.1016/j.ijbiomac.2021.08.197)

48. Raymond D.M., Abraham B.L., Fujita T., et al. (2019), Low-Molecular-Weight Supramolecular Hydrogels for Sustained and Localized in Vivo Drug Delivery, *ACS Appl. Bio Mater.* 2, 2116–2124 (DOI: 10.1021/acsabm.9b00125)
49. Ma Q., Zhang M., Yao C., et al. (2020), Supramolecular hydrogel with luminescence tunability and responsiveness based on co-doped lanthanide and deoxyguanosine complex, *Chem. Eng. J.* 394, 124894 (DOI: 10.1016/j.cej.2020.124894)
50. Xu W., Chen A. (2024), Application of supramolecular hydrogel in supercapacitors: Opportunities and challenges, *Aggregate* 5, e581. (DOI: 10.1002/agt2.581)
51. Shi Y., Feng A., Mao S., et al. (2024), Hydrogels in solar-driven water and energy production: Recent advances and future perspectives, *Chem. Eng. J.* 492, 152303 (DOI: 10.1016/j.cej.2024.152303)
52. Tena-Solsona M., Nanda J., Díaz-Oltra S., et al. (2016), Emergent Catalytic Behavior of Self-Assembled Low Molecular Weight Peptide-Based Aggregates and Hydrogels, *Chem. – Eur. J.* 22, 6687–6694 (DOI: 10.1002/chem.201600344)
53. Draper E.R., Dietrich B., Brasnett C., et al. (2018), P-Type Low-Molecular-Weight Hydrogelators, *Macromol. Rapid Commun.* 39, 1700746 (DOI: 10.1002/marc.201700746)
54. Jain D., Karajic A., Murawska M., et al. (2017), Low-Molecular-Weight Hydrogels as New Supramolecular Materials for Bioelectrochemical Interfaces, *ACS Appl. Mater. Interfaces* 9, 1093–1098 (DOI: 10.1021/acsami.6b12890)
55. Draper E.R., Adams D.J. (2017), Low-Molecular-Weight Gels: The State of the Art, *Chem* 3, 390–410 (DOI: 10.1016/j.chempr.2017.07.012)

56. Draper E.R., Adams D.J. (2019), Controlling the Assembly and Properties of Low-Molecular-Weight Hydrogelators, *Langmuir* 35, 6506–6521 (DOI: 10.1021/acs.langmuir.9b00716)
57. Hanabusa K., Yamada M., Kimura M., et al. (1996), Prominent Gelation and Chiral Aggregation of Alkylamides Derived from trans-1,2-Diaminocyclohexane, *Angew. Chem. Int. Ed.* 35, 1949–1951 (DOI: 10.1002/anie.199619491)
58. de Loos M., Feringa B.L., van Esch J.H. (2005), Design and Application of Self-Assembled Low Molecular Weight Hydrogels, *Eur. J. Org. Chem.* 2005, 3615–3631 (DOI: 10.1002/ejoc.200400723)
59. Raeburn J., Cardoso A.Z., Adams D.J. (2013), The importance of the self-assembly process to control mechanical properties of low molecular weight hydrogels, *Chem. Soc. Rev.* 42, 5143–5156 (DOI: 10.1039/C3CS60030K)
60. Raeburn J., Cardoso A.Z., Adams, D.J. (2013), The importance of the self-assembly process to control mechanical properties of low molecular weight hydrogels, *Chem. Soc. Rev.* 42, 5143–5156 (DOI: 10.1039/C3CS60030K)
61. Estroff L.A., Hamilton A.D. (2004), Water Gelation by Small Organic Molecules, *Chem. Rev.* 104, 1201–1218 (DOI: 10.1021/cr0302049)
62. Yu G., Yan X., Han C., et al. (2013), Characterization of supramolecular gels, *Chem. Soc. Rev.* 42, 6697–6722 (DOI: 10.1039/C3CS60080G)
63. Nebot V.J., Smith D.K. (2013), Techniques for the Characterisation of Molecular Gels, *Functional Molecular Gels*, 30-66 (DOI: 10.1039/9781849737371-00030)
64. Wang C., Fadeev M., Zhang J., et al. (2018), Shape-memory and self-healing functions of DNA-based carboxymethyl cellulose hydrogels

- driven by chemical or light triggers, *Chem. Sci.*, 7145–7152 (DOI: 10.1039/C8SC02411A)
65. Chivers P.R.A., Smith D.K. (2019), Shaping and structuring supramolecular gels, *Nat. Rev. Mater.* 4, 463–478 (DOI: 10.1038/s41578-019-0111-6)
66. Häring M., Díaz D.D. (2016), Supramolecular metallogels with bulk self-healing properties prepared by in situ metal complexation, *Chem. Commun.* 52, 13068–13081 (DOI: 10.1039/C6CC06533C)
67. Thakur N., Sharma B., Bishnoi S., et al. (2018), Multifunctional Inosine Monophosphate Coordinated Metal–Organic Hydrogel: Multistimuli Responsiveness, Self-Healing Properties, and Separation of Water from Organic Solvents, *ACS Sustain. Chem. Eng.* 6, 8659–8671 (DOI: 10.1021/acssuschemeng.8b00963)
68. Skilling K.J., Citossi F., Bradshaw T.D., et al. (2013), Insights into low molecular mass organic gelators: a focus on drug delivery and tissue engineering applications, *Soft Matter* 10, 237–256 (DOI: 10.1039/C3SM52244J)
69. Webber M.J., Pashuck E.T. (2021), Macromolecular self-assembly for hydrogel drug delivery, *Adv. Drug Deliv. Rev.* 172, 275–295 (DOI: 10.1016/j.addr.2021.01.006)
70. Chakraborty A., Dash S., Thakur N., et al. (2024), Polyoxometalate-Guanosine Monophosphate Hydrogels with Haloperoxidase-like Activity for Antibacterial Performance, *Biomacromolecules* 25, 104–118 (DOI: 10.1021/acs.biomac.3c00845)
71. Willner I. (2017), Stimuli-Controlled Hydrogels and Their Applications, *Acc. Chem. Res.* 50, 657–658 (DOI: 10.1021/acs.accounts.7b00142)

72. Vázquez-González M., Willner I. (2020), Stimuli-Responsive Biomolecule-Based Hydrogels and Their Applications, *Angew. Chem. Int. Ed.* 59, 15342–15377 (DOI: 10.1002/anie.201907670)
73. Grassi G., Farra R., Caliceti P., et al. (2005), Temperature-sensitive hydrogels, *Am. J. Drug Deliv.* 3, 239–251 (DOI: 10.2165/00137696-200503040-00004)
74. Schmaljohann D. (2006), Thermo- and pH-responsive polymers in drug delivery, *Adv. Drug Deliv. Rev.* 58, 1655–1670 (DOI: 10.1016/j.addr.2006.09.020)
75. Park T.G. (1999), Temperature modulated protein release from pH/temperature-sensitive hydrogels, *Biomaterials* 20, 517–521 (DOI: 10.1016/S0142-9612(98)00197-5)
76. Salama R., Hoe S., Chan H.-K., et al. (2008), Preparation and characterisation of controlled release co-spray dried drug-polymer microparticles for inhalation 1: Influence of polymer concentration on physical and in vitro characteristics, *Eur. J. Pharm. Biopharm.* 69, 486–495 (DOI: 10.1016/j.ejpb.2007.12.019)
77. Yoshida R., Sakai K., Okano T., et al. (1993), Pulsatile drug delivery systems using hydrogels, *Adv. Drug Deliv. Rev.* 11, 85–108 (DOI: 10.1016/0169-409X(93)90028-3)
78. Zheng S.-T., Yin H.-H., Ma Z.-G., et al. (2019), Low-molecular-weight photoresponsive supramolecular hydrogel based on a dicationic azobenzene-bridged pyridinium hydrogelator, *Chin. Chem. Lett.* 30, 707–709 (DOI: 10.1016/j.ccllet.2018.10.024)
79. L. Pianowski Z., Karcher J., Schneider K. (2016), Photoresponsive self-healing supramolecular hydrogels for light-induced release of DNA and doxorubicin, *Chem. Commun.* 52, 3143–3146 (DOI: 10.1039/C5CC09633B)

80. Draper E.R., Adams D.J. (2016), Photoresponsive gelators, *Chem. Commun.* 52, 8196–8206 (DOI: 10.1039/C6CC03485C)
81. Pramanik B., Ahmed S. (2022), Peptide-Based Low Molecular Weight Photosensitive Supramolecular Gelators, *Gels* 8, 533 (DOI: 10.3390/gels8090533)
82. Ohseido Y., Oono M., et al. (2017), Thixotropic stiff hydrogels from a new class of oleoyl-D-glucamine-based low-molecular-weight gelators, *RSC Adv.* 7, 41686–41692 (DOI: 10.1039/C7RA07244A)
83. Higashi D., Yoshida M., Yamanaka M. (2013), Thixotropic Hydrogel Formation in Various Aqueous Solutions through Self-Assembly of an Amphiphilic Tris-Urea, *Chem. Asian J.* 8, 2584–2587 (DOI: 10.1002/asia.201300779)
84. Tsekova D., Kondova V., et al. (2024), pH-dependent hydrogels obtained by low molecular weight derivatives of aspartic acid and glutamic acid (L-Asp and L-Glu), *Curr. Res. Biotechnol.* 8, 100257 (DOI: 10.1016/j.crbiot.2024.100257)
85. Lange S.C., Unsleber J., et al. (2014), pH response and molecular recognition in a low molecular weight peptide hydrogel, *Org. Biomol. Chem.* 13, 561–569 (DOI: 10.1039/C4OB02069C)
86. Lange S.C., Unsleber J., et al. (2015), pH response and molecular recognition in a low molecular weight peptide hydrogel, *Org. Biomol. Chem.* 13, 561–569 (DOI: 10.1039/C4OB02069C)
87. Ikeda M., Tanida T., et al. (2014), Installing logic-gate responses to a variety of biological substances in supramolecular hydrogel–enzyme hybrids, *Nat. Chem.* 6, 511–518 (DOI: 10.1038/nchem.1937)
88. Yoshii T., Ikeda M., Hamachi I. (2014), Two-Photon-Responsive Supramolecular Hydrogel for Controlling Materials Motion in Micrometer Space, *Angew. Chem. Int. Ed.* 53, 7264–7267 (DOI: 10.1002/anie.201404158)

89. Sun P., Ren S., et al. (2018), Smart low molecular weight hydrogels with dynamic covalent skeletons, *Soft Matter* 14, 6678–6683 (DOI: 10.1039/C8SM01482E)
90. Wojciechowski J.P., Martin A.D., Thordarson P. (2018), Kinetically Controlled Lifetimes in Redox-Responsive Transient Supramolecular Hydrogels, *J. Am. Chem. Soc.* 140, 2869–2874 (DOI: 10.1021/jacs.7b12198)
91. Rooth C., Pratihar S., et al. (2024), A multi-stimuli responsive carbazole based low molecular weight gelator: nanomolar sensing of cyanide ions and electrochromic switching in real-time, *New J. Chem.* 48, 14311–14320 (DOI: 10.1039/D4NJ02029D)
92. Zhang J., Jin J., et al. (2013), Reversible photo-controllable gels based on bithienylethene-doped lecithin micelles, *Chem. Commun.* 49, 9926–9928 (DOI: 10.1039/C3CC45805A)
93. Wei S.C., Pan M., et al. (2014), A Multistimuli-Responsive Photochromic Metal-Organic Gel, *Adv. Mater.* 26, 2072–2077 (DOI: 10.1002/adma.201304404)
94. Zhou H., Zhu Y., et al. (2024), Stimuli-responsive peptide hydrogels for biomedical applications, *J. Mater. Chem. B* 12, 1748–1774 (DOI: 10.1039/D3TB02610H)
95. Saha S., Bachl J., et al. (2014), Amino acid-based multiresponsive low-molecular weight metallohydrogels with load-bearing and rapid self-healing abilities, *Chem. Commun.* 50, 3004–3006 (DOI: 10.1039/C3CC49869G)
96. Chakraborty S., Keightley A., et al. (2010), Synthesis and Optical Properties of a Rod–Coil Diblock Copolymer with Polyoxometalate Clusters Covalently Attached to the Coil Block, *Chem. Mater.* 22, 3995–4006 (DOI: 10.1021/cm1007075)

97. Jang J., Hong J., Cha C. (2017), Effects of precursor composition and mode of crosslinking on mechanical properties of graphene oxide reinforced composite hydrogels, *J Mech. Behav. Biomed. Mater.* 69, 282–293 (DOI: 10.1016/j.jmbbm.2017.01.025)
98. Liu K., Zang S., Xue R., et al. (2018), Coordination-Triggered Hierarchical Folate/Zinc Supramolecular Hydrogels Leading to Printable Biomaterials, *ACS Appl. Mater. Interfaces* 10, 4530–4539. <https://doi.org/10.1021/acsami.7b18155>.
99. Chen R., Xu C., et al. (2021), Facile construction of a family of supramolecular gels with good levofloxacin hydrochloride loading capacity, *RSC Adv.* 11, 12641–12648 (DOI: 10.1039/D1RA00809A)
100. Zhu J., Wang R., et al. (2019), A facile preparation method for new two-component supramolecular hydrogels and their performances in adsorption, catalysis, and stimuli-response, *RSC Adv.* 9, 22551–22558 (DOI: 10.1039/C9RA03827B)
101. Yahia L.H., Chirani N., et al. (2015), History and Applications of Hydrogels, *J. Biomed. Sci.* 4, (DOI: 10.4172/2254-609X.100013)
102. Ramin M.A., Latxague L., et al. (2017), Low molecular weight hydrogels derived from urea based-bolaamphiphiles as new injectable biomaterials, *Biomaterials* 145, 72–80 (DOI: 10.1016/j.biomaterials.2017.08.034)
103. Nour H.F., Salama A.M., et al. (2023), Low-Molecular-Weight Hydrogels: Synthetic Methodologies, Gelation Mechanisms, and Biomedical Applications. In *Hydrogels and Nanogels - Applications in Medicine* (IntechOpen), (DOI: 10.5772/intechopen.1002012)
104. Araújo M., Escuder, B. (2017), Transient Catalytic Activity of a Triazole-based Gelator Regulated by Molecular Gel Assembly/Disassembly, *ChemistrySelect* 2, 854–862 (DOI: 10.1002/slct.201601816)

105. Jin Q., Zhang L., Cao H., et al. (2011), Self-Assembly of Copper(II) Ion-Mediated Nanotube and Its Supramolecular Chiral Catalytic Behavior, *Langmuir* 27, 13847–13853 (DOI: 10.1021/la203110z)
106. Kyarikwal R., Munjal R., et al. (2023), Design and synthesis of hydrophobic mixed organogels with complementary hydrogen-bond donor–acceptor sites: removal of heavy metal ions Hg^{2+} , Cd^{2+} and Pb^{2+} from aqueous solution, *Mater. Adv.* 4, 3603–3618 (DOI: 10.1039/D3MA00300K)
107. Saha S., Schön E.M., et al. (2013), Proton-Conducting Supramolecular Metallogels from the Lowest Molecular Weight Assembler Ligand: A Quote for Simplicity, *Chem. Eur. J.* 19, 9562–9568 (DOI:10.1002/chem.201204542)
108. Alam N., Mondal S., Sarma, D. (2024), Amide functional low molecular weight gelator based metallogel, *Coord. Chem. Rev.* 504, 215673 (DOI: 10.1016/j.ccr.2024.215673)
109. Moro A.J., Rome B. (2015), A coumarin based gold(i)-alkynyl complex: a new class of supramolecular hydrogelators, *Organic & Biomolecular Chemistry* 13, 2016–2033 (DOI: 10.1039/C4OB02077D)
110. McEwen H., Du Y., et al. (2017), Tuning hydrogels through metal-based gelation triggers, *J. Mater. Chem. B* 5, 9412–9417 (DOI: 10.1039/C7TB02140B)
111. Fortunato A., Mba M. (2021), Metal Cation Triggered Peptide Hydrogels and Their Application in Food Freshness Monitoring and Dye Adsorption, *Gels* 7, 85 (DOI: 10.3390/gels7030085)
112. Dhibar S., Pal B., et al. (2023), A 5-aminoisophthalic acid low molecular weight gelator based novel semiconducting supramolecular Zn(ii)-metallogel: unlocking an efficient Schottky barrier diode for microelectronics, *Nanoscale Adv.* 5, 6714–6723 (DOI: 10.1039/D3NA00671A)

113. Pal B., Dhibar S., et al. (2023), A semiconducting supramolecular novel Ni(II)-metallogel derived from 5-aminoisophthalic acid low molecular weight gelator: an efficient Schottky barrier diode application, *Mater. Adv.* 4, 3628–3635 (DOI: 10.1039/D3MA00260H)
114. Luo W., Hu B., et al. (2023), Antibacterial, photothermal and stable Ag-titanium-oxo-clusters hydrogel designed for wound healing, *Mater. Des.* 226, 111674 (DOI: 10.1016/j.matdes.2023.111674)
115. Li X., Cai L., et al. (2022), Gelation of metal oxide clusters for redox-active proton conductors in supercapacitor, *Electrochimica Acta* 406, 139844 (DOI: 10.1016/j.electacta.2022.139844)
116. Liu C., Xiang G., et al. (2016), Hybrid organic–inorganic supramolecular hydrogel reinforced with CePO₄ nanowires, *Polym. Chem.* 7, 6485–6489 (DOI: 10.1039/C6PY01127F)
117. Feng Y., Yin J., et al. (2020), Facile Synthesis of Ag/Pd Nanoparticle-Loaded Poly(ethylene imine) Composite Hydrogels with Highly Efficient Catalytic Reduction of 4-Nitrophenol, *ACS Omega* 5, 3725–3733 (DOI: 10.1021/acsomega.9b04408)
118. Tsekova D., Kondova V., et al. (2024), pH-dependent hydrogels obtained by low molecular weight derivatives of aspartic acid and glutamic acid (L-Asp and L-Glu), *Curr. Res. Biotechnol.* 8, 100257 (DOI: 10.1016/j.crbiot.2024.100257)
119. Weng Y., Song Z., et al. (2021), Hybrid hydrogel reactor with metal–organic framework for biomimetic cascade catalysis, *Chem. Eng. J.* 425, 131482 (DOI: 10.1016/j.cej.2021.131482)
120. Li X., Cai L., et al. (2022), Gelation of metal oxide clusters for redox-active proton conductors in supercapacitor, *Electrochimica Acta* 406, 139844 (DOI: 10.1016/j.electacta.2022.139844)

121. Hua Y., Pu G., et al. (2017), Gd(III)-induced Supramolecular Hydrogelation with Enhanced Magnetic Resonance Performance for Enzyme Detection, *Sci. Rep.* 7, 40172 (DOI: 10.1038/srep40172)
122. Tang L., Chen X., et al. (2017), Metallo-supramolecular hydrogels based on amphiphilic polymers bearing a hydrophobic Schiff base ligand with rapid self-healing and multi-stimuli responsive properties, *Polym. Chem.* 8, 4680–4687 (DOI: 10.1039/C7PY00739F)
123. Piras C.C., Slavik P., Smith D.K. (2019), Self-Assembling Supramolecular Hybrid Hydrogel Beads, *Angew. Chem. Int. Ed.* 59, 853 – 859 (DOI: 10.1002/anie.201911404)
124. Slavik P., Kurka W.D., Smith, D.K. (2018), Palladium-scavenging self-assembled hybrid hydrogels – reusable highly-active green catalysts for Suzuki–Miyaura cross-coupling reactions, *Chem. Sci.* 9, 8673–8681 (DOI: 10.1039/C8SC04561E)
125. Alam N., Sarma, D. (2020), Tunable Metallogels Based on Bifunctional Ligands: Precursor Metallogels, Spinel Oxides, Dye and CO₂ Adsorption, *ACS Omega* 5, 17356–17366 (DOI: 10.1021/acsomega.0c01710)
126. Dhibar S., Dey A., et al. (2018), A supramolecular Cd(II)-metallogel: an efficient semiconductive electronic device, *Dalton Trans.* 47, 17412–17420 (DOI: 10.1039/C8DT03773F)
127. Wu H., Zheng J., et al. (2019), Metallogels: Availability, Applicability, and Advanceability, *Adv. Mater.* 31, 1806204 (DOI: 10.1002/adma.201806204)
128. Zhang J., Su, C.Y. (2013), Metal-organic gels: From discrete metallogelators to coordination polymers, *Coord. Chem. Rev.* 257, 1373–1408 (DOI: 10.1016/j.ccr.2013.01.005)

129. Piepenbrock M.O.M., Lloyd G.O., et al. (2010), Metal- and Anion-Binding Supramolecular Gels, *Chem. Rev.* 110, 1960–2004 (DOI: 10.1021/cr9003067)
130. Rejab M.R.B.M., Hamdan M.H.B.M., et al. (2020), Historical Development of Hybrid Materials. In *Encyclopedia of Renewable and Sustainable Materials* (Elsevier), 45–455 (DOI: 10.1016/B978-0-12-803581-8.10546-6)
131. Kulikov V., Johnson, N.A.B., et al. (2017), Spontaneous Assembly of an Organic–Inorganic Nucleic Acid Z-DNA Double-Helix Structure, *Angew. Chem. Int. Ed.* 56, 1141–1145 (DOI: 10.1002/anie.201606658)
132. Vázquez-González M., Willner I. (2020), Stimuli-Responsive Biomolecule-Based Hydrogels and Their Applications, *Angew. Chem. Int. Ed.* 59, 15342–15377 (DOI: 10.1002/anie.201907670)
133. Du X., Zhou J., Xu, B. (2014), Supramolecular Hydrogels Made of Basic Biological Building Blocks, *Chem. Asian J.* 9, 1446–1472 (DOI: 10.1002/asia.201301693)
134. Xu T., Wang J., et al. (2023), Accelerating the prediction and discovery of peptide hydrogels with human-in-the-loop, *Nat. Commun.* 14, 3880 (DOI: 10.1038/s41467-023-39648-2)
135. Rumon Md.M.H., Akib A.A., et al. (2024), Polysaccharide-Based Hydrogels for Advanced Biomedical Engineering Applications, *ACS Polym. Au* 4, 463–486 (DOI: 10.1021/acspolymersau.4c00028)
136. Yang Q., Peng J., et al. (2022), Polysaccharide hydrogels: Functionalization, construction and served as scaffold for tissue engineering, *Carbohydr. Polym.* 278, 118952 (DOI: 10.1016/j.carbpol.2021.118952)

137. Yan C., Pochan, D.J. (2010), Rheological properties of peptide - based hydrogels for biomedical and other applications, *Chem. Soc. Rev.* 39, 3528–3540 (DOI: 10.1039/B919449P)
138. Sun, S., Xu, M., et al. (2023), Nucleobase-Modified Adhesive and Conductive Hydrogel Interface for Bioelectronics, *ACS Appl. Nano Mater.* 6, 21226–21235 (DOI: 10.1021/acsanm.3c04282)
139. Shao T., Falcone N., Kraatz, H.B. (2020), Supramolecular Peptide Gels: Influencing Properties by Metal Ion Coordination and Their Wide-Ranging Applications, *ACS Omega* 5, 1312–1317 (DOI: 10.1021/acsomega.9b03939)
140. Shukla M.P., Kaul G., et al. (2019), Nucleobase Soft Metallogel Composites with Antifouling Activities against ESKAPE Pathogens, *ChemistrySelect* 4, 1834–1839 (DOI: 10.1002/slct.201803693)
141. Blackburn G.M., Gait M.J., et al. (2006), Introduction and Overview. In *Nucleic Acids in Chemistry and Biology* (The Royal Society of Chemistry), 1–12 (DOI: 10.1039/9781847555380-00001)
142. Saenger W. (1984), *Principles of Nucleic Acid Structure* (Springer) (DOI: 10.1007/978-1-4612-5190-3)
143. Peters G.M., and Davis J.T. (2016), Supramolecular gels made from nucleobase, nucleoside and nucleotide analogs, *Chem. Soc. Rev.* 45, 3188–3206 (DOI: 10.1039/C6CS00183A)
144. Davis J.T., Spada G.P. (2007), Supramolecular architectures generated by self-assembly of guanosine derivatives, *Chem. Soc. Rev.* 36, 296–313 (DOI: 10.1039/B600282J)
145. Davis J.T. (2004), G-Quartets 40 Years Later: From 5'-GMP to Molecular Biology and Supramolecular Chemistry, *Angew. Chem. Int. Ed.* 43, 668–698 (DOI: 10.1002/anie.200300589)

146. Stefan L., Monchaud D. (2019), Applications of guanine quartets in nanotechnology and chemical biology, *Nat. Rev. Chem.* 3, 650–668 (DOI: 10.1038/s41570-019-0132-0)
147. Giorgi T., Lena S., et al. (2003), Supramolecular Helices via Self-Assembly of 8-Oxoguanosines, *J. Am. Chem. Soc.* 125, 14741–14749 (DOI: 10.1021/ja0364827)
148. Yoshikawa I., Li J., et al. (2004), Design and Fabrication of a Flexible and Self-Supporting Supramolecular Film by Hierarchical Control of the Interaction between Hydrogen-Bonded Sheet Assemblies, *Angew. Chem. Int. Ed.* 43, 100–103 (DOI: 10.1002/anie.200352641)
149. Peters G.M., Skala, L.P. et al. (2014), A G4-K⁺ Hydrogel Stabilized by an Anion, *J. Am. Chem. Soc.* 136, 12596–12599 (DOI: 10.1021/ja507506c)
150. Peters G.M., Skala L.P., et al. (2015), G4-Quartet·M⁺ Borate Hydrogels, *J. Am. Chem. Soc.* 137, 5819–5827 (DOI: 10.1021/jacs.5b02753)
151. Dash J., Patil A.J., et al. (2011), Supramolecular hydrogels derived from silver ion-mediated self-assembly of 5'-guanosine monophosphate, *Soft Matter* 7, 8120–8126 (DOI: 10.1039/C1SM05839H)
152. Ghosh A., Parasar B., et al. (2016), Chiral carbon dots derived from guanosine 5'-monophosphate form supramolecular hydrogels, *Chem. Commun.* 52, 11159–11162 (DOI: 10.1039/C6CC05947C)
153. Bang I. (1910), Untersuchungen über die Guanylsäure, *Biochem* 26, 293-311
154. Gellert M., Lipsett M.N., Davies D.R. (1962), Helix formation by guanylic acid, *Proc. Natl. Acad. Sci.* 48, 2013–2018 (DOI: 10.1073/pnas.48.12.2013)

155. Prasad B., Doimo M., et al. (2022), A complementary chemical probe approach towards customized studies of G-quadruplex DNA structures in live cells, *Chem. Sci.* 13, 2347–2354 (DOI: 10.1039/D1SC05816A)
156. Spiegel J., Adhikari S., Balasubramanian S. (2020), The Structure and Function of DNA G-Quadruplexes, *Trends Chem.* 2, 123–136 (DOI: 10.1016/j.trechm.2019.07.002)
157. Ghosh T., Biswas A., et al. (2021), Pt Nanoparticles Supported on a Dynamic Boronate Ester-Based G-quadruplex Hydrogel as a Nanoreactor, *Chem. Asian J.* 16, 215–223 (DOI: 10.1002/asia.202001284)
158. Renaud de la Faverie A., Guédin A., et al. (2014), Thioflavin T as a fluorescence light-up probe for G4 formation, *Nucleic Acids Res.* 42, e65 (DOI: 10.1093/nar/gku111)
159. Mohanty J., Barooah N., et al. (2013), Thioflavin T as an Efficient Inducer and Selective Fluorescent Sensor for the Human Telomeric G-Quadruplex DNA, *J. Am. Chem. Soc.* 135, 367–376 (DOI: 10.1021/ja309588h)
160. Perez C., Miti T., et al. (2019), Mechanism of Fibril and Soluble Oligomer Formation in Amyloid Beta and Hen Egg White Lysozyme Proteins, *J. Phys. Chem. B* 123, 5678–5689 (DOI: 10.1021/acs.jpcc.9b02338)
161. Carvalho J., Queiroz J.A., Cruz C. (2017), Circular Dichroism of G-Quadruplex: a Laboratory Experiment for the Study of Topology and Ligand Binding, *J. Chem. Educ.* 94, 1547–1551 (DOI: 10.1021/acs.jchemed.7b00160)
162. Forman S.L., Fetting J.C., et al. (2000), Toward Artificial Ion Channels: A Lipophilic G-Quadruplex, *J. Am. Chem. Soc.* 122, 4060–4067 (DOI: 10.1021/ja9925148)

163. Chakraborty A., Ghosh T., et al. (2024), A multi-stimuli responsive polyoxometalate-guanosine monophosphate hybrid chromogenic smart hydrogel, *J. Mater. Chem. C* 12, 13447–13456 (DOI: 10.1039/D4TC01973C)
164. Wong A., Fettinger J.C., et al. (2002), The Sodium Ions Inside a Lipophilic G-Quadruplex Channel as Probed by Solid-State ^{23}Na NMR, *J. Am. Chem. Soc.* 124, 742–743 (DOI: 10.1021/ja0120330)
165. Ida R., Kwan I.C.M., Wu G. (2007), Direct ^{23}Na NMR observation of mixed cations residing inside a G-quadruplex channel, *Chem. Commun.*, 795–797 (DOI: 10.1039/B613105K)
166. Cheng X., Chen H., et al. (2022), All-small-molecule supramolecular hydrogels assembled from guanosine 5'-monophosphate disodium salt and tobramycin for the treatment of bacterial keratitis, *Bioact. Mater.* 16, 293–300 (DOI: 10.1016/j.bioactmat.2021.12.024)
167. Li T., Luo Y., et al. (2023), Super-Rapid In Situ Formation of a Silver Ion-Induced Supramolecular Hydrogel with Efficient Antibacterial Activity for Root Canal Disinfection, *ACS Appl. Mater. Interfaces* 15, 29854–29865 (DOI: 10.1021/acsami.3c03335)
168. Godoy-Gallardo M., Merino-Gómez M., et al. (2023), Advanced Binary Guanosine and Guanosine 5'-Monophosphate Cell-Laden Hydrogels for Soft Tissue Reconstruction by 3D Bioprinting, *ACS Appl. Mater. Interfaces* 15, 29729–29742 (DOI: 10.1021/acsami.2c23277)
169. Gao W., Zhang D., (2024), Guanosine-Based Multidrug Strategy Delivery for Synergistic Anti-Inflammation, *ACS Macro Lett.* 13, 260–265 (DOI: 10.1021/acsmacrolett.3c00562)
170. Sarma S., Thakur N., et al. (2024), Chromatin inspired biocondensation between biomass DNA and guanosine monophosphate

- produces all-nucleic hydrogel as a hydrotropic drug carrier, *Commun. Chem.* 7, 1–13 (DOI: 10.1038/s42004-024-01353-6)
171. Thakur N., Sharma B., et al. (2019), Biocompatible Fe³⁺ and Ca²⁺ Dual Cross-Linked G-Quadruplex Hydrogels as Effective Drug Delivery System for pH-Responsive Sustained Zero-Order Release of Doxorubicin, *ACS Appl. Bio Mater.* 2, 3300–3311 (DOI: 10.1021/acsabm.9b00334)
172. Bai J., Sun X., et al. (2020), Guanosine-Based Self-Assembly as an Enantioselective Catalyst Scaffold, *J. Org. Chem.* 85, 2010–2018 (DOI: 10.1021/acs.joc.9b02718)
173. Chen Z., Zhou P., et al. (2022), Guanosine Borate Hydrogel and Self-Assembled Nanostructures Capable of Enantioselective Aldol Reaction in Water, *J. Org. Chem.* 87, 2624–2631 (DOI: 10.1021/acs.joc.1c02573)
174. Lala B., Chaudhuri R., et al. (2024), Guanosine-based hydrogel as a supramolecular scaffold for template-assisted macrocyclization, *Chem. Commun.* 60, 3433–3436 (DOI: 10.1039/D4CC00129J)
175. Hu X., Wang G., et al. (2023), The construction of Fe-porphyrin nanozymes with peroxidase-like activity for colorimetric detection of glucose, *Anal. Biochem.* 675, 115224 (DOI: 10.1016/j.ab.2023.115224)
176. Bhattacharyya T., Kumar Y.P., Dash J. (2017), Supramolecular Hydrogel Inspired from DNA Structures Mimics Peroxidase Activity, *ACS Biomater. Sci. Eng.* 3, 2358–2365 (DOI: 10.1021/acsbiomaterials.7b00563)
177. Thakur N., Chaudhary A., et al. (2021), Ion Conductive Phytic Acid-G Quadruplex Hydrogel as Electrolyte for Flexible Electrochromic Device, *ChemNanoMat* 7, 613–619 (DOI: 10.1002/cnma.202100072)

178. Li J., Wei H., et al. (2019), A multifunctional self-healing G-PyB/KCl hydrogel: smart conductive, rapid room-temperature phase-selective gelation, and ultrasensitive detection of alpha-fetoprotein, *Chem. Commun.* 55, 7922–7925 (DOI: 10.1039/C9CC02770J)

Chapter 2

Polyoxometalate-Guanosine Monophosphate Hydrogel with Haloperoxidase-like Activity for Antibacterial Performance

2.1 Introduction

Biofouling takes place due to the gradual growth of microorganism colonies on different surfaces.¹ These microorganisms irreversibly grow on a surface by producing extracellular polysaccharides, resulting in attachment and matrix formation on the surface, thus developing a biofilm.² The omnipresence of these biofilms causes heaps of complications in biofouling-prone surfaces, such as ships or submarines, industrial equipment, pipes, water bodies, etc. along with causing serious threats to public health due to a significant decrease in antimicrobial susceptibility on medical devices.²⁻⁵ Therefore, a huge effort is dedicated to developing biocides that can prevent biofouling in an ecologically sound approach. Although several antifouling coatings and paints based on metal complexes are available to coat external surfaces, they come at the risk of environmental damage through metal leaching.⁶ One of the approaches that natural systems such as marine algae adopt is to secrete an enzyme known as haloperoxidase, through which they develop a defense mechanism against microorganisms. Based on differences in prosthetic groups, haloperoxidases are classified into two types: (i) heme dependent haloperoxidase and (ii) vanadium-dependent haloperoxidase. This class of enzymes catalyzes the oxidation of halide ions (Cl^- , Br^- , I^-) to hypohalous acids (HOX). The HOX produced in this process deactivates the intercellular communication in microorganisms responsible for biofilm formation.^{7,8} Thus, haloperoxidases provide an applicable pathway for developing non-toxic antifouling paints and coatings. However, natural enzymes have their limitations, as they function under highly specific conditions (optimal

pH, temperature, and ionic strength) and get denatured in extreme conditions. Also, their production is quite expensive, thus making them unsuitable for large-scale use. Therefore, much attention is being given to enzyme mimetic systems, which are artificial enzymes that can emulate natural enzymes, and are biocompatible, cost-effective, have better stability, and have good catalytic activity.^{9–14}

Based on the fact that the natural haloperoxidases contain vanadium metal in its active site, most of the functional haloperoxidase mimicking systems are based on vanadium such as vanadium Schiff base complexes and peroxovanadium complexes.^{15,16} Tremel *et al.* first demonstrated the activity of vanadium pentoxide nanoparticles as haloperoxidase mimics that showed high activity to prevent marine biofouling.¹⁷ CeO_{2-x} based nanorods also show high haloperoxidase mimicking activity that has been used to combat biofouling.^{18–20} Polyoxometalates (POM) are complexes of early transition metal-oxygen clusters and have emerged as an attractive functional material due to their interesting physicochemical properties such as high electronegativity, controllable morphology, oxo-enriched surface, tunable acid-base character, and redox property.²¹ Most POMs have a small surface area and are highly soluble in aqueous medium but they can also interact with various substrates via electrostatic forces, hydrogen bonding, and non-covalent interactions to provide multifunctional POM hybrid materials. Subsequently, POM-based functional materials show potential in a wide range of applications such as photochromic or electrochromic devices²², magnetic materials²³, organic and photocatalysis^{24–26}, artificial enzymes^{27–31}, environmental remediations³² along with biological activities such as anticancer, antibacterial, and antiviral properties.^{33–36} Most of these applications are attributed to their high proficiency in receiving and liberating electrons without any structural change or decomposition.^{21,37} Despite all the advantages associated with POMs, their unspecified interactions with biomolecules and toxicity generated after prolonged use limits their biological applications.^{33,38} Further, developing uniform coating with these nanocrystalline solids is a major

issue since they form non-homogeneous films with accumulated particles.³⁹ Hydrogels are three-dimensional networks that can absorb a large amount of water and have structural properties similar to tissues. Further, depending on their chemical composition, they show responsiveness to various stimuli such as temperature, pH, or chemicals.^{40,41} Therefore, incorporating POMs into a hydrogel matrix can provide solutions to the inherent drawbacks of POMs in the solution state.^{38,42} Most focus in this direction has been devoted to covalently attaching organic functionalities onto the POM surface.³⁸ However, the anionic nature of the surface and the presence of metal-oxo bonds also provide opportunities for supramolecular formulations via non-covalent interactions. Anionic POM can electrostatically interact with cationic surfactants to form organic gels. POM-loaded hydrogels have been reported by incorporating POM in a gel matrix or using biomolecules such as peptides as the organic component.^{38,43-47}

Among the commonly available biomolecules, the ability of nucleotides to function as a low molecular weight gelator (LMWG) is well documented.⁴⁸ Various binding sites in a nucleotide can induce different interactions such as coordination bonds with metal ions, hydrogen bonding, π - π stacking, and electrostatic interaction that leads to the formation of macromolecular superstructures.^{48,49} Guanosine monophosphate is of particular interest as various types of supramolecular assemblies such as G-Quartet,⁴⁹⁻⁵¹ dimer,^{52,53} ribbon,⁵⁴ sheet⁵⁵, *etc.* are formed due to the participation of both Watson-Crick and Hoogsteen faces in hydrogen bonding. Cronin *et al.* reported the formation of a well-defined Z-DNA double helix structure obtained through the condensation reaction of GMP and sodium molybdate. The resultant POM-nucleotide complex formed through covalent interaction could act as a gelator to form an organogel.⁵³ However, there is no report of POM-nucleotide hydrogel formed through non-covalent interactions which might be advantageous from the fabrication point of view that brings additional properties.

Herein, we report the formation of POM-GMP hybrid hydrogels through a simple mixing of two commercially available tungsten-based Keggin polyoxometalates, phosphotungstic acid (PTA) and tungstosilicic acid (STA) with GMP in aqueous medium at room temperature. The hydrogels thus obtained were mechanically robust, shape-sustaining, and showed thixotropic properties. Further, the hydrogels showed reversible thermoresponsive sol-gel transition. The POM-GMP hydrogels showed better biocompatibility as compared to the bare POMs dispersed in an aqueous medium. Both the hydrogels showed efficient haloperoxidase activity, although the enzyme mimetic activity of PTA-GMP hydrogel was found to be significantly higher as compared to STA-GMP hydrogel. The PTA-GMP hydrogel showed significant antibacterial activity against both gram-positive and gram-negative bacteria. The simplicity in the synthesis, high biocompatibility, thixotropic properties, ability to form uniform film, and efficient antibacterial activity make the POM-GMP hydrogel a potent anti-biofouling agent.⁵⁶

2.2. RESULTS AND DISCUSSION

2.2.1 Synthesis of the hydrogels

A simple mixture of POMs (60 mM) and GMP (180 mM) at a 1:3 molar ratio in an aqueous medium was slightly heated to 50 °C to get a homogeneous mixture, which upon cooling to room temperature resulted in the spontaneous formation of a self-assembled hydrogel. The formation of POM-GMP hydrogel was confirmed physically by a ‘vial-inversion’ test (Figure 2.1).

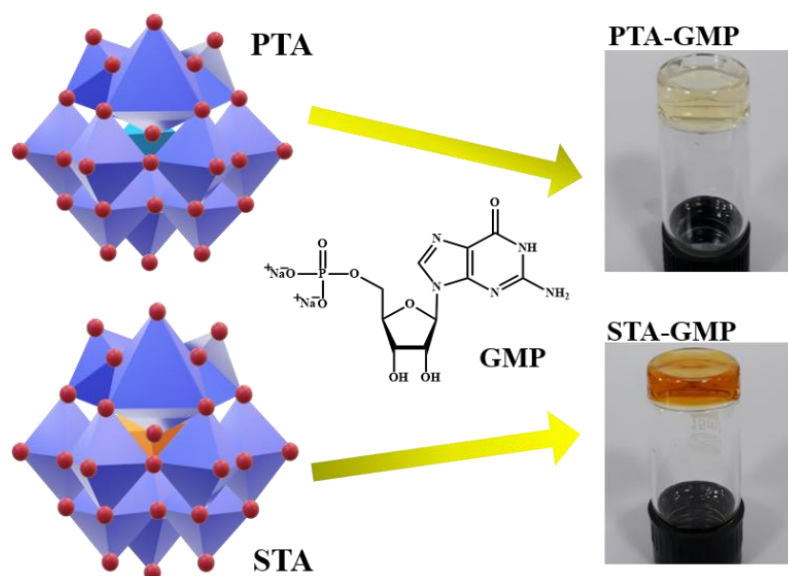


Figure 2.1. Formation PTA and STA hydrogels with GMP

The concentration ratio (POM and GMP) dependent formation of the hydrogel was observed visually (Figures 2.2 a-d). Experiments were performed by initially keeping the concentration of POM constant (60 mM) and varying GMP concentration from 90 mM to 360 mM. No gelation was observed at a 1:1.5 ratio of POM: GMP. From a POM: GMP concentration ratio of 1:2, stable gels were observed with no solvent flow under gravity when the vial was inverted. Stronger gels were obtained as the concentration of GMP was increased. Next, the concentration of GMP was kept constant (180 mM) and the concentration of POM was varied from 30 to 120 mM. It was observed that the color of the system gets more intense with an increase in the amount of POM. As the concentration of POM was increased a weak and opaque gel was obtained in the case of PTA. However, in the case of STA, a clear homogeneous orange solution was obtained. Based on these results, a POM:GMP ratio of 1:3 was used for gel formation in all subsequent studies.

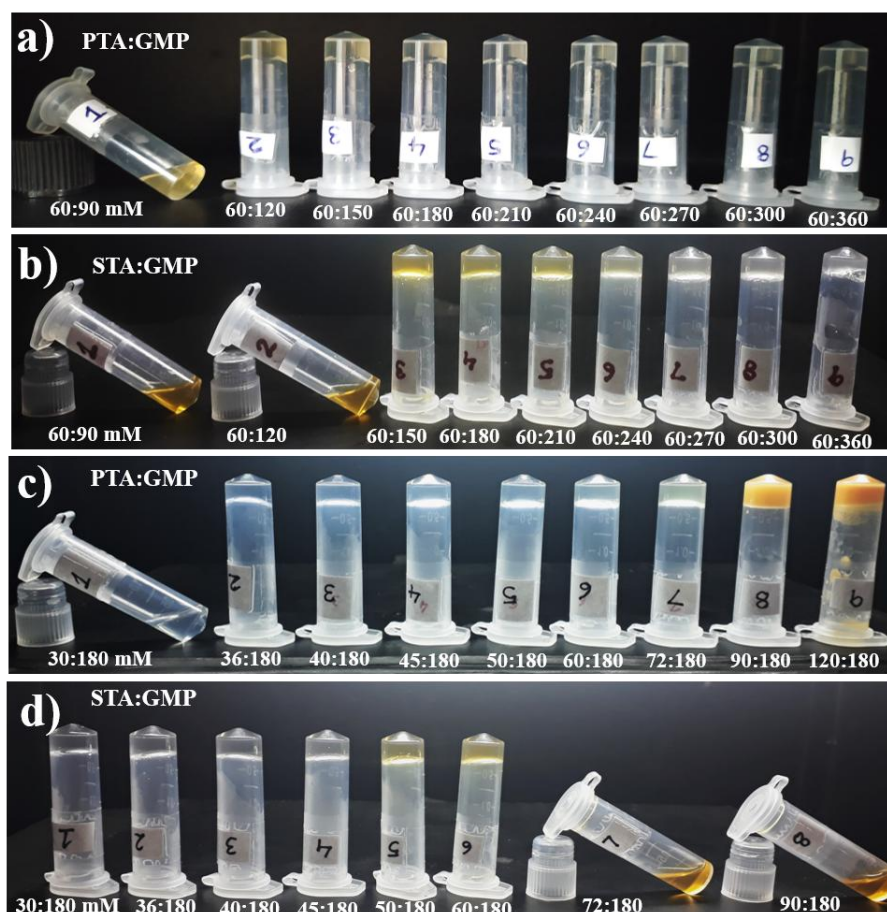


Figure 2.2. Digital images of POM-GMP system with different concentrations (a, b) varying the concentration of GMP with respect to (a) PTA and (b) STA, respectively, (c, d) varying the concentration of (c) PTA and (d) STA with respect to GMP, respectively.

Both PTA-GMP and STA-GMP showed thermo-reversible properties enabling them to convert to sol at an elevated temperature of 50 °C and 48 °C respectively (Figure 2.3a, b). The sol can be converted back to hydrogel upon cooling. This property of the gels was utilized to mold them into different shapes (Figure 2.3c, d). Stimuli responsiveness of both the gels was studied by treating them with 100 mM of histidine, aspartic acid, urea, and ammonium hydroxide (Figures 2.3e, f). Urea and aspartic acid did not affect the stability of the hydrogel. Upon exposure to histidine and ammonium hydroxide, the gel was converted into a sol initially but hydrogels were again reformed after two days. We also observed the formation of thin films when a layer of PTA-GMP and STA-GMP hydrogels were left to dry for 3-4 hours. PTA-GMP thin film

obtained was transparent, where we could see the word gel written on paper through it. (Figure 2.3 g-l)

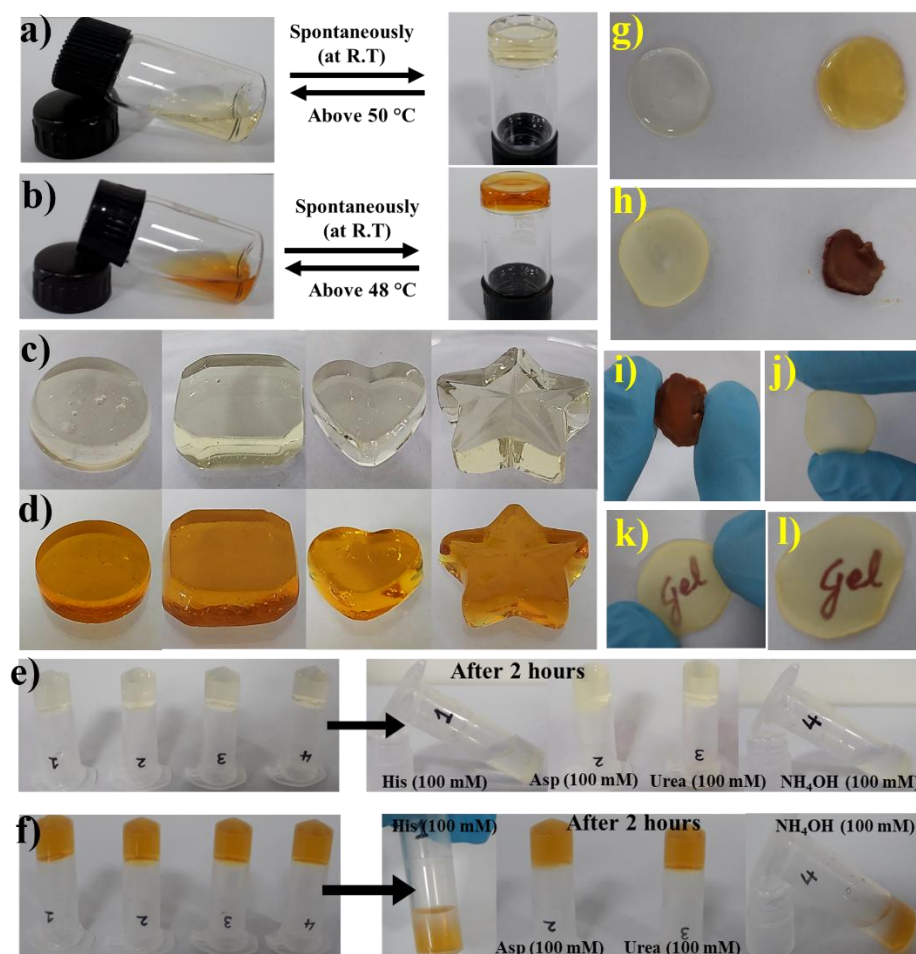


Figure 2.3. (a,b) Thermoreversibility of the PTA-GMP and STA-GMP hydrogels respectively, (c,d) PTA-GMP and STA-GMP hydrogel molded into different shapes, (e,f) stimuli-responsive behavior of PTA-GMP and STA-GMP hydrogel with respect to histidine, aspartic acid, urea, NH_4OH , (g-l) thin films of PTA-GMP and STA-GMP obtained on drying the hydrogel and (k,l) transparency of PTA-GMP film where we can see the word gel written on paper.

2.2.2 Morphological Evaluation

Morphological analysis of the hydrogel was carried out using various microscopic techniques. Scanning electron microscopy (SEM) images of PTA-GMP and STA-GMP showed highly entangled fibrillar structures (Figure 2.4a, b). The average diameter of the fibers were calculated to be 130-160 nm in the case of PTA-GMP and 90-120 nm in the case of STA-GMP and were several micrometers in length in both cases. Transmission

electron microscopy (TEM) further reinforced the observation of web-like fiber formation (Figure 2.4c, d). The fiber diameter calculated from the TEM images was in the range of 10 to 15 nm in the case of STA-GMP and 30-50 nm in the case of PTA-GMP gel. From the microscopic images it could be observed that the POM-GMP strands were bundled up to form the nanofibers and cross-linking of the fibers effectively resulted in the dense entangled network.

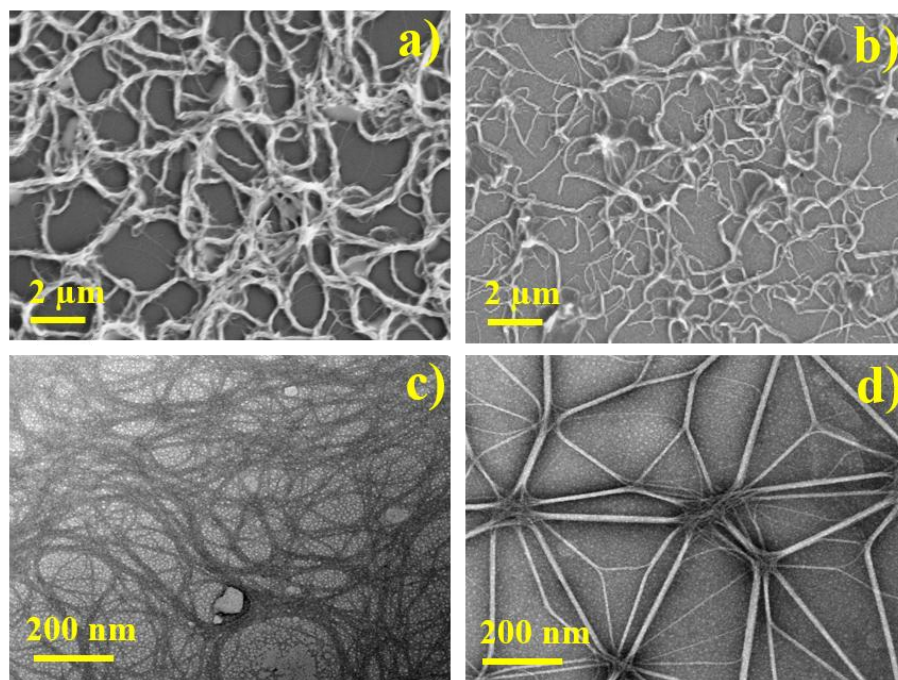


Figure 2.4. (a, b) FESEM images of PTA-GMP and STA-GMP hydrogel respectively, (c, d) TEM images of PTA-GMP and STA-GMP hydrogel respectively

2.2.3 Spectroscopic Characterization.

The UV-visible spectrum of GMP showed an absorption maximum at 252 nm and a shoulder band at 272 nm. On the other hand, absorption maxima were obtained at 254 and 262 nm for PTA and STA solutions respectively (Figure 2.5a, b). A hypsochromic shift in both the POM solutions was observed upon the addition of GMP solution, which indicates the interaction of GMP with POM to form a metal-organic composite and the absorbance spectra of the hydrogels are a hybrid of both precursors. From the Job's plot, the most suitable stoichiometry for POM-GMP interaction was found to be at the ratio of 2:3 (Figure 2.5 c-f). However, at this concentration ratio, a very weak heterogeneous gel was obtained in the

case of PTA-GMP, whereas a clear orange solution was obtained for STA-GMP. Based on the experimental studies, a 1:3 concentration ratio of the POM and GMP was used for gel formation considering the robustness and stability of the gel.

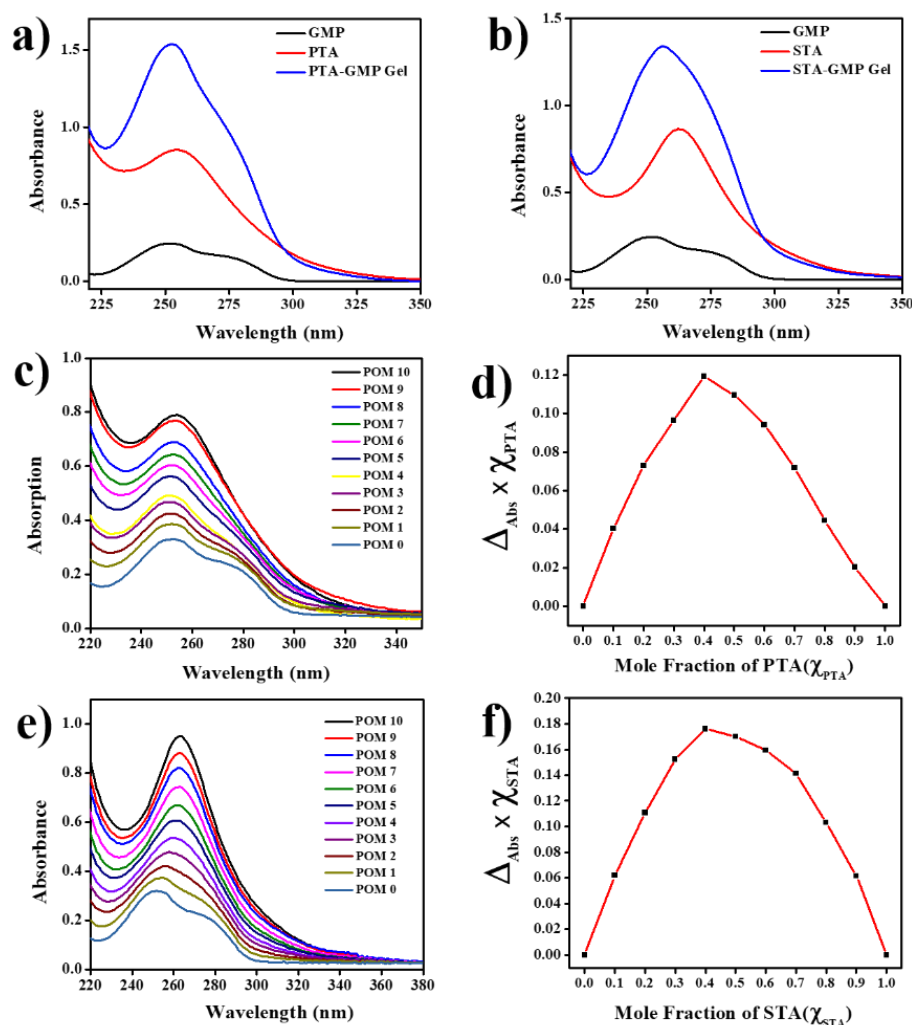


Figure 2.5. (a, b) UV-Visible spectra of aqueous solutions of 0.025 mM GMP, 0.025 mM POM (PTA and STA), and 0.025 mM POM-GMP system, (c, e) UV spectra upon addition of an equimolar solution of GMP to PTA and STA solutions respectively at different ratios, (d, f) their respective Job's plot calculated at 252 nm from absorption maxima.

Circular dichroism (CD) analysis was performed to study the chirality of the hydrogels (Figure 2.6a, b). An aqueous solution of GMP shows a positive band at 213 nm that corresponds to an $n-\pi^*$ transition of purine base and a negative Cotton band at about 250 nm, which suggests the presence of the β -anomeric form of sugar moieties in the GMP

solution.^{50,57,58} In the CD spectra of the hydrogels, we obtained similar trends as monomeric GMP suggesting that the GMP was present in its monomeric form in the composite.⁵⁸ Compared to GMP, positive cotton effects for both the gels appeared slightly weaker, which could be attributed to the non-covalent interactions of the purine base with the polyoxometalates.⁵⁹ Thus, it can be implied from CD studies that the chirality of GMP was well preserved in the supramolecular POM-GMP assembly. CD spectra were recorded for both the POMs by varying POM to GMP concentration ratios (Figure 2.6c, d).

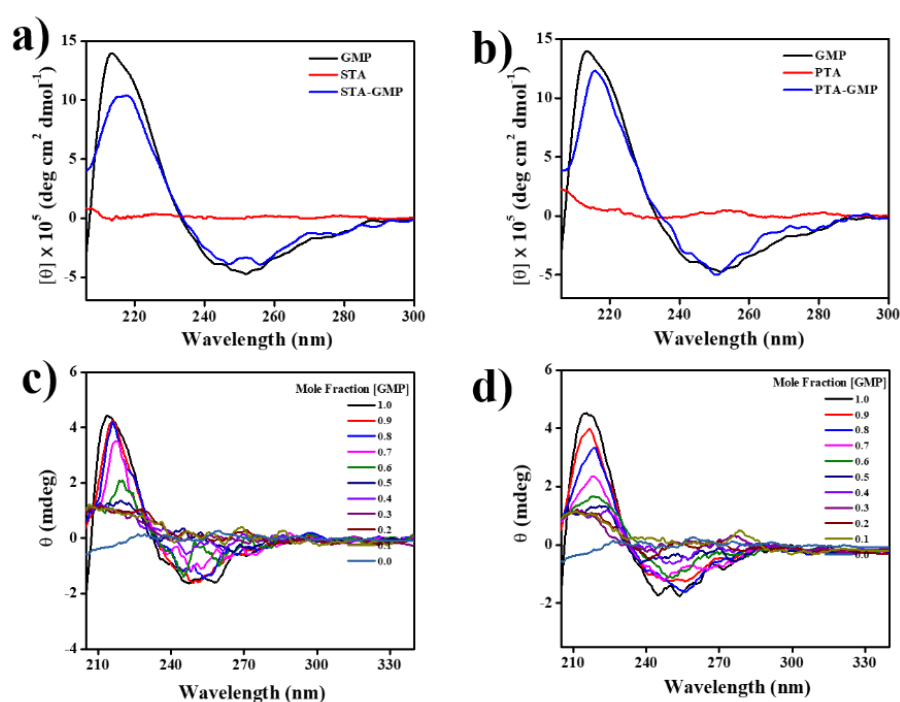


Figure 2.6. (a, b) CD Spectra of 0.25 mM GMP, 0.25 mM POM (PTA and STA), and 0.25 mM POM-GMP hydrogel, (c,d) Circular dichroism spectra of PTA-GMP and STA-GMP complex recorded with decreasing mole fraction of GMP respectively.

FTIR spectroscopy was performed to assess the interactions between GMP and POM responsible for gelation (Figure 2.7a, b). The characteristic peaks of PTA and STA appear in the range of 1100 to 700 cm^{-1} . The four characteristic peaks of a Keggin structure for PTA around 1072 cm^{-1} , 971 cm^{-1} , 913 cm^{-1} , and 782 cm^{-1} are attributed to the stretching vibrations of P-O, W-O_t, W-O_c-W, and W-O_e-W respectively (where O_t is terminal oxygen, O_c is centered oxygen and O_e is edge oxygen). Similar characteristic peaks for STA at 1020 cm^{-1} , 975 cm^{-1} , 904

cm^{-1} , and 735 cm^{-1} are observed corresponding to Si-O, W-O_t, W-O_e-W, and W-O_e-W respectively.⁶⁰⁻⁶² The FTIR traits for both POMs are retained in the gels with a slight shift in their stretching frequency, thus indicating that the basic Keggin structure of the polyoxometalates was preserved in the gel. N7 of the purine base is one of the well-known interacting sites that induce the formation of supramolecular assembly and its role in gelation is evident through the shift observed in the stretching vibration of the C(8)-N(7) bond. The peak at 1481 cm^{-1} in GMP assigned to the C(8)-N(7) stretching frequency was slightly shifted to 1473 and 1470 cm^{-1} in PTA-GMP and STA-GMP, respectively. This slight shift without any characteristic change in the spectra is indicative of non-covalent interactions such as hydrogen bonding.⁶³ A shift was also observed in the C=O peak towards a higher frequency from 1668 cm^{-1} to 1690 cm^{-1} for both PTA-GMP and STA-GMP. A shift in the C=O stretching frequency was observed from 1668 cm^{-1} to 1690 cm^{-1} in both PTA-GMP and STA-GMP systems. This shift can be attributed to the electron-rich, anionic nature of PTA and STA, whose proximity to the carbonyl group influenced its vibrational characteristics.⁶⁴ Moreover, the shoulder peak at 1633 cm^{-1} corresponding to the bending vibration of the -NH₂ group of GMP, showed a shift to 1643 and 1644 cm^{-1} for PTA-GMP and STA-GMP, respectively. This indicates that the -NH₂ group is also interacting with the POMs through H-bonding to one of the oxygens present on the POM shell. To confirm, gelation experiments were carried out by adding POMs to an aqueous solution of Inosine monophosphate (IMP), which is structurally similar to GMP except for the -NH₂ group. No gelation was observed in this case confirming the involvement of the -NH₂ group in gel formation (Figure 2.7c).

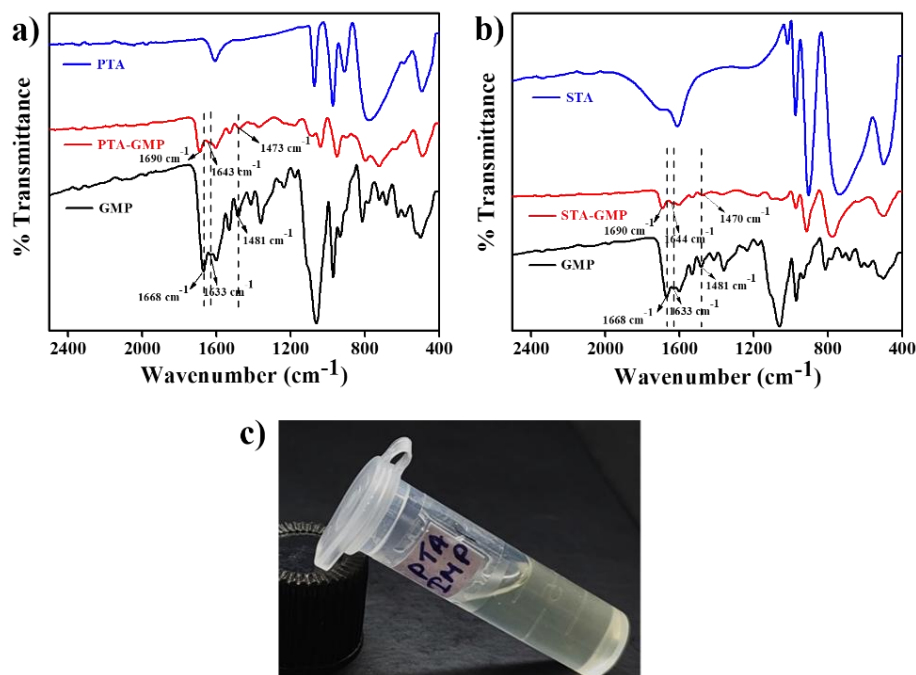


Figure 2.7. (a) FTIR spectra of (a) GMP, PTA, and PTA-GMP xerogel (b) FTIR spectra of GMP, STA, and STA-GMP xerogel, and (c) Digital image of PTA-IMP system showing the inability of POM to form a hydrogel with IMP.

Further ¹H NMR studies were performed for GMP and both the POM-GMP hydrogels (Figure 2.8a). The ¹H NMR of GMP showed resonance spectra at 8.13 ppm for H8, 5.85 ppm for H1', 4.69 ppm and 4.44 ppm for H2' and H3' respectively, 4.27 ppm for H4' and 3.96 ppm for H5',5''. All the protons exhibited a slight downfield shift indicating a non-covalent interactive environment, except for H2' and H3' which means the -OH group of the sugar had no role in the gelation. ³¹P NMR spectra showed an upfield shift from 3.8 ppm corresponding to the -PO₃²⁻ group in GMP to 0.2 ppm in the case of both the hydrogels (Figure 2.8b). This shift in the resonance spectra suggests the involvement of PO₃²⁻ moiety in non-covalent interactions leading to the formation of hydrogels.

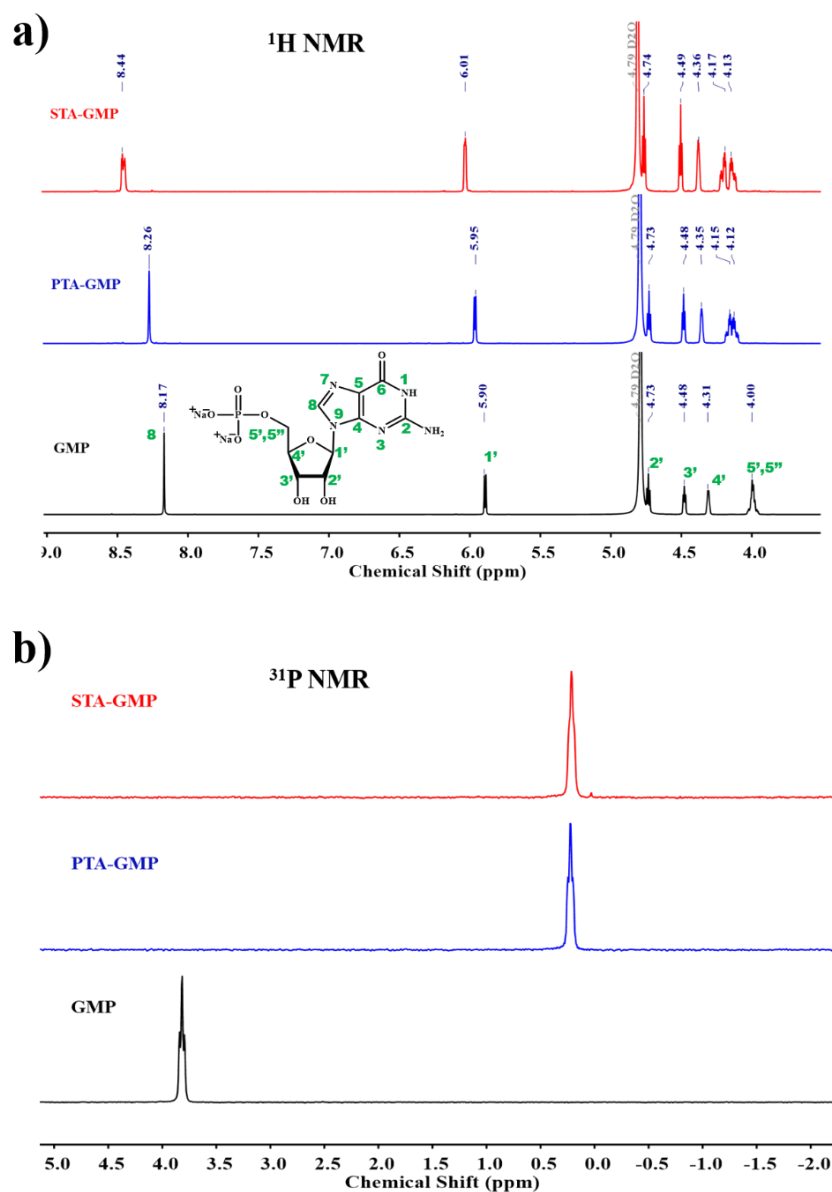


Figure 2.8. (a) ^1H and (b) ^{31}P NMR spectra of GMP, PTA-GMP, and STA-GMP.

To understand the driving forces for gel formation and structural aspects, we attempted to grow X-ray-quality crystals directly from the hydrogels, however, the crystals obtained were not of good quality for crystallographic analysis. Therefore, a probable mechanism is proposed based on the spectroscopic evidence. The self-assembly occurs through the interaction of the N7 and $-\text{NH}_2$ groups of the purine base and the $-\text{PO}_3^{2-}$ group in GMP with POM through H-bonding. It is well known that at highly acidic conditions, protonation occurs at the phosphate group and guanine ring at the N7 position. Protonation at the N7 position of the purine base blocks the H-bonding between the N7 and NH_2 group of

another guanine ring, thus preventing the G-Quadruplex formation.⁶⁵ PTA and STA are strong Bronsted acids, where they can donate three and four protons respectively.^{66–71} Therefore, protonation occurs in the N7 of the purine base. A plausible structure is depicted in Figure 2.9, where GMP interacts with POM through three sites (PO_3^{2-} , $\text{N}(7)\text{H}^+$, and $-\text{NH}_2$) via H-Bonding. Further entanglement occurs through π - π stacking of aromatic base and H-bonding leading to the formation of a fibril network.

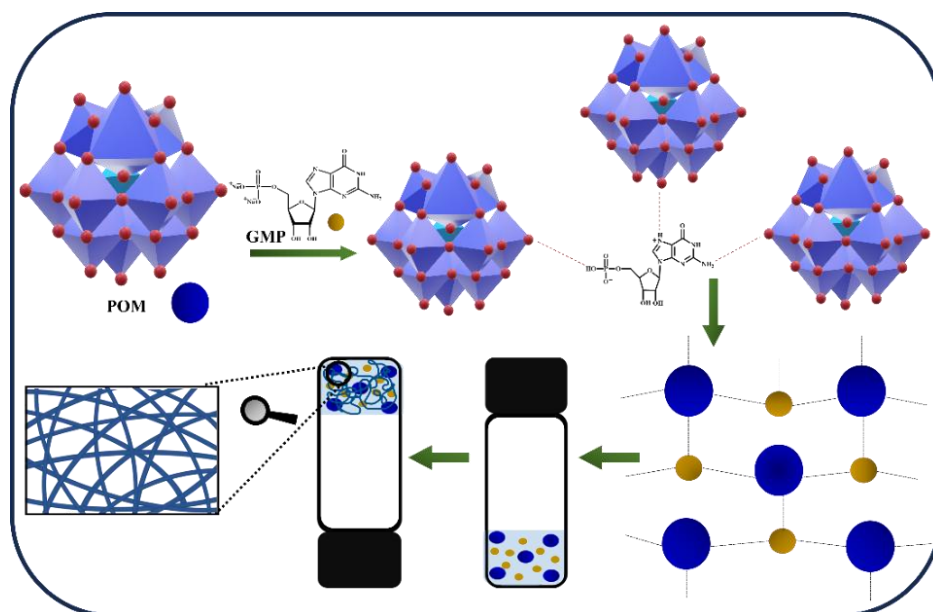


Figure 2.9. A schematic representation for the proposed self-assembly of the POM (PTA, STA) and GMP leading to a hydrogel.

2.2.4. Rheological Studies.

Rheological studies were performed to study the viscoelastic nature of the hydrogels. Strain, stress, and frequency sweep studies showed the dominance of elastic property over viscous property as the magnitude of storage modulus (G') was greater than the loss modulus (G'') over a range of strain and angular frequency (Figure 2.10). The strain-sweep rheological study showed that the magnitude of G' was greater than G'' till strain percentage of 32% and 83% for PTA-GMP and STA-GMP respectively (Figure 2.10 a,c). A thixotropic loop test was performed to check the recoverability of the gel (Figure 2.10 e,f). Successive low and high strains were applied at a time interval of 100 s to ensure complete loss and recoument of elastic behavior. Both the gels preserved their

elastic property ($G' > G''$) at a strain of 0.1 %. Both the gels started to lose their elastic property ($G'' > G'$), upon increasing the strain to 100%. The elastic property of the gels was restored after removing the strain. The reversible sol-gel transition was observed over several cycles. They could recover to their gel state in a time interval of 100 seconds, indicating dynamic behavior and rapid restoration of the self-assembled supramolecular network.

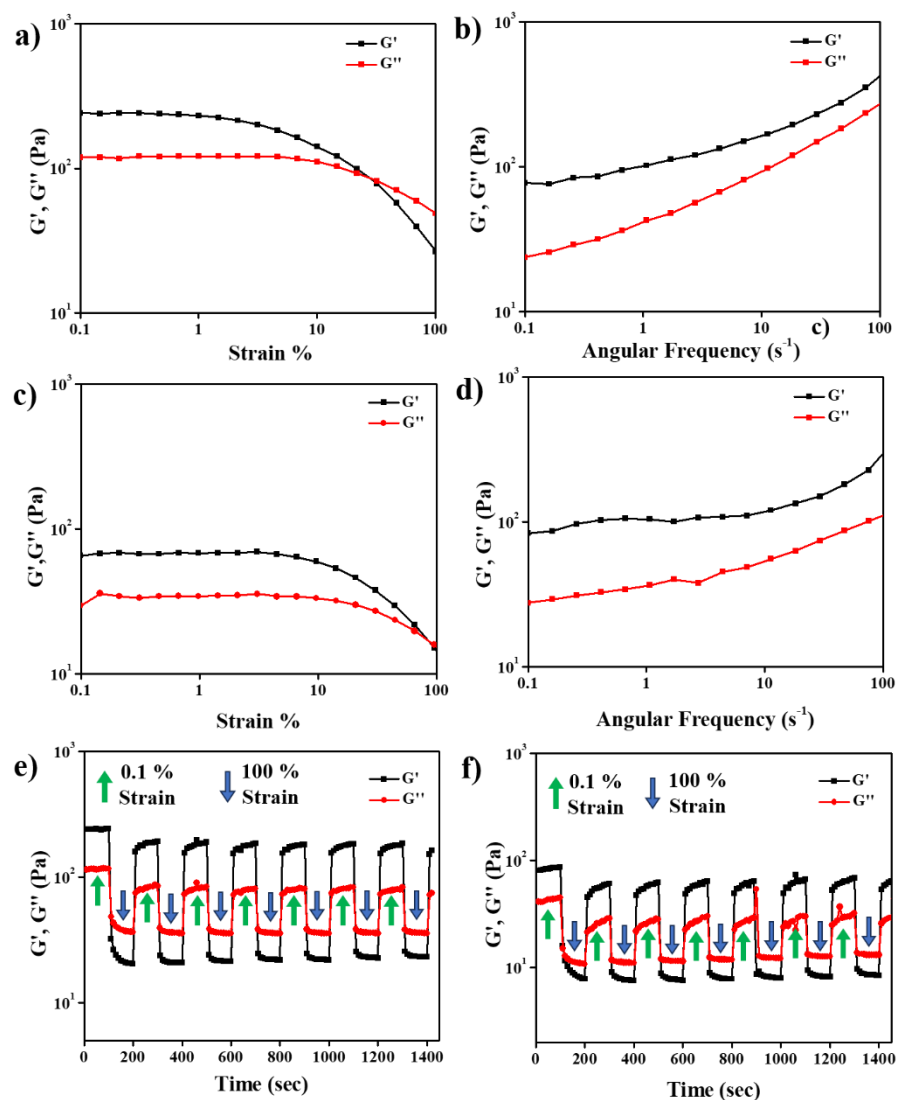


Figure 2.10. (a, c) Dynamic strain sweep of PTA-GMP and STA-GMP hydrogels, respectively; (b, d) Frequency sweep measurements of PTA-GMP and STA-GMP hydrogels at a constant strain of 1%, (e, f) Thixotropic loop measurements for PTA-GMP and STA-GMP hydrogels at a constant angular frequency of 10 rad s^{-1} .

Both gels showed rigidity and self-sustaining properties, which were physically observed by putting a weight of 3 pebbles (total weight

of 122 g) on them. Upon removing weight, they showed no appreciable change in shape or height (Figure 2.11a). Also, both hydrogels were highly injectable (Figure 2.11b).

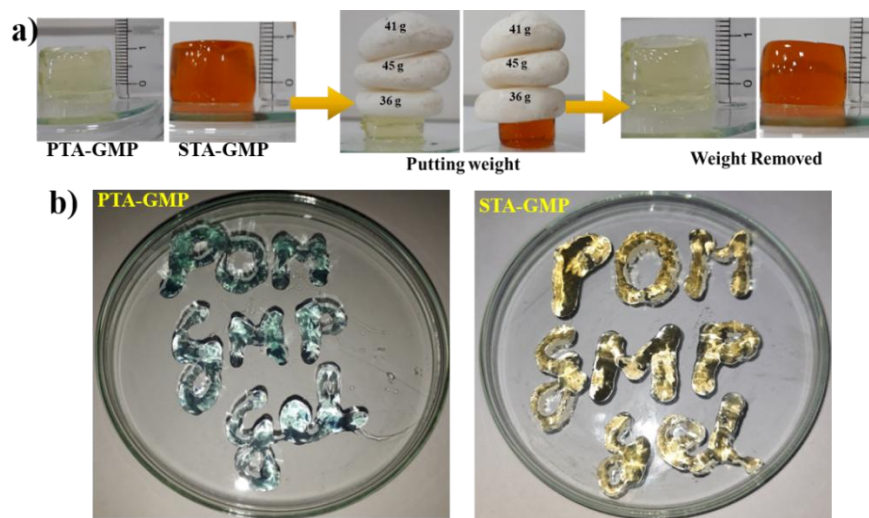


Figure 2.11. (a) Pictorial depiction of the rigidity and mechanical strength of the hydrogels where it can bear a total weight of 122g without deformation, and (b) Digital images showing injectability of (left) PTA-GMP hydrogel (loaded with methylene blue dye for visual ease), (right) STA-GMP hydrogel.

2.2.5 Haloperoxidase Activity

Although vanadium-based complexes and nanomaterials are commonly used for mimicking haloperoxidase enzymes, their large-scale usability for anti-biofouling applications is hindered due to vanadium compounds' carcinogenic and mutagenic nature. Therefore, we explored the possibility of using the polyoxometalates and polyoxometalate-GMP hydrogels as haloperoxidase mimics. Two colorimetric assays were performed using thymol blue (TB) and phenol red (PR) as substrates under two different pH conditions at pH 8 and 5.6 respectively. Both the substrates changed color from yellow to blue/violet, in the presence of iodide and H_2O_2 (Figure 2.12a). The haloperoxidase-like activity of the POMs and hydrogels leads to two-fold and four-fold oxidative halogenation of TB and PR resulting in TBX_2 and PRX_4 respectively which can be monitored spectrophotometrically from the absorbance maxima of the dyes and their halogenated products in milli-Q water. UV-visible studies were carried out to compare the reactivity of the POMs

and their respective gels by plotting the absorbance at 610 nm to time for TB assay (Figure 2.12b). The studies show that both the POMs demonstrate haloperoxidase activity and the catalytic activities were retained even after gelation with GMP. Bare PTA and PTA-GMP hydrogel showed significantly higher haloperoxidase activity than STA and STA-GMP hydrogel. Haloperoxidase activity of STA-GMP was found to be 4.5 times lower than the PTA-GMP hydrogel, as calculated by comparing the slope values by linear fitting. The catalytic activity of PTA-GMP hydrogel was slightly higher than bare PTA, and it was confirmed by performing three different experimental sets of haloperoxidase activity. Due to its higher activity, further kinetic studies were carried out with the PTA-GMP hydrogel.

ivity than STA and STA-GMP hydrogel. Haloperoxidase activity of STA-GMP was found to be 4.5 times lower than the PTA-GMP hydrogel, as calculated by comparing the slope values by linear fitting. The catalytic activity of PTA-GMP hydrogel was slightly higher than bare PTA, and it was confirmed by performing three different experimental sets of haloperoxidase activity. Due to its higher activity, further kinetic studies were carried out with the PTA-GMP hydrogel.

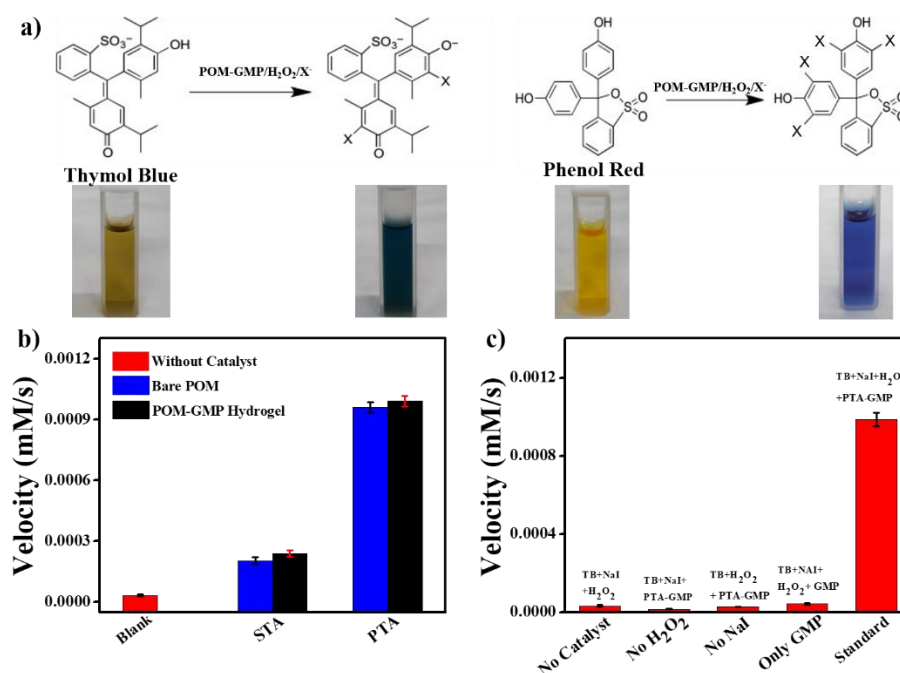


Figure 2.12. (a) Visual observation of haloperoxidase assay; change in solution color and structure of (left) Thymol blue and (right) Phenol red upon iodination in the presence of H₂O₂ using PTA-GMP hydrogel as catalyst, (b) comparison of haloperoxidase activity of STA, PTA, and their respective hydrogels, and (c) Control samples of the oxidative halogenation reaction of TB in (i) absence of PTA-GMP hydrogel, (ii) in the absence of H₂O₂, (iii) in the absence of NaI, and (iv) Standard system (in the presence of NaI, H₂O₂, and PTA-GMP catalyst).

Control experiments showed that the absence of the PTA-GMP xerogel did not result in the halogenation of the substrates, as no

characteristic absorbance for the halogenated products was observed. Similarly, the lack of either H_2O_2 or NaI resulted in no iodination of the substrates (Figure 2.12c).

Time-dependent UV-visible spectra were taken for 45 minutes for bromination and iodination of both PR and TB (Figure 2.13). The increment in absorption maxima at 610 nm (in the case of TB) and 590 nm (in PR) was due to the formation of TBX_2 or PRX_4 , respectively, which was responsible for the solution's blue coloration. The decrement in absorbance at 430 nm denotes the reduction in the amount of free TB/PR in the system.

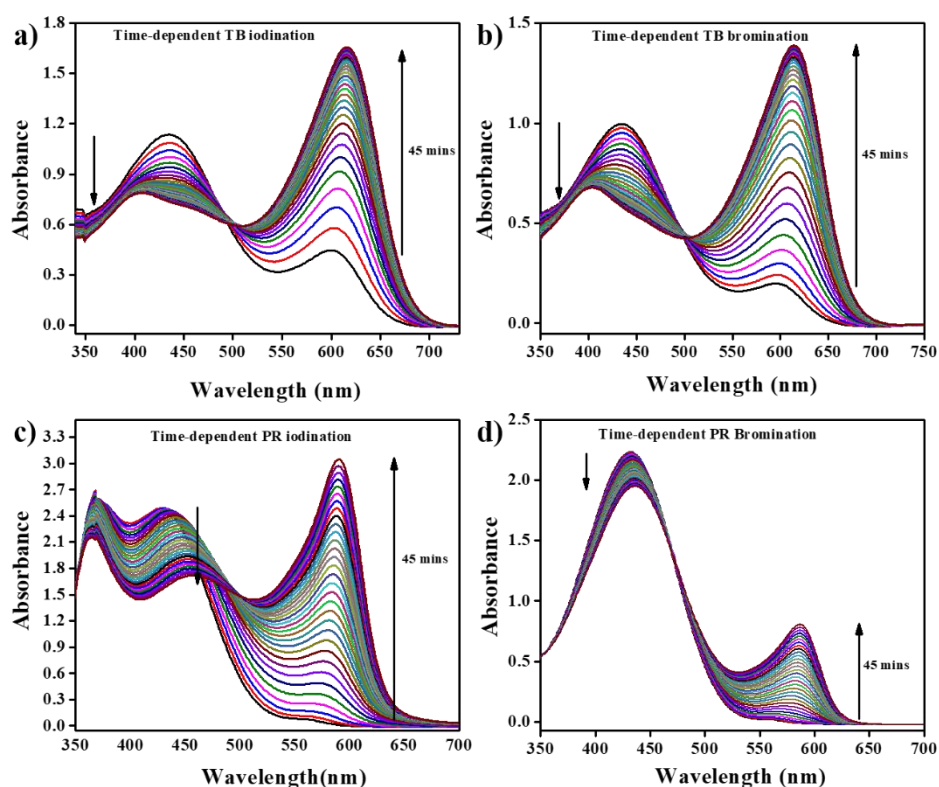


Figure 2.13. Time-dependent UV-visible spectra of (a) Iodination and (b) bromination of thymol blue respectively, and (c) Iodination and (d) Bromination of phenol red respectively using PTA-GMP as the catalyst.

The pH and temperature-dependent iodoperoxidase activity of PTA-GMP hydrogel was evaluated (Figure 2.14). It was observed that the PTA-GMP hydrogel showed the highest activity at pH 7.0. Natural haloperoxidases are abundant in sea-water (pH 7.8-8.2)^{72,73} and in humic soil (pH 4.8-6.0).⁷⁴ To have an idea about the performance of the PTA-

GMP hydrogels under these conditions, we evaluated the kinetic parameters at pH 8.0 and 5.6. Further, the PTA-GMP hydrogels showed enhanced enzymatic activity with an increase in temperature. However, all the kinetic studies were performed at room temperature (25 °C).

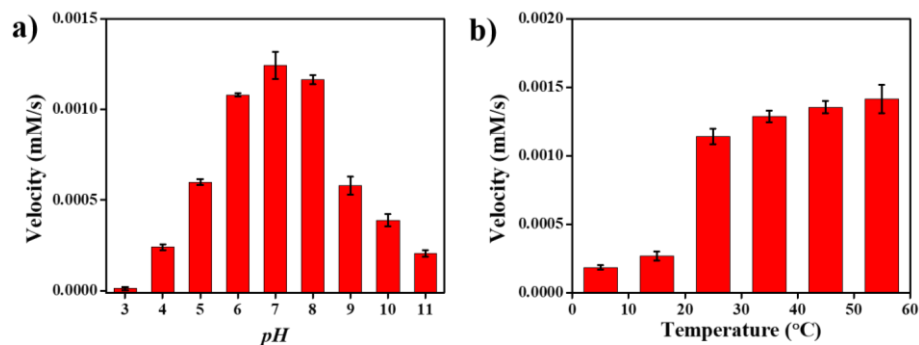


Figure 2.14. Effect of (a) pH and (b) temperature on haloperoxidase activity.

To calculate various kinetic parameters such as K_m and V_{max} , the catalytic rate was determined as the function of I^- , Br^- , and H_2O_2 concentrations. In the presence of the catalyst, the concentration of one substrate was varied while keeping the concentration of other substrates constant (Figure 2.15). Kinetic studies were performed on both the substrates TB and PR at pH 8 and 5.6 respectively at 25 °C (Table 1). A Non-linear Hill fitting plot verified the enzyme mimetic activity of the PTA-GMP gel. Using TB as a substrate (pH 8) and iodide as halogen, the Michaelis constant $K_m(I^-)$ and maximum velocity $V_{max}(I^-)$ were calculated to be 0.127 mM and 1×10^{-3} mM/s respectively. The $K_m(H_2O_2)$ and $V_{max}(H_2O_2)$ for the TB-iodide system were 1.6 mM and 1.9×10^{-3} mM/s respectively. When PR and iodide were taken as substrate (at pH 5.6) the kinetic parameters obtained were $K_m(I^-) = 0.3$ mM, $V_{max}(I^-) = 8 \times 10^{-4}$ mM/s, $K_m(H_2O_2) = 3.53$ mM, and $V_{max}(H_2O_2) = 2 \times 10^{-3}$ mM/s. The $K_m(I^-)$ value for PTA-GMP hydrogel at both acidic (PR) and basic conditions (TB) was found to be lower than naturally occurring iodoperoxidase enzymes, Z-VIPO ($K_m(I^-)$ value for Zg-VIPO1 and Zg-VIPO2 is 0.22 mM) and many of their mutants ($K_m(I^-) = 0.79$ mM for Tyr263Phe mutant, 0.44 mM Tyr263Ala mutant and 0.91 mM Cys320Ser mutant etc.).⁷⁵ The lower K_m values for PTA-GMP hydrogel suggest that I^- has a higher affinity towards the hydrogel than natural vanadium

iodoperoxidases. The catalytic turnover frequency, and k_{cat} value (ratio of V_{max} to the concentration of the catalyst) with respect to I^- were calculated to be $5.3 \times 10^{-3} \text{ s}^{-1}$ and $4.26 \times 10^{-3} \text{ s}^{-1}$ for pH 8 and pH 5.6 respectively.

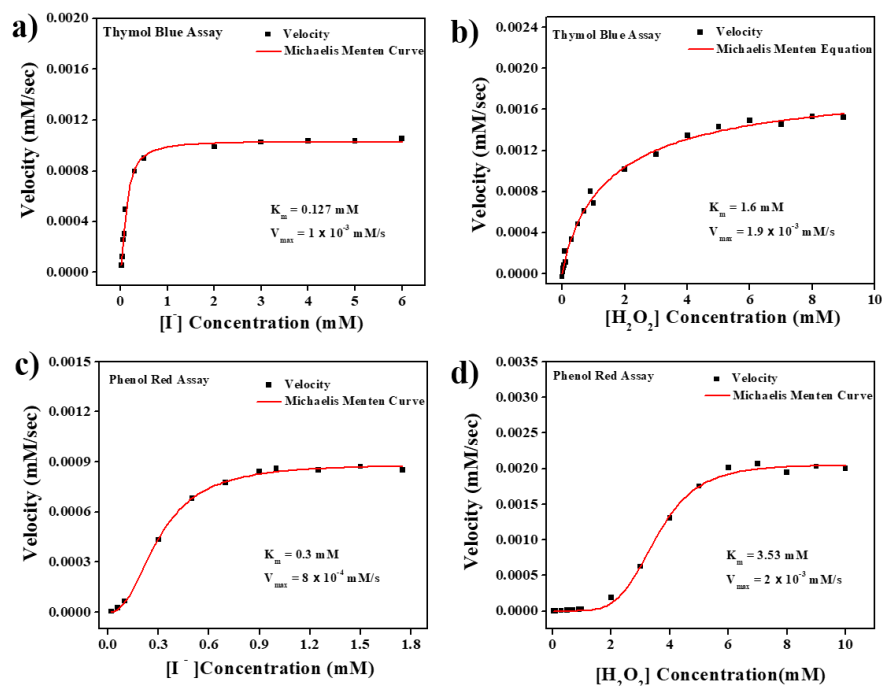


Figure 2.15. Steady-state kinetic assay of haloperoxidase activity of PTA-GMP hydrogel by (a) varying the concentration of iodide and keeping H_2O_2 constant for TB assay (b) varying the concentration of H_2O_2 and keeping iodide constant for TB assay (c) varying the concentration of iodide and keeping H_2O_2 constant for PR assay (d) varying the concentration of H_2O_2 and keeping iodide constant for PR assay.

Kinetic parameters were further evaluated for Br^- in both acidic (PR) and basic (TB) conditions using NaBr as the halogen source (Figure 2.16 and Table 2). When TB was used as a substrate (pH 8.0), the obtained values of kinetic parameters were $K_m(Br^-) = 127.8 \text{ mM}$, $V_{max}(Br^-) = 1.4 \times 10^{-3} \text{ mM/s}$, $K_m(H_2O_2) = 3.46 \text{ mM}$, and $V_{max}(H_2O_2) = 1.34 \times 10^{-3} \text{ mM/s}$. Similarly, for PR, the values were found to be $K_m(Br^-) = 501.6 \text{ mM}$, $V_{max}(Br^-) = 5.9 \times 10^{-3} \text{ mM/s}$, $K_m(H_2O_2) = 1 \text{ mM}$, and $V_{max}(H_2O_2) = 1.3 \times 10^{-4} \text{ mM/s}$. The higher K_m values for bromide compared to iodide suggested a very high inclined affinity of PTA-GMP hydrogel towards I^- compared to Br^- . The catalytic efficiency ratio (k_{cat}/K_m) of I^- to Br^- was

found to be 730 and 225 in pH 8 and 5.6 respectively. Although the PTA-GMP hydrogel shows both bromo and iodoperoxidase activity, the efficiency for oxidizing iodide was much higher as compared to bromide.

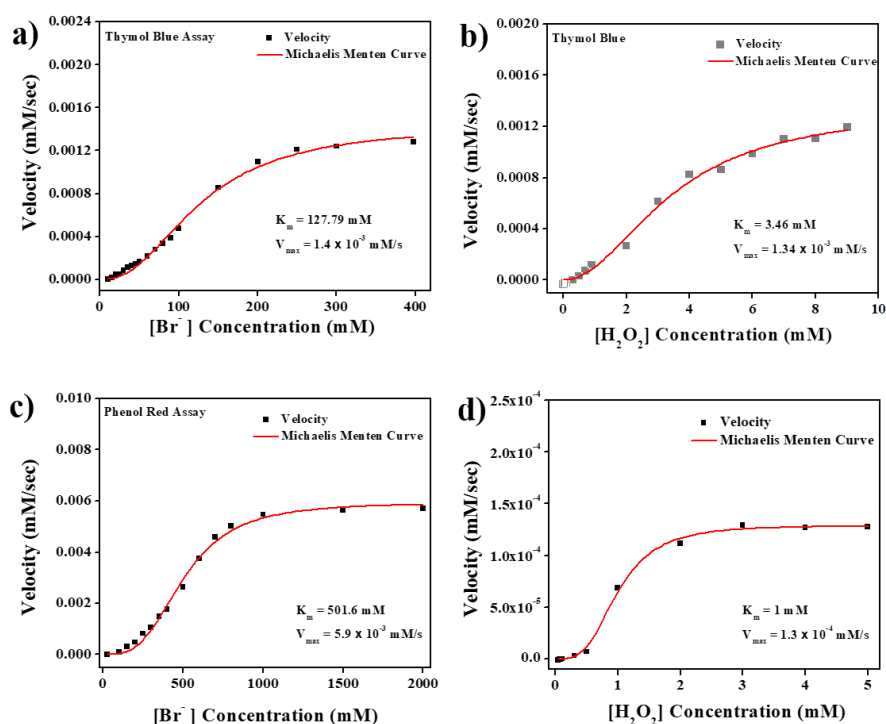


Figure 2.16. Steady-state kinetic assay of haloperoxidase activity of PTA-GMP hydrogel by (a) varying the concentration of Bromide with respect to H_2O_2 for TB assay (b) varying the concentration of H_2O_2 with respect to bromide for TB assay (c) varying the concentration of Bromide and keeping H_2O_2 constant for PR assay (d) varying the concentration of H_2O_2 and keeping Bromide constant for PR assay.

S.No.	Substrate	K_m (mM)	V_{max} (mM/s)
Thymol Blue Assay (pH 8)			
1	I^-	0.127	10^{-3}
2	H_2O_2	1.6	1.9×10^{-3}
Phenol Red Assay (pH 5.6)			
1	I^-	0.303	8×10^{-4}
2	H_2O_2	3.529	2×10^{-3}

Table 2.1. K_m and V_{max} values with respect to I^- , and H_2O_2 .

S.No.	Substrate	K_m (mM)	V_{max} (mM/s)
Thymol Blue Assay (pH 8)			
1	Br^-	127.79	1.4×10^{-3}
2	H_2O_2	3.46	1.34×10^{-3}
Phenol Red Assay (pH 5.6)			
1	Br^-	501.6	5.9×10^{-3}
2	H_2O_2	1	1.3×10^{-4}

Table 2.2. K_m and V_{max} values with respect to Br^- and H_2O_2 .

In nature, haloperoxidase follows two mechanistic pathways. Heme containing haloperoxidase follows a radical mechanism and vanadium haloperoxidases undergo a mechanism that involves metal- η^2 -peroxo intermediates. The addition of natural antioxidants such as cysteine and ascorbic acid to a reaction mixture of TB, NaI, H_2O_2 , and PTA-GMP hydrogel resulted in no change in reaction rate (Figure 2.17). The observations rule out the possibility of a radical pathway. Thus, we predict that the PTA-GMP hydrogel follows a pathway similar to the naturally occurring vanadium haloperoxidases (VHPO).

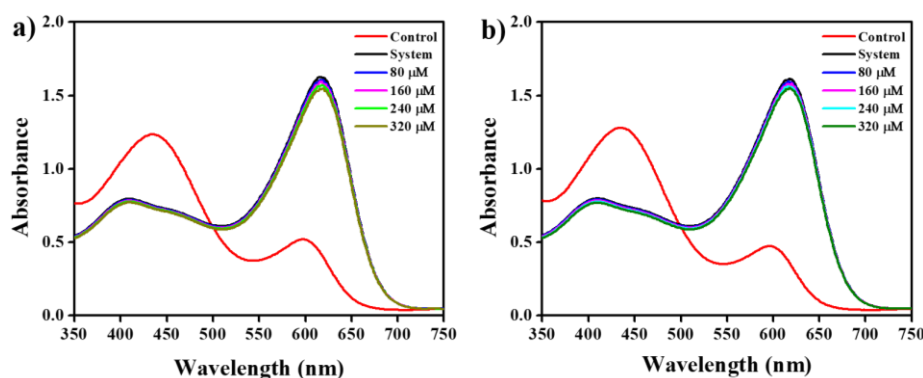


Figure 2.17. UV-vis spectra of oxidative iodination of thymol blue in the presence of natural anti-oxidants (a) ascorbic acid and (b) cysteine.

VHPO provokes halide-assisted disproportionation of H_2O_2 through the formation of metal-peroxo species. PTA interacts with H_2O_2 to form stable polyperoxo species such as $PO_4[MO(\mu-O_2)(O_2)]_4^{3-}$,^{76,77} which can oxidize the halide (I^-/Br^-) leading to the formation of intermediate HOX (HOI/HOBr). The oxidized halogenated species (HOI/HOBr) halogenates the organic substrate (phenol red and thymol

blue) to give the colored products. In the absence of an organic substrate, the hypohalous acid obtained reacts with the second equivalent of H_2O_2 to produce O_2 and X^- .^{78,79} PTA shows much higher haloperoxidase activity as compared to STA, probably due to the formation of stable peroxy species in case of PTA, whereas no stable polyperoxy species are known in the case of silicotungstic acid (STA).⁷⁷ A slight enhancement in the haloperoxidase activity was observed for PTA-GMP xerogel as compared to PTA alone, which can be attributed to the H-bonding and π - π interactions induced by GMP supramolecular assembly around the catalytically active PTA. The interaction of I^- with the polyperoxometalate might be more facile through anion- π interactions of I^- with the GMP supramolecular network, which might influence the diffusion of the substrate to interact with the active catalyst. A probable mechanism is proposed in Figure 2.18.

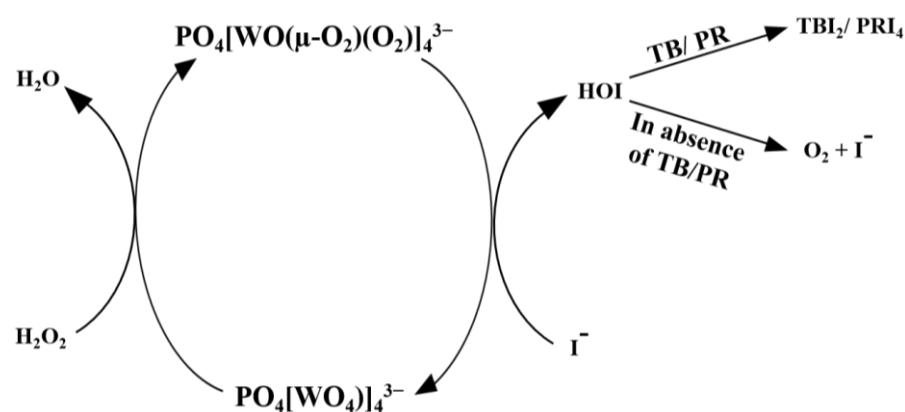


Figure 2.18. A probable mechanism for the iodoperoxidase reaction of PTA-GMP.

We also observed O_2 evolution in the absence of any organic substrate using an O_2 sensor (Figure 2.19). In the presence of only H_2O_2 and PTA-GMP hydrogel, no O_2 evolution was taking place, signifying no catalase-like activity of PTA-GMP hydrogel. In the absence of PTA-GMP hydrogel, no O_2 evolution was taking place even in the presence of NaI and H_2O_2 . On the other hand, significant O_2 release was taking place in a mixture of PTA-GMP, NaI and H_2O_2 . When thymol blue was added to the reaction mixture, there was an immediate decline in the amount of O_2 released, signifying that the HOI produced reacted with TB to give TBI_2

which otherwise breaks down to oxygen and iodide in the absence of any organic substrate.

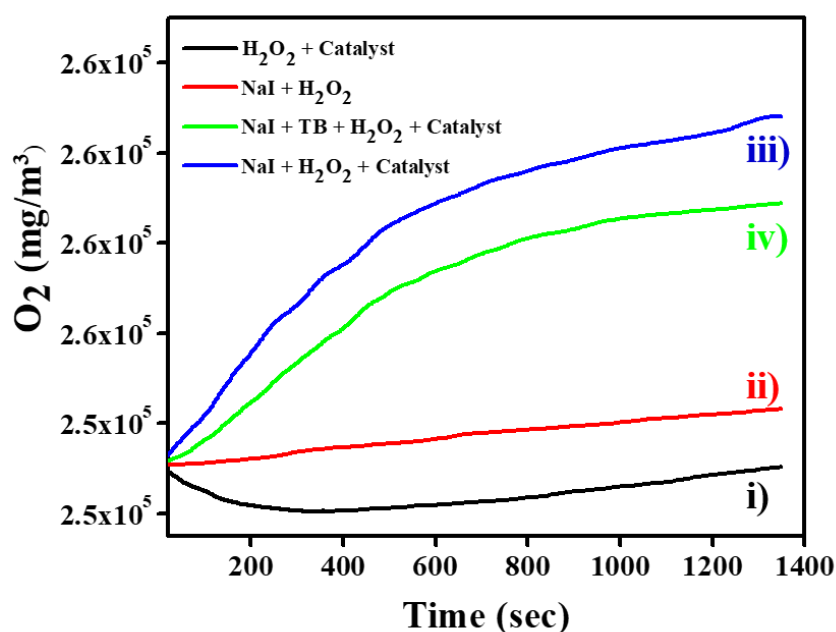


Figure 2.19. Graphical evidence using Vernier O_2 sensor to measure the amount of oxygen released for: i) $H_2O_2 + catalyst$, ii) $NaI + H_2O_2$, iii) $NaI + H_2O_2 + PTA-GMP$ hydrogel iv) $TB + NaI + H_2O_2 + PTA-GMP$ hydrogel system.

2.2.6 Biocompatibility assay

Cell viability tests of both the polyoxometalates (PTA and STA) and their respective gels were carried out in a range of concentration from 50 μM to 600 μM against HEK 293 cells. As shown in Figure 2.20a, there is a prominent increase in the cell viability of PTA-GMP and STA-GMP hydrogels as compared to their respective bare polyoxometalate solution. The IC_{50} (half maximal inhibitory concentration) values of PTA and its hydrogel with GMP were found to be 201 μM and 749.5 μM respectively. Similarly, for STA and its GMP hydrogel, the values were 205 μM and 826 μM respectively. The results suggested that the IC_{50} value of PTA-GMP and STA-GMP hydrogels increased by the factors of 3.7 and 4.1 when compared to the bare POM solution respectively. The higher IC_{50} values in the case of hydrogels against HEK 293 cell lines suggest that a higher amount of sample is required to suppress the biological activity of

the cells by 50% as compared to the POMs alone, thus showing higher biocompatibility.

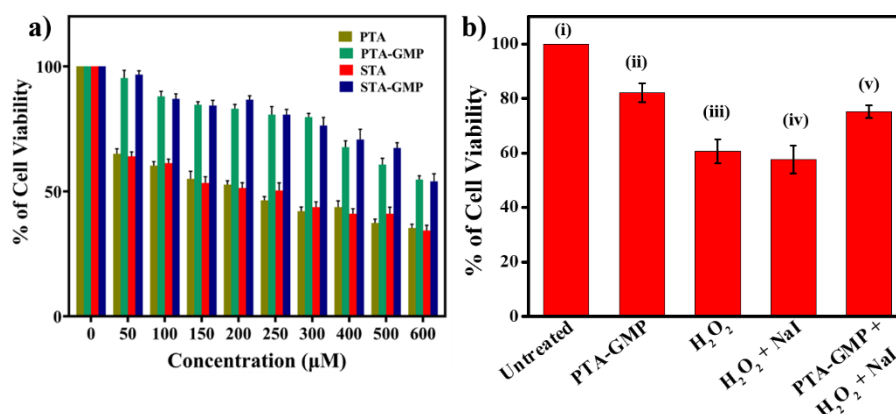


Figure 2.20. (a) Cell viability % of HeK cells after treatment with bare POM solutions (PTA and STA) and their hydrogels (PTA-GMP and STA-GMP) at various concentrations ranging from 50-600 μM (b) Cell viability % of HeK cells after treatment with (i) Untreated (ii) PTA-GMP hydrogel, (iii) only H_2O_2 , (iv) $\text{H}_2\text{O}_2 + \text{NaI}$, and (v) PTA-GMP + $\text{NaI} + \text{H}_2\text{O}_2$ system.

Further cell viability studies were performed to understand the impact of H_2O_2 and NaI on the biocompatibility of the PTA-GMP hydrogel. For this, HEK239 cells were incubated with (i) 0.5 mg/ml PTA-GMP xerogel, (ii) 0.05 mM of H_2O_2 , (iii) 0.05 mM H_2O_2 and 0.5 mM NaI, and (iv) 0.05 mM H_2O_2 , 0.5 mM NaI, and 0.5 mg/ml PTA-GMP xerogel. The percentage of viable cells was found to be 83% in case of PTA-GMP hydrogel, whereas, 60.6% and 57.63% viable cells were obtained in the case of 0.05 mM H_2O_2 and upon addition of 0.5 mM NaI to 0.05 mM H_2O_2 . On the other hand, the cell viability was improved to 75.2% in the presence of H_2O_2 , NaI, and PTA-GMP Hydrogel (Figure 2.20b). It is well known that H_2O_2 causes oxidative stress in the cells by producing free radicals. The addition of NaI resulted in similar cell viability as in the case of H_2O_2 alone. On the other hand, there was a substantial enhancement in cell viability in the presence of PTA-GMP hydrogels (along with H_2O_2 and NaI) to 75%, suggesting that the PTA-GMP hydrogels were involved in converting H_2O_2 to HOI, which turned to be more biocompatible than free radicals. Although the cell viability of the PTA-GMP hydrogel was affected marginally (from 82% to 75%)

in the presence of H_2O_2 and NaI, the system was sufficiently biocompatible for further studies.

2.2.7. Antibacterial Study

The pronounced haloperoxidase activity of the PTA-GMP hydrogels could be harnessed for potential antibacterial activities, which is essential for biomedical applications. The antibacterial activity can be attributed to the formation of hypohalous acid in the process, which is well known to induce quorum sensing disruption along with its cidal effects. Quorum sensing is an intercellular communication process that leads to the development of bacterial biofilms. HOI formed during this process catalyzes the oxidative halogenation (Iodination) of bacterial signaling molecules such as homoserine lactones (HSL) leading to its inactivation.^{7,8,12,19} The antibacterial activity of PTA-GMP gel (0.5 mg/mL) was evaluated for gram-negative *E.Coli* and gram-positive *B. subtilis* in the presence of NaI (0.5 mM) and H_2O_2 (0.05 mM). A significant reduction in bacterial growth by 99.9% for both *E. coli* and *B. subtilis* was observed for PTA-GMP hydrogel. Improvement was observed in the antibacterial activity when compared to the bare PTA solution, which was 80% and 94% for *E.Coli* and *B. subtilis* respectively. It can also be visually seen in Figure 2.21, that a clear difference in the number of bacterial colonies in the case of PTA-GMP hydrogel and bare PTA solution for both *E.Coli* and *B. subtilis* could be observed. In control experiments, with H_2O_2 /NaI (without gel) and PTA-GMP hydrogel (without NaI and H_2O_2), an inferior suppression was observed in the bacterial growth by 12% and 30% for *E. coli* and 35% and 40% for *B. subtilis*, confirming that the strong antibacterial activity is a synergistic effect between the PTA-GMP, NaI, and H_2O_2 . The haloperoxidase activity of PTA was responsible for the inducement of the antibacterial activity. However, gelation of PTA with GMP led to the formation of a biocompatible antibacterial material with the ability to form a uniform film causing an improvement in the antibacterial activity as compared to bare PTA.

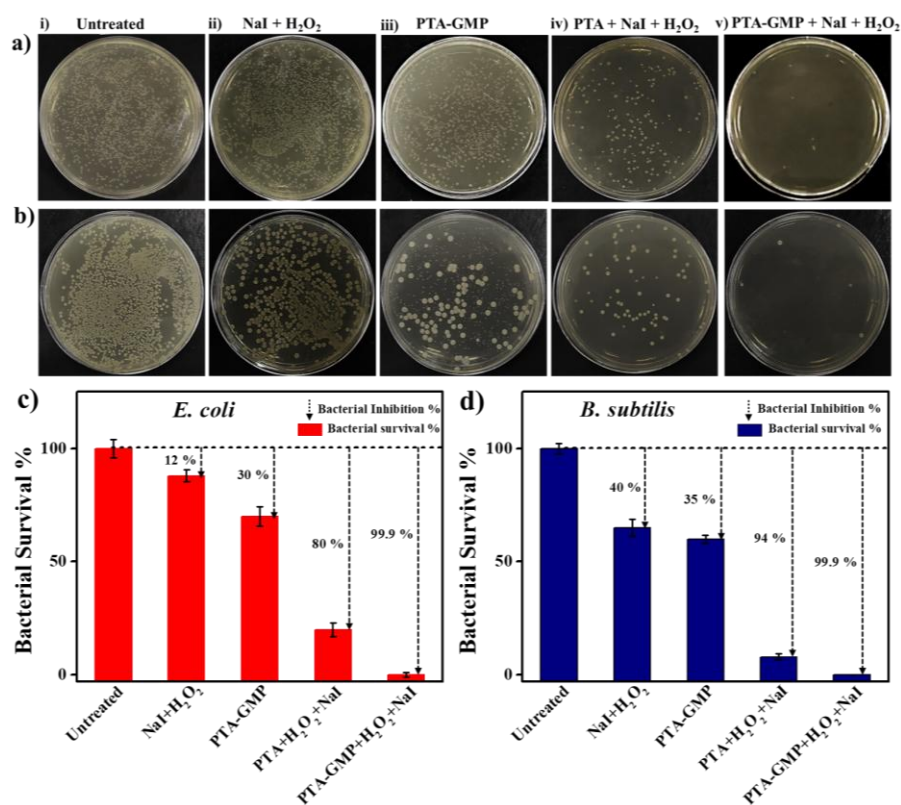


Figure 2.21. (a, b) Digital image of colony forming units (CFU) for *E. coli* and *B. subtilis* respectively after different treatments: (i) without treatment, (ii) NaI + H₂O₂ (iii) PTA-GMP gel, (iv) NaI + H₂O₂ + bare PTA and (v) NaI + H₂O₂ + PTA-GMP Gel (c, d) Bacterial survival and inhibition percentage of different controls and PTA-GMP + NaI + H₂O₂ system for *E. coli* and *B. subtilis* respectively.

Though in the solution state, we do not observe a significant difference in the rate of haloperoxidase activity of bare PTA and PTA-GMP gel, however, an improved antifouling activity could be observed in the case of the PTA-GMP hydrogel which can be attributed to the ability of the hydrogel to form a uniform film on the surface, thus making it more suitable to be used as paint or coating. This was experimentally studied, wherein dilute solutions of PTA and PTA-GMP were kept and allowed to dry in two separate wells (Figure 2.22). Upon drying, stark differences were observed with uneven coating from the dried POM and a uniform coating from the PTA-GMP hydrogel. When TB, NaI, and H₂O₂ were added in both wells, the iodination of TB was distinctly observed through a visual color change in the well containing the dried PTA-GMP gel. On the other hand, no coloration was observed in the well containing dried PTA.

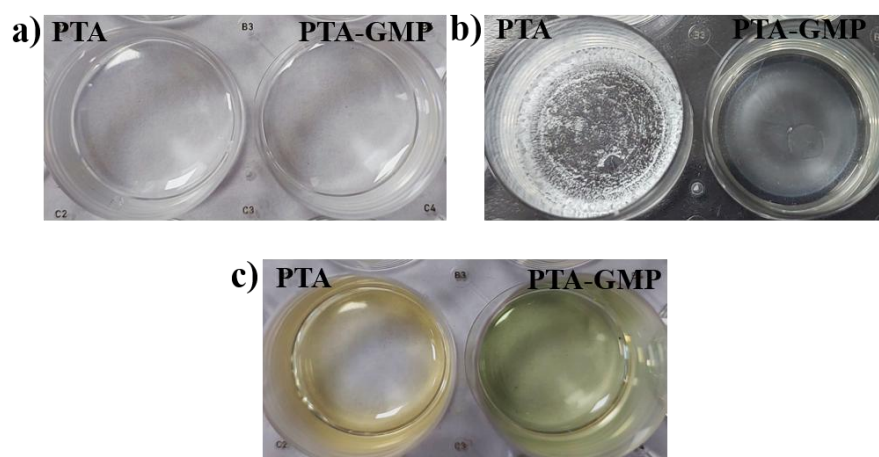


Figure 2.22. (a) Diluted solutions of PTA (left) and PTA-GMP gel (right) was poured into the well plate and allowed to dry. (b) PTA solution was observed to dry in a non-uniform manner (left) and PTA-GMP dried to form a uniform coating. (c) solution of 100 μM TB, 3 mM NaI, and 2 mM H_2O_2 was poured into the well. For bare PTA, no change in colour was observed but positive haloperoxidase was observed for PTA-GMP, thus demonstrating the coating ability of the gel.

Based on the result of the antibacterial activity of PTA-GMP catalyzed haloperoxidase activity, we further proceeded to evaluate its biofilm inhibiting performance (Figure 2.23). Crystal violet staining assay experiment was performed for both gram-negative *E. coli* and gram-positive *B. subtilis*. The PTA-GMP system showed excellent biofilm inhibition against both strains of bacteria in the presence of both NaI and H_2O_2 . Biofilm formation was least in a mixture of PTA-GMP, NaI and H_2O_2 as compared to other control systems, thus showing the synergistic effect of all the components. Performance against biofilm formation was also checked for only PTA in the presence of NaI and H_2O_2 against both strains of bacteria. Whereas 92.8 % biofilm inhibition of *E. coli* and 88.1 % inhibition in biofilm formation for *B. subtilis* was observed in case of PTA-GMP hydrogel, 82 % biofilm inhibition of *E. coli* and 67.2 % inhibition in biofilm formation for *B. subtilis* was observed in case of PTA. The results clearly indicate that even though iodoperoxidase activity of PTA is responsible for the inhibition of biofilm, but upon gelation with GMP, its ability to form a uniform coating on the surface leads to improvement in biofilm inhibiting activity.

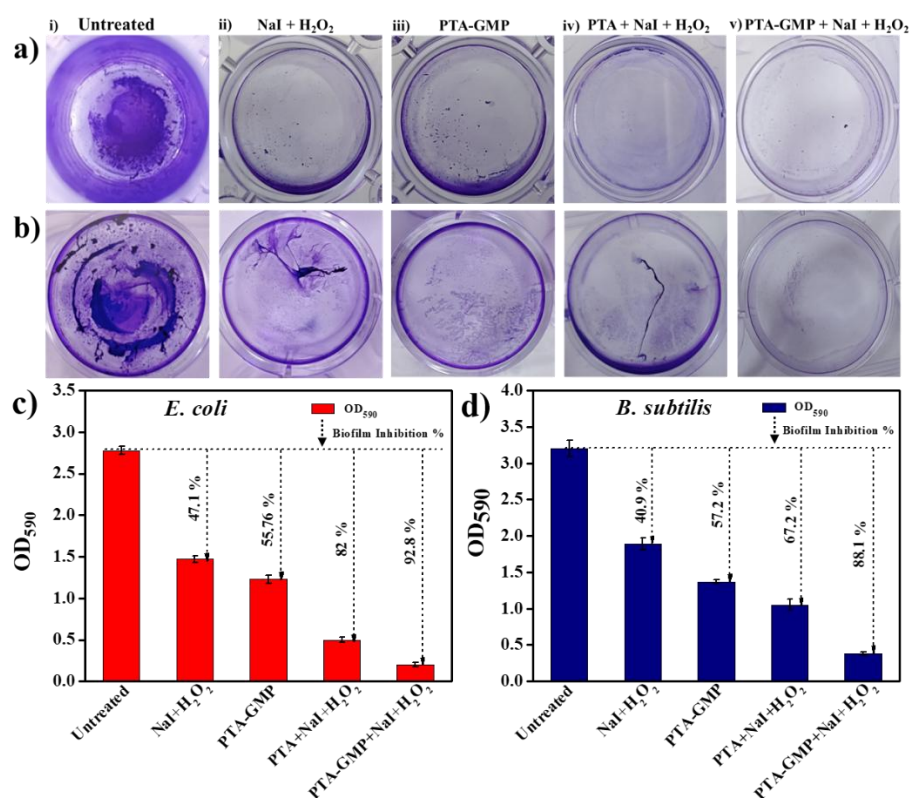


Figure 2.23. (a, b) Digital image of crystal staining of biofilms formed by *E. coli* and *B. subtilis* respectively after following treatments: (i) Untreated, (ii) NaI + H₂O₂ (iii) PTA-GMP gel, (iv) NaI + H₂O₂ + bare PTA and (v) NaI + H₂O₂ + PTA-GMP Gel (c, d) OD₅₉₀ and their biofilm inhibiting percentage of different controls and PTA-GMP + NaI + H₂O₂ system for *E. coli* and *B. subtilis* respectively.

2.3. CONCLUSION

In conclusion, we successfully fabricated supramolecular hydrogels through a simple self-assembly strategy by mixing two polyoxometalates, phosphotungstic acid, and silicotungstic acid with guanosine monophosphate as a low molecular-weight hydrogelator. The hydrogels were stimuli-responsive, mechanically robust, thixotropic, and showed enhanced biocompatibility compared to bare POM. Detailed spectroscopic evaluation of both gels was carried out to understand the interactions between the polyoxometalates and GMP. Kinetic studies for the haloperoxidase activities showed that the hydrogel was more specific towards the oxidation of iodide than bromide, thus showing specific iodoperoxidase activity. The iodoperoxidase activity of the PTA-GMP gel was further exploited as an antifouling agent towards both gram-

positive and gram-negative bacteria. The ability of the PTA-GMP hydrogel to form a uniform film on the surface resulted in better antibacterial activity as compared to only PTA solution. The polyoxometalate-GMP hydrogel with haloperoxidase mimicking activity can be a biocompatible, sustainable, and easy approach to substitute conventional toxic biocides and inconvenient enzyme-embedded systems.

2.4. EXPERIMENTAL SECTION

2.4.1. Materials

Guanosine-5'-monophosphate disodium salt hydrate ($\text{Na}_2\text{-GMP}$), Phosphotungstic acid hydrate $\text{H}_3[\text{P}(\text{W}_3\text{O}_{10})_4]\cdot\text{aq}$, Tungstosilicic acid hydrate $\text{H}_4[\text{Si}(\text{W}_3\text{O}_{10})_4]\cdot\text{aq}$, Sodium Iodide (NaI), Thymol Blue, and Phenol Red were commercially purchased from Sisco Research Laboratory (SRL), India. Sodium Bromide (NaBr) and Methylene Blue were purchased from Alfa Aesar by Thermo Fisher Scientific. Sodium Phosphate dibasic anhydrous (Na_2HPO_4), Sodium Phosphate Monobasic monohydrate ($\text{NaH}_2\text{PO}_4\cdot\text{H}_2\text{O}$), Hydrogen Peroxide (H_2O_2 , 30 %), and Milli-Q were purchased from Merck, India. All the chemicals were used as purchased with no further purification.

2.4.2. Synthesis of Hydrogels

An aqueous solution of Polyoxometalate (PTA and STA) was mixed with an aqueous solution of GMP in a 1:3 molar ratio, where the concentration of POM was maintained at 60 mM and GMP concentration was 180 mM. The mixture was slightly heated on the stirrer at 50 °C to make the system homogeneous. The hydrogel was formed spontaneously within a few minutes at room temperature. Gelation was confirmed visually by inverting the vial where no flow of the solvent was observed. The hydrogel with phosphotungstic acid (PTA) was pale yellow in appearance and the tungstosilicic acid-GMP hydrogel was bright orange in colour.

2.4.3. Instrumentation

UV-Vis and Circular Dichroism (CD) studies were recorded on a Perkin Elmer UV-Vis-NIR spectrophotometer (Model: Lambda 1050) and JASCO J-815 spectropolarimeter using a quartz cuvette of path length 1 cm. Field emission scanning electron microscopy (FESEM) images were taken on Carl Zeiss Supra 55 instruments after Cu coating. Transmission Electron microscope (TEM) images were taken from the electron microscope of model JEM-2100 at an accelerating voltage of 200 kV. Rheological studies were done using an Anton Paar Physica MCR 301 rheometer with parallel plate geometry (diameter 25 mm). Dynamic strain sweep experiments were performed using a constant frequency of 10 rad s⁻¹. The dynamic frequency sweep of the hydrogels was measured as a function of frequency in the range of 0.05–100 rad s⁻¹ with a constant strain value of 1%. The thixotropic loop test was carried out at a constant frequency of 10 rad s⁻¹, and the applied strain was changed from 0.1% to 100%. Powder X-ray diffraction patterns (XRD) of the xerogels were recorded on a Rigaku Smartlab, Automated Multipurpose X-ray diffractometer with Cu K α source (the wavelength of the X-rays was 0.154 nm). FTIR study of xerogels was done on Bruker Alpha II Platinum ATR. ¹H and ³¹P NMR spectra were recorded using a 500 MHz Bruker AV500 NMR instrument at 298 K using D₂O as solvent.

2.4.4. Characterization Methods.

Field Emission Scanning Electron Microscopy (FESEM). The hydrogels were diluted up to 200 times in milli Q water and 20 μ l of it was drop-casted on a clean coverslip and left for air drying for 24 hours. The drop-casted samples were then coated with copper and imaged under the electron microscope.

UV-visible spectroscopy. UV-Visible spectra of the hydrogels, POMs, and GMP were recorded at a concentration of 0.025 mM each using a 1 cm path length cuvette. A Job's plot was obtained from the UV spectra at 252 nm upon successive addition of 0.025 mM GMP to a 0.025 mM aqueous solution of POM at variable mole ratio.

Circular Dichroism (CD). The CD spectra of the hydrogels, POM, and GMP were recorded by diluting the samples up to 0.25 mM using a quartz cell of 1 cm path length with a scan range of 200-300 nm. The spectra were recorded with a slit width of 1 mm and a scan rate of 50 nm/s. Titration spectra were performed upon successive addition of 0.25 mM GMP to a 0.25 mM aqueous solution of POM at a variable mole ratio.

Rheological Studies. Rheological studies were performed at room temperature (25 °C) using a parallel plate (25 mm diameter). A small amount of the gel was scooped out with the help of a spatula and kept on the plate for measurement. The strain sweep measurements of the hydrogels were carried out at a constant frequency (10 rads^{-1}). The frequency sweep studies were performed in a 0.1–100 rad s^{-1} frequency range maintaining a constant strain of 1%. For the thixotropic loop studies, the strain was varied from 0.1% to 100% at an applied frequency of 10 rad s^{-1} . Successive low and high strains were applied at a time period of 100 seconds.

2.4.5. Haloperoxidase Assay

The haloperoxidase mimicking activity of the POM-GMP hydrogels was determined by colorimetric assessment and UV-visible absorption spectroscopy. Oxidative halogenation (iodination, bromination) of substrates thymol blue (TB) and phenol red (PR) was carried out using both the hydrogels and their respective precursor POM. 2.5 mg of the xerogel was added to a system of 3 mL of phosphate buffer (0.1 M, pH 8 for TB, and pH 5.6 for PR) containing 80 μM of TB, 1 mM NaI, and 2 mM H_2O_2 and a visual colour change confirmed the enzymatic activity of the hydrogels. Time-dependent UV-Visible spectra were recorded for the PTA-GMP system for iodination and bromination of the substrates. Control experiments were performed in the absence of the POM-GMP xerogel or the POM, which showed no characteristic absorption for the halogenation of the substrates. Similarly, absence of H_2O_2 or NaI also showed no iodination of the substrates. Increasing the amount of the POM catalyst resulted in the enhanced rate of the

enzymatic reaction, however, the concentration of the catalyst and substrate was optimized for following the kinetics.

Kinetic studies were carried out with PTA-GMP hydrogel due to its superior catalytic activity over STA-GMP hydrogel. The kinetic experiments for oxidative halogenation (iodide and bromide) of both TB and PR, were monitored for 15 minutes at an absorbance of 615 nm and 590 nm respectively on a UV-Visible spectrometer. The studies were performed by varying the concentration of halide while keeping the concentration of H₂O₂ constant and vice-versa under optimal reaction conditions.

2.4.6. MTT Assay

The cell viability of POM hydrogels and their respective precursor POM were studied through a 3-(4,5-dimethylthiazol-2-yl)-2,5-diphenyltetrazolium bromide (MTT) assay. For the test, normal HEK cells were seeded in a 96-well plate having a cell density of 1×10^4 cells per well and incubated with 5% CO₂ for 24 h at 37 °C. Different concentrations of samples ranging from 50-600 μM were incubated with cells for 24 hrs in triplicates. For controlled experiments, untreated cells were used as standard. After the respective time duration, 10 μL of MTT reagents (5 mg/mL) were added to each well. The medium was removed after incubation for another 4 h in the dark, and 100 μL of DMSO was added to each well. The cell viability was estimated by measuring the absorbance at 570 nm using a Synergy H1BioTek multimode microplate reader. HEK 293 is a homogeneous cell line and consists of immortalized human embryonic kidney cells, which are commonly used in MTT assay due to their robustness and low maintenance. They are highly reproducible, robust and ensures the consistency of cellular response and reproducibility of the data.

2.4.7. Antibacterial Study

Gram-negative *E. coli* and gram-positive *B. subtilis* bacteria were used for the antibacterial experiments. *E. coli* and *B. subtilis* were incubated separately in sterile Luria-Bertani medium at 37 °C overnight

in a shaker. After culturing, the bacteria were separated from the medium by centrifuging at the speed of 5000 rpm for 5 minutes. The bacterial pellet obtained at the bottom was washed with sterile 0.9% NaCl solution and then diluted and dispersed up to 10^6 CFU mL in 0.1 M phosphate buffer saline (PBS). A total of 4 sets of experiments were performed for each *E. coli* and *B. subtilis* to confirm the synergistic effect of the catalyst with H_2O_2 and halide. Also, a comparison of the antibacterial activity of the bare POM solution was done as compared to its gel. Antibacterial studies were carried out using PTA and PTA-GMP hydrogel due to their higher catalytic activity. The bacterial suspension was incubated with: (i) 0.5 mM of NaI and 0.05 mM of H_2O_2 (ii) only gel (3 mg/mL) without H_2O_2 and NaI (iii) 0.5 mM NaI, 0.05 mM H_2O_2 and xerogel (0.5 mg/mL) (iv) 0.5 mM NaI, 0.05 mM H_2O_2 and bare POM solution (0.5 mg/mL). After 15 minutes of incubation, the bacterial suspensions were serially diluted, and the 10^{-6} diluent was spread on four nutrient agar plates to avoid overlapping of colonies while calculating the antibacterial efficiency. Subsequently, the viable bacterial colonies were manually counted and the colony-forming unit (CFU) for each set was estimated using the following equation:

$$\text{CFU Ratio} = C/C_0 \times 100$$

Where C and C_0 stand for the CFU of the treated and untreated (control) bacterial cells respectively.

2.4.8. Crystal violet assay for Biofilm Quantification

Two strains of bacteria *i.e* gram-positive *B. subtilis* and gram-negative *E. coli* were used to test anti-biofilm property of the compounds. The bacteria were grown overnight in plain LB-broth at 37 °C. The cultures were diluted 1000 times to achieve OD_{600} of 0.5 *i.e* 10^6 CFU of bacteria. 300 μ l bacterial suspension was plated on the well of a flat bottom polystyrene 12-well plate. The plates were incubated for 64 h at 37 °C with or without the treatment of POM-GMP hydrogels in triplicates. After 24 h of growth half volume of the bacterial suspension of 10^6 CFU was added along with half of the volumes of compounds (0.5

mM NaI, 0.05 mM H₂O₂, and xerogel (0.5 mg/mL). after 48 h of incubation same process was repeated. After 64 h, the bacteria suspension was removed. The plate was washed thrice with 0.9% NaCl solution. Biofilms were fixed with 200µl of 4% paraformaldehyde along with 200 µl of 0.1% of crystal violet solution (N=3). It was kept for 2 h, then washed with water. The images were taken after complete drying of samples. After dissolving with 95% ethanol, OD₅₉₀ was taken using Perkin-Elmer victor Nivo Multi-mode plate reader.

2.5. References

1. Gu J.-D. (2012). 8 - Biofouling and Prevention: Corrosion, Biodeterioration and Biodegradation of Materials. In Handbook of Environmental Degradation of Materials (Second Edition), M. Kutz, ed. (William Andrew Publishing), pp. 243–282 (DOI: 10.1016/B978-1-4377-3455-3.00008-0).
2. Donlan R. M. Biofilms: Microbial Life on Surfaces - Volume 8, Number 9—September 2002 - Emerging Infectious Diseases journal - CDC (DOI: 10.3201/eid0809.020063).
3. Uzun D., Sezen S., Ozyurt R., Atlar M., Turan O. (2021), A CFD study: Influence of biofouling on a full-scale submarine. Appl. Ocean Res. 109, 102561 (DOI: 10.1016/j.apor.2021.102561).
4. Cloete E., Molobela I., Van Der Merwe A., Richards, M. (2009), 1 - Biofilms in the food and beverage industries: an introduction. In Biofilms in the Food and Beverage Industries Woodhead Publishing Series in Food Science, Technology and Nutrition., P. M. Fratamico, B. A. Annous, and N. W. Gunther, eds. (Woodhead Publishing), pp. 3–41 (DOI: 10.1533/9781845697167.1.3).
5. Harding J. L., Reynolds M. M. (2014). Combating medical device fouling. Trends Biotechnol. 32, 140–146 (DOI: 10.1016/j.tibtech.2013.12.004).

6. Turley P. A., Fenn R. J., Ritter J. C. (2000), Pyrithiones as antifoulants: Environmental chemistry and preliminary risk assessment. *Biofouling* 15, 175–182 (DOI: 10.1080/08927010009386308).
7. Butler A., Sandy M. (2009), Mechanistic considerations of halogenating enzymes. *Nature* 460, 848–854 (DOI: 10.1038/nature08303).
8. Borchardt S. A., Allain E. J., Michels J. J., *et al.* (2001), Reaction of Acylated Homoserine Lactone Bacterial Signaling Molecules with Oxidized Halogen Antimicrobials. *Appl. Environ. Microbiol.* 67, 3174–3179 (DOI: 10.1128/AEM.67.7.3174-3179.2001).
9. Zeb A., Xie X., Yousaf A. B. *et al.* (2016), Highly Efficient Fenton and Enzyme-Mimetic Activities of Mixed-Phase VO_x Nanoflakes. *ACS Appl. Mater. Interfaces* 8, 30126–30132 (DOI: 10.1021/acsami.6b09557).
10. Ghosh S., Roy P., Karmodak N., Jemmis E. D., Mugesh G. (2018), Nanoisozymes: Crystal-Facet-Dependent Enzyme-Mimetic Activity of V₂O₅ Nanomaterials. *Angew. Chem., Int. Ed.* 130, 4600–4605 (DOI: 10.1002/ange.201800681).
11. Perez-Baena I., Barroso-Bujans F., Gasser U., *et al.* (2013), Endowing Single-Chain Polymer Nanoparticles with Enzyme-Mimetic Activity. *ACS Macro Lett.* 2, 775–779 (DOI: 10.1021/mz4003744).
12. Chen Z., Wang Z., Ren J., Qu X. (2018), Enzyme Mimicry for Combating Bacteria and Biofilms. *Acc. Chem. Res.* 51, 789–799 (DOI: 10.1021/acs.accounts.8b00011).
13. Wei H., Wang E. (2013), Nanomaterials with enzyme-like characteristics (nanozymes): next-generation artificial enzymes. *Chem. Soc. Rev.* 42, 6060–6093. (DOI: 10.1039/C3CS35486E).

14. Korschelt K., Tahir M. N., Tremel W. (2018), A Step into the Future: Applications of Nanoparticle Enzyme Mimics. *Chem. – Eur. J.* 24, 9703–9713 (DOI: 10.1002/chem.201800384).
15. Crans D. C., Smee J. J., Gaidamauskas E., Yang L. (2004), The Chemistry and Biochemistry of Vanadium and the Biological Activities Exerted by Vanadium Compounds. *Chem. Rev.* 104, 849–902 (DOI: 10.1021/cr020607t).
16. Mimoun H., Saussine L., Daire E., *et al.* (1983), Vanadium(V) peroxy complexes. New versatile biomimetic reagents for epoxidation of olefins and hydroxylation of alkanes and aromatic hydrocarbons. *J. Am. Chem. Soc.* 105, 3101–3110 (DOI: 10.1021/ja00348a025).
17. Natalio F., André R., Hartog A. F. *et al.* (2012), Vanadium pentoxide nanoparticles mimic vanadium haloperoxidases and thwart biofilm formation. *Nat. Nanotechnol.* 7, 530–535 (DOI: 10.1038/nnano.2012.91).
18. Hu M., Korschelt K., Viel M., *et al.* (2018). Nanozymes in Nanofibrous Mats with Haloperoxidase-like Activity To Combat Biofouling. *ACS Appl. Mater. Interfaces* 10, 44722–44730. (DOI: 10.1021/acsami.8b16307).
19. Herget K., Frerichs H., Pfitzner F., Tahir M. N., Tremel, W. (2018), Functional Enzyme Mimics for Oxidative Halogenation Reactions that Combat Biofilm Formation. *Adv. Mater.* 30, 1707073 (DOI: 10.1002/adma.201707073).
20. He X., Tian F., Chang J., *et al.* (2020). Haloperoxidase Mimicry by CeO_{2-x} Nanorods of Different Aspect Ratios for Antibacterial Performance. *ACS Sustain. Chem. Eng.* 8, 6744–6752 (DOI: 10.1021/acssuschemeng.0c01113).
21. Gumerova N. I., Rompel A. (2018), Synthesis, structures and applications of electron-rich polyoxometalates. *Nat. Rev. Chem.* 2, 1–20 (DOI: 10.1038/s41570-018-0112).

22. Yamase T. (1998), Photo- and Electrochromism of Polyoxometalates and Related Materials. *Chem. Rev.* 98, 307–326 (DOI: 10.1021/cr9604043).
23. Clemente-Juan J. M., Coronado E., Gaita-Ariño A. (2012), Magnetic polyoxometalates: from molecular magnetism to molecular spintronics and quantum computing. *Chem. Soc. Rev.* 41, 7464–7478 (DOI: 10.1039/C2CS35205B).
24. Podgoršek A., Zupan M., Iskra J. (2009), Oxidative Halogenation with “Green” Oxidants: Oxygen and Hydrogen Peroxide. *Angew. Chem., Int. Ed.* 48, 8424–8450 (DOI: 10.1002/anie.200901223).
25. Wang S. -S., Yang G. -Y. (2015). Recent Advances in Polyoxometalate-Catalyzed Reactions. *Chem. Rev.* 115, 4893–4962 (DOI: 10.1021/cr500390v).
26. Lv H., Geletii Y. V., Zhao C., (2012). Polyoxometalate water oxidation catalysts and the production of green fuel. *Chem. Soc. Rev.* 41, 7572–7589 (DOI: 10.1039/C2CS35292C).
27. Van-Rompuy L. S., Parac-Vogt T. N. (2019), Interactions between polyoxometalates and biological systems: from drug design to artificial enzymes. *Curr. Opin. Biotechnol.* 58, 92–99 (DOI: 10.1016/j.copbio.2018.11.013).
28. Li X., Yang X. -Y., Sha J. -Q., *et al.* (2019), POMOF/SWNT Nanocomposites with Prominent Peroxidase-Mimicking Activity for l-Cysteine “On–Off Switch” Colorimetric Biosensing. *ACS Appl. Mater. Interfaces* 11, 16896–16904 (DOI: 10.1021/acsami.9b00872).
29. Chen K., Liu S., Zhang Q. (2022), Degradation and Detection of Endocrine Disruptors by Laccase-Mimetic Polyoxometalates. *Front. Chem.* 10. (DOI: 10.3389/fchem.2022.854045).
30. Yadav N., Singh S. (2021), Polyoxometalate-Mediated Vacancy-Engineered Cerium Oxide Nanoparticles Exhibiting Controlled

- Biological Enzyme-Mimicking Activities. *Inorg. Chem.* 60, 7475–7489 (DOI: 10.1021/acs.inorgchem.1c00766).
31. Sap A., Van-Tichelen L., Mortier A., *et al.* (2016), Tuning the Selectivity and Reactivity of Metal-Substituted Polyoxometalates as Artificial Proteases by Varying the Nature of the Embedded Lewis Acid Metal Ion. *Eur. J. Inorg. Chem.* 2016, 5098–5105 (DOI: 10.1002/ejic.201601098).
32. Sivakumar R., Thomas J., Yoon M. (2012), Polyoxometalate-based molecular/nano composites: Advances in environmental remediation by photocatalysis and biomimetic approaches to solar energy conversion. *J. Photochem. Photobiol. C Photochem. Rev.* 13, 277–298. (DOI: 10.1016/j.jphotochemrev.2012.08.001).
33. Lu F., Wang M., Li N., Tang B. (2021), Polyoxometalate-Based Nanomaterials Toward Efficient Cancer Diagnosis and Therapy. *Chem. – Eur. J.* 27, 6422–6434 (DOI: 10.1002/chem.202004500).
34. Sarafianos S. G., Kortz U., Pope M. T., Modak M. J. (1996), Mechanism of polyoxometalate-mediated inactivation of DNA polymerases: an analysis with HIV-1 reverse transcriptase indicates specificity for the DNA-binding cleft. *Biochem. J.* 319, 619–626 (DOI: 10.1042/bj3190619).
35. Rhule J. T., Hill C. L., Judd D. A., Schinazi R. F. (1998), Polyoxometalates in Medicine. *Chem. Rev.* 98, 327–358 (DOI: 10.1021/cr960396q).
36. Bijelic A., Aureliano M., Rompel A. (2018), The antibacterial activity of polyoxometalates: structures, antibiotic effects and future perspectives. *Chem. Commun.* 54, 1153–1169 (DOI: 10.1039/C7CC07549A).
37. Ammam M. (2013), Polyoxometalates: formation, structures, principal properties, main deposition methods and application in

- sensing. *J. Mater. Chem. A* 1, 6291–6312 (DOI: 10.1039/C3TA01663C).
38. Pandya V. M., Kortz U., Joshi S. A. (2014), Encapsulation and stabilization of polyoxometalates in self-assembled supramolecular hydrogels. *Dalton Trans.* 44, 58–61 (DOI: 10.1039/C4DT01372G).
39. Wang S. -M., Hwang J., Kim E. (2019), Polyoxometalates as promising materials for electrochromic devices. *J. Mater. Chem. C* 7, 7828–7850 (DOI: 10.1039/C9TC01722D).
40. Miao T., Fenn S. L., Charron P. N., Floreani R. A. (2015), Self-Healing and Thermoresponsive Dual-Cross-Linked Alginate Hydrogels Based on Supramolecular Inclusion Complexes. *Biomacromolecules* 16, 3740–3750 (DOI: 10.1021/acs.biomac.5b00940).
41. Thakur N., Sharma B., Bishnoi S. *et al.* (2018). Multifunctional Inosine Monophosphate Coordinated Metal–Organic Hydrogel: Multistimuli Responsiveness, Self-Healing Properties, and Separation of Water from Organic Solvents. *ACS Sustain. Chem. Eng.* 6, 8659–8671 (DOI: 10.1021/acssuschemeng.8b00963).
42. Geisberger G., Paulus S., Carraro M. *et al.* (2011). Synthesis, Characterisation and Cytotoxicity of Polyoxometalate/Carboxymethyl Chitosan Nanocomposites. *Chem. – Eur. J.* 17, 4619–4625 (DOI: 10.1002/chem.201002815).
43. Dolbecq A., Dumas E., Mayer C. R., Mialane P. (2010), Hybrid Organic–Inorganic Polyoxometalate Compounds: From Structural Diversity to Applications. *Chem. Rev.* 110, 6009–6048. (DOI: 10.1021/cr1000578).
44. Cameron J. M., Guillemot G., Galambos T., *et al.* (2022), Supramolecular assemblies of organo-functionalized hybrid polyoxometalates: from functional building blocks to hierarchical

- nanomaterials. *Chem. Soc. Rev.* 51, 293–328 (DOI: 10.1039/D1CS00832C).
45. Stuckart M., Monakhov K. Y. (2019), Polyoxometalates as components of supramolecular assemblies. *Chem. Sci.* 10, 4364–4376 (DOI: 10.1039/C9SC00979E).
46. Baroudi I., Simonnet-Jégat C., Roch-Marchal C. *et al.* (2015), Supramolecular Assembly of Gelatin and Inorganic Polyanions: Fine-Tuning the Mechanical Properties of Nanocomposites by Varying Their Composition and Microstructure. *Chem. Mater.* 27, 1452–1464 (DOI: 10.1021/cm502605q).
47. Zhang, G., Zhang, J., Wang, Y., Wu, Y., Li, Q., Liang, Y., Qi, W., Rao, H., Su, R., and He, Z. (2020), Self-assembly of multifunctional hydrogels with polyoxometalates helical arrays using nematic peptide liquid crystal template. *J. Colloid Interface Sci.* 578, 218–228. <https://doi.org/10.1016/j.jcis.2020.05.116>.
48. Du X., Zhou J., Shi J., Xu B. (2015), Supramolecular Hydrogelators and Hydrogels: From Soft Matter to Molecular Biomaterials. *Chem. Rev.* 115, 13165–13307. (DOI: 10.1021/acs.chemrev.5b00299).
49. Stefan L., Monchaud D. (2019), Applications of guanine quartets in nanotechnology and chemical biology. *Nat. Rev. Chem.* 3, 650–668 (DOI: 10.1038/s41570-019-0132-0).
50. Thakur N., Sharma B., Bishnoi S., *et al.* (2019), Biocompatible Fe³⁺ and Ca²⁺ Dual Cross-Linked G-Quadruplex Hydrogels as Effective Drug Delivery System for pH-Responsive Sustained Zero-Order Release of Doxorubicin. *ACS Appl. Bio Mater.* 2, 3300–3311. (DOI: 10.1021/acsabm.9b00334).
51. Thakur N., Chaudhary A., Chakraborty A., Kumar R., Sarma T. K. (2021), Ion Conductive Phytic Acid-G Quadruplex Hydrogel as

- Electrolyte for Flexible Electrochromic Device. *ChemNanoMat* 7, 613–619 (DOI: 10.1002/cnma.202100072).
52. Loo K., Degtyareva N., Park J. *et al.* (2010). Ag⁺-Mediated Assembly of 5'-Guanosine Monophosphate. *J. Phys. Chem. B* 114, 4320–4326 (DOI: 10.1021/jp908085s).
53. Kulikov V., Johnson N. A. B., Surman A. J. *et al.* (2017), Spontaneous Assembly of an Organic–Inorganic Nucleic Acid Z-DNA Double-Helix Structure. *Angew. Chem., Int. Ed.* 56, 1141–1145 (DOI: 10.1002/anie.201606658).
54. Giorgi T., Lena S., Mariani P., *et al.* (2003), Supramolecular Helices via Self-Assembly of 8-Oxoguanosines. *J. Am. Chem. Soc.* 125, 14741–14749. (DOI: 10.1021/ja0364827).
55. Yoshikawa I., Li J., Sakata Y., Araki K. (2004), Design and Fabrication of a Flexible and Self-Supporting Supramolecular Film by Hierarchical Control of the Interaction between Hydrogen-Bonded Sheet Assemblies. *Angew. Chem., Int. Ed.* 43, 100–103 (DOI: 10.1002/anie.200352641).
56. Fan B., Cui N., Xu Z., *et al.* (2022), Thermoresponsive and Self-Healing Hydrogel Based on Chitosan Derivatives and Polyoxometalate as an Antibacterial Coating. *Biomacromolecules* 23, 972–982 (DOI: 10.1021/acs.biomac.1c01368).
57. Zheng C. Y., Li H. (2013), Chirality delivery through multiple and helical H-bonding from chiral coordination complex to its supramolecular architecture. *Inorg. Chem. Commun.* 34, 30–33. (DOI: 10.1016/j.inoche.2013.04.038).
58. Sprecher C. A., Johnson Jr. W. C. (1977), Circular dichroism of the nucleic acid monomers. *Biopolymers* 16, 2243–2264 (DOI: 10.1002/bip.1977.360161012).

59. Jose D., Weitzel S. E., Baase W. A. *et al.* (2015), Mapping the interactions of the single-stranded DNA binding protein of bacteriophage T4 (gp32) with DNA lattices at single nucleotide resolution: polynucleotide binding and cooperativity. *Nucleic Acids Res.* 43, 9291–9305 (DOI: 10.1093/nar/gkv818).
60. Zhu H., Song S., Wang, R. (2020), Removal of NO_x by Adsorption/Decomposition on H₃PW₁₂O₄₀·6H₂O Supported on Ceria. *Aerosol Air Qual. Res.* 20, 2273–2279 (DOI: 10.4209/aaqr.2020.03.0110).
61. Rao U., Sekharnath K. V. *et al.* (2014), Mixed matrix membranes of sodium alginate and hydroxy propyl cellulose loaded with phosphotungstic heteropolyacid for the pervaporation separation of water-isopropanol mixtures at 30 °C. *Int. J. Sci. Technol. Res.* 3, 129–137.
62. da Silva M. J., da Silva Andrade P. H., Ferreira S. O. *et al.* (2018), Monolacunary K₈SiW₁₁O₃₉-Catalyzed Terpenic Alcohols Oxidation with Hydrogen Peroxide. *Catal. Lett.* 148, 2516–2527 (DOI: 10.1007/s10562-018-2434-0).
63. Tajmir-Riahi H. A. (1991), Interaction of Purine Nucleotides with Cobalt-Hexammine, Cobalt-Pentammine and Cobalt- Tetrammine Cations. Evidence for the Rigidity of Adenosine and Flexibility of Guanosine and Deoxyguanosine Sugar Conformations. *J. Biomol. Struct. Dyn.* 8, 1169–1186 (DOI: 10.1080/07391102.1991.10507877).
64. Andrushchenko V., Bouř P. (2009), Infrared Absorption Detection of Metal Ion-Deoxyguanosine Monophosphate Binding: Experimental and Theoretical Study. *J. Phys. Chem. B* 113, 283–291 (DOI: 10.1021/jp8058678).
65. Zhang J., Li X., Sun X., Song A., Tan Y., Hao J. (2018), GMP-quadruplex-based hydrogels stabilized by lanthanide ions. *Sci. China Chem.* 61, 604–612 (DOI: 10.1007/s11426-017-9187-x).

66. Kozhevnikov I. V. (1998), Catalysis by Heteropoly Acids and Multicomponent Polyoxometalates in Liquid-Phase Reactions. *Chem. Rev.* 98, 171–198 (DOI: 10.1021/cr960400y).
67. Bardin B. B., Bordawekar S. V., Neurock M., Davis R. J. (1998). Acidity of Keggin-Type Heteropolycompounds Evaluated by Catalytic Probe Reactions, Sorption Microcalorimetry, and Density Functional Quantum Chemical Calculations. *J. Phys. Chem. B* 102, 10817–10825 (DOI: 10.1021/jp982345y).
68. Kulikov S. M., Kozhevnikov I. V. (1982), Acidity function of concentrated solutions of 12-tungstophosphoric acid. *Bull. Acad. Sci. USSR Div. Chem. Sci.* 31, 441–442 (DOI: 10.1007/BF00949754).
69. Misono M., Okuhara, T. (1994) Heteropoly Compounds: Efficient Superacid Catalysts. *MRS Online Proc. Libr.* 368, 215–221 (DOI: 10.1557/PROC-368-215).
70. Omwoma S., Gore C. T., Ji Y. (2015), Environmentally benign polyoxometalate materials. *Coord. Chem. Rev.* 286, 17–29 (DOI: 10.1016/j.ccr.2014.11.013).
71. Zhang Q., Duan X., *et al.* (2023). Catalytic performance of amino acid/phosphotungstic acid as bi-functional heterogeneous catalyst for biodiesel production. *Environ. Eng. Res.* 28 (DOI: 10.4491/eer.2021.560).
72. Marion G. M., Millero, F. J. *et al.* (2011). pH of seawater. *Mar. Chem.* 126, 89–96 (DOI: 10.1016/j.marchem.2011.04.002).
73. La Barre S., Potin P., Leblanc C., Delage L. (2010), The Halogenated Metabolism of Brown Algae (Phaeophyta), Its Biological Importance and Its Environmental Significance. *Mar. Drugs* 8, 988–1010 (DOI: 10.3390/md8040988).
74. Wever R., Barnett P. (2017). Vanadium Chloroperoxidases: The Missing Link in the Formation of Chlorinated Compounds and

Chloroform in the Terrestrial Environment? Chem. – Asian J. 12, 1997–2007 (DOI: 10.1002/asia.201700420).

75. Fournier J. -B., Rebuffet E. *et al.* (2014), The Vanadium Iodoperoxidase from the Marine Flavobacteriaceae Species *Zobellia galactanivorans* Reveals Novel Molecular and Evolutionary Features of Halide Specificity in the Vanadium Haloperoxidase Enzyme Family. Appl. Environ. Microbiol. 80, 7561–7573 (DOI: 10.1128/AEM.02430-14).
76. Sels B., Vos D. D., Buntinx M., *et al.* (1999). Layered double hydroxides exchanged with tungstate as biomimetic catalysts for mild oxidative bromination. Nature 400, 855–857 (DOI: 10.1038/23674).
77. Te M., Fairbridge C., Ring Z. (2001), Oxidation reactivities of dibenzothiophenes in polyoxometalate/H₂O₂ and formic acid/H₂O₂ systems. Appl. Catal. Gen. 219, 267–280 (DOI: 10.1016/S0926-860X(01)00699-8).
78. Archer S. D., Posman, K. M., *et al.* (2019), Fluorescent Detection of Bromoperoxidase Activity in Microalgae and Planktonic Microbial Communities Using Aminophenyl Fluorescein. Front. Mar. Sci. 6 (DOI: 10.3389/fmars.2019.00068).
79. Everett R. R., Kanofsky J. R., Butler, A. (1990), Mechanistic investigations of the novel non-heme vanadium bromoperoxidases. Evidence for singlet oxygen production. J. Biol. Chem. 265, 4908–4914 (DOI: 10.1016/S0021-9258(19)34060-8).

Chapter 3

A multi-stimuli responsive polyoxometalate-guanosine monophosphate hybrid chromogenic smart hydrogel

3.1 Introduction

Chromogenic materials are a class of smart materials that show reversible changes in their optical properties in response to stimuli, both physical (strain, temperature, light, current, etc) or chemical (metals, pH, solvent, or exposure to any other chemicals). Chromogenic materials are gaining technological importance due to their versatile applications as smart windows, displays, photonic devices, sensors, information encryption, green printing, etc.¹⁻⁷ Polyoxometalates (POM), which consist of inorganic metal oxide clusters comprising transition metals like V, Mo, W, etc., in their highest oxidation state, are exceptionally suitable for chromic applications owing to their diverse redox chemistry. The metal ions in POM can accept electrons resulting in a mixed-valence colored species upon exposure to various stimuli such as electricity, light, temperature, etc. without any variation in structural aspects.⁸⁻¹² However, using bare polyoxometalate has its limitations such as heterogeneous aggregation, opacity, low or negligible absorption in the visible light region, high water solubility leading to leaching, etc.¹³

Integrating POM into soft matter such as gels can provide a simple alternative for the practical utility of these materials.¹⁴⁻¹⁸ POM-based inorganic-organic functional materials are usually obtained through covalently linking the POM clusters with organic linkers.¹⁹⁻²² However, this strategy usually involves tedious synthetic steps such as harsh reaction conditions and inefficient purification might result in significant alterations of the inherent physicochemical properties of the POMs.²³ On the other hand, the use of non-covalent interactions that include electrostatic, hydrogen bonding, and π - π interactions provide various

options for straightforward integration of these anionic nanoclusters into functional architectures and devices.²⁴ Supramolecular gels formed through non-covalent interactions have attracted widespread attention due to their impact on biomaterials, sensing, stimuli-responsive, and self-healing materials. Because of the dynamic and reversible nature of the non-covalent interactions, the gels show reversibility in response to various external stimuli such as temperature, pH, light, etc.^{25–27} There have been some reports of photochromic POM containing hydrogels, formed through electrostatic interactions between anionic POM clusters and cationic polymers, amphiphiles or peptides. However, the strong electrostatic interactions between the two components often led to water-insoluble complexes, resulting in optically opaque gels, thus limiting their practical applications in aqueous systems.^{25,28} Therefore, there is scope for exploring elegant self-assembly processes leading to POM-integrated hydrogels with high transparency and enhanced chromic properties responsive to various external stimuli.

Small biomolecules, with extensive coordination and hydrogen bonding sites, can provide a simple route for the formation of self-assembled hydrogel with enhancement of their inherent properties owing to the formation of supramolecular assembly.²⁹ Nucleotides are well-known low molecular weight gelators (LMWGs) and can induce diverse non-covalent interactions leading to hydrogels.³⁰ Further, the supramolecular assembly of nucleotides with metal ions results in improved biocompatibility as compared to the bare metal counterpart.^{29,31} The ability of guanosine monophosphate (GMP) to self-assemble into a G-quartet structure is attributed to its engagement of both Watson–Crick and Hoogsteen face hydrogen bonding, thus making it a prime target for supramolecular self-assembly.³² G-quartets further assemble, stacking upon each other to create a G-quadruplex strand, and the internal axial channel serves as an optimal pathway for ion conduction.^{33,34} Cronin et al. developed a distinct Z-DNA double helix through condensation of GMP and sodium molybdate. The resulting covalently linked POM-nucleotide complex behaved as an organogelator.³⁵ On the other hand, a

physically crosslinked POM-nucleotide hydrogel through spontaneous self-assembly into hierarchical nanoarchitecture will not only simplify the fabrication process but also impart additional properties such as thermo-reversibility, thixotropy, etc. due to the dynamic nature of the interactions.

In our pursuit of studying the self-assembly of nucleotides leading to hydrogels for diverse applications,^{29,31,34,36} herein, we report a facile method to develop a polyoxometalate-nucleotide supramolecular hydrogel simply by mixing aqueous solutions of Keggin-structured phosphomolybdic acid (PMA) and GMP, resulting in a yellow transparent hydrogel at room temperature. The hydrogel obtained was thermoreversible, mechanically robust, shape-sustaining, mouldable, and thixotropic in nature. The hydrogel displayed chromic properties under stress, visible light, electricity, temperature, and metal exposure without gel disintegration. The hydrogel also displayed a stimuli-responsive change in optical properties towards iodide and thiol groups. To the best of our knowledge, this is the first report of a POM-based hydrogel exhibiting chromism for five distinct stimuli using a single material.

3.2 Results and Discussion

3.2.1. Synthesis of PMA-GMP hydrogel

Mixing aqueous solutions of PMA (60 mM) and GMP (180 mM), and slightly heating the mixture to 65 °C for 5 minutes resulted in a homogeneous yellow-colored solution which spontaneously formed a hydrogel upon cooling to room temperature (Figure 3.1a). Gelation could be visually confirmed when the solvent did not flow on inverting the vial. The hydrogel showed thermoreversible behavior, as the gel could be converted to sol at ~ 68 °C and the gel was reformed upon cooling to 25 °C. This property of the hydrogel could be utilized to mold the hydrogel into different shapes (Figure 3.1b). Critical gelation concentration was measured in two sets of experiments by varying the concentration of one component while keeping the other one constant and found to be 15 mM and 90 mM for PMA and GMP respectively (Figure 3.1c).

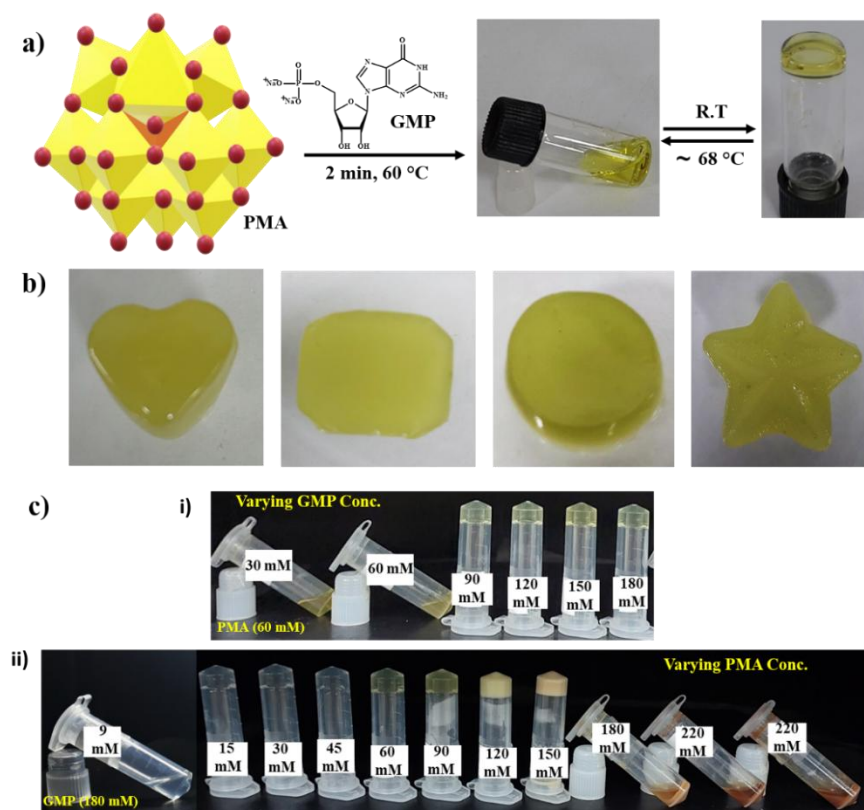


Figure 3.1. (a) Schematic representation of the formation of PMA-GMP hydrogel and its thermoreversible property, (b) Digital images depicting the shape moulding ability of PMA-GMP hydrogel owing to its thermo-reversible property, and (c) Concentration dependent studies of PMA-GMP system (i) varying the concentration of GMP while keeping the concentration of PMA constant at 60 mM, (ii) varying the concentration of PMA while keeping GMP concentration constant at 180 mM.

3.2.2. Morphological Evaluation

Scanning electron microscopy (SEM) (Figure 3.2a) showed highly entangled crosslinked fibrillar morphology. Further, Transmission electron microscopy (TEM) studies showed ribbon-like fiber formation with an average diameter of 30-50 nm (Figure 3.2b). Atomic force microscopy (AFM) reaffirmed the fibrillar morphology with an average diameter of the fibers ranging from 20-30 nm (Figure 3.2c).

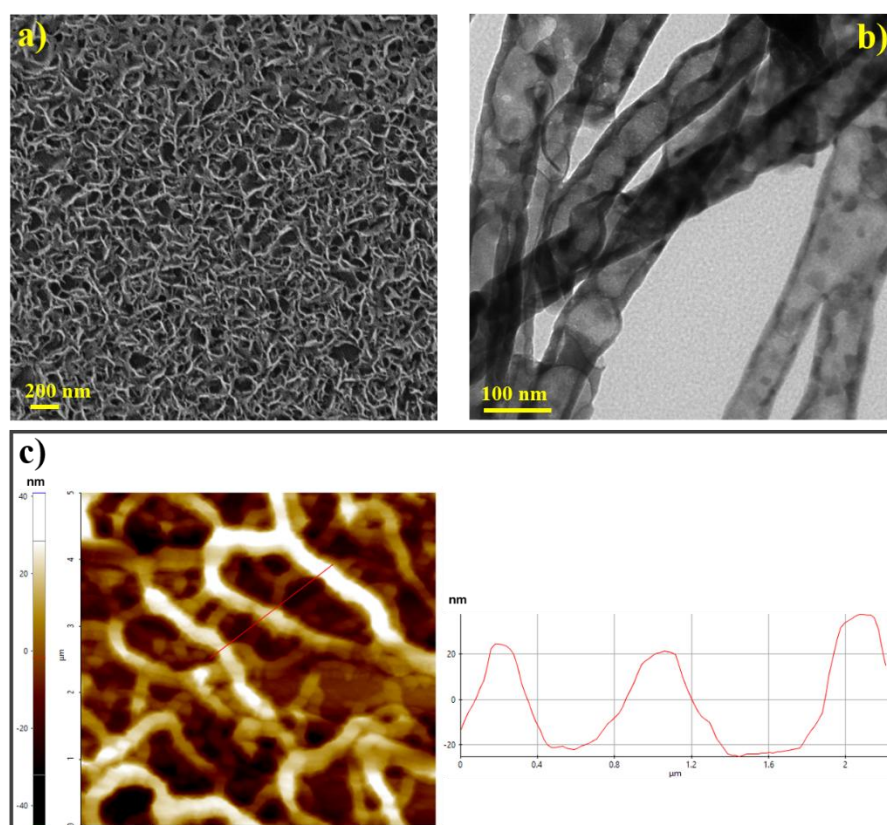


Figure 3.2. (a) FESEM image of PMA-GMP hydrogel showing highly tangled fibrillar morphology, (b) HRTEM image of the fibril strands, and (c) AFM image of the hydrogel.

3.2.3. Spectroscopic Characterization

CD spectrum of PMA-GMP hydrogel resembles the shape of a hybrid G-Quartet with a positive cotton band at 280 nm, a shoulder at 247 nm, and a negative cotton band at 220 nm (Figure 3.3a). The observed shift from the assigned peak positions in a hybrid structure could be attributed to the interaction with PMA leading to alteration in base tilting.^{37,38} The influence of PMA on GMP assembly is further established through proton NMR of the hydrogel and GMP (Figure 3.3b). In ^1H NMR of PMA-GMP assembly, the protons experience a downfield shift owing to the hydrogen bonding. Also, new peaks at 6.07 ppm and a doublet at 9.27 and 9.3 ppm were observed. These peaks correspond to the $-\text{NH}_2$ proton in GMP, which are generally not observed in D_2O owing to the proton exchange process, however in the case of PMA-GMP hydrogel, the appearance of these peaks is probably due to the slowing of proton exchange owing to extensive hydrogen bonding.³⁹ The peaks at

6.07 ppm correspond to the amine proton, which is not involved in G-quartet formation. The hydrogen involved in G-quartet formation showed a downfield shift to 9.27 and 9.3 ppm. The appearance of 2 equi-intensity peaks at 9.27 and 9.3 ppm is characteristic of GMP hexadecamer, consisting of 4 layers of G-Quartet. The peak at 9.27 ppm corresponds to the amine protons of the inner layers involved in quartet formation and the peak at 9.3 ppm is attributed to the protons of the outer layer.⁴⁰

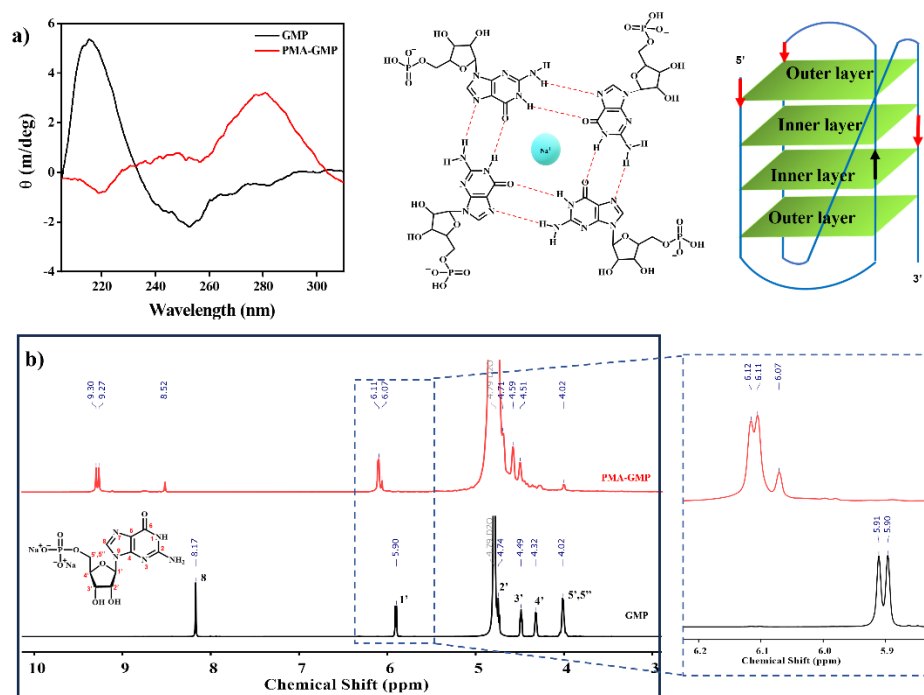


Figure 3.3. (a) CD spectra and (b) ¹H NMR spectra of GMP and PMA-GMP hydrogel.

The UV-visible spectrum of GMP exhibited an absorption peak at 252 nm and a shoulder band at 276 nm, whereas the absorption peak for PMA was observed at 222 nm (Figure 3.4a). Upon adding PMA to GMP, the UV-visible spectrum of the hydrogel broadened and showed a hypsochromic shift from 252 nm to 248 nm, indicating their self-assembly. At varying PMA to GMP ratios, the absorbance spectra showed the self-assembly of the two precursors (Figure 3.4b). CD spectra were also recorded while varying the PMA to GMP ratio (Figure 3.4c).

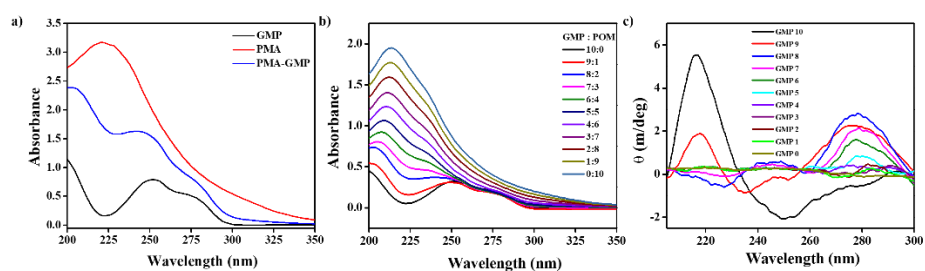


Figure 3.4. (a) UV-visible spectra of GMP, PMA, and PMA-GMP solution, (b, c) UV-visible and circular dichroism spectra of PMA-GMP recorded with decreasing mole fraction of GMP respectively.

The interaction between the phosphate group in GMP and PMA was confirmed by observing an upfield shift in the ^{31}P NMR spectrum of the PMA-GMP hydrogel as compared to free GMP (Figure 3.5a). FTIR spectroscopy studies were further carried out to understand the involvement of various functional groups in the self-assembly process (Figure 3.5b). The peaks at 1695 cm^{-1} and 1483 cm^{-1} corresponding to C(6)=O and C(8)-N(7) bond vibration were shifted to 1698 cm^{-1} and 1465 cm^{-1} respectively, confirming their involvement in the formation of G-Quartet.⁴¹ In PMA, the four characteristic keggin peaks at 1054 cm^{-1} , 953 cm^{-1} , 877 cm^{-1} , and 749 cm^{-1} correspond to the stretching vibrations of P-O, Mo-Ot, Mo-Oc-Mo, and Mo-Oe-Mo, respectively (where Ot is terminal oxygen, Oc is corner sharing oxygen, and Oe is edge oxygen).⁴² These peaks were present in the hydrogel with some frequency shift indicating their involvement in non-covalent interactions while the Keggin structure is still preserved. Powder XRD studies of PMA-GMP xerogel revealed the characteristic peaks of the PMA Keggin structure were retained (Figure 3.5c). However, the broadening of the peaks was observed for PMA-GMP due to the amorphous nature of the xerogel.

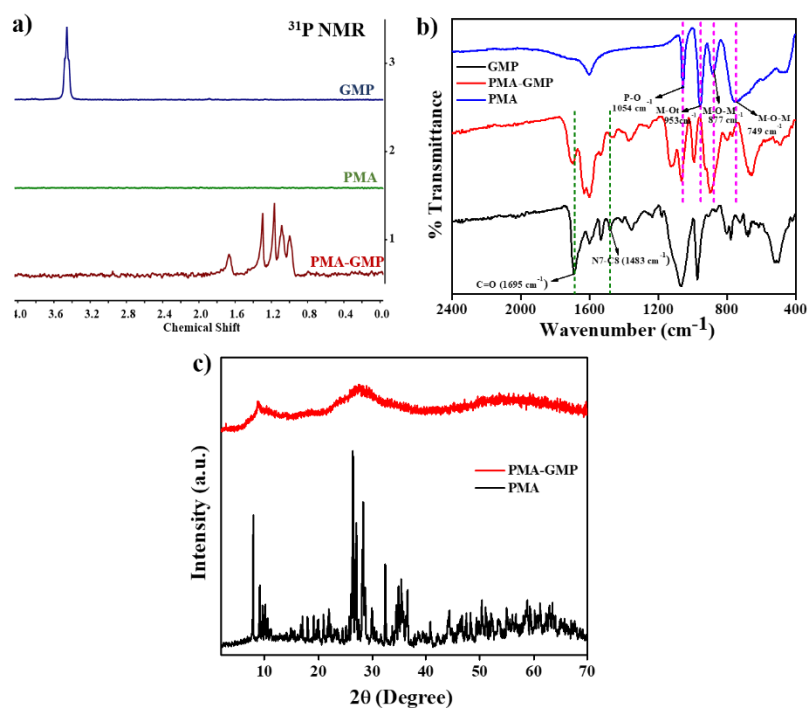


Figure 3.5. (a) ^{31}P NMR of GMP, PMA, and PMA-GMP hydrogel, (b) FTIR spectra of GMP, PMA, and PMA-GMP hydrogel, and (c) PXRD of PMA and PMA-GMP hydrogel.

Based on the spectroscopic evidence, a plausible self-assembly mechanism is proposed. From CD we observed that GMP is assembled into a G-quartet of hybrid conformation in the presence of PMA and from ^1H NMR, we conclude that four G-quartets are stacking over each other to form a hexadecamer (G16). GMP is reported to form hydrogel under acidic conditions.^{43–46} The phosphate group protonation of GMP takes place in acidic pH, leading to the formation of PO_3H^- from PO_3^{2-} . The lowering of anionic charge reduces the repulsion among the G-Quartets, thus facilitating their stacking. The protonation of the phosphate group also makes it an H-donor thus favoring the formation of a 3-D network through cross-linking.^{47,48} The acidity, in this case, is provided by the polyoxometalate (POM) since they are well-known Bronsted acids.^{49,50} ^{31}P NMR and FTIR studies suggest the interaction between PMA and GMP through the H-bonding between the protonated phosphate group (PO_3H^-) of GMP with the oxygens of the phosphomolybdic acid, leading to crosslinking between G-quartets and the polyoxometalate. Thus, along with providing acidic pH, POM also acts as a crosslinker here, since its oxygen-rich surface acts as an H-bond acceptor. A plausible structure

depicting the interaction between GMP and PMA is proposed in Figure 3.6. Further entanglement leading to gelation takes due to various non-covalent interactions such as H-bonding, electrostatic interactions, Van-der-Waal forces, π - π stacking, etc.

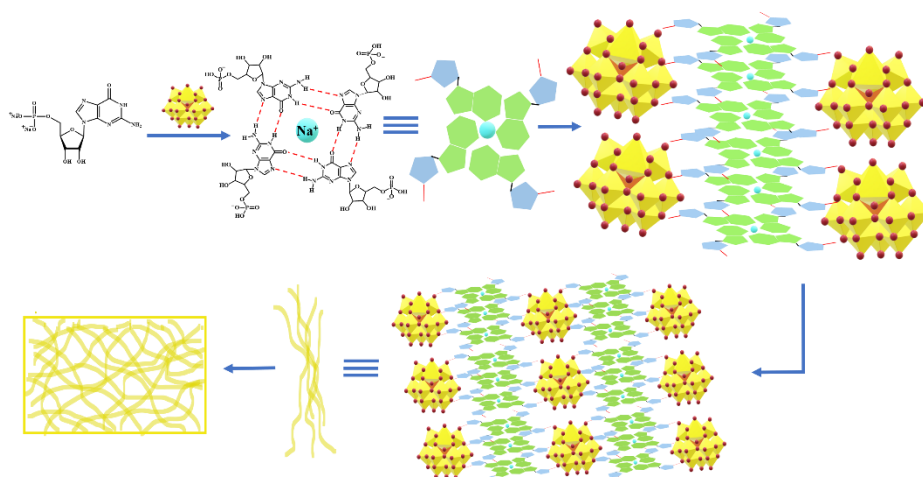


Figure 3.6. Schematic representation for the proposed self-assembly of the PMA and GMP leading to fibrillar morphology resulting in gelation.

3.2.4. Mechanical Strength

Shear Strength. Rheological investigations were carried out to evaluate the viscoelastic behavior of the hydrogel. The viscoelastic property of the hydrogel was studied as the function of shear stress. Both strain and frequency sweep studies indicated the prevalence of elastic characteristics over viscous properties as the storage modulus (G') exhibited a higher magnitude than the loss modulus (G'') (Figure 3.7a, b). The flow point for the hydrogel was found to be as high as 100% from the strain-sweep experiment. To check the recoverability of the hydrogel, a thixotropic loop test was performed by imposing alternate low and high strains of 0.1 and 200% respectively (Figure 3.7c). The hydrogel was robust and could withstand the weight of 150 g without a change in shape (Figure 3.8a). The hydrogel was also injectable (Figure 3.8b)

Tensile strength. We observed that the hydrogel was highly tensile and it could be stretched up to a thread-like thin strand before breaking. This observation propelled us to perform experiments on a universal testing machine (UTM), to study and quantify the tensile strength and fracture

strain percent for the hydrogel (Figure 3.7d). The tensile strength and fracture strain were found to be 72 kPa and 6590% respectively. An elongation of 264 mm (26.4 cm) was observed when stretched by the UTM instrument (Figure 3.8c). Although hydrogels obtained through the self-assembly of small biomolecules have poor mechanical strength, the cross-linking of the inorganic clusters probably influenced the enhancement of the mechanical properties of the hydrogel matrix.⁵¹

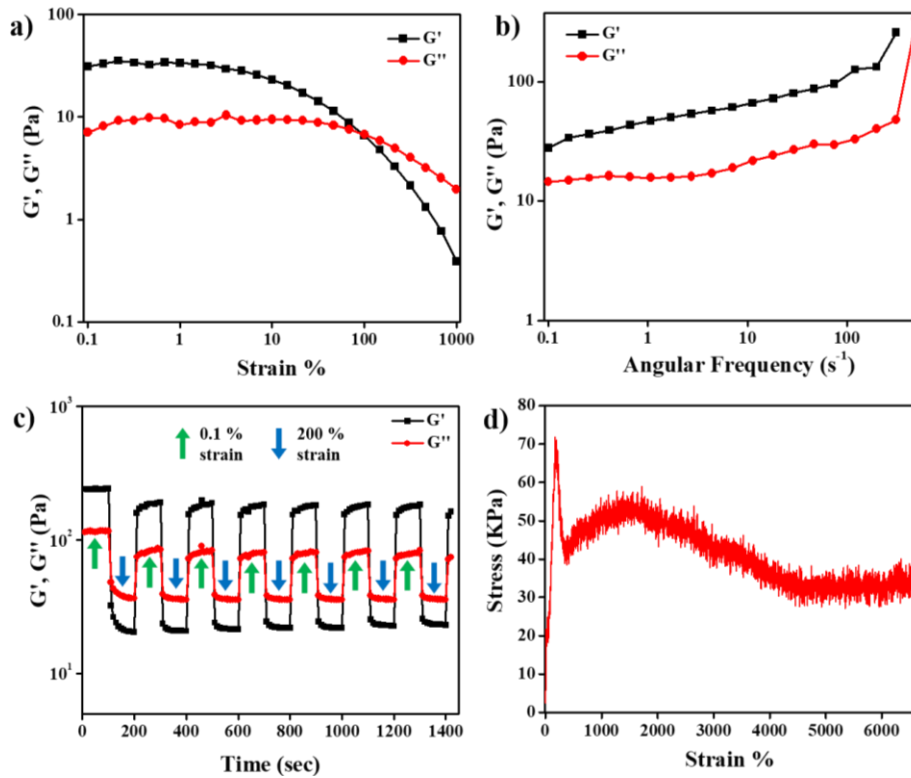


Figure 3.7. (a) Dynamic strain-sweep of PMA-GMP hydrogel, (b) Frequency sweep measurements of PMA-GMP hydrogel at a constant strain of 1%, (c) Thixotropic loop measurements for PMA-GMP hydrogel at a constant angular frequency of 10 rad s⁻¹, (d) Tensile stress vs tensile strain curve of PMA-GMP hydrogel.

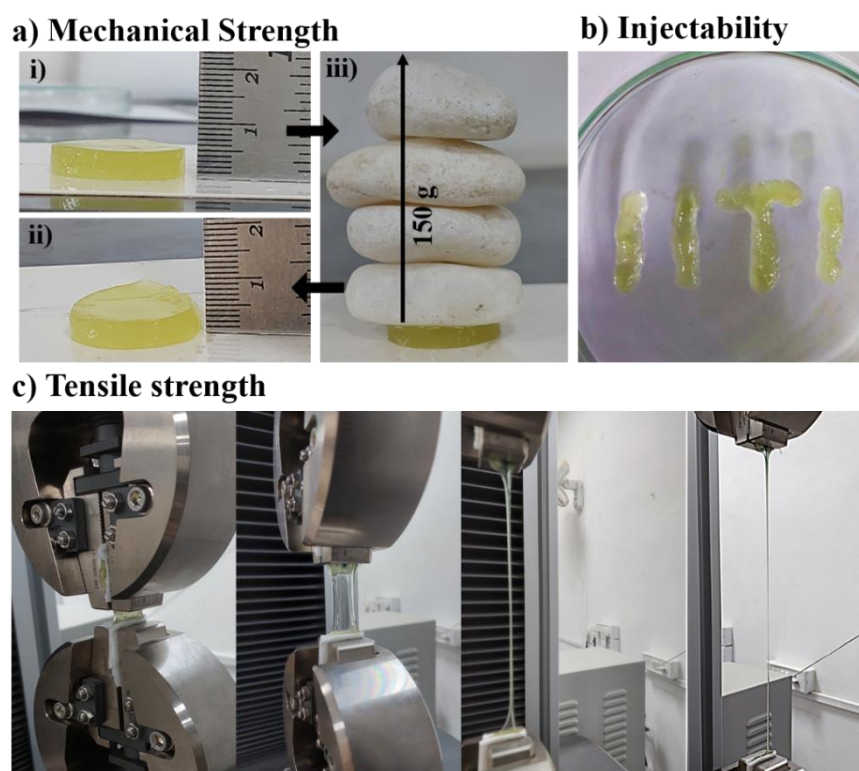


Figure 3.8. Digital images showing (a) the mechanical strength, (b) the injectability of the hydrogel, and (c) the hydrogel stretched in the universal testing machine to quantify the tensility of the hydrogel.

3.2.5 Chromogenic response to physical stimuli

The hydrogel changed from yellow to blue upon exposure to various physical stimuli such as electricity, visible light, temperature, and mechanical stress (Figure 3.9a). The hydrogel demonstrated a color change from yellow to dark blue by applying a potential of 1.5 V for 3 seconds. Under a reverse bias of 2.5 V for 200 seconds, the hydrogel turned light blue. It maintained this reversible on/off transition between light blue and dark blue states, upon applying the forward and reverse bias respectively. A similar change in the optical behavior from yellow to blue of the hydrogel was observed upon exposure to visible light for 3 hours (white LED). Similarly, heating the hydrogel at 90 °C for 40 minutes resulted in a blue-colored sol which would be converted to a blue-colored hydrogel upon cooling to 25 °C. The hydrogel also showed mechanochromic behavior as the shear stress caused by grinding the hydrogel in a mortar pestle for 10 minutes resulted in a blue-colored hydrogel without any collapse in its gel state. The blue-colored hydrogel

could be quickly reverted to its original yellow color after exposure to H_2O_2 (4 mM).

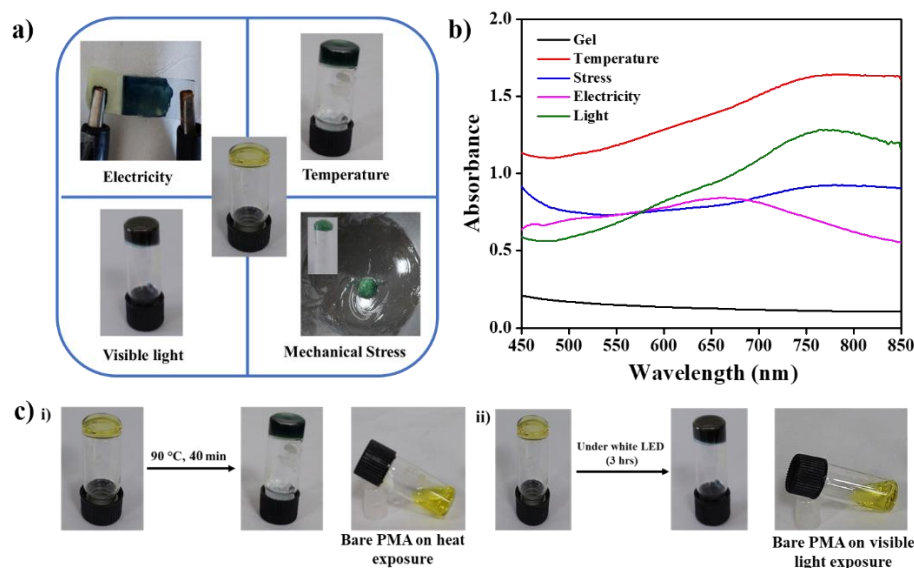


Figure 3.9. (a) Digital image of PMA-GMP hydrogel before and after exposure to electricity, visible light, temperature, and mechanical stress, (b) UV-visible spectra of the hydrogel and after triggered by stimuli, (c) i) PMA-GMP hydrogel and bare PMA solution on heating at 90 °C for 40 mins, ii) PMA-GMP hydrogel and bare PMA solution after exposure to light for 3 hrs.

UV-visible studies were carried out to further investigate the change in optical properties of the hydrogel before and after exposure to the physical stimuli (Figure 3.9b). The absorption band in the broad range of 650 nm to 900 nm is attributed to the heteropolyblue species formed due to oxygen to molybdenum ($\text{O} \rightarrow \text{Mo}$) ligand to metal charge transfer (LMCT). Absorption maxima at different wavelengths is attributed to the formation of different heteropolyblue species under different conditions.^{52–54} Interestingly, only PMA solution when exposed to visible light for 3 hours or heated at 90 °C for 40 min, did not change color as observed in the hydrogel (Figure 3.9c). The improved stimuli-responsiveness of PMA upon gelation with GMP could be attributed to the proximity of the amino group in GMP to PMA. It is well-established that the presence of an amino group near POM stabilizes the reduced O-Mo^{V} species by donating its lone pair of electrons to the hole left at oxygen, thus assisting their reduction.^{52,55} Another contributing factor may be the formation of self-assembled supramolecular structure as non-

covalent interactions like π - π stacking and H-bonding can contribute to reducing the system bandgap.^{56,57} UV-visible absorbance studies at variable temperatures (70-120 °C) showed the increasing formation of the heteropolyblue species at elevated temperatures (Figure 3.10a). Time-dependent UV-visible spectra of the hydrogel on exposure to 90 °C and visible light irradiation showed an increase in absorbance with time (Figure 3.10b, c).

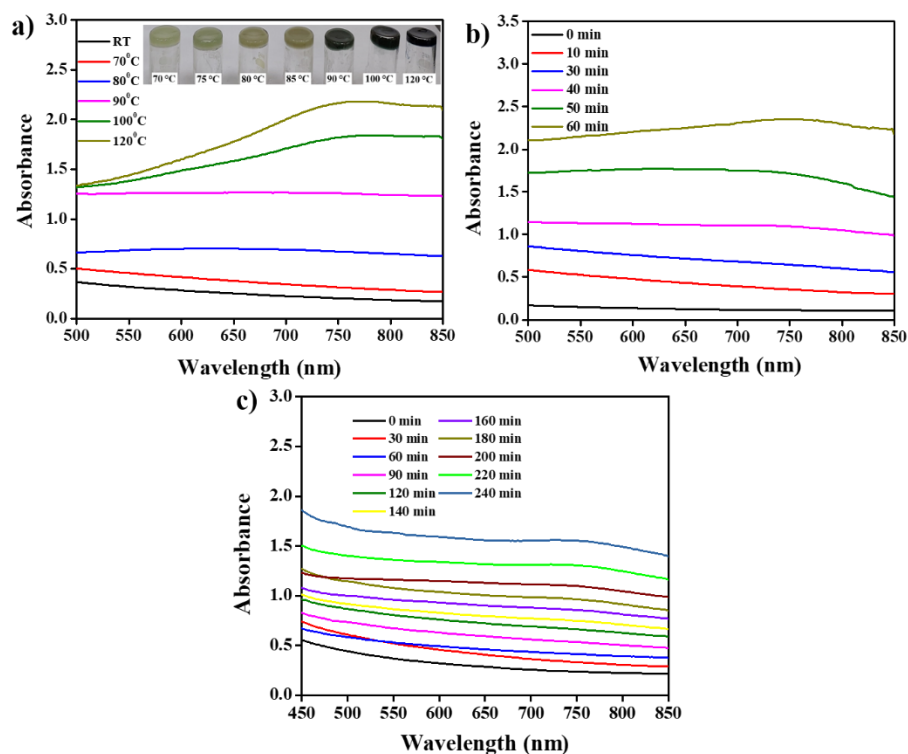


Figure 3.10 (a) UV-visible absorbance spectra of the hydrogel heated at different temperatures for 40 mins (inset: digital images), (b) Time-dependent UV-visible spectra of PMA-GMP hydrogel exposed to 90 °C for 60 mins, and (c) Time-dependent UV-visible spectra of the hydrogel after exposure to light.

Designing a 2-layered electrochromic device

Cyclic voltammetry studies of bare PMA showed one-electron reversible cycle with a reduction peak at -1.24 V and an oxidation peak at +1.23 V. The hydrogel also inherited a similar reversible redox cycle with a reduction peak at -1.1 V and an oxidation peak at +1.21 V (Figure 3.11a). As the G-quartet assemblies are known to show ion-conducting behavior,^{33,34} the conductivity of the PMA-GMP hydrogel was measured using a Swagelok cell, and conductivity of 1.45 mScm⁻¹ was calculated

by fitting the Nyquist plot using electrochemical impedance spectroscopy (EIS) (Figure 3.11b). The results propelled us to design a 2-layered electrochromic device (ECD) where the hydrogel itself can act as an electrode. This can substitute the traditional 5-layered electrochromic device (Figure 3.11c), making it cost-effective, simple, and eliminating steps such as electrodeposition. Figure 3.11d shows a digital image of the ECD where a film of hydrogel is simply deposited over the ITO plate, supported via a glass slide.

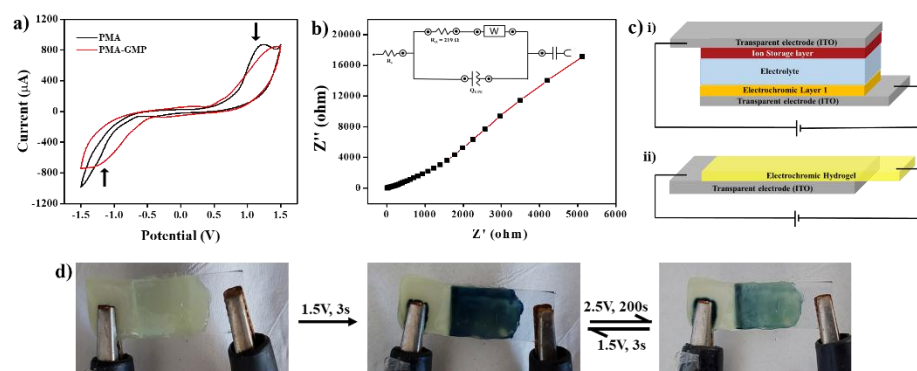


Figure 3.11. (a) Cyclic voltammogram of bare PMA solution and PMA-GMP hydrogel at the scan rate of 50 mV s^{-1} , (b) Electrochemical impedance spectroscopy (Nyquist plot) of the PMA-GMP hydrogel, (c) i) traditional electrochromic device with five layers (top), and ii) proposed electrochromic device with two layers (bottom), and (d) digital image of the electrochromic device.

3.2.6. Chromogenic response to chemical stimuli

Further possibilities of exploring the hydrogel as metallochromic material were evaluated by exposing them to common metals (Figure 3.12a). PMA-GMP hydrogel changed its color from yellow to blue in contact with metals like Fe, Cu, Zn, Pb, and Sn, owing to a reduction of Mo^{VI} to Mo^{V} which is further confirmed by the presence of an absorption peak in the region of 700-750 nm in UV-visible spectra. The hydrogel was oxidized back to yellow color with the addition of H_2O_2 . The collapse of hydrogel was observed when metallic Mg ribbon was exposed to it despite the occurrence of a blue color. Mg is known for its affinity to bind with GMP which could potentially be the contributing factor towards the disintegration of the hydrogel.⁵⁸

The PMA-GMP hydrogel was also prone to reduction in the presence of thiol-containing compounds (Figure 3.12b) and iodide (Figure 3.12c). The hydrogel turned to blue from yellow maintaining its gel state when triggered with the thiol group (such as cysteine, glutathione, and 2,3-dimercaptosuccinic acid) and selectively iodide among other halides. The absorption peak obtained in the region of 700-750 nm shows the formation of Mo^{V} species. This characteristic change in optical property due to the formation of Mo^{V} could help in the visual monitoring of biomolecules like cysteine or glutathione or ions of biological importance such as iodide selectively among the halides.

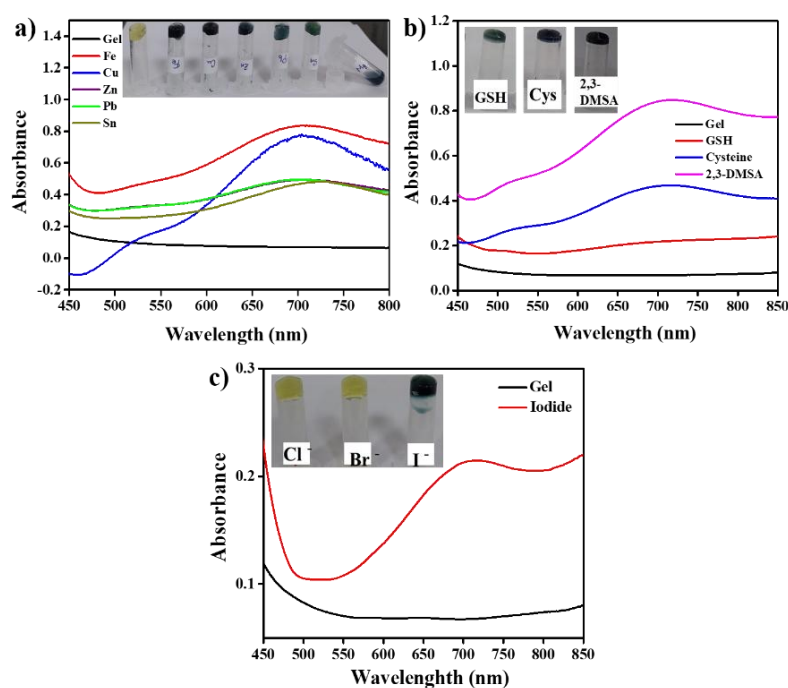


Figure 3.12. (a) Absorbance spectra of the hydrogel after exposure to various metals (Inset: digital image), (b) UV-visible spectra of the hydrogel in response to glutathione (7 mM), cysteine (7 mM), 2,3 – dimercaptosuccinic acid (7 mM), (c) UV-vis spectra of the hydrogel in response to iodide (30 mM). (Digital image inset)

UV-visible studies were also performed to assess the concentration-dependent absorption of the thiol-containing compounds and iodide demonstrating an increase in absorbance with the increase in their concentration (Figure 3.13).

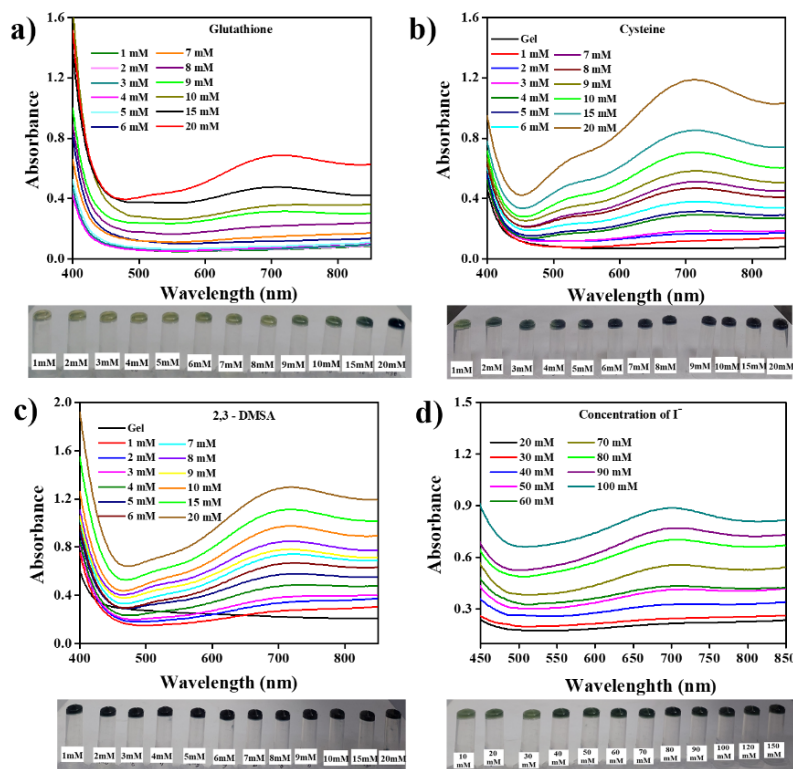


Figure 3.13. Concentration-dependent absorbance spectra of the hydrogel when treated with varying concentrations of (a) GSH, (b) cysteine, (c) 2,3-DMSA, and (d) Iodide respectively, and their digital images (below).

We also checked the pH responsiveness of the hydrogel (Figure 3.14). The hydrogel showed stability under acidic conditions in the range of pH 3-6. Upon increasing the pH by adding NaOH, the hydrogel slowly became viscous and the hydrogel was completely converted into a sol at pH 10, with a blue coloration. The deprotonation of PO_3H^- to PO_3^{2-} in basic pH increases the electrostatic repulsion among G-quartets and also the disruption of H-bonding in the system, thus causing a gel-to-sol transition. The bluish coloration observed in the basic pH is due to the reduction of PMA in the presence of OH^- .⁵⁹ However, this phenomenon is reversible and upon lowering the pH of the system back to the range of 4 to 5, reformation of the hydrogel took place and the PMA oxidized back to yellow, thus also showing halochromic behavior.



Figure 3.14. (a) Hydrogel before exposure to pH change, (b) increasing pH by adding base leading to gel to sol transition of the hydrogel with bluish colour, and (c) acid added to the previous system to lower pH leading to restoration of the gel.

3.2.7. Reversibility Cycle

The stimuli-responsive chromic behavior of the PMA-GMP hydrogel was evaluated for reversibility under mechanical stress, visible light, electricity, temperature, and metal over five cycles (Figure 3.15).

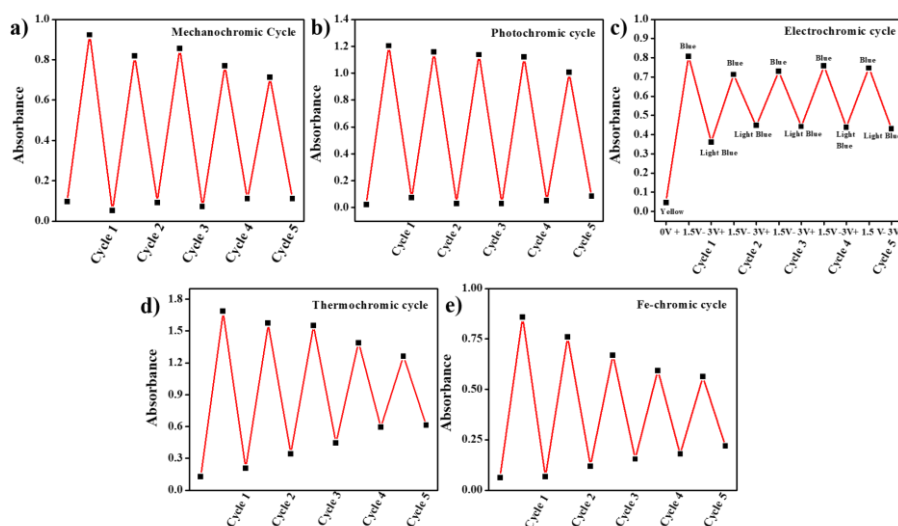


Figure 3.15. Reversibility cycle for chromism induced by various stimuli (a) mechanical stress, (b) visible light, (c) electricity, (d) temperature, and (e) metal (Fe).

3.2.8. Reduction of Mo^{VI} to Mo^V

The confirmation of the reduction of Mo^{VI} to Mo^V upon exposure to various stimuli was supported by X-ray photoelectron spectroscopy (XPS) (Figure 3.16). The deconvoluted Mo 3d spectrum consists of peaks at binding energies of 232.6 and 235.7 eV assigned to Mo 3d_{5/2} and Mo 3d_{3/2} respectively for the Mo^{VI} state. The presence of the Mo^V state was ascertained from the two deconvoluted peaks at lower binding energies of 231.5 and 234.7 eV owing to Mo 3d_{5/2} and 3d_{3/2} respectively.^{60–63} The reduction of Mo is evidenced by the broadening and increase in the

intensity of Mo^V deconvoluted peaks. Initially, the Mo^V content in the hydrogel was only 15% before exposure to any stimuli. However, upon subsequent exposure to stress, light, temperature, electricity, and metal, the Mo^V content increased to 37.6%, 46.2%, 45.4%, 45%, and 45.1% respectively.

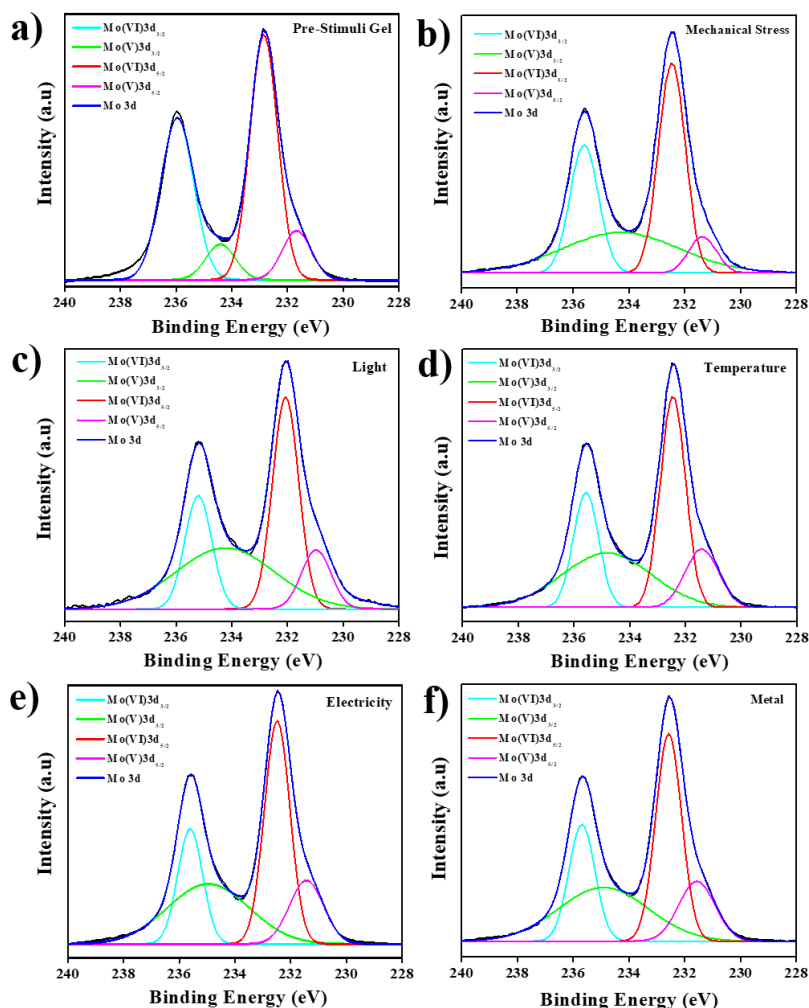


Figure 3.16. Deconvoluted XPS spectra of PMA-GMP xerogel (a) Before exposure to stimuli, (b) after exposure to mechanical stress, (c) after exposure to visible light, (d) after exposure to elevated temperature of 90 °C, (e) after exposed to electricity, and (f) after exposed to Cu metal.

3.3 Conclusion

In conclusion, a mechanically robust, thermoreversible hydrogel could be spontaneously obtained simply by mixing aqueous solutions of commercially available POM (phosphomolybdic acid) and (GMP) guanosine monophosphate, a small biomolecule. This hydrogel shows

chromic responsiveness to multiple stimuli such as mechanical stress, light, temperature, electricity, metals, pH, iodide, and biologically relevant thiols owing to the redox property of PMA. Unlike bare PMA, the hydrogel displayed changes in optical properties under visible light and mild temperature. The conductive nature of the hydrogel also enabled the development of a two-layered electrochromic device, simplifying the process by eliminating the electrodeposition step and reducing resource consumption as compared to traditional five-layered devices. The simplicity of fabrication of the hydrogel, biocompatibility, and responsiveness to multi-stimuli make it highly appealing for smart device applications.

3.4 Experimental Section

3.4.1 Materials

Phosphomolybdic acid hydrate $H_3[P(Mo_3O_{10})_4]_{aq}$ and 2,3-Dimercaptosuccinic acid was purchased from Sigma Aldrich. Guanosine-5'-monophosphate disodium salt hydrate (Na_2 -GMP), Glutathione reduced ($C_{10}H_{17}N_3O_6S$), Sodium Iodide (NaI), and Sodium Chloride (NaCl) were purchased from Sisco Research Laboratory (SRL). Sodium Bromide (NaBr) was purchased from Alfa-Aesar. L-cysteine was purchased from HIMEDIA. Milli-Q was purchased from Merck, India. All the chemicals were used as purchased with no further purification.

3.4.2. Synthesis of the hydrogel

60 mM phosphomolybdic acid (PMA) and 180 mM of guanosine monophosphate (GMP) were added to milli-Q in a vial while kept on continuous stirring for 2-5 minutes at 65 °C. The obtained clear yellow solution was allowed to rest and it spontaneously formed a hydrogel upon cooling to room temperature.

3.4.3 Instrumentation

UV-Vis and Circular Dichroism (CD) studies were recorded on a Perkin Elmer UV-Vis-NIR spectrophotometer (Model: Lambda 1050) and JASCO J-815 spectropolarimeter using a quartz cuvette of path length 1

mm respectively. Field emission scanning electron microscopy (FESEM) images were taken on Carl Zeiss Supra 55 instruments after Au coating. Transmission Electron microscope (TEM) images were taken from the electron microscope of model JEM-2100 at an accelerating voltage of 200 kV. Rheological studies were done using an Anton Paar Physica MCR 301 rheometer with parallel plate geometry (diameter 25 mm). A dynamic strain sweep experiment was performed using a constant frequency of 10 rad s⁻¹. The dynamic frequency sweep of the hydrogel was measured as a function of frequency in the range of 0.1–500 rad s⁻¹ with a constant strain value of 1%. The thixotropic loop test was carried out at a constant frequency of 10 rad s⁻¹, and the applied strain was changed from 0.1% to 200%. Powder X-ray diffraction patterns (PXRD) of the xerogel were recorded on a Rigaku Smartlab, Automated Multipurpose X-ray diffractometer with Cu K α source (the wavelength of the X-rays was 0.154 nm). FTIR study of xerogel was done on Bruker Alpha II Platinum ATR. ¹H and ³¹P NMR spectra were recorded using a 500 MHz Bruker AV500 NMR instrument at 298 K using D₂O as solvent. X-ray photoelectron spectroscopy (XPS) study for the xerogels was carried out on ThermoScientific NEXA Surface analyser.

3.4.4. Characterization Methods

Field Emission Scanning Electron Microscopy (FESEM). The hydrogels were diluted up to 250 times in milli Q water and 20 μ l of it was drop-casted on a clean coverslip and left for air drying for 24 hours. The drop-casted samples were then coated with Au and imaged under the electron microscope.

UV-visible spectroscopy. UV-visible spectra of the hydrogel, PMA, and GMP were recorded at a concentration of 0.025 mM each using a 1 cm path length cuvette. Titration spectra were performed upon successive addition of 0.025 mM GMP to a 0.025 mM aqueous solution of POM at a variable mole ratio.

Circular Dichroism (CD). The CD spectra of the hydrogels, POM, and GMP were recorded by diluting the samples up to 1 mM using a quartz

cell of 1 mm path length with a scan range of 200-300 nm. The spectra were recorded with a slit width of 1 mm and a scan rate of 50 nm/s. Titration spectra were performed upon successive addition of 1 mM GMP to a 1 mM aqueous solution of PMA at a variable mole ratio.

Nuclear Magnetic Resonance (^1H and ^{31}P). The NMR studies were performed for PMA, GMP, and PMA-GMP at similar concentrations as for hydrogel (PMA: 60 mM, GMP: 180 mM, and PMA-GMP 60:180 mM). To study the NMR of the hydrogel, it was converted to sol owing to its thermoreversible property and then transferred into the NMR tube.

Rheological Studies. Rheological studies were performed at room temperature (25 °C) using a parallel plate (25 mm diameter). A small amount of the gel was scooped out with the help of a spatula and kept on the plate for measurement. The strain sweep measurements of the hydrogels were carried out at a constant frequency (10 rad s^{-1}). The frequency sweep studies were performed in a 0.1–500 rad s^{-1} frequency range maintaining a constant strain of 1%. For the thixotropic loop studies, the strain was varied from 0.1% to 200% at an applied frequency of 10 rad s^{-1} . Successive low and high strains were applied at a period of 100 seconds.

Universal Testing Machine. The hydrogel was moulded into a rectangular shape. The gauge length was 3 mm and the width was 18 mm. The stretching speed was 15 mm/min.

3.4.5. UV-visible studies for chromism

The hydrogel was triggered by various stimuli such as mechanical stress (ground in mortar pestle for 10 mins), visible light (exposed to 3 white LEDs of 30 W in a dark box for 3 hrs), temperature (90 °C, 50 min), metals (various metal strips such as Fe, Cu, Zn, Pb, Sn, and Mg were dipped into the hydrogel for few minutes). Then UV-vis spectra of the hydrogel before any exposure to stimuli and after exposure to stimuli were recorded by sandwiching 125 μl of the hydrogel in between two quartz glasses with the help of double-sided adhesive.

To prepare an electrochromic device, a thin layer of hydrogel was prepared by pouring 200 μl (in liquid state) onto a mold of dimension 1.5 cm x 3 cm. Then the layer of hydrogel was simply layered on an ITO plate from one end and was supported over a glass slide over the other end (the non-conductive side of the ITO adhered to the glass slide using an adhesive) such that the hydrogel itself acted as an electrode now.

The hydrogel was oxidized back to a yellow color by adding H_2O_2 to the blue hydrogel except in the case of electrochromism where a reversible cycle was obtained by providing reverse bias.

3.4.6. Cyclic Voltammetry

The cyclic voltammogram was recorded using a Swagelok cell with two parallel stainless-steel electrodes. The data was recorded on Metrohm Autolab potentiostat (PGSTAT302 N) within a range of -1.5 V to +1.5 V at a scan rate of 50 mV s^{-1} .

3.4.7. Conductivity Measurement

The conductivity of synthesized PMA-GMP hydrogel was measured by the electrochemical impedance spectroscopy (EIS) method using a Swagelok cell with two parallel stainless-steel electrodes. The EIS data were recorded on Metrohm Autolab potentiostat (PGSTAT302 N) within the 0.1 Hz to 10 kHz frequency range at room temperature. The conductivity of hydrogel was calculated using the following Equation:

$$\sigma = L / (R_{ct} * A)$$

Where σ is the conductivity, A is the area, L stands for the height of the gel in the cell, and RCT is the resistance of the gel.

3.4.8. X-ray photoelectron spectroscopy (XPS).

XPS was recorded for Mo in the case of pre-stimuli xerogel and xerogel after exposure to stress, light, temperature, electricity, and metal (Cu). The percentage for reduced Mo^{V} was calculated by the ratio of the area under the curve due to Mo^{V} to the area under the curve for total Mo present.

3.5. References

1. Bandyopadhyay J., Sinha Ray S. (2012), 10 - Clay-containing poly(ethylene terephthalate) (PET)-based polymer nanocomposites. In *Advances in Polymer Nanocomposites* Woodhead Publishing Series in Composites Science and Engineering., F. Gao, ed. (Woodhead Publishing), pp. 277–320 (DOI: 10.1533/9780857096241.2.277).
2. Lampert C. M. (2004), Chromogenic smart materials. *Mater. Today* 7, 28–35 (DOI: 10.1016/S1369-7021(04)00123-3).
3. Seok H., Son S., Cho J. *et al.* (2022), Chromism-Integrated Sensors and Devices for Visual Indicators. *Sensors* 22, 4288 (DOI: 10.3390/s22114288).
4. Cannavale A. (2020), Chromogenic Technologies for Energy Saving. *Clean Technol.* 2, 462–475 (DOI: 10.3390/cleantechnol2040029).
5. Li S. -L., Han M., Zhang Y. *et al.* (2019), X-ray and UV Dual Photochromism, Thermochromism, Electrochromism, and Amine-Selective Chemochromism in an Anderson-like Zn_7 Cluster-Based 7-Fold Interpenetrated Framework. *J. Am. Chem. Soc.* 141, 12663–12672 (DOI: 10.1021/jacs.9b04930).
6. Sun C., Yu X. -Q., Wang M. -S., Guo, G. -C. (2019), A Smart Photochromic Semiconductor: Breaking the Intrinsic Positive Relation Between Conductance and Temperature. *Angew. Chem. Int. Ed.* 58, 9475–9478 (DOI: 10.1002/anie.201904121).
7. Radha G., Roy S., Chakraborty C., Aggarwal H. (2022), Electrochromic and photochromic behaviour in a single metal–organic framework containing a redox-active linker. *Chem. Commun.* 58, 4024–4027 (DOI: 10.1039/D2CC00288D).
8. Duan Y., Waerenborgh J. C., Clemente-Juan J. M., Giménez-Saiz C., Coronado E. (2016), Light-induced decarboxylation in a photo-

- responsive iron-containing complex based on polyoxometalate and oxalato ligands. *Chem. Sci.* 8, 305–315 (DOI: 10.1039/C6SC01919F).
9. Yu S., Tian A., Lu Q., Xu X., Ma S., Wang X., Wang Z. (2023), Polyoxometalate–Viologen Thermochromic Hybrids for Organic Amine Detectors and Memristors with Temperature-Regulating Resistance Switching Characteristics. *Inorg. Chem.* 62, 1549–1560 (DOI: 10.1021/acs.inorgchem.2c03746).
 10. Wang S. -M., Hwang J., Kim E. (2019), Polyoxometalates as promising materials for electrochromic devices. *J. Mater. Chem. C* 7, 7828–7850 (DOI: 10.1039/C9TC01722D).
 11. Wang S. -M., Jin Y. -H., Zhou L., Wang K. -H., *et al.* (2023), Hydrogen-Bonded Organic Framework-Polyoxometalate-Based System for Electrochromic Devices. *ACS Appl. Mater. Interfaces* 15, 56242–56252. (DOI: 10.1021/acsami.3c11948).
 12. Wales D. J., Cao Q., Kastner K., Karjalainen E., Newton G. N., Sans V. (2018), 3D-Printable Photochromic Molecular Materials for Reversible Information Storage. *Adv. Mater.* 30, 1800159. (DOI: 10.1002/adma.201800159).
 13. Zhang G., Yang W., Yao, J. (2005), Thermally Enhanced Visible-Light Photochromism of Phosphomolybdic Acid–Polyvinylpyrrolidone Hybrid Films. *Adv. Funct. Mater.* 15, 1255–1259 (DOI: 10.1002/adfm.200500179).
 14. Zhang Y. -J., Shen F. -J., Li Y. -J., Pang X. -L. *et al.* (2020), A Zr-cluster based thermostable, self-healing and adaptive metallogel with chromogenic properties responds to multiple stimuli with reversible radical interaction. *Chem. Commun.* 56, 2439–2442 (DOI: 10.1039/D0CC00241K).
 15. Saengdet P. M., Ogawa M. (2022), Mechanochromic luminescence of a bionanocomposite hydrogel. *Chem. Commun.* 58, 3278–3281 (DOI: 10.1039/D1CC07249H).

16. Draper E. R., Adams, D.J. (2017), Low-Molecular-Weight Gels: The State of the Art. *Chem* 3, 390–410 (DOI: 10.1016/j.chempr.2017.07.012).
17. Kruse J. -H., Langer M., Romanenko I., Trentin I. *et al.* (2022), Polyoxometalate-Soft Matter Composite Materials: Design Strategies, Applications, and Future Directions. *Adv. Funct. Mater.* 32, 2208428. (DOI: 10.1002/adfm.202208428).
18. Zhao Z., Liu J., Wu M. *et al.* (2024), A Soft, Adhesive Self-Healing Naked-Eye Strain/Stress Visualization Patch. *Adv. Mater.* 36, 2307582. (DOI: 10.1002/adma.202307582).
19. Macdonell A., Johnson N. A. B., Surman A. J., Cronin L. (2015), Configurable Nanosized Metal Oxide Oligomers via Precise “Click” Coupling Control of Hybrid Polyoxometalates. *J. Am. Chem. Soc.* 137, 5662–5665 (DOI: 10.1021/jacs.5b02466).
20. Han Y., Xiao Y., Zhang Z., Liu B. *et al.* (2009), Synthesis of Polyoxometalate–Polymer Hybrid Polymers and Their Hybrid Vesicular Assembly. *Macromolecules* 42, 6543–6548 (DOI: 10.1021/ma9011686).
21. Lv C., Khan R. N. N., Zhang J., Hu J., Hao J., Wei, Y. (2013), Bifunctionalization of Polyoxometalates with Two Different Organoimido Ligands. *Chem. – Eur. J.* 19, 1174–1178 (DOI: 10.1002/chem.201203204).
22. Proust A., Matt B., Villanneau R. *et al.* (2012), Functionalization and post-functionalization: a step towards polyoxometalate-based materials. *Chem. Soc. Rev.* 41, 7605–7622 (DOI: 10.1039/C2CS35119F).
23. Chakraborty S., Keightley A., Dusevich V., Wang Y., Peng Z. (2010), Synthesis and Optical Properties of a Rod–Coil Diblock Copolymer with Polyoxometalate Clusters Covalently Attached to the Coil Block. *Chem. Mater.* 22, 3995–4006 (DOI: 10.1021/cm1007075).

24. Gao J., Miao J., Li Y. *et al.* (2015), Dye-sensitized polyoxometalate for visible-light-driven photoelectrochemical cells. *Dalton Trans.* 44, 14354–14358 (DOI: 10.1039/C5DT01769F).
25. Sun N., Wu A., Yu Y., Gao X., Zheng, L. (2019), Polyoxometalate-Based Photochromic Supramolecular Hydrogels with Highly Ordered Spherical and Cylindrical Micellar Nanostructures. *Chem. – Eur. J.* 25, 6203–6211 (DOI: 10.1002/chem.201900478).
26. He P., Xu B., Liu H., He S. *et al.* (2013). Polyoxometalate-based Supramolecular Gel. *Sci. Rep.* 3, 1833 (DOI: 10.1038/srep01833).
27. Lin C. -G., Fura G. D., Long Y., Xuan W., Song, Y. F. (2017), Polyoxometalate-based supramolecular hydrogels constructed through host–guest interactions. *Inorg. Chem. Front.* 4, 789–794 (DOI: 10.1039/C7QI00030H).
28. Wei H., Du S., Liu Y. *et al.* (2014), Tunable, luminescent, and self-healing hybrid hydrogels of polyoxometalates and triblock copolymers based on electrostatic assembly. *Chem. Commun.* 50, 1447–1450 (DOI: 10.1039/C3CC48732F).
29. Chakraborty A., Dash S., Thakur N. *et al.* (2024), Polyoxometalate-Guanosine Monophosphate Hydrogels with Haloperoxidase-like Activity for Antibacterial Performance. *Biomacromolecules* 25, 104–118 (DOI: 10.1021/acs.biomac.3c00845).
30. Du X., Zhou J., Shi J., Xu B. (2015), Supramolecular Hydrogelators and Hydrogels: From Soft Matter to Molecular Biomaterials. *Chem. Rev.* 115, 13165–13307 (DOI: 10.1021/acs.chemrev.5b00299).
31. Agarwal V., Varshney N., Singh S. *et al.* (2023), Cobalt-Adenosine Monophosphate Supramolecular Hydrogel with pH-Responsive Multi-Nanozymatic Activity. *ACS Appl. Bio Mater.* 6, 5018–5029 (DOI: 10.1021/acsabm.3c00719).

32. Stefan L., Monchaud D. (2019), Applications of guanine quartets in nanotechnology and chemical biology. *Nat. Rev. Chem.* 3, 650–668 (DOI: 10.1038/s41570-019-0132-0).
33. Ngo V. A., Di Felice R., Haas S. (2014), Is the G-Quadruplex an Effective Nanoconductor for Ions? *J. Phys. Chem. B* 118, 864–872 (DOI: 10.1021/jp408071h).
34. Thakur, N., Chaudhary, A., Chakraborty, A., Kumar, R., Sarma, T.K. (2021), Ion Conductive Phytic Acid-G Quadruplex Hydrogel as Electrolyte for Flexible Electrochromic Device. *ChemNanoMat* 7, 613–619 (DOI: 10.1002/cnma.202100072).
35. Kulikov V., Johnson N. A. B., Surman A. J. *et al.* (2017), Spontaneous Assembly of an Organic–Inorganic Nucleic Acid Z-DNA Double-Helix Structure. *Angew. Chem. Int. Ed.* 56, 1141–1145 (DOI: 10.1002/anie.201606658).
36. Thakur, N., Sharma, B., Bishnoi, S. *et al.* (2019), Biocompatible Fe³⁺ and Ca²⁺ Dual Cross-Linked G-Quadruplex Hydrogels as Effective Drug Delivery System for pH-Responsive Sustained Zero-Order Release of Doxorubicin. *ACS Appl. Bio Mater.* 2, 3300–3311 (DOI: 10.1021/acsabm.9b00334).
37. Olejko L., Dutta A., Shahsavari K., Bald I. (2022), Influence of Different Salts on the G-Quadruplex Structure Formed from the Reversed Human Telomeric DNA Sequence. *Int. J. Mol. Sci.* 23, 12206 (DOI: 10.3390/ijms232012206).
38. Goncharova I., Novotná J., Urbanová M. (2012). Stacked and continuous helical self-assemblies of guanosine monophosphates detected by vibrational circular dichroism. *Anal. Bioanal. Chem.* 403, 2635–2644 (DOI: 10.1007/s00216-012-6014-7).
39. Pieber M., Reitboeck H. *et al.* (1970), Magnetic Resonance Studies on a Gel of Guanylic Acid and a Guanosine Monophosphate-

- Copper(II) Complex. *J. Biol. Chem.* 245, 4141–4143 (DOI: 10.1016/S0021-9258(18)62895-9).
40. Kaucher M. S., Harrell W. A., Davis J. T. (2006), A Unimolecular G-Quadruplex that Functions as a Synthetic Transmembrane Na⁺ Transporter. *J. Am. Chem. Soc.* 128, 38–39 (DOI: 10.1021/ja056888e).
41. Kumar A., Khandelwal M., Gupta S. K., Kumar V., Rani R. (2019), Chapter 6 - Fourier transform infrared spectroscopy: Data interpretation and applications in structure elucidation and analysis of small molecules and nanostructures. In *Data Processing Handbook for Complex Biological Data Sources*, G. Misra, ed. (Academic Press), pp. 77–96 (DOI: 10.1016/B978-0-12-816548-5.00006-X).
42. Zhang Q., Yue C., Pu Q., Yang T., Wu Z., Zhang Y. (2019), Facile Synthesis of Ferric-Modified Phosphomolybdic Acid Composite Catalysts for Biodiesel Production with Response Surface Optimization. *ACS Omega* 4, 9041–9048 (DOI: 10.1021/acsomega.9b01037).
43. Yamase T. (1998), Photo- and Electrochromism of Polyoxometalates and Related Materials. *Chem. Rev.* 98, 307–326, (DOI: 10.1021/cr9604043).
44. Bang I. (1910), Examination of the guanyle acid. *Biochem. Z* 26, 293–311.
45. Wu G., Kwan I. C. M., Yan Z., Huang Y., Ye E. (2017), On the Helical Structure of Guanosine 5'-Monophosphate Formed at pH 5: Is It Left- or Right-Handed? *J. Nucleic Acids* 2017, 6798759 (DOI: 10.1155/2017/6798759).
46. Zhang J., Li X., Sun X., Song A., Tan Y., Hao J. (2018), GMP-quadruplex-based hydrogels stabilized by lanthanide ions. *Sci. China Chem.* 61, 604–612 (DOI: 10.1007/s11426-017-9187-x).

47. Gellert M., Lipsett M. N., Davies, D. R. (1962), Helix formation by guanylic acid. *Proc. Natl. Acad. Sci.* 48, 2013–2018 (DOI: 10.1073/pnas.48.12.2013).
48. Umesh, Sarkar S., Bera S., Moitra P., Bhattacharya S. (2023), A self-healable and injectable hydrogel for pH-responsive doxorubicin drug delivery *in vitro* and *in vivo* for colon cancer treatment. *Mater. Today Chem.* 30, 101554 (DOI: 10.1016/j.mtchem.2023.101554).
49. Yoneda J. S., de Araujo D. R., Sella F. *et al.* (2021), Self-assembled guanosine-hydrogels for drug-delivery application: Structural and mechanical characterization, methylene blue loading and controlled release. *Mater. Sci. Eng. C* 121, 111834 (DOI: 10.1016/j.msec.2020.111834).
50. Kozhevnikov I. V. (1998), Catalysis by Heteropoly Acids and Multicomponent Polyoxometalates in Liquid-Phase Reactions. *Chem. Rev.* 98, 171–198 (DOI: 10.1021/cr960400y).
51. Zhao Z., Li Y., Wang H., Shan Y. *et al.* (2023), Ultra-Tough Self-Healing Hydrogel via Hierarchical Energy Associative Dissipation. *Adv. Sci.* 10, 2303315 (DOI: 10.1002/advs.202303315).
52. Fuhrer R., Athanassiou E. K., Luechinger N. A., Stark W. J. (2009). Crosslinking Metal Nanoparticles into the Polymer Backbone of Hydrogels Enables Preparation of Soft, Magnetic Field-Driven Actuators with Muscle-Like Flexibility. *Small* 5, 383–388 (DOI: 10.1002/sml.200801091).
53. Vo K. T. K., Bui L. T. T., Oko G. E. *et al.* (2018), Validation of UV - VIS Spectrophotometry for Phosphorous Molybdenum Determination in Soils of Vietnam. *Chem. Sci. Int. J.*, 1–15 (DOI: 10.9734/CSJI/2018/42128).
54. Nagul E. A., McKelvie I. D., Worsfold P., Kolev S. D. (2015), The molybdenum blue reaction for the determination of orthophosphate

- revisited: Opening the black box. *Anal. Chim. Acta* 890, 60–82 (DOI: 10.1016/j.aca.2015.07.030).
55. Noguchi T., Chikara C., Kuroiwa K. *et al.* (2011), Controlled morphology and photoreduction characteristics of polyoxometalate(POM)/lipid complexes and the effect of hydrogen bonding at molecular interfaces. *Chem. Commun.* 47, 6455–6457 (DOI: 10.1039/C1CC10231A).
56. Tao K., Makam P., Aizen R., Gazit E. (2017), Self-assembling peptide semiconductors. *Science* 358, eaam9756 (DOI: 10.1126/science.aam9756).
57. de Souza Freitas H. A., Chaves Neto A. M. J., de Sousa F. F. *et al.* (2021). Hydration-dependent band gap tunability of self-assembled phenylalanyl tryptophan nanotubes. *Phys. E Low-Dimens. Syst. Nanostructures* 134, 114910 (DOI: 10.1016/j.physe.2021.114910).
58. Anastassopoulou J., Theophanides T. (2002), Magnesium–DNA interactions and the possible relation of magnesium to carcinogenesis. Irradiation and free radicals. *Crit. Rev. Oncol. Hematol.* 42, 79–91 (DOI: 10.1016/S1040-8428(02)00006-9).
59. Wu W., Wu X. -Y., Wang S. -S., Lu C. -Z. (2020), Phosphomolybdic Acid-Bipolar Membrane: An Efficient and Reversible Coupling for Alkaline Water Electrolysis. *ACS Sustain. Chem. Eng.* 8, 18528–18534. (DOI: 10.1021/acssuschemeng.0c06444).
60. Lei M., Gao Q., Zhou K. *et al.* (2021). Catalytic degradation and mineralization mechanism of 4-chlorophenol oxidized by phosphomolybdic acid/H₂O₂. *Sep. Purif. Technol.* 257, 117933 (DOI: 10.1016/j.seppur.2020.117933).
61. Zeng Q., Guo S., Sun Y., Li Z., Feng W. (2020). Protonation-Induced Enhanced Optical-Light Photochromic Properties of an Inorganic-Organic Phosphomolybdic Acid/Polyaniline Hybrid Thin Film. *Nanomaterials* 10, 1839 (DOI: 10.3390/nano10091839).

62. Ilbeygi H., Kim S., Kim I. Y. (2022), Super-reductive mesoporous phosphomolybdate with high crystallinity and its excellent performance for Li-ion battery application. *J. Mater. Chem. A* 10, 12132–12140 (DOI: 10.1039/D1TA10960J).
63. Ohisa S., Kagami S., Pu Y. -J., *et al.* (2016). A Solution-Processed Heteropoly Acid Containing MoO₃ Units as a Hole-Injection Material for Highly Stable Organic Light-Emitting Devices. *ACS Appl. Mater. Interfaces* 8, 20946–20954 (DOI: 10.1021/acsami.6b06723)

Chapter 4

Zinc-histidine complex hydrogel with GMP, a supramolecular approach to structurally mimic carbonic anhydrase enzyme

4.1. Introduction

Carbonic anhydrases (CAs), are one of the most crucial metalloenzymes for their ability to catalyze the hydration of carbon dioxide to bicarbonate with high efficiency.^{1,2} It is the second most abundant protein in red blood cells next to hemoglobin³ and plays a very important role in multiple physiological functions, such as pH regulation, ion transport, bone resorption, and the secretion of gastric, cerebrospinal, and pancreatic fluids.^{4,5} CA is also gaining an opportunity to be explored as an important tool for industrial applications such as CO₂ remediation. Excessive emission of greenhouse gases such as CO₂ has caused a rise in temperature over the past several decades and is leading to serious climate change and global warming cases. Given the urgency of the issue, CA has become increasingly popular as a biocatalyst for capturing CO₂ owing to its high efficiency.⁶⁻⁸ Additionally, CA also exhibits esterase activity thus finding application in the treatment of industrial pollutants.⁹⁻¹¹ Despite the promising potential of CA, significant drawbacks such as the high cost of synthesis or isolation, thermal instability, and sensitivity to the environment limit its application outside physiological conditions.¹²⁻¹⁴ Thus, it is of utmost importance to develop CA analogs that can structurally mimic or replicate the active site of the metalloenzyme. The active site of carbonic anhydrase (CA) features a divalent zinc ion coordinated in a tetrahedral geometry by three histidine groups and a hydroxide (or water) molecule deep-seated in the hydrophobic cavity created by protein antiparallel β -strands.^{15,16} Developing structural mimics of enzyme active sites is important from the activity perspective and will help better understand the synthesis of artificial enzymes.

There have been some reports on modeling the active site of the CA by synthesizing tetrahedral Zn complexes by designing suitable ligands¹⁷⁻¹⁹ or by designing a tetrahedrally coordinated Zn-triazole metal-organic framework (MOF).^{3,20-23} While these biomimetic synthetic zinc-coordinated complexes and metal-organic frameworks show promising results, their synthesis involves complex methods with extensive ligand modifications and structural limitations. Small molecule zinc complexes face a major challenge in structurally mimicking the CA enzyme due to the lack of 3D geometry of protein, often leading to dimerization of the zinc complex resulting in loss of activity. MOFs can solve this drawback through structural regulation; however, they often do not remain stable under aqueous medium or physiological conditions and are typically composed of rigid materials that lack the structural flexibility of CA proteins.²⁴⁻²⁶ The flexibility provided by the tertiary protein frame plays a role as major as the active site of the enzyme. They facilitate the access of substrate to the active site or product release, and other functions such as mediating the transfer of protons, etc.²⁷ Bin Fan et. al. proposed a hydrogel polymer of tetrahedrally coordinated Zn-vinyl imidazole complex with N-tert-butyl acrylamide (TBAm) as the hydrophobic monomer and N-isopropylacrylamide (NIPAm) as the backbone inert monomer to emulate the flexibility of natural enzyme.²⁶ Even though loading the Zn tetrahedral complex in hydrogel provides flexibility, it also requires a tedious synthetic route and two monomers to provide the amphiphilic property of the protein chain. In contrast, metal complexes surrounded by supramolecular assemblies can provide us with a closer structural mimic since native enzymes form well-organized tertiary structures through non-covalent interactions among the protein chain creating a specific environment around the active site in the hydrophobic pocket. Along with providing structural similarity to the natural enzyme, self-assembled systems are also a simpler route from the fabrication point of view.^{28,29} Despite all the advantages of the supramolecular approach, there are still very few reports on self-assembled structural mimics of CA which could be due to the challenge posed by small molecules in creating an appropriate coordination sphere

around the metal center thus inhibiting the successful structural imitation of natural enzymes.

Nucleotides are well-known low molecular weight gelators (LMWG) that self-assemble and form supramolecular, well-defined complex hierarchal fibrillar structures like proteins.³⁰⁻³⁴ Additionally, nucleotides like proteins are also amphiphilic thus, nucleotide self-assemblies can imitate the hydrophobic and hydrophilic phase interactions of the protein tertiary structure. Guanosine monophosphate (GMP) is important as both Watson-Crick and Hoogsteen faces are available for hydrogen bonding leading to the formation of various types of assemblies such as dimer, G-Quartet, ribbon, sheet, etc.³⁴⁻³⁸ This inspired us to exploit GMP, to create a self-assembled structure around the metal active site that could mimic the tertiary protein environment of the natural CA enzymes.

Herein, we present a state-of-the-art approach to design a tetrahedrally coordinated (histidine)₃Zn-OH₂ complex (ZnH) that has been stabilized within a self-assembled guanosine monophosphate (GMP)-based fibrillar network through non-covalent interactions. The facile fabrication method required no synthetic steps or modified ligand environments. Instead, we directly utilized pristine L-histidine and guanosine monophosphate disodium salt with divalent Zn ions for self-assembly. This tetrahedral zinc-histidine complex accurately replicates the N₃Zn-OH moiety of the enzyme's active site, while the self-assembled GMP provides a confined environment that mimics the cross β -sheet secondary amyloid structure of the natural enzyme. The ZnHG hydrogel exhibited both ester hydrolysis and CO₂ hydration activity in the aqueous medium. Further CO₂ sequestration was performed via biomineralization of various metal salts with complex architectures. Biomineralization was further exploited for the separation of toxic metal ions from the aqueous medium. To the best of our knowledge, this is the first example of designing a structural mimic that imitates the active center within a nucleotide fibrillar confinement, using pristine

biomolecules as precursors applying a supramolecular self-assembled approach with no synthetic steps.

4.2. Results and Discussion

4.2.1. Synthesis of ZnHG hydrogel

ZnSO₄ salt (25 mM) and Histidine (75 mM) were mixed in a 1:3 ratio in water to obtain a homogeneous mixture, followed by the addition of GMP (75 mM) which upon aging for 7 days at room temperature resulted in a self-assembled hydrogel. The formation of the ZnHG hydrogel was confirmed physically by a ‘vial-inversion’ test (Figure 4.1a).

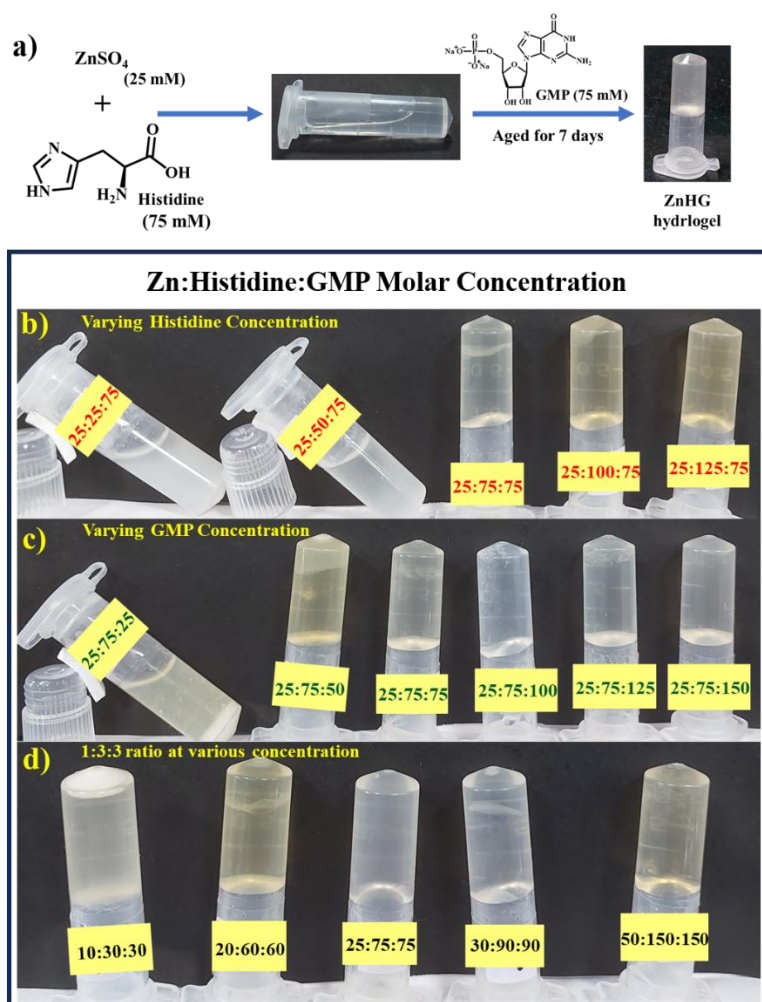


Figure 4.1. (a) Schematic representation of the formation of ZnHG Hydrogel through the intermediate step of ZnH complex, (b-d) Digital image of ZnHG system varying the component ratio (Zn:His:GMP)

Ratio dependency of the gelation was observed by varying the ratio of histidine and GMP (Figure 4.1 b-d). In Figure 4.1b, we observed that gelation formation starts occurring when Zn:Histidine concentration is at 1:3 molar ratio. The best gelation was observed at the 1:3:3 ratio for Zn^{2+} , histidine, and GMP respectively. The critical gelation concentration was 10 mM, 30 mM, and 30 mM for ZnSO_4 , histidine, and GMP respectively (Figure 4.1d). The hydrogel showed excellent thermal stability and did not convert to a sol state even at a high temperature of 95 °C. We also performed a control gelation experiment with only histidine (75 mM) and GMP (75 mM) and no gelation was observed. Hydrogel formation only occurred when GMP was added to the solution of the zinc-histidine complex.

4.2.2. Morphological Evaluation

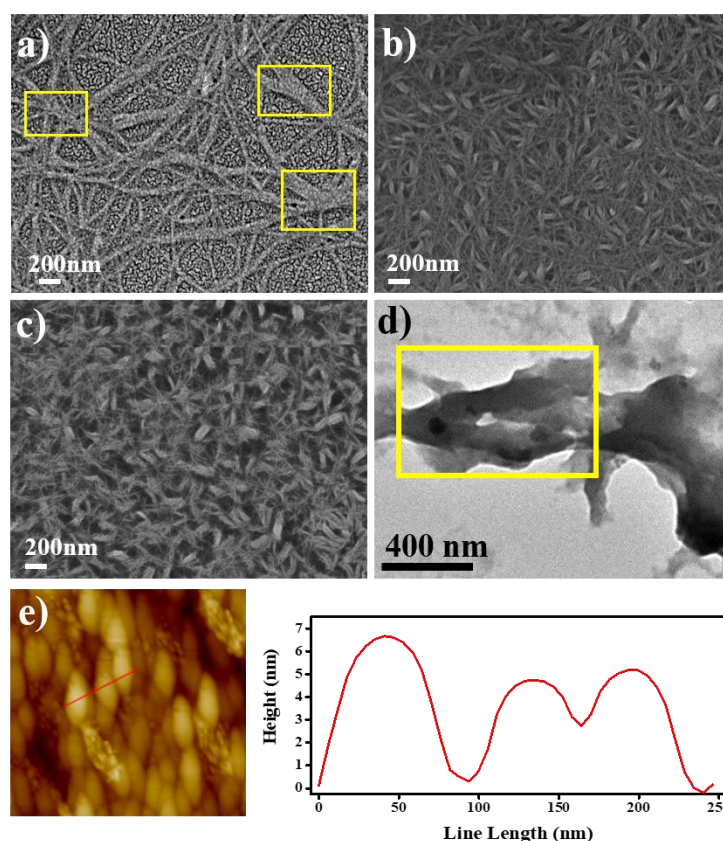


Figure 4.2. (a-c) SEM images of ZnHG supramolecular system for day 2, day 7, and day 14 respectively, (d) TEM image of ZnHG hydrogel, (e) AFM image of the hydrogel.

Various microscopic techniques were used to study the morphology of the ZnHG hydrogel. Time-dependent scanning electron

microscopy (SEM) images for the ZnHG supramolecular assembly were taken for day 2, day 7, and day 14. Day 2 image of the ZnHG system when gelation had not yet taken place, showed fibrillar structures (Figure 4.2a). The average diameter of the fibers was calculated to be 75-100 nm and was several micrometers in length. SEM images for day 7 (Figure 4.2b), by then gelation had occurred, showed a highly entangled dense fibrillar morphology where the fibrils are aggregated by bundling together leading to an apparent thickening of fibers. This aggregation or thickening of fibers is even more evident and uniform when the ZnHG supramolecular system is allowed to age for 14 days (Figure 4.2c). We could see the initiation of the fibril bundling taking place on day 2 image highlighted in the yellow box in Figure 4.2a, which only got more prominent with an increase in the aging time. Transmission electron microscopy (TEM) further reinforced the observation of the fibrillar thickening induced by the interaction of several fibers highlighted by the yellow box in Figure 4.2d. The height of these aggregates was found to be in the range of 4-6 nm from atomic force microscopy (AFM) (Figure 4.2e). Thus, from the microscopic images, it could be observed that the ZnHG strands were bundled up to form the nanofibers, and cross-linking of the fibers effectively resulted in the dense entangled network.

4.2.3. Spectroscopic Characterization.

The UV-visible spectrum of GMP showed a characteristic absorption maximum of 253 nm with a shoulder band of 273 nm (Figure 4.3a). ZnSO₄ salt and histidine did not show any absorption in that region. The UV-visible spectrum for the ZnHG hydrogel showed a hypochromic shift compared to GMP, implying the formation of an ordered secondary assembly.³⁹ Absorption spectra were recorded by varying the concentration ratio of histidine to GMP (Figure 4.3b). From Job's plot, the most suitable stoichiometry for histidine to GMP was found to be at the ratio of 1:1.

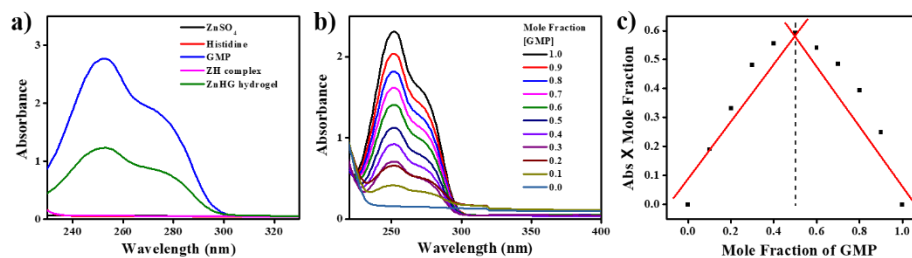


Figure 4.3. (a) UV-visible spectra of $ZnSO_4$, histidine, GMP, ZnH complex, and ZnHG hydrogel, (b) UV-vis spectra upon addition of GMP to ZnH solution at variable concentration ratio, and (c) Job's plot calculated at 253 nm absorbance maxima.

Proton NMR studies were done to study the binding interaction of histidine with Zn to form ZnH complex (Figure 4.4a). The 1H NMR of Histidine showed resonance spectra at 8.14 ppm for H6, 7.09 ppm for H8, 3.87 ppm for H2, and 3.12 ppm for H3,3'.⁴⁰ H5 exhibited an upfield shift from 8.14 to 8.02 ppm on binding with Zn and H8 displayed a very slight shift to 7.06 ppm whereas H2 and H3,3' peaks did not show any significant shift. The 1H NMR result implies that histidine is binding to Zn through N8 of the imidazole group. To further understand the interaction between Zn and histidine, X-ray photoelectron spectroscopy (XPS) was performed (Figure 4.4b, c). The deconvoluted N 1s spectrum consists of peaks at the binding energy of 398.58 and 400.68 eV assigned to -NH (amine group of side chain and N5) and N8 of the imidazole group respectively.⁴¹ On the formation of the ZnH complex, we can see the hump for N8 disappearing. On deconvolution, the peak for N8 is shifted to 399.23 eV and reduced in intensity indicating its role in binding with metal. The peak assigned to -NH in the ZnH complex is observed at 400.68 eV without any shift. Thus, the involvement of N8 from the imidazole group as implied by the NMR was further validated by XPS.

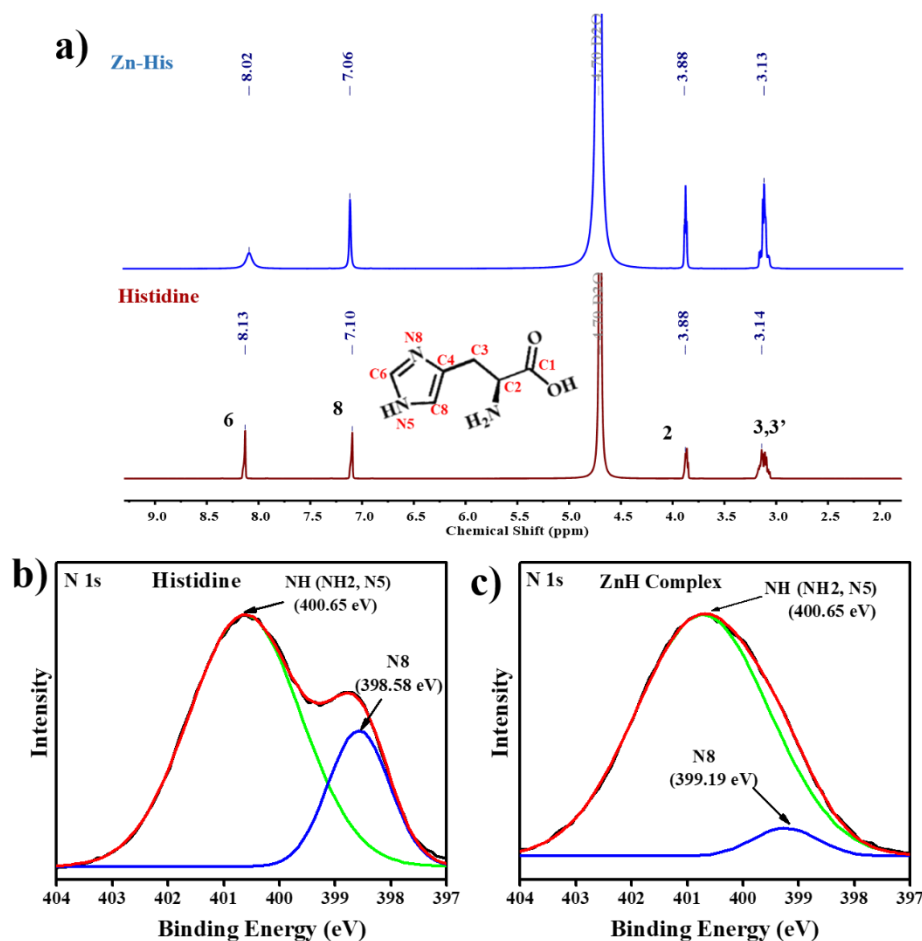


Figure 4.4. (a) ^1H NMR of histidine and Zn-histidine complex, (b, c) Deconvoluted $\text{N } 1s$ XPS spectra for histidine and Zn-histidine complex.

The addition of GMP to the ZnH complex caused the formation of a self-assembled hierarchy leading to gelation. Here we are using a fluorogenic dye, Thioflavin T (ThT) to detect the type of G-motif formed by studying enhancement in its fluorescence intensity in the presence of ZnHG assembly, compared to ThT in its free form (Figure 4.5a). Fluorescence emission was obtained at 475 nm for free ThT and 485 nm for ThT + ZnHG system after excitation at 425 nm. We observed an increase in fluorescence intensity by 2.8 times for the ThT + ZnHG system. This increment in emission intensity upon binding to a self-assembled system can be explained by the restriction of molecular rotor behavior of ThT since it experiences strong non-covalent interactions, upholding the dye in a more rigid and planar form.^{42,43} In Figure 4.5b, the fluorescence increment of ThT in the various types of assemblies is compared. The increment for ZnHG is similar to a duplex system.⁴⁴

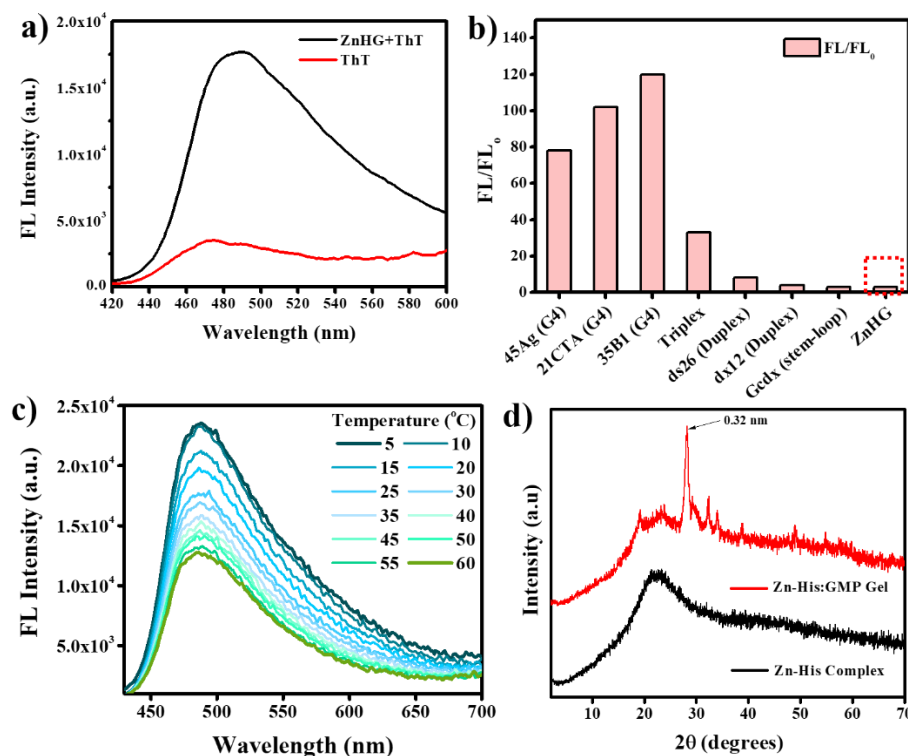


Figure 4.5. (a) Emission spectra for free ThT and ThT in ZnHG system, (b) Comparison of ThT+ZnHG emission with different reported assemblies, (c) Temperature dependent emission spectra of ThT+ZnHG system, and (d) PXRD data of ZnH complex and ZnHG hydrogel.

Temperature-dependent study for ThT in the ZnHG system has been performed. We can see a decrease in the fluorescence with an increase in temperature which is probably due to disturbance in non-covalent interactions with increasing temperature (Figure 4.5c). The PXRD pattern of ZnHG xerogel exhibited a diffraction peak at $2\theta = 28.23^\circ$ corresponding to an interlayer separation of 0.32 nm, which is interplanar spacing for π - π stacking spacing. (Figure 4.5d).^{32,45}

To understand the interacting sites in GMP, the FTIR spectrum for ZnHG xerogel was recorded and compared to GMP (Figure 4.6a). The peak corresponding to the carbonyl group stretching frequency in GMP shifted from 1686 cm^{-1} to 1695 cm^{-1} for the xerogel. The shoulder at 1654 cm^{-1} in GMP attributed to the $-\text{NH}_3$ stretching frequency was also shifted to 1643 cm^{-1} . The involvement of the CO group and amine group suggests GMP duplex formation through the Watson-Crick face. The involvement of the $-\text{NH}_3$ group was further verified by

replacing GMP with inosine monophosphate (IMP) which is structurally similar to GMP, leaving the NH_3 group and no gel formation took place. Also, the peaks at 1062 and 970 cm^{-1} corresponding to antisymmetric and symmetric stretching for PO_3^{2-} group shifted to 1070 and 975 cm^{-1} respectively for the ZnHG xerogel.⁴⁶ This observation indicates the interaction of GMP to ZnH through the hydrogen bonding of the phosphate group. The interaction of the phosphate group in GMP with ZnH complex leading to gelation was also confirmed from the ^{31}P NMR spectrum of the ZnHG by observing an upfield shift from 3.8 ppm to 2.8 ppm compared to free GMP (Figure 4.6b)

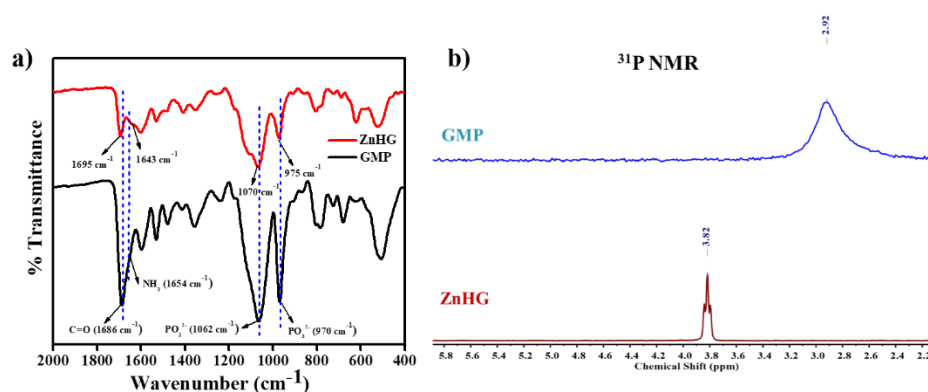


Figure 4.6. (a) FTIR of GMP and ZnHG xerogel and (b) ^{31}P NMR of GMP and ZnHG hydrogel.

The mass spectrum for ZnH consisted of 3 peaks with m/z at 156.0849 , 373.0878 , and 592.0770 corresponding to free histidine, $\text{Zn}(\text{His})_2 + \text{K}^+$, and $\text{Zn}(\text{His})_3(\text{H}_2\text{O}) + 3\text{H}^+ + \text{K}^+$ respectively (Figure 4.7a). $\text{Zn}(\text{His})_2$ is a commonly reported structure where histidine acts as a tridentate ligand, binding to metal through COO^- , NH_3 , and N7 of the imidazole ring and thus forms an octahedral complex.⁴⁷ In $\text{Zn}(\text{His})_3(\text{H}_2\text{O})$, three histidines are bonded to Zinc and one water molecule, which suggests histidine is acting as a monodentate ligand here and binding to Zn through N7 as suggested by NMR and XPS and a tetrahedral structure is obtained that is similar to the active site of the carbonic anhydrase enzyme.

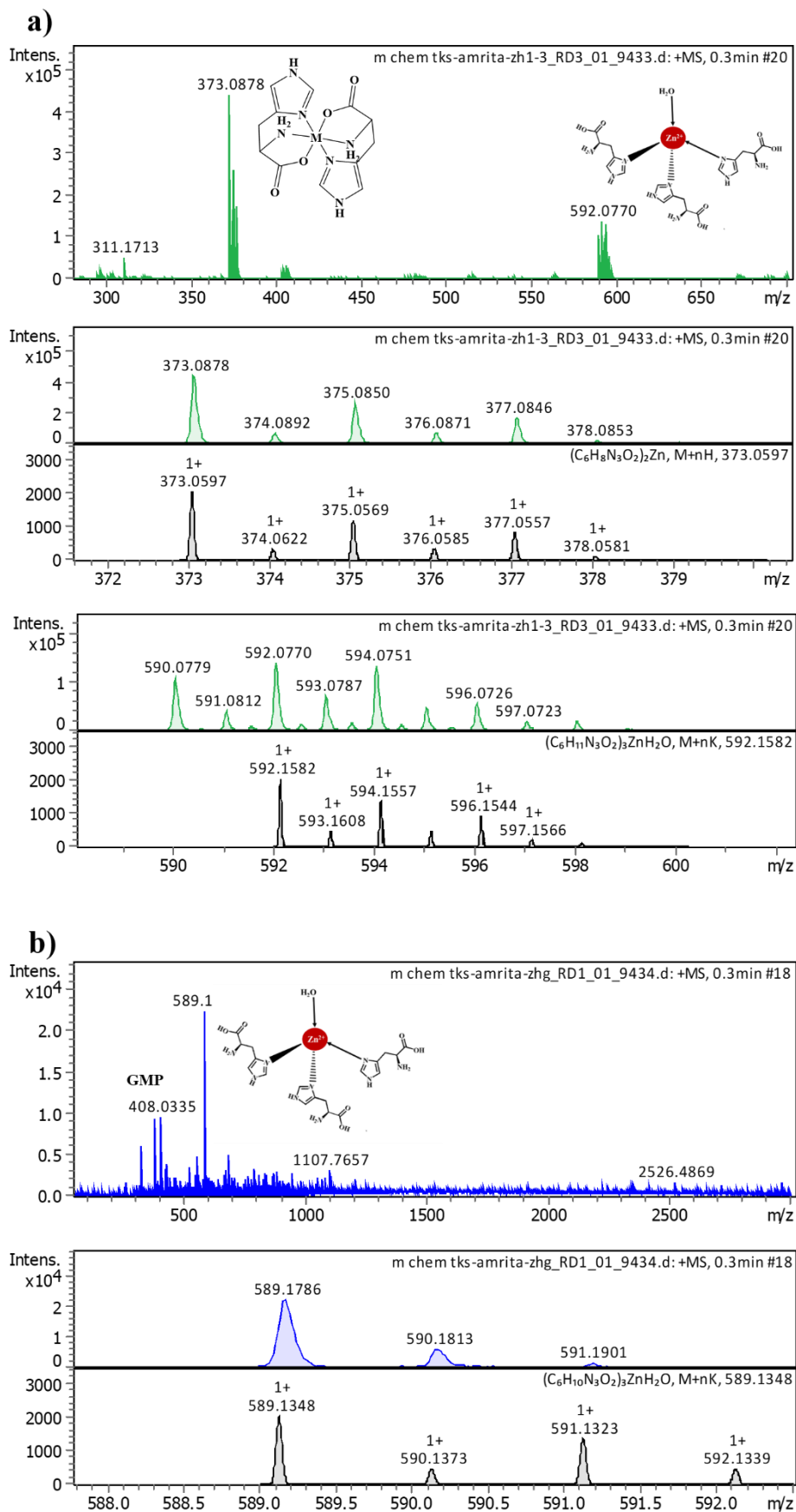


Figure 4.7. LCMS spectra of (a) ZnH complex and (b) ZnHG Hydrogel.

However, in the case of ZnHG hydrogel, the mass spectrum shows 2 peaks with m/z at 408.0335 and 589.1786 corresponding to GMP + H and $\text{Zn}(\text{His})_3(\text{H}_2\text{O}) + \text{K}^+$ respectively (Figure 4.7b). This suggests that the tetrahedral $\text{Zn}(\text{His})_3(\text{H}_2\text{O})$ complex becomes more stable upon gelation with GMP. This increased stability may be due to the fibrillar assembly of GMP, which mimics the crowded environment of protein chains and can form additional non-covalent interactions with the free-binding sites of histidine. The binding of H_2O and N to Zn metal can also be observed from the deconvoluted Zn 2p spectrum of both the ZnH complex and ZnHG hydrogel (Figure 4.8). 2 p splitting into $2p_{3/2}$ and $2p_{1/2}$ is observed for Zn. The peaks at 1047.38 and 1024 eV are assigned to Zn-O bond and peaks at 1045.27 and 1022.2 are assigned to Zn-N, since the binding energy for Zn-O bond is higher than Zn-N bond.^{48,49}

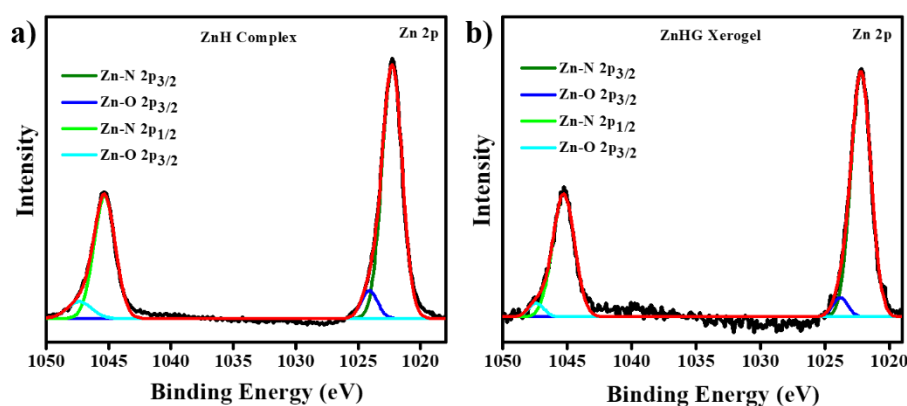


Figure 4.8. Deconvoluted Zn 2p xps spectra of (a) ZnH complex and (b) ZnHG xerogel.

Figure 4.9 illustrates a plausible self-assembled structure, based on the spectroscopic evidence obtained.

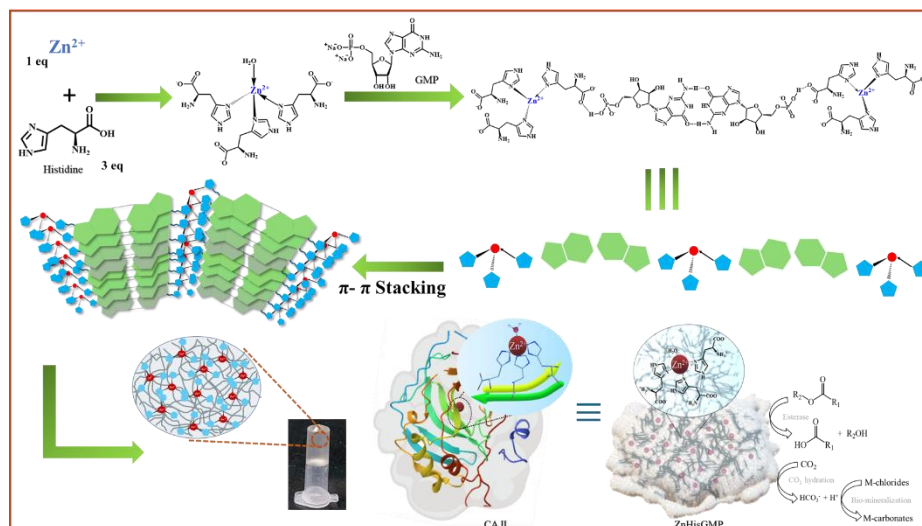


Figure 4.9. A schematic representation of the plausible building mechanism of the ZnHG Hydrogel.

4.2.4. Rheological studies

The viscoelastic nature of the hydrogel was evaluated through rheological studies. The strain and frequency sweep experiment showed us a greater value of storage modulus (G') over loss modulus (G'') over a range, indicating superior elastic property over the viscous property. ZnHG hydrogel was found to have a flow point of 53 % from the strain-sweep experiment (Figure 4.10a, b). The Thixotropy loop test was performed at alternate low and high strains of 1% and 100 % up to five cycles to check the strain-based recoverability of the hydrogel. Significant recovery was observed in the elastic property at the strain of 1% for five consecutive cycles (Figure 4.10c). Steady-state flow curves of the ZnHG demonstrated that the hydrogels showed shear rate dependence and shear thinning behavior (Figure 4.10d).

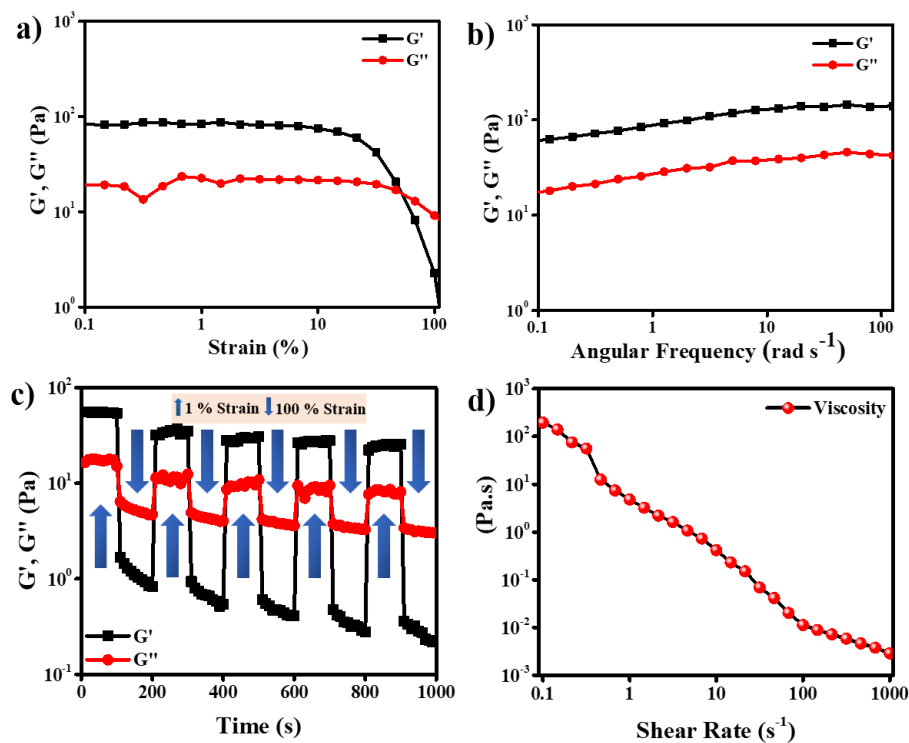


Figure 4.10. (a) Dynamic strain sweep of ZnHG hydrogel, (b) Frequency sweep measurements of ZnHG Hydrogel at a constant strain of 1%, (c) Thixotropic loop measurements for ZnHG hydrogel at a constant angular frequency of 10 rads^{-1} , and (d) Viscosity measurement as a function of shear rate.

4.2.5. Esterase activity of ZnHG xerogel

The carbonic anhydrase (CA) mimicking activity of the ZnHG xerogel was studied using a widely used colorimetric assay, where colorless p-nitrophenyl acetate (pNPA) is hydrolyzed to a yellow product, p-nitrophenol (pNP) (Figure 4.11a). The esterase-like activity of CA is well studied and established due to its mechanistic similarity to CO_2 hydration. Esterase activity for the ZnHG system was tested in a pH 8 phosphate buffer by monitoring the appearance of the absorbance band at 400 nm (Figure 4.11b). Further, time-dependent UV-visible spectra of pNPA hydrolysis were monitored for 25 minutes showing a gradual increment in absorbance with time (Figure 4.11c). Control experiments were performed to compare the activity of the hydrogel with its precursors and ZnH complex (Figure 4.11d). The esterase activity of the xerogel was enhanced by ~ 4 times compared to the free ZnH complex. This increment in ZnHG xerogel reactivity compared to ZnH complex is

probably due to the crowded microenvironment provided by the supramolecular assembly, The proximity of substrate to the active site increases reaction probability and thus reaction rate and this is similar to the environment around the active site in enzymes.²⁹

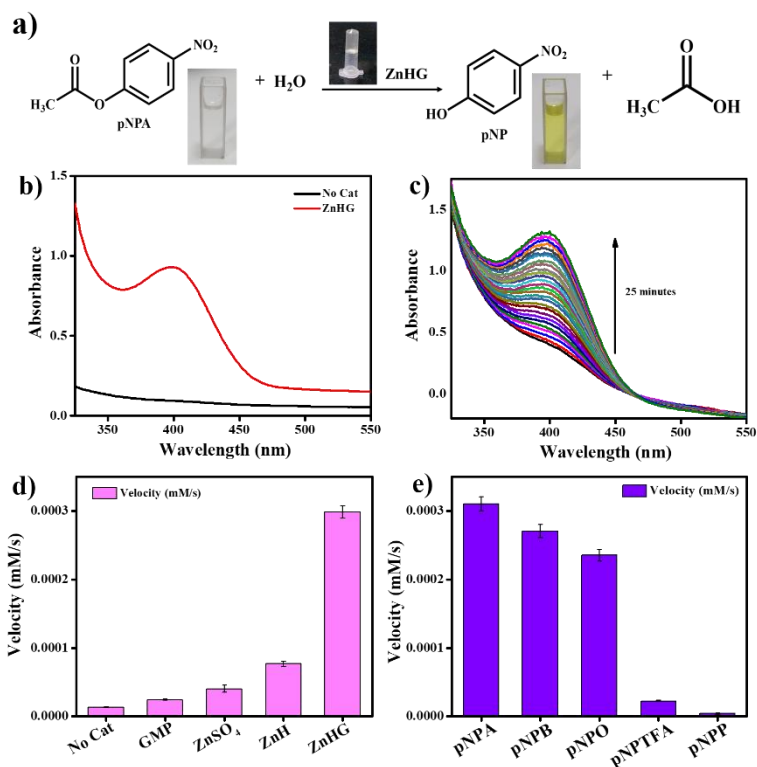


Figure 4.11. (a) Esterase activity of ZnHG Xerogel hydrolyzing pNPA to pNP producing yellow color; (b) UV-visible spectra for 1 mM pNPA in the absence of catalyst (black) and in the presence of 1 mg/ml ZnHG xerogel (red), (c) Time-dependent UV-visible spectra of 1 mM pNPA hydrolysis reaction for 30 minutes, (d) the control experiment to compare esterase activity of precursors, bare ZnH complex, and ZnHG xerogel, and (e) Hydrolysis rate for different nitrophenyl esters (experiments performed at temperature 25 °C)

Substrate specificity of the ZnHG xerogel was studied by analyzing the hydrolysis reaction kinetics of several nitrophenyl esters with different side-chain lengths: 4-nitrophenyl acetate (pNPA), 4-nitrophenyl octanoate (pNPO), 4-nitrophenyl butyrate (pNPB), side chain with an electron-withdrawing group, 4-nitrophenyl trifluoroacetate (pNPTFA) and chemically different substrate, p-nitrophenyl phosphate (pNPP) (Figure 4.11e). We observed that the hydrolysis reactivity reduces with an increase in the side chain length ($V_{\text{pNPA}} > V_{\text{pNPB}} >$

V_{pNPO}).⁹ However, the reactivity was minimal for bulky electron withdrawing side chain pNPTFA and almost absent for chemically distinct pNPP, thus indicating substrate specificity.

The catalytic rate with varying concentrations of pNPA was plotted against pNPA concentrations and a Michaelis-Menten curve was obtained, which proved the enzyme-like behavior of ZnHG xerogel (Figure 4.12a). Kinetic parameters such as Michaelis constant K_m and maximum velocity V_{max} were calculated to be 0.73 mM and 5.12×10^{-4} mM/s⁻¹ respectively through non-linear hill fitting of the Michaelis-Menten curve ($R^2 = 0.992$). K_m value for the ZnHG xerogel was found to be lower than naturally occurring carbonic anhydrases, since K_m value for carbonic anhydrases B and C at pH 8, were found to be 5.8 mM and 20.7 mM respectively.⁵⁰ The lower value of K_m for the xerogel suggests the higher affinity of the ester towards ZnHG than the natural carbonic anhydrase enzyme. The catalytic rate constant (k_{cat}) and catalytic efficiency (k_{cat}/K_m) were calculated to be 2×10^{-3} s⁻¹ and 2.74 M⁻¹s⁻¹ respectively.

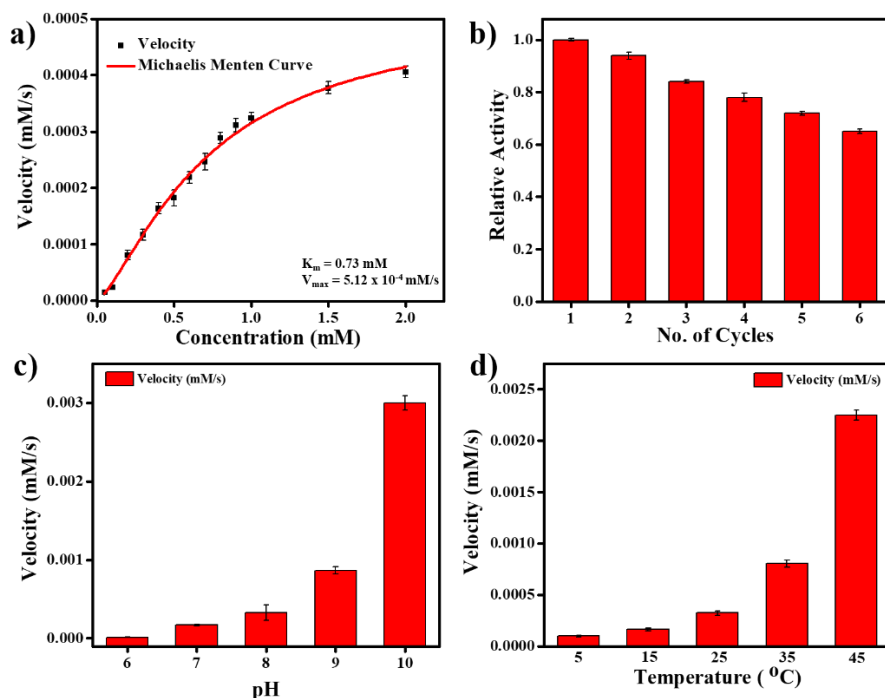


Figure 4.12. Steady-state kinetic assay for pNPA, (f,g) effect of pH and temperature in reaction rate respectively, and (h) Recyclability study for ZnHG xerogel

Owing to the very slow swelling rate of the ZnHG xerogel, it could be reused by separating it through centrifugation and then by washing it in DI water. The catalytic performance was studied for 6 cycles, and the catalytic efficiency was retained up to 65% till the 6th cycle (Figure 4.12b). The effect of pH and temperature on the hydrolysis rate was also studied (Figure 4.12c, d). We observed an exponential increase in the esterase activity of ZnHG xerogel with increased pH and temperature.

4.2.6. CO₂ hydration activity of ZnHG xerogel.

The actual purpose of CA is to reversibly catalyze the hydration of CO₂ to carbonate ions and protons. Since the hydration of CO₂ leads to an acidic environment, a drop in pH is expected. Thus, we measured the pH change when CO₂ was passed through the phosphate buffer, pH 8 for 360 seconds containing ZnHG xerogel (1mg/ml) (Figure 4.13a). We observed a steep drop in pH from 8 to 5.8 in the presence of ZnHG xerogel, but without any catalyst, the pH was reduced to only 7 even with continuous bubbling of CO₂. This showed us the efficient CO₂ hydration activity of the hydrogel. UV-visible spectra were obtained for 10 mM CO₂ dissolved in phosphate buffer at pH 8, both before and after adding ZnHG xerogel, with phenol red (PR) as an indicator (Figure 4.13b). A steady-state kinetic experiment was performed by varying CO₂ concentration (Figure 4.13c). The kinetic parameters such as Michaelis constant K_m and maximum velocity V_{max} were calculated to be 1.95 mM and 3.1×10^{-3} mM s⁻¹ respectively. The K_m value for natural carbonic anhydrase enzyme has been reported to vary from 4-18 mM based on different variants. The lower value of K_m for ZnHG xerogel than any CA variant signifies the excellent affinity of CO₂ towards the hydrogel than natural enzyme.^{51,52} The recyclability of the xerogel was checked by separating the catalyst from the system through centrifugation followed by washing with DI water, then reusing for 6 cycles. The catalyst retained 55% of its activity till the 6th cycle (Figure 4.13d).

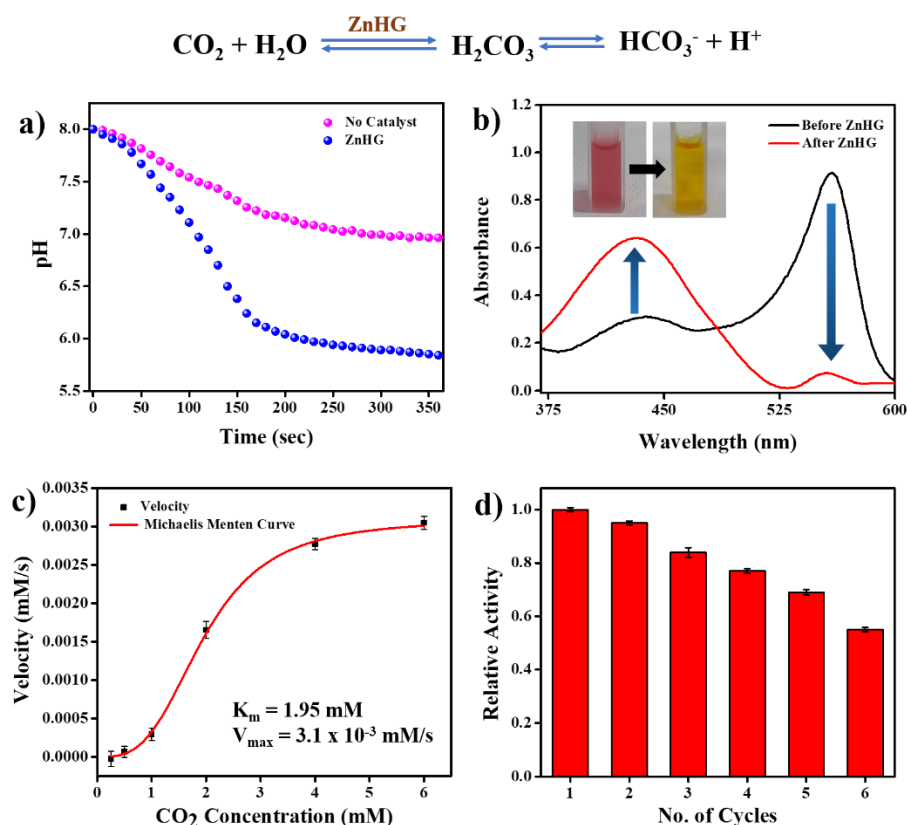


Figure 4.13. (a) Change in pH value under CO₂ bubbling condition in absence and in presence of ZnHG xerogel (1mg/ml), (b) change in UV-visible absorbance of PR in the presence of CO₂ (10 mM) before and after addition of ZnHG xerogel, (c) Michaelis-Menten curve fitting for CO₂ hydration by varying CO₂ concentration, (d) recyclability of the ZnHG xerogel.

4.2.7. Biomineralization method for CO₂ sequestration:

Formation of carbonated hydroxyapatite (CO₃Ap) for bone regrowth.

Biomineralization of metals was carried out in phosphate buffer, pH 7.4 to mimic the physiological conditions. Chloride salts of calcium and barium resulted in the formation of a white insoluble precipitate when added to CO₂-bubbling water. The obtained powder on mineralization of calcium was studied visually under SEM, where we observed a rod-like morphology (Figure 4.14a). EDS analysis revealed the presence of Ca, C, O, and P (Figure 4.14c). Then we further performed FTIR to analyze the presence of groups (Figure 4.14g). We obtained a peak at 1638 cm⁻¹ corresponding to the stretching frequency of water. The peaks at 782 and 871 cm⁻¹ stand for the in and out stretching frequency of the CO₃²⁻ group. The peaks at 1060 and 987 cm⁻¹ are attributed to the stretching frequency

for the PO_3^{2-} group. This observation suggests the incorporation of the phosphate group from the buffer in mineralization, thus implying the formation of carbonate hydroxyapatite. This observation was further validated by PXRD data, where we also obtained peak position specific to hydroxyapatite, in addition to CaCO_3 peaks (Figure 4.14h). Carbonated hydroxyapatite is a crucial mineral from the biological point of view since it's close to the chemical composition of bone. Due to its better resorption than pure hydroxyapatite, it is considered more suitable for bone tissue engineering.

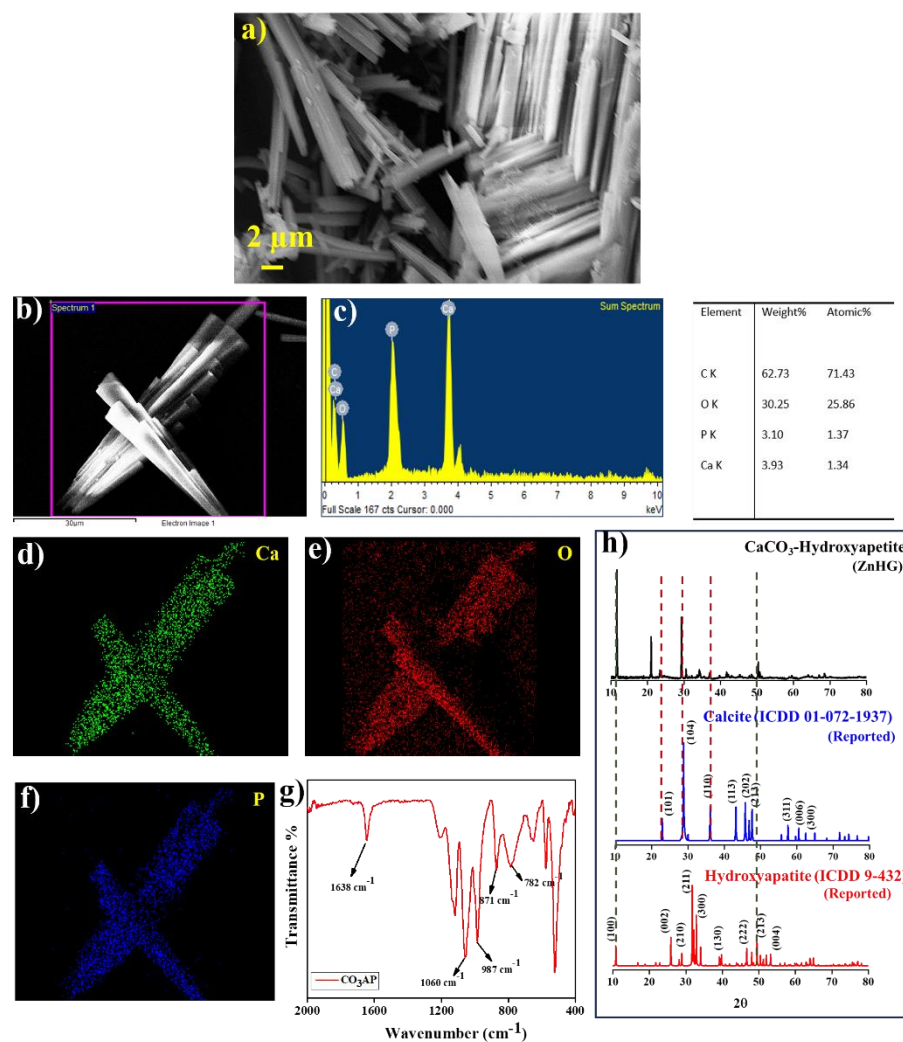


Figure 4.14. (a) SEM image, (b,c) SEM-EDS analysis, (d-f) EDS elemental mapping of the C, O, and P respectively, (g) FTIR, and (h) PXRD of CO_3Ap

To study the mineralization of calcium in the absence of phosphate ions, we also performed the biomineralization experiment in tris buffer. In this case, we obtained a coral-like morphology for the white

solid precipitated (Figure 4.15a). EDS analysis confirmed the presence of Ca, C, and O (Figure 4.15c). Further FTIR analysis was performed (Figure 4.15g), where the peak at 1638 cm^{-1} corresponds to the stretching frequency of water. The peak at 1043 cm^{-1} is attributed to the symmetric stretching frequency of CO_3^- and peaks at 795 and 869 cm^{-1} stand for the in and out bending of O-C-O. Also, peaks at 1491 and 560 cm^{-1} are for CO stretching frequency and M-O bonding respectively.^{53–57} From PXRD we can see the mixture of two types of CaCO_3 minerals, where $2\theta = 23.3$ and 32° is related to vaterite structure and $2\theta = 29.7, 36,$ and 39.8° are characteristic peaks for calcite structure, which is dominantly present (Figure 4.15h).

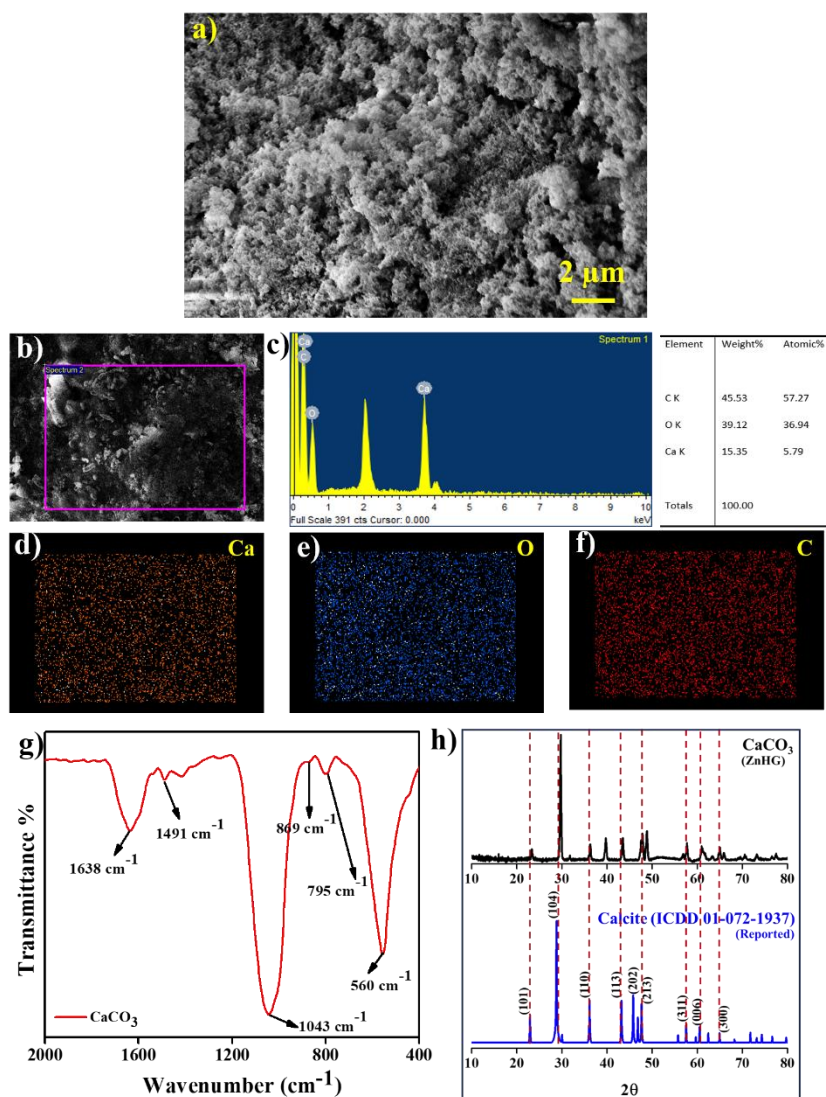


Figure 4.15. (a) SEM image, (b,c) SEM-EDS analysis (d-f) EDS elemental mapping of the Ca, O, and C respectively, (g) FTIR, and (h) PXRD of CaCO_3

Biom mineralization using silicate biomorph. Silica is often present in the mineralization process due to its abundance in nature. Alkaline earth metals are known to produce some unique structures in the presence of silica. The silica generally directs the formation of hierarchical structures that are usually performed by organic species; thus, it is called silicate biomorphs.⁵⁸ Thus, we performed mineralization of barium in the presence of silicate and we obtained a rosette-like morphology (Figure 4.16a, b). We observed the elemental presence of Ba, Si, C, and O from EDS analysis, thus, proving the incorporation of silica into the mineral structure (4.16d). In elemental mapping, we see the presence of Si only in the creeks of the structure thus showing the role of Si in controlling the architecture (Figure 4.16h). Further, the FTIR spectrum was performed to study the involvement of functional groups (Figure 4.16j). The peak at 1643 cm^{-1} is assigned to the stretching frequency of H_2O , while the peaks at 1247 and 1051 cm^{-1} are assigned to the asymmetric stretching of Si-O-Si. The peak at 990 cm^{-1} is the characteristic peak of the surface silanol group. The presence of CO_3^{2-} is validated by the peaks at 840 assigned to out plane bending of CO_3^{2-} and the characteristic peak of witherite (BaCO_3) at 2345 cm^{-1} .^{59,60} PXRD of barium silicate carbonate was furthered compared to the literature (Figure 4.16i).

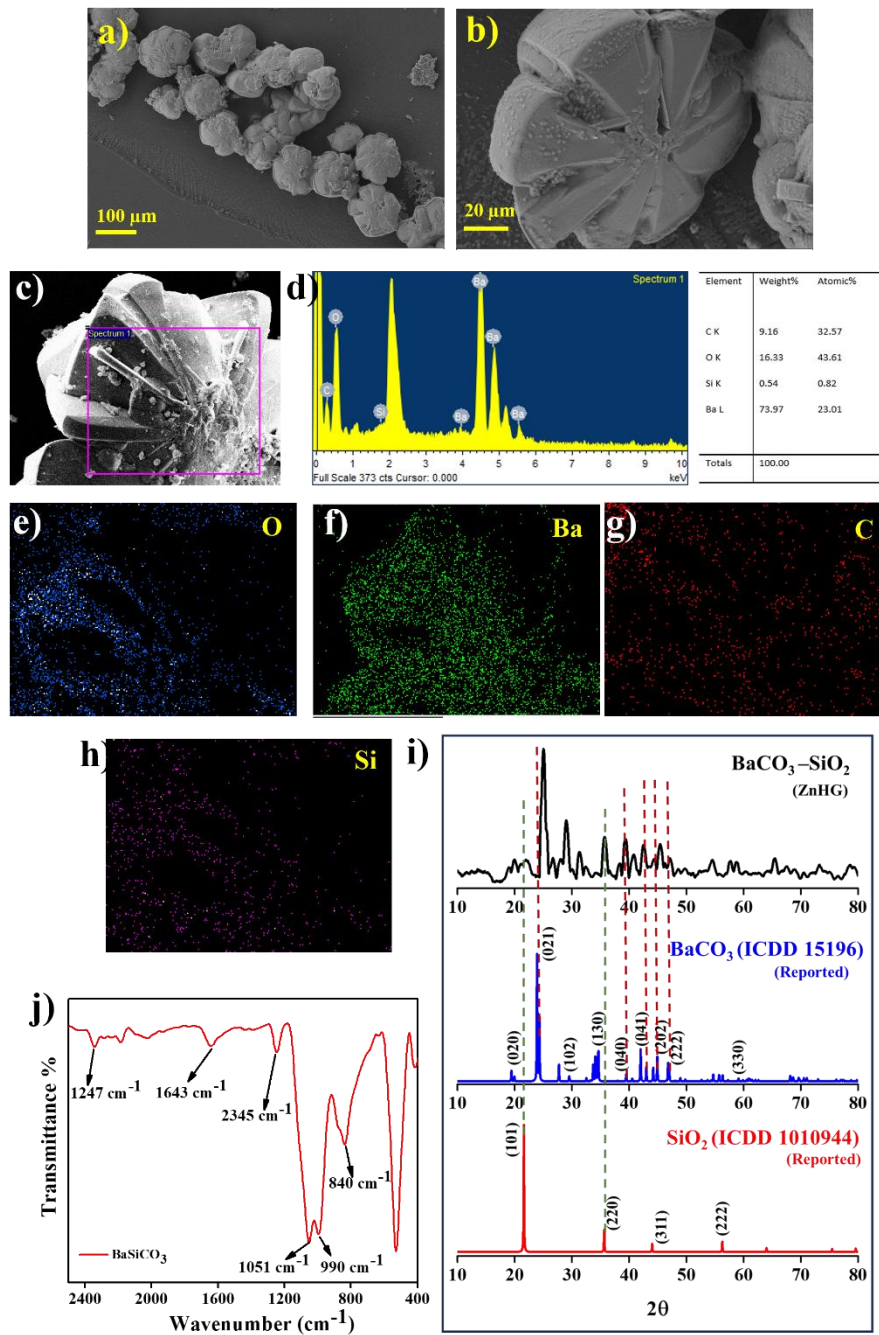


Figure 4.16. (a,b) SEM image (c,d) SEM-EDS analysis (e-h) EDS elemental mapping of the O, Ba, C, and P respectively, (j) FTIR, and (i) PXRD of silicate biomorph implying $BaCO_3$

To, further demonstrate the role of silica we also performed a control mineralization experiment in the absence of silicate to control directional growth, we obtained a block-like morphology instead of a rosette (Figure 4.17a). EDS analysis discovered the presence of Ba, C, and O hinting towards the formation of $BaCO_3$ (Figure 4.17c-f). From FTIR, (Figure 4.17g) the peak at 975 cm^{-1} is due to the adsorbed CO_2 on

BaO.⁵⁷ The peaks at 1060 and 880 cm^{-1} are due to the symmetric stretching of CO_3^- and out plane bending vibration of CO_3^{2-} . The formation of BaCO_3 is also confirmed from PXRD since the data for synthesized BaCO_3 matches with the literature (Figure 4.17h).

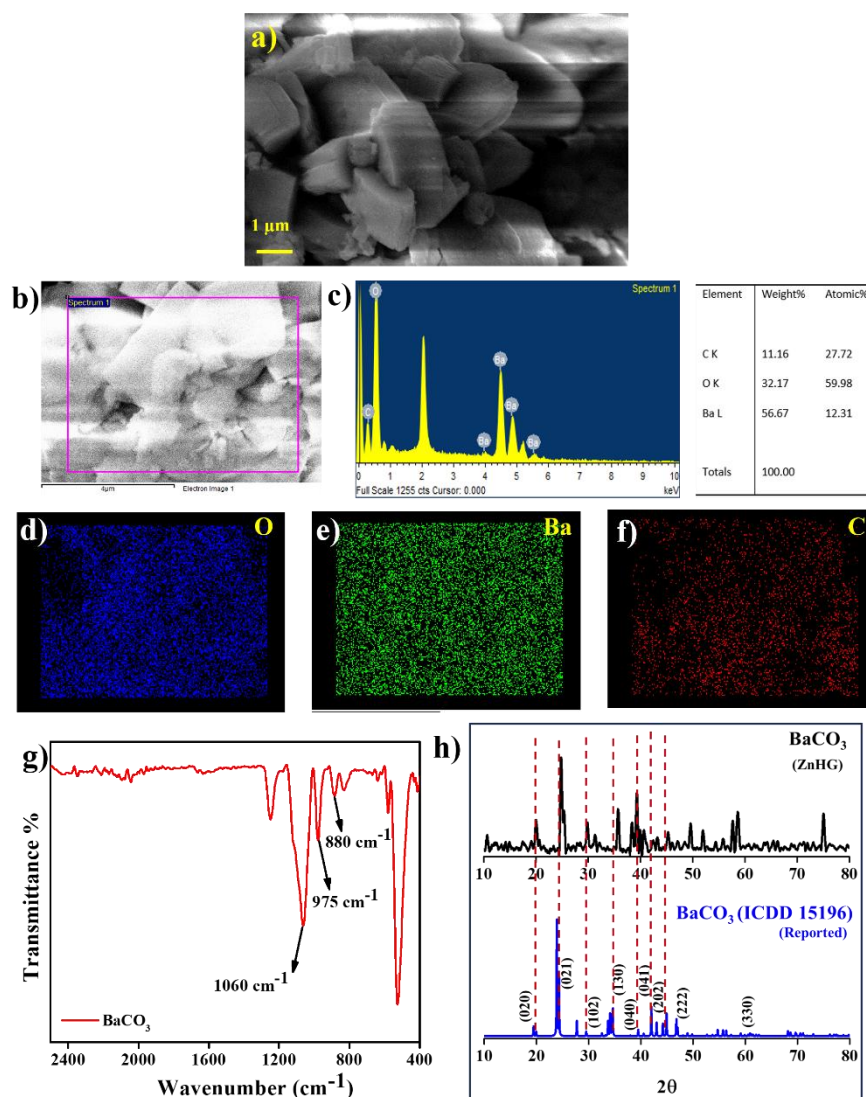


Figure 4.17. (a) SEM image (b,c) SEM-EDS analysis, (d-f) EDS elemental mapping of the O, Ba, and C respectively, (g) FTIR, and (h) PXRD of BaCO_3

Removal of toxic metals through biomineralization. Biomineralization can be used as a great solution to many environmental issues. CO_2 can form insoluble carbonate with soluble toxic metal ions and thus can be immobilized and removed from the system along with CO_2 containment at the same time. Common pollutant heavy metal ions, Pb and Cd were used for mineralization with CO_2 in the presence of ZnHG xerogel. Pb is

mineralized with a spherical morphology (Figure 4.18a) and Cd is mineralized with a uniform marigold flower-like morphology (Figure 4.19a-c).

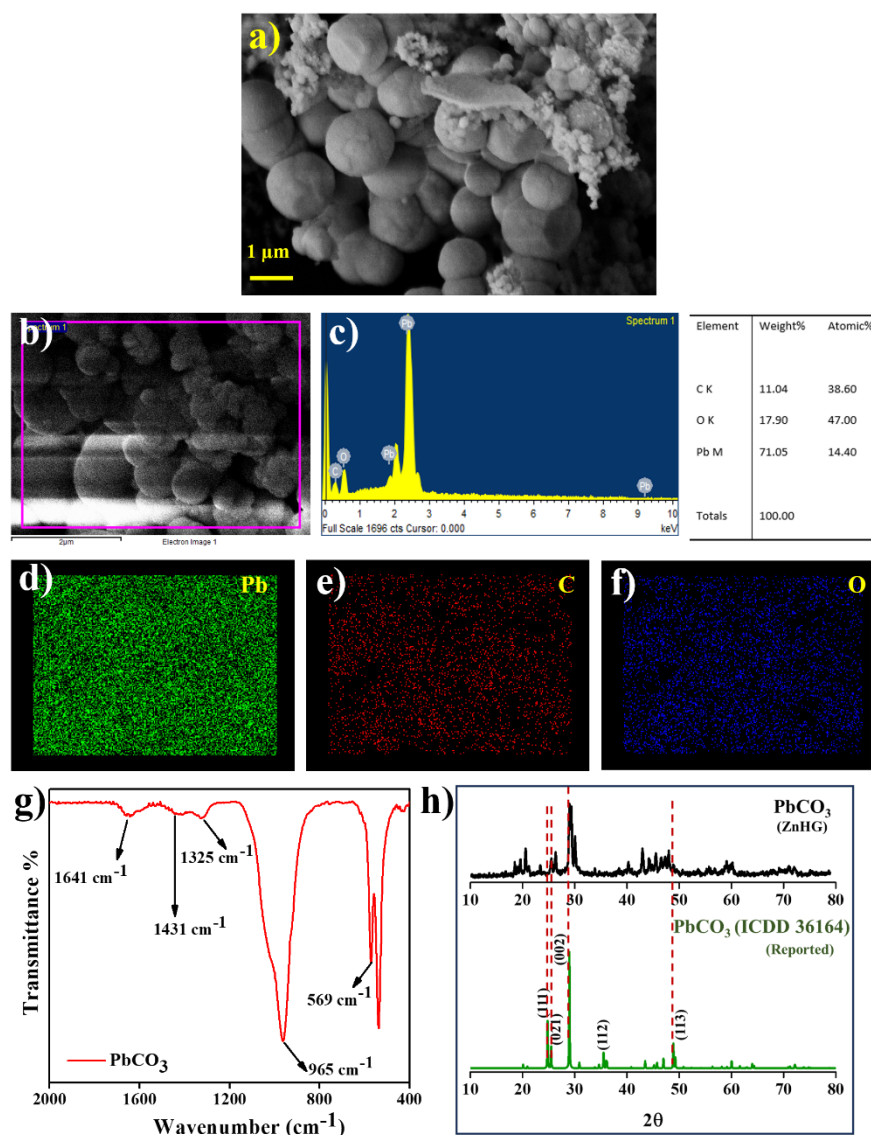


Figure 4.18. (a) SEM image, (b,c) SEM-EDS analysis, (d-f) EDS elemental mapping of the O, Pb, and C respectively, (g) FTIR, and (h) PXRD of $PbCO_3$

EDS analysis showed the presence of Pb, C, and O in the case of Pb mineral (Figure 4.18 c-f) and Cd, C, and O in the case of Cd mineral (Figure 4.19e-h). Elemental analysis suggested the formation of $PbCO_3$ and $CdCO_3$. This hypothesis is further confirmed by the FTIR experiment. In the case of Pb (figure 4.18h), the peak for water stretching is at 1641 cm^{-1} , and the peaks at 1431 and 1325 cm^{-1} stand for asymmetric

CO_3^{2-} stretching, and the peak at 965 cm^{-1} results from absorption of CO_2 on metal oxide.⁵⁷ For CdCO_3 (Figure 4.19i), the peak at 1640 cm^{-1} is due to the H_2O stretching, and peaks at 1052 and 1004 cm^{-1} are caused by symmetric stretching of CO_3^{2-} and in-plane O-C-O bending causing a peak at 733 cm^{-1} . The peak at 585 cm^{-1} in PbCO_3 and 585 cm^{-1} in CdCO_3 correspond to the metal-oxygen bond. corresponds to the Metal-Oxygen bonding.⁶⁰ Further, the similarity in PXRD spectra of both Pb and Cd minerals with the reported PbCO_3 (Figure 4.18h) and CdCO_3 (Figure 4.19j) confirmed their synthesis.

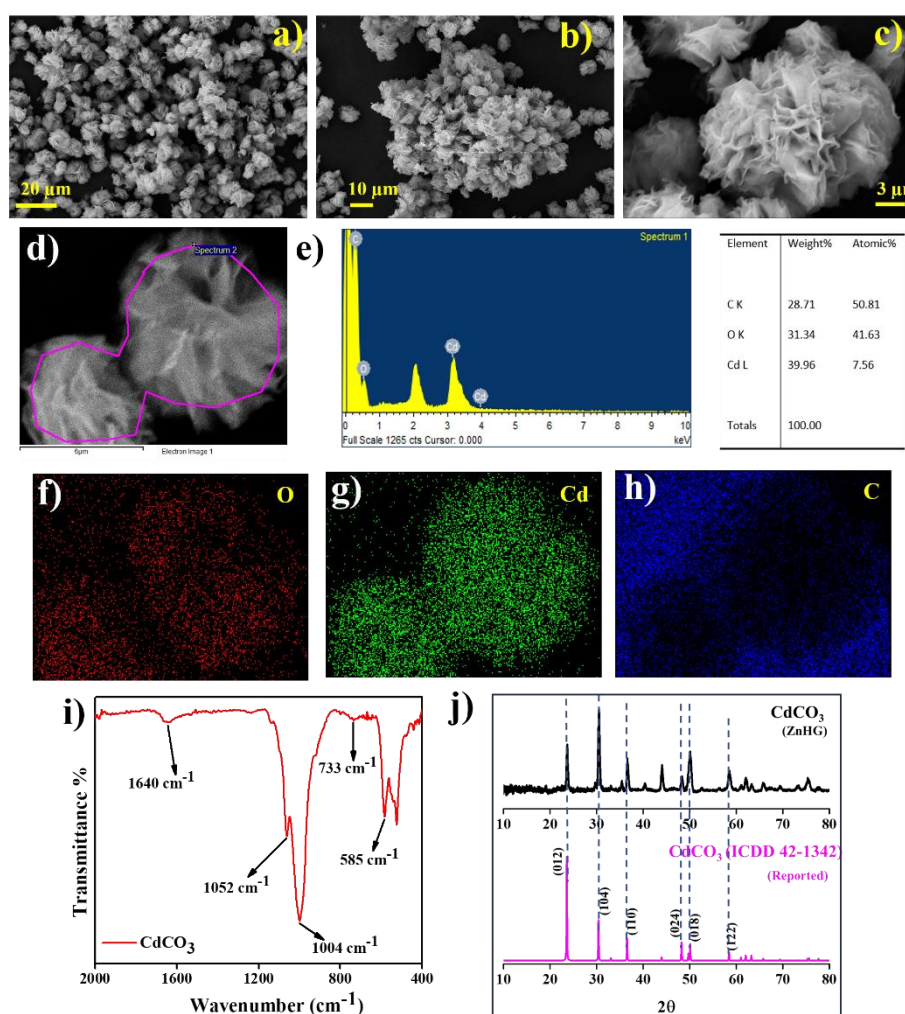


Figure 4.19. (a) SEM image (d,e) SEM-EDS analysis of CdCO_3 , (f-h) EDS elemental mapping of the O, Cd, and C respectively, (i) FTIR, and (j) PXRD of CdCO_3

4.3. CONCLUSION

In conclusion, we successfully managed to design a hydrogel that could structurally mimic the active site of the natural carbonic anhydrase

enzyme by applying a simple self-assembly strategy of the small molecule precursors. The fibrillar structure of GMP provided a crowded environment that is similar to the protein chain in enzymes and thus provided stability to the tetrahedral $\text{Zn}(\text{His})_3\text{H}_2\text{O}$ complex. The ZnHG hydrogel also functionally mimicked the carbonic anhydrase enzyme, which was confirmed by studying the kinetics of the esterase and CO_2 hydration activity. The hydrogel showed excellent enzymatic activity and better affinity towards the substrate than the natural enzyme. The hydrogel showed enhanced enzymatic activity than the bare ZnH complex by 4 times and also due to the very slow swelling rate of the hydrogel, it could also be separated after reaction and reused thus rendering recyclability. CO_2 sequestration was successfully performed via biomineralization with different metals which provided us with interesting complex architectural structures. The biomineralization technique was further applied for the removal of heavy toxic metal ions such as Pb^{2+} and Cd^{2+} . While the structural replication of the natural enzyme requires a tedious synthetic route, this simple self-assembly technique provided us with a very facile strategy to structurally and functionally mimic natural enzymes thus providing a significant step towards the direction of synthesizing various artificial enzymes.

4.4. Experimental Section

4.4.1. Materials and Reagents

Zinc sulphate heptahydrate, L-histidine base (extra pure), guanosine monophosphate disodium salt (GMPNa_2), 4-nitrophenyl acetate, 4-nitrophenyl phosphate, Thioflavin T (ThT), and metal chlorides including calcium(II) chloride dihydrate, cadmium(II) chloride anhydrous, and barium(II) chloride dihydrate were purchased from SRL Chemicals, India. Lead(II) chloride and sodium metasilicate were purchased from Sigma Aldrich. Phenol Red, sodium phosphate dibasic heptahydrate, sodium phosphate monobasic monohydrate, and sodium hydroxide were purchased from Finar, India. Reagent-grade organic solvents, including ethanol, methanol, and acetone, and mineral acids

such as hydrochloric acid and sulfuric acid were purchased from Merck, India, and used directly without further purification. Milli-Q water was used throughout the experiments. All chemicals were used as received without further purification.

4.4.2. Preparation of ZnHG hydrogel

A homogeneous, transparent solution was prepared by mixing 25 mM zinc sulphate heptahydrate and 75 mM L-histidine in deionized water. To this solution, 75 mM of Na₂GMP was added and stirred for 2 hours at 55 °C, resulting in another homogeneous, transparent solution. This solution was allowed to reach a steady state over 2 days, forming a light yellowish hydrogel. The resultant hydrogel was stable and rigid, capable of being prepared within a specific pH range. The hydrogel was then freeze-dried to produce a xerogel, which is suitable for solid-state characterization and catalytic applications. For dilute-phase spectroscopic and microscopic characterizations, the hydrogel was diluted with deionized water and incubated to allow for swelling.

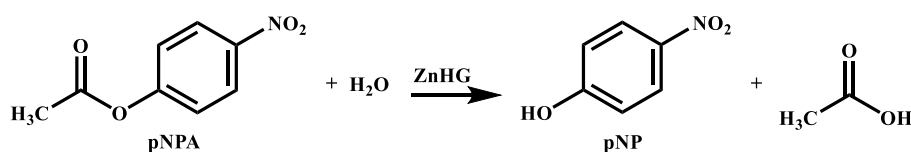
4.4.3. Characterization Methods and Physical Properties Determination

The UV-visible spectra of the diluted hydrogels and their constituents were recorded using a PerkinElmer Lambda 750 UV Spectrometer. All kinetic experiments were conducted by measuring absorbance over time with the same UV-visible spectrophotometer. The ¹H and ³¹P NMR spectra of the synthesized ZnHG hydrogel and its metal complex constituents (dissolved in deuterium oxide, D₂O) were obtained using a Bruker Biospin AVANCE NEO Ascend 500 MHz spectrometer. Steady-state fluorescence (FL) spectra were recorded using a Horiba JobinYvon Fluoromax-4p spectrofluorometer (FM-100). The Fourier transform infrared (FTIR) spectra of the dried hydrogels, their constituents, and the metal carbonates were acquired using a Bruker Alpha II instrument with an ATR extension. X-ray photoelectron spectroscopy (XPS) analysis was studied with the help of Thermo-Scientific NEXSA Surface analyser. The powder X-ray diffraction (pXRD) of all samples was measured with a

Bruker-D8 Advance X-ray diffractometer. The morphology of the hydrogel and the biomineralized products was examined using a Carl Zeiss Supra 55 field emission scanning electron microscope (FESEM), with EDX analysis performed using a Bruker EDX instrument attached to the FE-SEM. The surface morphology of the hydrogel was studied with a TECNAI G2, 200 kV high-resolution transmission electron microscope (HRTEM). Atomic Force Microscopy (AFM) images were obtained using a Park Systems NX10 Atomic Force Microscope. Rheological investigations of the DNA-GMP hydrogel were performed on an Anton Paar Physica MCR 301 rheometer using a parallel plate geometry with a diameter of 25 mm. Dynamic strain sweep measurements were taken at a constant angular frequency of 10 rad s^{-1} , and frequency sweep experiments were conducted at a constant strain (γ) value of 1% at $25 \text{ }^\circ\text{C}$. Thixotropic step-strain measurements were carried out with variable strain values of 1% and 100% at a constant ω of 10 rad s^{-1} . Spectra analysis and image analysis were performed using OriginPro 2016 and ImageJ software, respectively. All photographs were taken using a simple mobile phone camera.⁴⁰

4.4.4. Esterase activity and kinetic parameters

The catalytic activity of the ZnHG xerogel was examined in the 4-nitrophenol acetate (pNPA) (substrate) hydrolysis reaction:



The hydrolysis reaction rate was measured by analysing the formation of 4-nitrophenol (product) through UV-visible spectroscopy at $\lambda_{\text{max}} = 400 \text{ nm}$. In this process, 1 mg/mL solution of the xerogel (catalyst) were combined with 1 mM concentration of p-NPA (dissolved in acetonitrile) in a phosphate buffer (100 mM, pH 8) within a UV cuvette. The hydrolysis of p-NPA was monitored over time by recording the optical absorbance at 400 nm at room temperature. Various factors affecting the kinetic parameters, such as substrate concentration, solution pH, and

temperature were systematically examined. To study the catalyst effectiveness, controlled experiments with the precursors such as Zn-His complex, Zn-salt, histidine, and GMP as catalyst were also evaluated. Additionally, the substrate scope for the catalytic activities were assessed using various substrate with different side-length 4-nitrophenyl butyrate (pNPB), 4-nitrophenyl octanoate (pNPO) and bulky side chain 4-nitrophenyl trifluoroacetate (pNPTFA). Also, groups with chemically distinct substrate 4-nitrophenyl phosphate (pNPP) have been also assessed with the ZnHG catalyst for the validation of substrate specificity.

For the kinetic experiments, an appropriate amount of catalyst ($1 \text{ mg} \cdot \text{mL}^{-1}$) in phosphate buffer medium (100 mM, pH 8.0) was added and mixed in a $1 \times 1 \text{ cm}$ quartz cuvette. The reaction was initiated by adding an appropriate amount of substrate (pNPA) dissolved in acetonitrile. The reaction mixture was incubated for 2 minutes, and then the progress of the reaction was monitored at the absorbance wavelength of the product (pNP) ($\lambda_{\text{max}} = 400 \text{ nm}$) over time. A linear plot of absorbance versus time was obtained from the kinetic experiment, and the initial reaction rate (V_0) was determined at various substrate concentrations. These V_0 values were plotted as a function of substrate concentration and fitted to the Michaelis–Menten equation to obtain the V_{max} and K_{m} values.

To analyse the thermal activity and stability of the catalyst, kinetic experiments were carried out at variable temperatures ranging from 278 K to 328 K. Additionally, the pH dependency of the esterase activity was examined by varying the pH of the buffer medium from pH 3 to pH 10. To study the reusability of the catalyst, 3 mg of catalyst was placed into a 3 mL cuvette containing 1 mM pNPA in phosphate buffer medium (pH 8.0). The kinetic experiment was conducted, and then the solution was centrifuged at 8000 rpm for 15 minutes to precipitate the catalyst. The supernatant was separated, and the catalyst was washed with deionized water and then reused for the next cycle of the kinetic experiment.

4.4.5. Kinetics of CO₂ Hydration and pH Studies

The CO₂ hydration capability of the ZnHG hydrogel, which mimics carbonic anhydrase (CA), was evaluated. Pure CO₂ gas at a flow rate of 200 mL·min⁻¹ was purged into 200 mL of deionized water using a CO₂ flowmeter in an ice bath for 2 hours to prepare carbonated water. With a maximum CO₂ solubility of 3.48 g·L⁻¹ in water at 273.15 K and 1 atm pressure, the CO₂-saturated solution contained 77 mM dissolved CO₂, determined by Henry's constant. For activity measurement, the pH indicator phenol red (50 μM) and the ZnHG catalyst dissolved in a phosphate buffer (100 mM, pH 8) were used as the base. The CO₂ hydration reaction was conducted at various concentrations and dilutions of CO₂ water with different amounts of ZnHG catalyst. The pH change was measured using a colorimetric technique, monitoring the rate of change of absorbance at 560 nm over time. The initial reaction rate (V_0) was obtained from the kinetics data at different CO₂ concentrations. These V_0 values were plotted as a function of CO₂ concentration, and the V_{max} and K_M values for CO₂ hydration were calculated using a Michaelis-Menten kinetics plot.

Additionally, pH studies were conducted in a deionized water solution containing 1 mgmL⁻¹ ZnHG xerogel as a catalyst with a continuous CO₂ flow rate of 50 mL·min⁻¹. The system's pH change was continuously monitored and recorded for 400 seconds using a LABMAN LMPH10H pH meter. Control experiments for CO₂ hydration and pH studies were also performed with the individual catalyst constituents as well as without any catalyst.

4.4.6. Biomineralization of the Metal Carbonates

The biomineralization of several metal carbonates, such as calcium carbonate, barium carbonate, barium silico carbonate, cadmium carbonate, and lead carbonate, was conducted using the CA-mimicking ZnHG hydrogel as a catalyst. This mineralization process involved slowly purging (bubbling) CO₂ gas (50 cm³·min⁻¹) into a phosphate buffer (100 mM, pH 7.4) containing metal chlorides (10 mM) and ZnHG

xerogel ($1 \text{ mg}\cdot\text{mL}^{-1}$) for one hour. For the precipitation of barium silico carbonate, barium chloride, and sodium metasilicate were used as the precursors. After CO_2 purging, the solution was left to stand for 12 hours to allow the metal carbonates to precipitate. These precipitates were washed with deionized water to remove the catalyst or any unreacted metal chlorides. After drying the metal carbonates, SEM, EDX, FTIR, and PXRD analyses were performed.

4.5. References

1. Alterio V., Di Fiore A., D'Ambrosio K. *et al.* (2012), Multiple Binding Modes of Inhibitors to Carbonic Anhydrases: How to Design Specific Drugs Targeting 15 Different Isoforms?, *Chem. Rev.* 112, 4421–4468 (DOI: 10.1021/cr200176r)
2. Kumar S., Rulhania S., Jaswal S. *et al.* (2021), Recent advances in the medicinal chemistry of carbonic anhydrase inhibitors. *Eur. J. Med. Chem.* 209, 112923 (DOI: 10.1016/j.ejmech.2020.112923)
3. Li L., Xu W., Wu Z. *et al.* (2024), Engineering Zinc–Organic Frameworks-Based Artificial Carbonic Anhydrase with Ultrafast Biomimetic Centers for Efficient Hydration Reactions, *Small* 20, 2307537 (DOI: 10.1002/sml.202307537)
4. García-Llorca A., Carta F. *et al.* (2024), Carbonic anhydrase, its inhibitors and vascular function, *Front. Mol. Biosci.* 11 (DOI: 10.3389/fmolb.2024.1338528)
5. Chen Y., Yang Y., Orr A.A. *et al.* (2021), Self-Assembled Peptide Nano-Superstructure towards Enzyme Mimicking Hydrolysis, *Angew. Chem. Int. Ed.* 60, 17164–17170 (DOI: 10.1002/anie.202105830)
6. Xiang Y., Yu D. *et al.* (2024), Synergistic bimetallic nanozymes of Ni/ZIF-8 and Cu/ZIF-8 as carbonic anhydrase mimics, *Colloids Surf. Physicochem. Eng. Asp.* 689, 133711 (DOI: 10.1016/j.colsurfa.2024.133711)

7. Floyd W.C.I., Baker S.E., Valdez C.A. *et al.* (2013), Evaluation of a Carbonic Anhydrase Mimic for Industrial Carbon Capture, *Environ. Sci. Technol.* 47, 10049–10055 (DOI: 10.1021/es401336f)
8. Zhou Y., Wang Y., Chen Z. *et al.* (2023), Highly Hydrophilic ZIF-8 as a Carbonic Anhydrase Mimetic Catalyst for Promoting CO₂ Absorption, *J. Phys. Chem. C* 127, 7184–7196 (DOI: 10.1021/acs.jpcc.3c00345)
9. Makam P., Yamijala S.S.R.K.C., Tao K. *et al.* (2019), Non-proteinaceous hydrolase comprised of a phenylalanine metallo-supramolecular amyloid-like structure, *Nat. Catal.* 2, 977–985 (DOI: 10.1038/s41929-019-0348-x)
10. Ufarté L., Laville É. *et al.* (2015), Metagenomics for the discovery of pollutant degrading enzymes, *Biotechnol. Adv.* 33, 1845–1854 (DOI: 10.1016/j.biotechadv.2015.10.009)
11. Ji P., Park J. *et al.* (2021), Abiotic reduction of ketones with silanes catalysed by carbonic anhydrase through an enzymatic zinc hydride, *Nat. Chem.* 13, 312–318 (DOI: 10.1038/s41557-020-00633-7)
12. Nilouyal S., Karahan H.E., Ng E.W.H. *et al.* (2023), Nanobiomineralization of Carbon Dioxide by Molecularly Engineered Metal–Histidine Complex Nanozymes, *Chem. Mater.* 35, 1610–1623 (DOI: 10.1021/acs.chemmater.2c03169)
13. Liang S., Wu X.L. *et al.* (2020), Zn-triazole coordination polymers: Bioinspired carbonic anhydrase mimics for hydration and sequestration of CO₂, *Chem. Eng. J.* 398, 125530 (DOI: 10.1016/j.cej.2020.125530)
14. Kim M.C., Lee, S.Y. (2014), Carbonic Anhydrase-Mimetic Bolaamphiphile Self-Assembly for CO₂ Hydration and Sequestration. *Chem. Eur. J.* 20, 17019–17024 (DOI: 10.1002/chem.201404765)

15. Jin C., Zhang S. *et al.* (2018), Mimic Carbonic Anhydrase Using Metal–Organic Frameworks for CO₂ Capture and Conversion, *Inorg. Chem.* 57, 2169–2174 (DOI: 10.1021/acs.inorgchem.7b03021)
16. Lindskog, S. (1997), Structure and mechanism of carbonic anhydrase, *Pharmacol. Ther.* 74, 1–20 (DOI: 10.1016/S0163-7258(96)00198-2)
17. Višnjevac A., Gout J. *et al.* (2010), First ZnII Bowl-Complexes Modeling the Tris(histidine) Metallo-Site of Enzymes, *Org. Lett.* 12, 2044–2047 (DOI: 10.1021/ol100512n)
18. Gelinsky M., Vogler R., Ahrenkamp, H. (2002), Tripodal Pseudopeptides with Three Histidine or Cysteine Donors: Synthesis and Zinc Complexation, *Inorg. Chem.* 41, 2560–2564 (DOI: 10.1021/ic011263c)
19. Kelsey R.A., Miller D.A. *et al.* (2015), Carbonic anhydrase mimics for enhanced CO₂ absorption in an amine-based capture solvent. *Dalton Trans.* 45, 324–333 (DOI: 10.1039/C5DT02943K)
20. Wright A.M., Wu Z. *et al.* (2018), A Structural Mimic of Carbonic Anhydrase in a Metal-Organic Framework, *Chem* 4, 2894–2901 (DOI: 10.1016/j.chempr.2018.09.011)
21. Xiang Y., Yu D., Zhang H. *et al.* (2024), Synergistic bimetallic nanozymes of Ni/ZIF-8 and Cu/ZIF-8 as carbonic anhydrase mimics, *Colloids Surf. Physicochem. Eng. Asp.* 689, 133711 (DOI: 10.1016/j.colsurfa.2024.133711)
22. Huang Y., Zhang S. *et al.* (2019), A Zinc Coordination Complex Mimicking Carbonic Anhydrase for CO₂ Hydrolysis and Sequestration. *Inorg. Chem.* 58, 9916–9921 (DOI: 10.1021/acs.inorgchem.9b01059)
23. Fan C., Tang Y. *et al.* (2022), ZIF-90 with biomimetic Zn–N coordination structures as an effective nanozyme to mimic natural hydrolase, *Nanoscale* 14, 7985–7990 (DOI: 10.1039/D2NR01213H)

24. Nilouyal S., Karahan H.E., Isfahani A.P. *et al.* (2022), Carbonic Anhydrase-Mimicking Supramolecular Nanoassemblies for Developing Carbon Capture Membranes, *ACS Appl. Mater. Interfaces* 14, 37595–37607 (DOI: 10.1021/acsami.2c06270)
25. Zhang Z., Li F. *et al.* (2021), Zinc-based deep eutectic solvent – An efficient carbonic anhydrase mimic for CO₂ hydration and conversion. *Sep. Purif. Technol.* 276, 119446 (DOI: 10.1016/j.seppur.2021.119446)
26. Fan B., Zhang Y., Lv, Y. (2023), Synthetic hydrogel polymer nanoparticles as a structural mimic of carbonic anhydrase, *Matter* 6, 4245–4260 (DOI: 10.1016/j.matt.2023.09.015)
27. Bahrami F., Zhao Y. (2023), Carbonic anhydrase mimics with rationally designed active sites for fine-tuned catalytic activity and selectivity in ester hydrolysis, *Catal. Sci. Technol.* 13, 5702–5709 (DOI: 10.1039/D3CY00704A)
28. Xu S., Wu H. *et al.* (2023), A supramolecular metalloenzyme possessing robust oxidase-mimetic catalytic function, *Nat. Commun.* 14, 4040 (DOI: 10.1038/s41467-023-39779-6)
29. Morimoto M., Bierschenk S.M. *et al.* (2020), Advances in supramolecular host-mediated reactivity, *Nat. Catal.* 3, 969–984 (DOI: 10.1038/s41929-020-00528-3)
30. Agarwal V., Varshney N. *et al.* (2023), Cobalt-Adenosine Monophosphate Supramolecular Hydrogel with pH-Responsive Multi-Nanozymatic Activity, *ACS Appl. Bio Mater.* 6, 5018–5029 (DOI: 10.1021/acsabm.3c00719)
31. Chakraborty, A., Dash, S. *et al.* (2024), Polyoxometalate-Guanosine Monophosphate Hydrogels with Haloperoxidase-like Activity for Antibacterial Performance, *Biomacromolecules* 25, 104–118 (DOI: 10.1021/acs.biomac.3c00845)

32. Thakur N., Chaudhary A. *et al.* (2021), Ion Conductive Phytic Acid-G Quadruplex Hydrogel as Electrolyte for Flexible Electrochromic Device, *ChemNanoMat* 7, 613–619 (DOI: 10.1002/cnma.202100072)
33. Chakraborty A., Ghosh T. *et al.* (2024), A multi-stimuli responsive polyoxometalate-guanosine monophosphate hybrid chromogenic smart hydrogel, *J. Mater. Chem. C* 12, 13447–13456 (DOI: 10.1039/D4TC01973C)
34. Peters G.M., Davis J.T. (2016), Supramolecular gels made from nucleobase, nucleoside and nucleotide analogs, *Chem. Soc. Rev.* 45, 3188–3206 (DOI:10.1039/C6CS00183A)
35. Stefan L., Monchaud, D. (2019), Applications of guanine quartets in nanotechnology and chemical biology, *Nat. Rev. Chem.* 3, 650–668 (DOI: 10.1038/s41570-019-0132-0)
36. Loo K., Degtyareva N. *et al.* (2010), Ag⁺-Mediated Assembly of 5'-Guanosine Monophosphate, *J. Phys. Chem. B* 114, 4320–4326 (DOI: 10.1021/jp908085s)
37. Giorgi T., Lena S. *et al.* (2003), Supramolecular Helices via Self-Assembly of 8-Oxoguanosines, *J. Am. Chem. Soc.* 125, 14741–14749 (DOI: 10.1021/ja0364827)
38. Yoshikawa I., Li J. *et al.* (2004), Design and Fabrication of a Flexible and Self-Supporting Supramolecular Film by Hierarchical Control of the Interaction between Hydrogen-Bonded Sheet Assemblies, *Angew. Chem. Int. Ed.* 43, 100–103 (DOI: 10.1002/anie.200352641)
39. Chantot J.F., Sarocchi M.T., Guschlbauer, W. (1971), Physico-chemical properties of nucleosides: Gel formation by guanosine and its analogues, *Biochimie* 53, 347–354 (DOI: 10.1016/S0300-9084(71)80101-3)

40. Ajikumar A., Premkumar A.K.N., Narayanan, S.P. (2023), The self-assembly of l-histidine might be the cause of histidinemia, *Sci. Rep.* 13, 17461 (DOI: 10.1038/s41598-023-44749-5)
41. Feyer V., Plekan O. *et al.* (2010), Adsorption of Histidine and Histidine-Containing Peptides on Au(111), *Langmuir* 26, 8606–8613 (DOI: 10.1021/la904684e)
42. Qin Z., Sun Y. *et al.* (2017), Kinetic Mechanism of Thioflavin T Binding onto the Amyloid Fibril of Hen Egg White Lysozyme. *Langmuir* 33, 5398–5405 (DOI: 10.1021/acs.langmuir.7b00221)
43. Mohanty J., Barooah N. *et al.* (2013), Thioflavin T as an Efficient Inducer and Selective Fluorescent Sensor for the Human Telomeric G-Quadruplex DNA, *J. Am. Chem. Soc.* 135, 367–376 (DOI: 10.1021/ja309588h)
44. Renaud de la Faverie A., Guédin A., Bedrat A. *et al.* (2014), Thioflavin T as a fluorescence light-up probe for G4 formation, *Nucleic Acids Res.* 42, e65 (DOI: 10.1093/nar/gku111)
45. Gu C., Peng Y., Li J. *et al.* (2020), Supramolecular G4 Eutectogels of Guanosine with Solvent-Induced Chiral Inversion and Excellent Electrochromic Activity, *Angew. Chem. Int. Ed.* 59, 18768–18773 (DOI: 10.1002/anie.202009332)
46. Kumar A., Khandelwal M., Gupta S.K. *et al.* (2019), Fourier transform infrared spectroscopy: Data interpretation and applications in structure elucidation and analysis of small molecules and nanostructures. In *Data Processing Handbook for Complex Biological Data Sources*, (Academic Press), pp. 77–96 (DOI: 10.1016/B978-0-12-816548-5.00006-X)
47. Zhou L., Li S., Su Y. *et al.* (2013), Interaction between Histidine and Zn(II) Metal Ions over a Wide pH as Revealed by Solid-State NMR Spectroscopy and DFT Calculations, *J. Phys. Chem. B* 117, 8954–8965 (DOI: 10.1021/jp4041937)

48. Wang G., Huang B., Li Z. *et al.* (2015), Synthesis and characterization of ZnS with controlled amount of S vacancies for photocatalytic H₂ production under visible light, *Sci. Rep.* 5, 8544 (DOI: 10.1038/srep08544)
49. Haider, M.B. (2017), XPS Depth Profile Analysis of Zn₃N₂ Thin Films Grown at Different N₂/Ar Gas Flow Rates by RF Magnetron Sputtering, *Nanoscale Res. Lett.* 12, 5 (DOI: 10.1186/s11671-016-1769-y)
50. Verpoorte J.A., Mehta S., Edsall, J.T. (1967), Esterase Activities of Human Carbonic Anhydrases B and C, *J. Biol. Chem.* 242, 4221–4229 (DOI: 10.1016/S0021-9258(18)95800-X)
51. Khalifah, R. (1971), The carbon dioxide hydration activity of carbonic anhydrase. I. Stop-flow kinetic studies on the native human isoenzymes B and C, *J. Biol. Chem.* 246, 2561–2573 (DOI: 10.1016/S0021-9258(18)62326-9)
52. Ye X., Lu Y. (2014), CO₂ absorption into catalyzed potassium carbonate–bicarbonate solutions: Kinetics and stability of the enzyme carbonic anhydrase as a biocatalyst, *Chem. Eng. Sci.* 116, 567–575 (DOI: 10.1016/j.ces.2014.05.040)
53. Possenti E., Colombo C. *et al.* (2021), Time-Resolved ATR–FTIR Spectroscopy and Macro ATR–FTIR Spectroscopic Imaging of Inorganic Treatments for Stone Conservation, *Anal. Chem.* 93, 14635–14642 (DOI: 10.1021/acs.analchem.1c02392)
54. Han B., Zhang B. *et al.* (2022), Beauty and chemistry: the independent origins of synthetic lead white in east and west Eurasia, *Humanit. Soc. Sci. Commun.* 9, 1–12 (DOI: 10.1057/s41599-022-01290-6)
55. Nosenko V., Strutynska N., Vorona I. *et al.* (2015), Structure of Biocompatible Coatings Produced from Hydroxyapatite

- Nanoparticles by Detonation Spraying, *Nanoscale Res. Lett.* 10, 464 (DOI: 10.1186/s11671-015-1160-4)
56. Rehman I., Bonfield, W. (1997), Characterization of hydroxyapatite and carbonated apatite by photo acoustic FTIR spectroscopy, *J. Mater. Sci. Mater. Med.* 8, 1–4 (DOI: 10.1023/A:1018570213546)
57. Solis B.H., Cui Y., Weng X. *et al.* (2017), Initial stages of CO₂ adsorption on CaO: a combined experimental and computational study, *Phys. Chem. Chem. Phys.* 19, 4231–4242 (DOI: 10.1039/C6CP08504K)
58. García-Ruiz J.M., Hyde S.T. *et al.* (2003), Self-Assembled Silica-Carbonate Structures and Detection of Ancient Microfossils, *Science* 302, 1194–1197 (DOI: 10.1126/science.1090163)
59. Tan K.H., Iqbal A. *et al.* (2020), Synthesis and characterization of bubble wrap-like hollow barium silicate–carbonate nanospheres for the epoxidation of styrene, *J. Mater. Res. Technol.* 9, 11087–11098 (DOI: 10.1016/j.jmrt.2020.07.109)
60. Shedam M.R., Shedam R.M., Mathad S.N. (2017), Morphological and FTIR Studies of Barium Oxalate Single Crystals, *Acta Chem. Iasi* 25, 195–207 (DOI: 10.1515/achi-2017-0016)

Chapter 5

Guanosine-monophosphate Induced Solubilization of Folic Acid Leading to Hydrogel Formation for Targeted Delivery of Hydrophilic and Hydrophobic Drugs

5.1 Introduction

Cancer is one of the leading causes of death across the globe. Despite the advancement in medical science, there are nearly 10 million deaths per year due to cancer as declared by WHO.^{1,2} A variety of treatment methods are adopted such as surgical procedures followed by chemotherapy treatments,^{3,4} however, bare chemotherapeutic agents or anti-cancer drugs have severe side effects, originating from their non-specificity, toxicity, and poor water-solubility which limits their permeation through the cell membrane, etc.⁵ To mitigate these problems, drugs are loaded into drug carrier systems to make them biocompatible, bioavailable, selective in targeting tumors, and highly efficient.^{6,7} Subsequently, the formulation of new drug delivery systems is of high priority. Hydrogels have emerged as a prominent therapeutic vehicle for efficient drug delivery owing to their biocompatibility, high water content, tissue-like micro-environment, and injectability. These supramolecular systems can encapsulate drugs within their fibrillar morphology resulting in a controlled and sustained release, thus reducing toxicity and side-effects.⁸⁻¹⁴ With the slow and sustained release, targeted delivery is also essential for a smart delivery system. Tumor-targeted drug delivery helps to overcome the adverse effects of conventional chemotherapy, by targeting biomarkers expressed in malignant cells and minimizing toxicity to the healthy cells.¹⁵⁻²¹

A family of glycoproteins known as folate receptors have 100-300 times higher expression in malignant cells as compared to normal cells, making folic acid a suitable agent for targeted delivery.²²⁻²⁵ The

high binding affinity of folate receptors towards folic acid (FA) has led to the development of several folic acid-based drug carriers, where folic acid is anchored on the common delivery systems.²⁶⁻³⁰ Folic acid, also known as vitamin B9, is an essential vitamin that is required for DNA synthesis and tissue growth. A deficiency of folic acid may lead to several other health problems such as anemia, heart diseases, and certain cancers as well as developing irregularities in infants.³¹ However, one major drawback of folic acid is its very low solubility in water of less than 0.01 mg/ml at 25 °C in the pH range of 1-8.³² Therefore, most of the folic acid-based gels are reported to be formed only in organic solvents such as DMSO, DMF, acetonitrile, etc.³³⁻³⁵ Since the human body consists of 70 % water, developing folic acid-based hydrogels will be more potent as a drug-delivery system from a biocompatibility and controlled drug release point of view. There are reports of folic acid hydrogels fabricated through covalent interaction, but these strategies often involve tedious synthetic processes modifying the original FA structure.³⁶⁻³⁹ On the other hand, supramolecular hydrogels, formed through non-covalent interactions have several advantages such as ease of fabrication, stimuli responsiveness, self-healing, and injectability while keeping the original structure and properties of FA intact. Only a few examples of folic acid-based metallo-supramolecular hydrogels have been reported till now which are formed through the coordination bond formation between Zn and FA.^{40,41} For example, a Zn-FA metallogel has been reported that has been used for constructing bio-printable materials.⁴⁰ Another way of formulating supramolecular assemblies involving highly water-insoluble moieties such as FA could be through entrapping inside a self-assembled amphiphile.⁴² The hydrophobic group of the amphiphile can associate with poorly water-soluble compounds to form a self-assembled supramolecular architecture through non-covalent interactions such as hydrogen bonding, π - π stacking, Van-der-Waal forces, electrostatic interactions, etc.

Nucleotides such as adenosine triphosphate (ATP) or guanosine triphosphate (GTP) self-assemble to generate amphiphilic systems that

can prevent disordered protein aggregation at the physiological level. The hydrophobic purine base has several non-covalent interactive sites such as aromatic rings, hydrogen bond donors, and acceptor groups that can provide a hydrophobic environment for scarcely water-soluble compounds.⁴³⁻⁴⁶ Folic acid also interacts with negatively charged hydrophilic phosphate groups of DNA which can further be manifested into a self-assembled structure.⁴⁷ Guanosine monophosphate (GMP) is a widely used low molecular weight gelator (LMWG) as it can form various types of supramolecular assemblies such as G-Quartets, dimers, ribbons, and sheets, owing to the presence of a higher number of hydrogen-bonding sites in guanine as compared to other nucleobases.⁴⁸⁻⁵⁴ Our group has recently shown that GMP-based hydrogels have both hydrophobic and hydrophilic grooves that can load both water-soluble and insoluble drugs, thus making it a universal drug delivery system.¹⁴

Herein, we report the development of a folic acid-GMP hydrogel in a straightforward and synergistic approach, where folic acid helps in self-assembly of GMP into G-quadruplex, which in turn solubilizes folic acid in an aqueous medium by trapping them into the hydrophobic grooves. This results in a thermo-reversible, injectable, thixotropic, and biocompatible self-assembled hydrogel. Incorporating folic acid into a supramolecular hierarchy enhanced its water solubility and resulted in a homogeneous hydrogel. The hydrogel could encapsulate hydrophilic drug doxorubicin hydrochloride (Dox.HCl) and hydrophobic drug curcumin by improving its water solubility. Curcumin is a natural compound extracted from turmeric and is a potent anticancer drug, however poor water solubility reduces its bioavailability. Due to the hydrotropic nature of the hydrogel, curcumin remains water-dispersible for a prolonged time when loaded in the hydrogel, demonstrating significant enhancement in anticancer activity and cellular uptake as compared to their bare forms. Thus, the all-bioderived FA-GMP hydrogel can efficiently lower the drug dosage, reducing the damage to normal tissues and making it a potent drug delivery vehicle for anticancer treatment.

5.2 Results and Discussions.

5.2.1. Fabrication of FA-GMP Hydrogel

Folic Acid (FA) in its bare form was completely insoluble in water; however, adding GMP to it in a 1:3 ratio resulted in a water-soluble homogeneous self-assembled system that ultimately led to the formation of a hydrogel. 100 mM of FA was added to a 300 mM aqueous solution of GMP at physiological pH. The solution was heated until FA was completely dissolved (65 °C) to give a bright orange-colored solution, which turned into a homogeneous self-assembled hydrogel upon cooling to room temperature (Figure 5.1). The formation of self-assembled FA-GMP hydrogel was visually confirmed by the vial-inversion test method, where the solvent remained trapped inside the gel matrix upon inversion. The FA-GMP hydrogel exhibited a thermoreversible behavior, allowing it to undergo a reversible transition to solution state when heated to 50 °C and subsequently turn back to a hydrogel when cooled to room temperature.

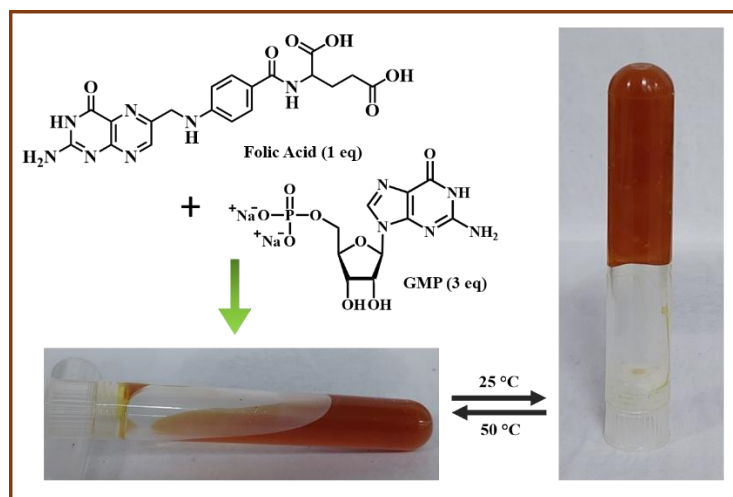


Figure 5.1. Formation of FA-GMP hydrogel and its thermoreversible property.

Concentration-dependent studies were performed for the hydrogel (Figure 5.2a). Even though the hydrogel was formed at a 1:2.5 ratio of FA and GMP, the gel was opaque and heterogenous and the hydrogel turned homogenous only when FA and GMP ratio was 1:3. Critical gelation concentration of FA and GMP was measured by varying

the FA and GMP concentration while keeping a fixed ratio of 1:3 (Figure 5.2a ii). The minimum concentration for gelation at a 1:3 molar ratio was 75 mM and 225 mM for FA and GMP respectively. The hydrogel and bare FA solution (100 mM) were diluted up to 3 times (Figure 5.2b) to demonstrate the improved solubility of folic acid when incorporated into the hydrogel as compared to bare folic acid.

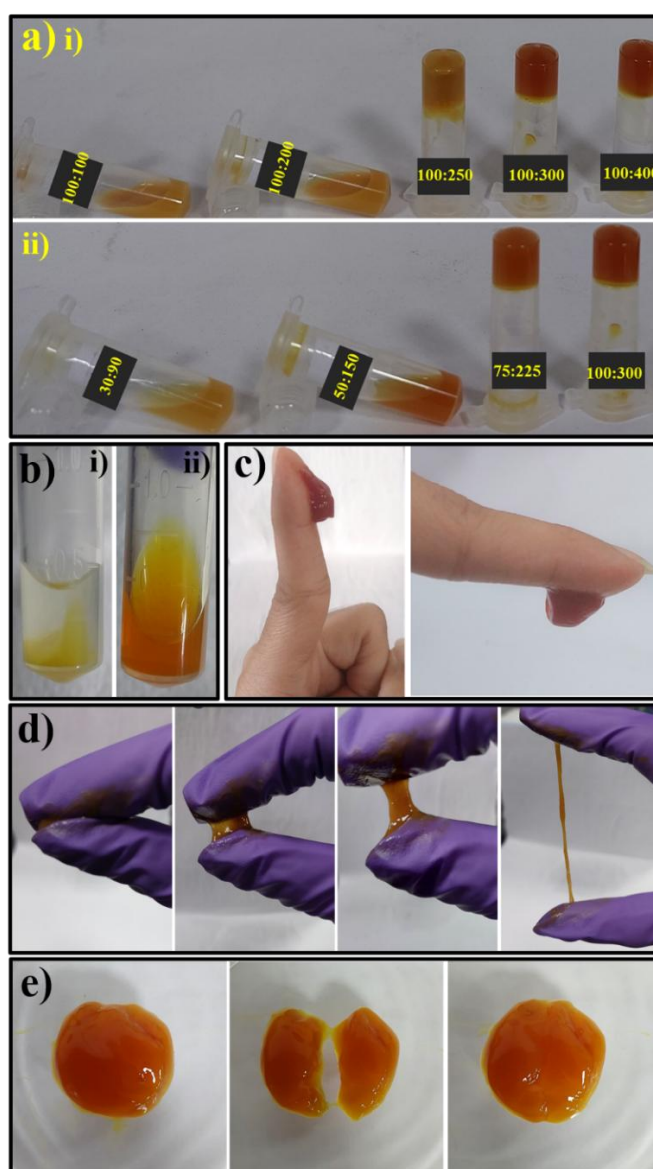


Figure 5.2. Digital images demonstrating (a) Concentration-dependent experiment (i) varying the concentration ratio between FA and GMP from 1: to 1:4 and (ii) varying concentrations of FA and GMP at a fixed 1:3 molar ratio, (b) (i) 100 mM of stock FA solution diluted by 3 times and (ii) 100 mM FA hydrogel with 300 mM GMP diluted up to 3 times to obtain a clear solution, (c) self-adhesive property of the FA-GMP hydrogel, (d) flexibility of the hydrogel where it can be compressed and stretched to a thin line.

The self-adhesive nature of the hydrogel keeps it stuck to the glove, and (e) the self-healing property of the hydrogel.

The diluted FA-GMP system was a homogenous solution whereas bare FA was sparingly soluble in water. The hydrogel also showed self-adhesive behavior as shown in figure 5.2c. The FA-GMP hydrogel was also flexible since it could be compressed and stretched to a string (Figure 5.2d). The self-healing nature of the hydrogel was demonstrated by cutting a piece into two halves and joining them together resulting in the recovery of the dissected pieces back to the original shape (Figure 5.2e).

5.2.2. Morphological Evaluation.

The morphology of the FA-GMP hydrogel was analyzed using a variety of microscopy techniques. The dried Fe-GMP hydrogel on a glass plate showed the formation of highly entangled nanofibers with an average diameter of 10-15 nm in scanning electron microscopy (Figure 5.3a).

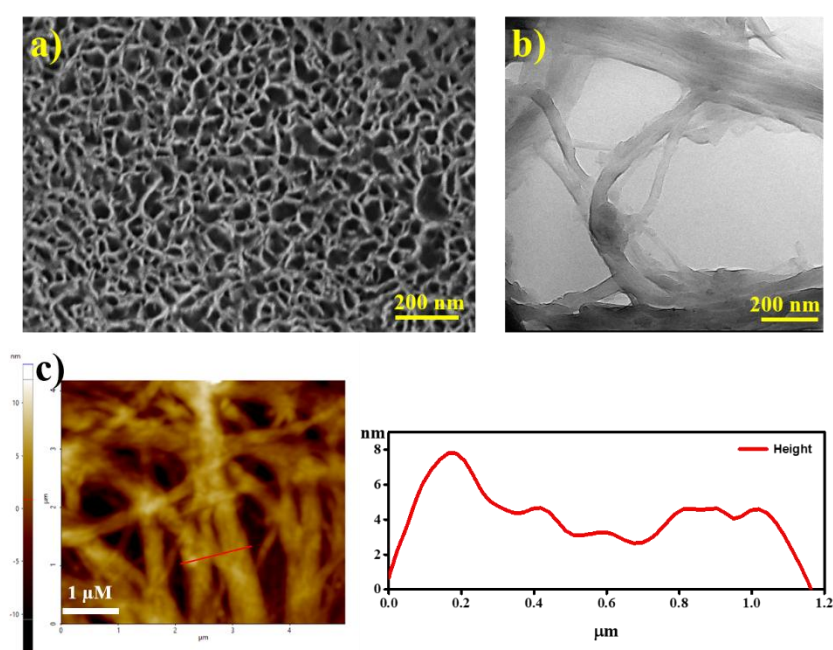


Figure 5.3. (a) FESEM, (b) TEM, and (c) AFM images of the FA-GMP hydrogel showing highly tangled fibrillar morphology.

Further, transmission electron microscopy (TEM) revealed the detailed crosslinking and bundling of thin fibers into larger, intertwined bundles that could extend up to a diameter of 150-200 nm (Figure 5.3b). Possibly,

individual G-quadruplex strands were intensely crosslinked through noncovalent bonding interactions to form bundles resulting in the formation of the entangled fibrillar network. Atomic force microscopy (AFM) further confirmed the formation of interwoven fibrils with an average height of 3-7 nm (Figure 5.3 c).

5.2.3. Spectroscopic Characterization.

Various spectroscopic techniques were utilized to study the self-assembly mechanism of the FA-GMP hydrogel. UV-visible spectrum for GMP showed its characteristic peaks at 253 nm and a shoulder at 275 nm (Figure 5.4a). The UV-visible spectrum for folic acid was recorded at a slightly basic pH, to increase solubility. The folic acid molecule consists of three distinct moieties, pterin (PT), p-aminobenzoic acid (p-ABA), and L-glutamic acid (Glu). The band at 280 nm is attributed to the π - π^* electronic transition of enone in pterin and carboxylate from the glutamic acid, whereas the band at 346 nm is assigned to the n - π^* electronic transition in pterin.⁵⁵⁻⁵⁹ The absorption maximum of GMP at 253 nm was retained in the FA-GMP hydrogel. In the FA-GMP hydrogel, the absorption peak was observed at 274 nm (a hypsochromic shift of 6 nm as compared to FA solubilized in basic medium), which is an indicator that the hydrogel was formed at near-neutral condition.^{58,59} To further understand the self-assembly of the FA-GMP hydrogel, a powder XRD experiment was performed (Figure 5.4b). The diffraction peaks obtained at 2θ of 4.4° ($d = 1.97$ nm) and 2θ of 27.26° ($d = 0.32$ nm) are attributed to the diameter of a single G-quartet and interplanar separation between π - π stacked G-quartets respectively.^{49,60} The formation of G-quartet was also validated by comparing the ^{23}Na NMR spectra of Na_2GMP solution and FA-GMP hydrogel (Figure 5.4c). GMP and FA-GMP hydrogel showed a sharp peak near 0 ppm, attributed to the free sodium ions. However, FA-GMP hydrogel also showed an additional peak at -18.07 ppm corresponding to the sodium ion inside the G-quadruplex channel.⁶¹⁻⁶⁴ Thioflavin T (ThT) binding assay also reaffirmed the formation of G-quadruplex structure in the FA-GMP self-assembly (Figure 5.4d). ThT is a fluorogenic dye showing multifold fluorescence enhancement at 472

nm when excited at 405 nm upon binding to FA-GMP hydrogel compared to its free form. This enhancement in emission phenomenon is observed due to the binding of ThT between the π - π stacking of G-quartet-induced fibrils, thus restricting their intramolecular motions, which otherwise leads to quenching in its free form.^{65–67} The amplification in fluorescence intensity of ThT in hydrogel as compared to free ThT solution could also be observed visually when both the vials were exposed to long-range UV light (Figure 5.4d inset).

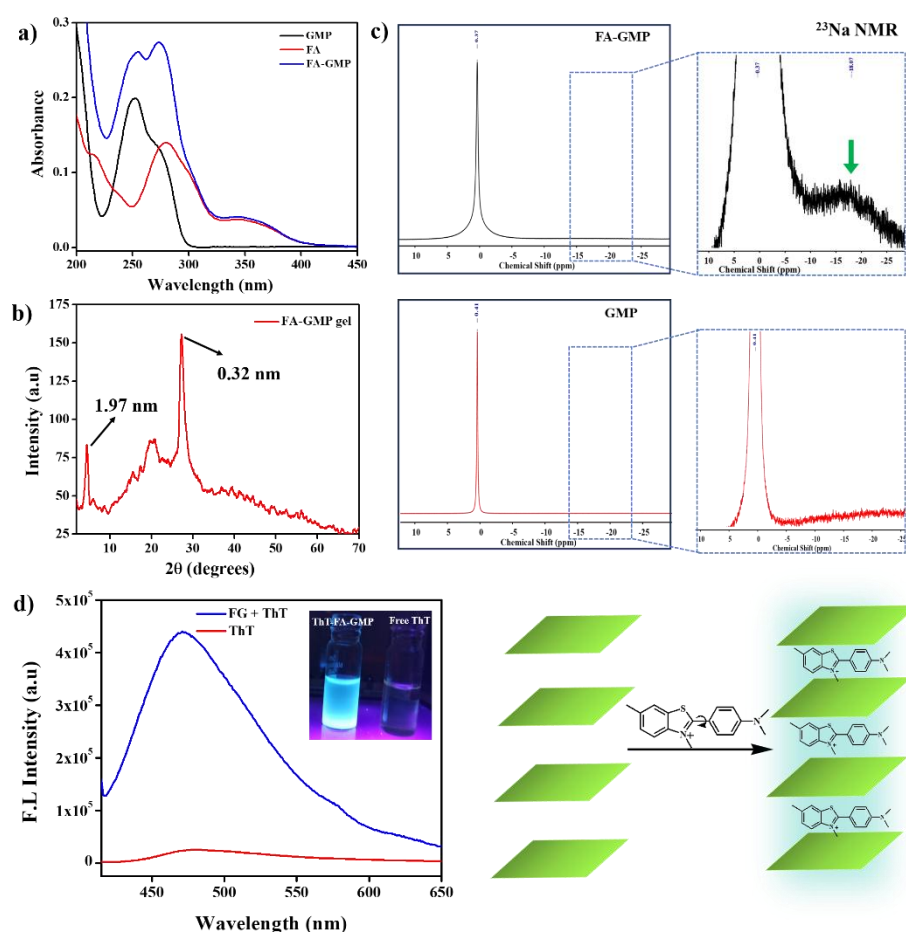


Figure 5.4. (a) UV-visible spectra of FA, GMP, and FA-GMP hydrogel, (b) PXRD of FA-GMP xerogel, (c) ^{23}Na NMR spectra for GMP and FA-GMP hydrogel, (d) Fluorescence spectra of free ThT solution (10 μM) and ThT (10 μM) loaded to FA-GMP system, inset: digital image of ThT bound to FA-GMP system (left) and free ThT solution (right)

To investigate the interaction between FA and GMP within the hydrogel, we analyzed ^{31}P NMR spectra of GMP and FA-GMP hydrogel (Figure 5.5a). The upfield shift of the phosphate group signal from 3.5

ppm to 1.8 ppm in the FA-GMP hydrogel spectrum, as compared to free GMP, confirmed its involvement in the crosslinking of G-quartets with FA to form the hydrogel. FTIR was performed to further delve into the functional groups involved in FA-GMP interactions (Figure 5.5b). In the case of GMP, the peaks at 1687 cm^{-1} and 1478 cm^{-1} attributed to $\text{C}(6)=\text{O}$ and $\text{C}(8)-\text{N}(7)$ bond vibration were shifted to 1692 cm^{-1} and 1473 cm^{-1} respectively in FA-GMP xerogel, showing their involvement in the formation of G-Quartet.⁶⁸ Further, the peaks at 1065 and 967 cm^{-1} corresponding to the PO_4^{3-} group in GMP, were shifted to 1037 and 972 cm^{-1} in the xerogel showing the involvement of the phosphate group which is in good agreement with the ^{31}P NMR spectra.^{68,69} In the FTIR spectrum of folic acid, the stretching frequencies at 3544 , 3414 , and 3324 cm^{-1} are associated with the $-\text{OH}$ bond of the glutamic acid moiety, and their disappearance in the FA-GMP hydrogel further indicates their involvement in H-bonding for self-assembly formation.^{70,71}

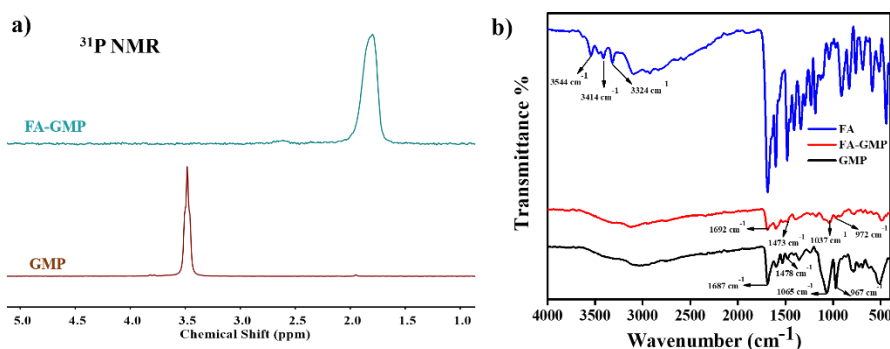


Figure 5.5. (a) ^{31}P NMR of GMP and FA-GMP hydrogel and (b) FTIR of FA, GMP, and FA-GMP xerogel.

Based on the spectroscopic observations, a plausible mechanism for the FA- GMP hydrogel formation is proposed (Figure 5.6). From PXRD, ^{23}Na NMR, and ThT binding assay, we confirmed the G-quartet formation in the hydrogel. The glutamic acid functionality in FA induces the self-assembly of guanine into G-quadruplex. The protonation of the phosphate group leads to a reduction in the anionic charge and decreases repulsion among G-Quartets, which in turn promotes the stacking of the tetrads. Phosphate group protonation further enables H-bonding, facilitating a 3D network formation through cross-linking.^{72–75} ^{31}P NMR

and FTIR studies suggest that the interaction between FA and GMP occurs through H-bonding between the phosphate group (PO_3H^-) of GMP with the carboxylate group of FA. Folic Acid here acts as a crosslinker between the stacks of G-quartets leading to the formation of a highly entangled three-dimensional fibril network. Also, the amphiphilic nature of the nucleotide provided sufficient hydrophobicity and strong hydrogen bonding that promoted the co-assembly of water-insoluble FA into homogeneous water-soluble supramolecular structure. Thus, non-covalent interactions like π - π stacking of aromatic moiety, H-bonding, Van-der-Waal forces, hydrophobic interactions, electrostatic interactions, etc., resulted in the formation of a self-assembled FA-GMP hydrogel.

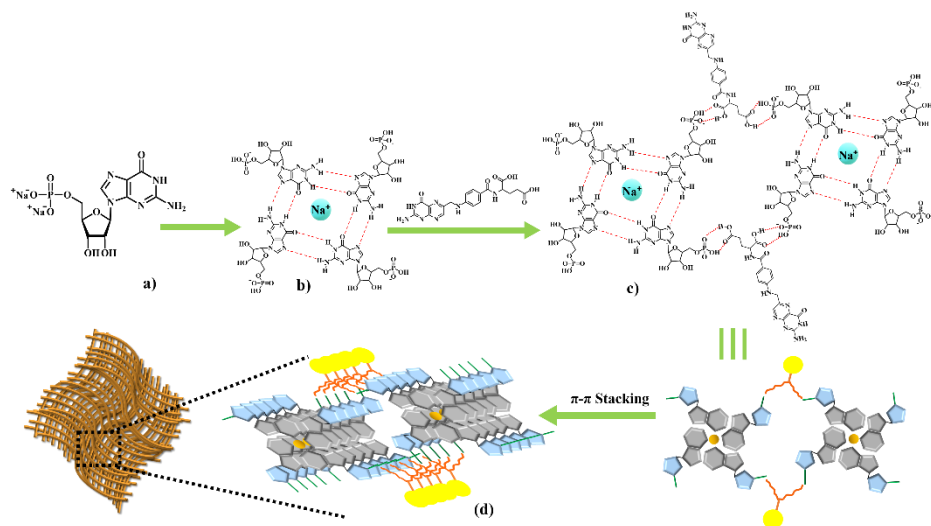


Figure 5.6. Schematic representation for the proposed self-assembly mechanism of FA and GMP leading to hydrogel formation.

5.2.4. Rheological Studies

Rheological studies were conducted to assess the viscoelastic properties of the hydrogel. Both strain and frequency sweep measurements revealed a predominantly elastic behavior over viscous behavior, with the storage modulus (G') value exceeding the loss modulus (G'') (Figure 5.7a, b). The hydrogel exhibited a high breaking point of 235%, as determined by strain sweep experiments. Shear stress-dependent recoverability of the hydrogel was determined by performing the thixotropic loop test, by providing alternating low (0.1%) and high (300%) strain with a rest period of 100 seconds in between (Figure 5.7c).

The hydrogel demonstrated excellent recoverability up to 7 cycles without any loss in mechanical properties. Additionally, the hydrogel also showed injectable properties (Figure 5.7d).

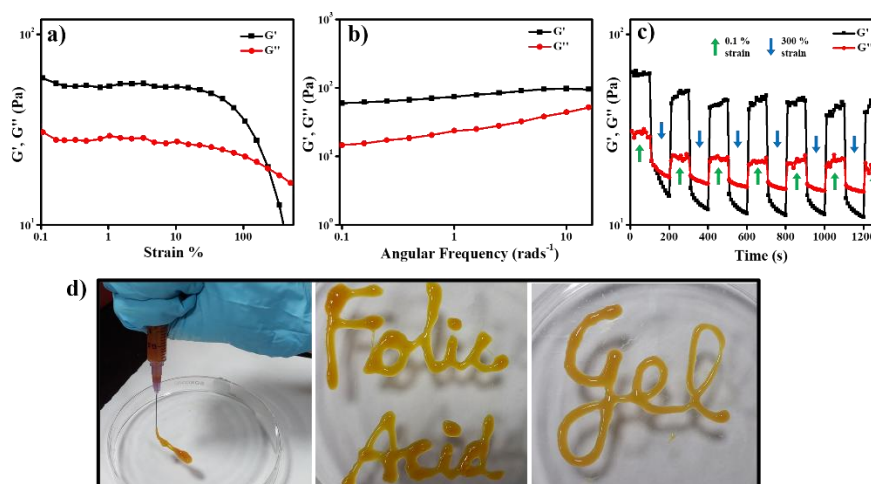


Figure 5.7. (a) Dynamic strain-sweep analysis, (b) Frequency sweep measurement at a constant strain of 1%, (c) Thixotropic loop measurements at a constant angular frequency of 10 rad s⁻¹ for FA-GMP hydrogel, and (d) digital images showing injectability of FA-GMP hydrogel.

5.2.5. Drug encapsulation and release

Folate receptors are common biomarkers for cancer cells due to their overexpression on the cell surface of numerous cancer types. Owing to the high binding affinity of folic acid to the folate receptors, we employed the FA-GMP hydrogel as a vehicle for targeted drug delivery. The ease of in situ drug encapsulation makes the hydrogel a suitable drug delivery vehicle. This approach facilitates precise control over drug concentration through uniform drug dispersion within the solution before gelation. In this study, we used doxorubicin hydrochloride (Dox), a commercially used drug in chemotherapy as the hydrophilic drug, and curcumin (Cur), a bio-extract material from turmeric as the hydrophobic drug (Figure 5.8a). The mechanical strength of the drug-loaded hydrogels was measured by performing an amplitude strain sweep experiment (Figure 5.8b). To attain uniform drug dispersion in the gel matrix, 500 μ g/ml of Dox and 300 μ g/ml of Curcumin were added in situ during hydrogel formation. A mixture of ethanol and water at a 1:4 ratio was used to fabricate curcumin-loaded FA-GMP hydrogel. Bare curcumin started

precipitating in the solution mixture, however, it stayed homogeneously dispersed in the solvent when entrapped in the hydrogel matrix. For demonstration, 300 $\mu\text{g/ml}$ curcumin in EtOH-Water mixture, both bare and loaded in the FA-GMP hydrogel were diluted up to three times and left for 1h (Figure 5.8c). The settling down of curcumin was observed in the bare solution, whereas curcumin loaded in the FA-GMP matrix stayed dispersed maintaining a homogeneous solution even after 30 days, thus, improving the bioavailability of curcumin. This improved solubility of curcumin in aqueous medium suggests that the hydrophobic molecules can be trapped in the hydrophobic grooves of the hydrogel and stabilized by π - π interactions between the aromatic G-quartet planes.

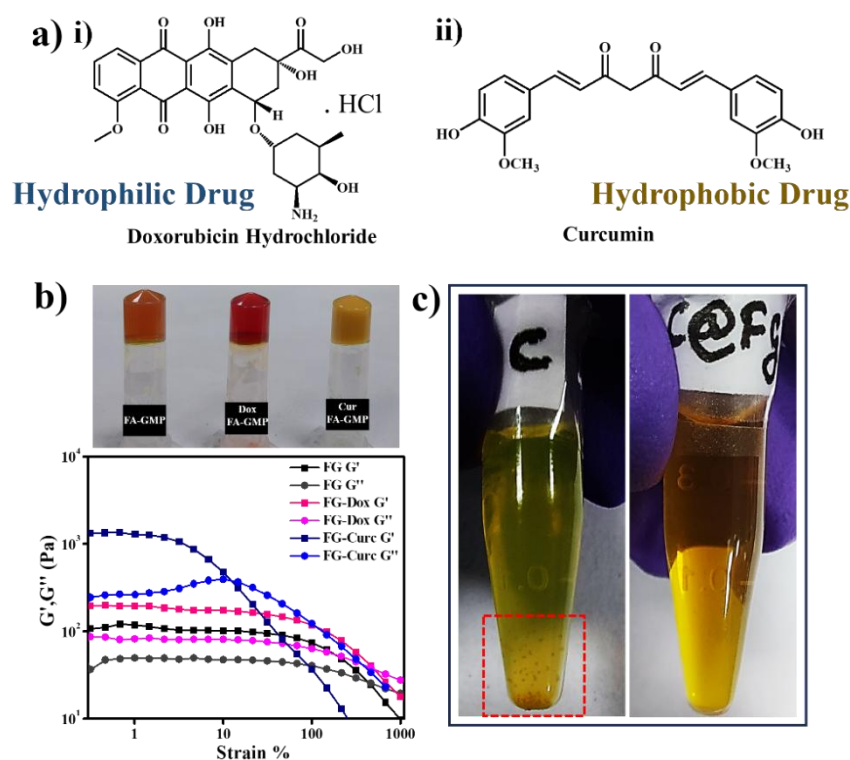


Figure 5.8. (a) Structure of (i) hydrophilic drug: Doxorubicin hydrochloride and (ii) hydrophobic drug: curcumin, (b) Digital images of FA-GMP hydrogel, Dox-loaded FA-GMP hydrogel, and curcumin-loaded FA-GMP hydrogel and their amplitude strain-sweep analysis, and (c) Digital image of Left: 300 $\mu\text{g/ml}$ of bare curcumin in 1:4 EtOH-Water mixture diluted by 3 times, Right: 300 $\mu\text{g/ml}$ of curcumin loaded in hydrogel (1:4 EtOH-Water) and diluted by 3 times.

Both the drug-loaded hydrogels were washed in the PBS buffer of pH 7.4, to remove the unbound drug. The encapsulation efficiency for

Dox and curcumin were calculated to be 82.5% and 89% from the calibration curve (Figure 5.9) respectively. The higher encapsulation efficiency of the hydrophobic drug is attributed to its low water solubility, which minimizes leaching during washing once encapsulated inside the matrix.⁷⁶

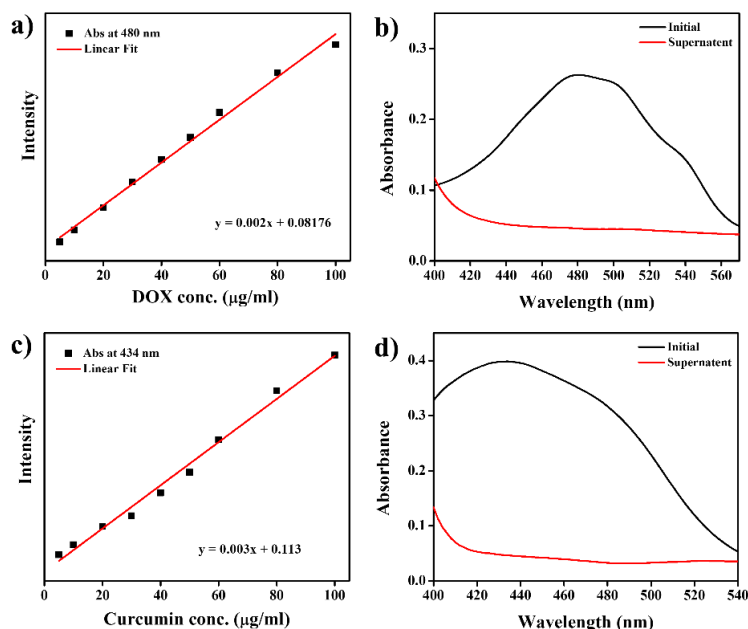


Figure 5.9. (a) Calibration curve of Doxorubicin, (b) UV-visible absorbance spectra of Dox taken initially and of the supernatant obtained after washing the Dox loaded hydrogel, (c) Calibration curve of Curcumin, (d) UV-visible absorbance spectra of curcumin taken initially and of the supernatant obtained after washing the curcumin loaded hydrogel.

To study the drug release process of the hydrogel, 1 ml of both the Dox-FA-GMP and Cur-FA-GMP gels were kept undisturbed in 4 ml of PBS buffer to make the total volume of 5 ml. An aliquot of 400 μl was taken out at regular time intervals and replenished with the same amount of fresh buffer. The drug release profile for Dox and curcumin was evaluated through UV-visible spectrophotometry (Figure 5.10). Both the drugs followed a first-order release profile with an initial lag period required for swelling of the hydrogel matrix. This facilitated the release of the trapped drug molecules into the buffer medium through diffusion. Subsequently, a gradual release occurs, followed by the final stage where the release rate reaches saturation after complete swelling. Dox-FA-GMP

and Cur-FA-GMP exhibited lag periods of 1.5 and 3 hours, followed by a gradual release reaching 83% and 57% respectively within 20 hours. The release slowed to saturation, reaching 91% for Dox-FA-GMP and 63% for Cur-FA-GMP after 40 hours. The lower release of curcumin could be due to the higher mechanical robustness of the curcumin-loaded hydrogel. Cur-FA-GMP gel had higher mechanical strength than Dox-FA-GMP hydrogel system. G' (storage modulus) for Cu-FA-GMP was higher than 10^3 Pa, whereas, in the case of FA-GMP and Dox-FA-GMP, G'' lies around 10^2 Pa. (Figure 5.8b). Adding a small amount of EtOH probably led to additional non-covalent interactions, resulting in higher stiffness of Cur-FA-GMP hydrogel.

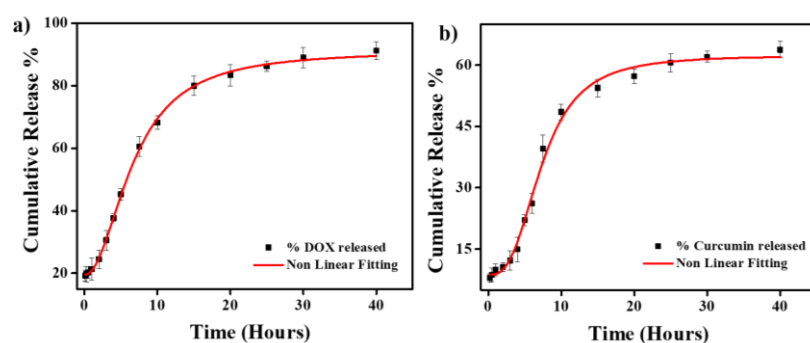


Figure 5.10. The cumulative release profile of (a) Doxorubicin and (b) Curcumin from FA-GMP hydrogel.

5.2.6. Biocompatibility of FA-GMP hydrogel

The biocompatibility of FA-GMP hydrogel and its precursors GMP and FA were evaluated by performing an MTT assay on the human embryonic kidney (HEK) 293T cell line (Figure 5.11). HEK293T are healthy non-cancerous cells, commonly used for biological studies to assess the effect of drugs and materials. FA and GMP exhibited IC_{50} values of 1.8 mg/ml and 5.6 mg/ml, respectively showing their high biocompatibility. In the case of FA-GMP hydrogel, the IC_{50} value was calculated to be 18 mg/ml. Thus, the FA-GMP hydrogel was highly biocompatible, which is a highly desirable property for a drug carrier.

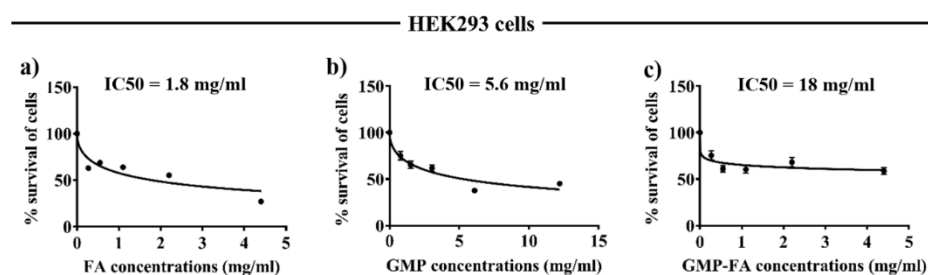


Figure 5.11. Assessment of HEK293T cells viability after treatment with a) FA, b) GMP, and c) FA-GMP.

5.2.7. Cytotoxicity against cancerous cell line

MCF – 7 cells

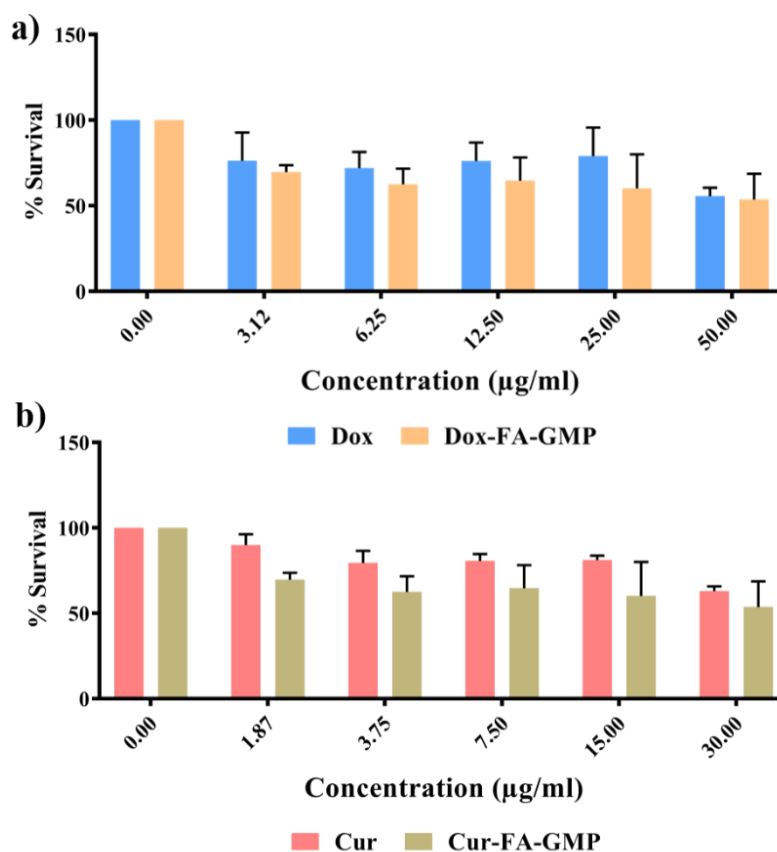


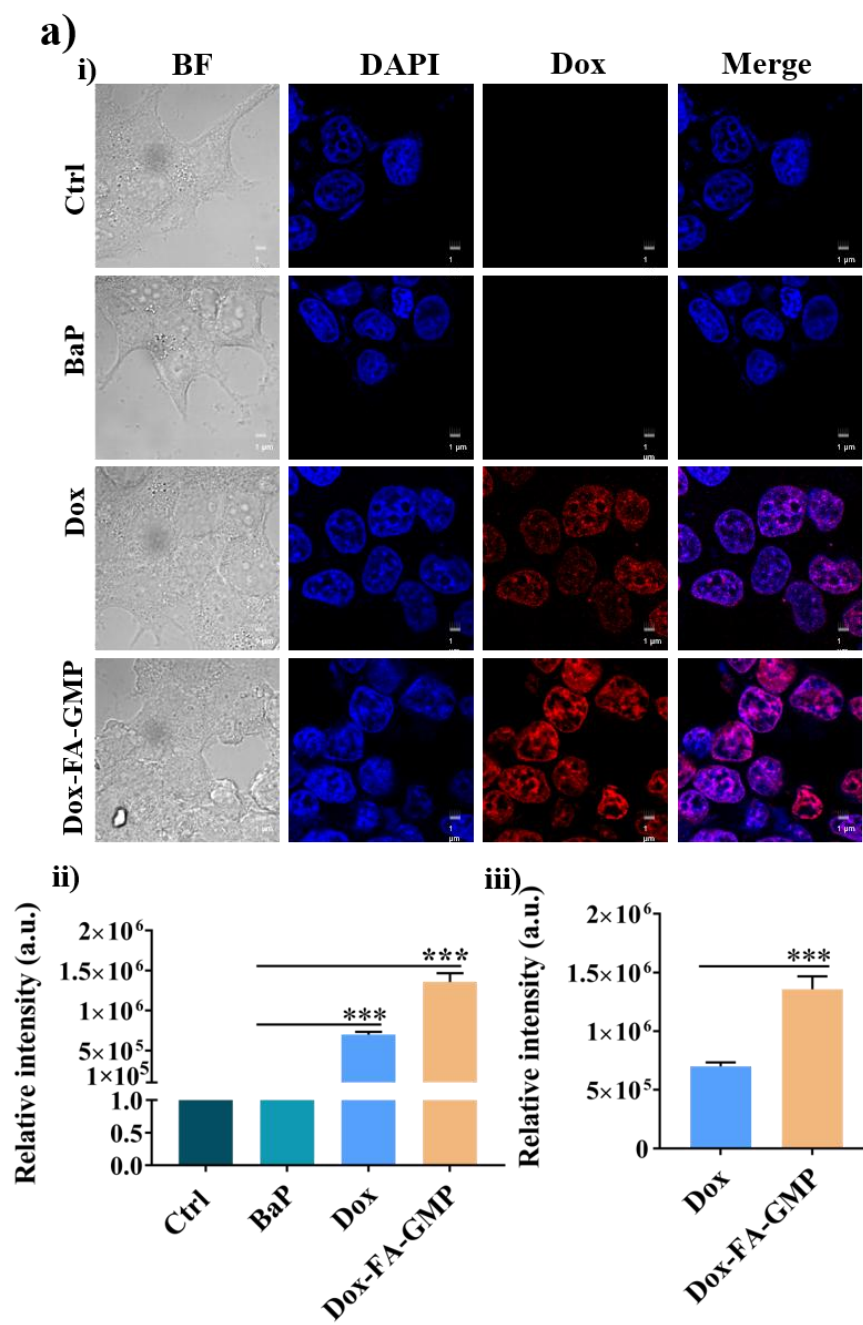
Figure 5.12. Cell viability of MCF-7 cells after treatment with (a) Dox, (b) Dox-FA-GMP, (c) Cur, and (d) Cur-FA-GMP

The MCF-7 cell lines were used to examine the viability of cancer cells when treated with Dox and curcumin in their free state and after their loading into the FA-GMP hydrogel (Figure 5.12). MCF-7 is a well-established human breast cancer cell line and has over-expressed folate receptors on its surface. MTT assay was performed by varying the

concentration of the samples with respect to the concentration of the drugs. The percentage survival of MCF 7 cells was higher in the case of pristine Dox and curcumin as compared to Dox-FA-GMP (Figure 6a) and Cur-FA-GMP hydrogel systems (Figure 6b). These results demonstrated that encapsulating the drugs within the FA-GMP hydrogel system increases their cytotoxicity against the cancer cells. This enhancement in cytotoxicity could be explained by the targeted interaction of folic acid with the folate receptors.

5.2.8. Cellular uptake Evaluation

Based on the MTT assay test against MCF7 cells, we further assessed the cellular internalization of the drugs in their free state and after loading in the FA-GMP hydrogel (Figure 5.13). The cellular uptake of Dox and Dox-FA-GMP was studied through their fluorescence signal in CLSM and the cellular uptake in the case of curcumin and Cur-FA-GMP was studied through their fluorescence signal in fluorescence microscopy. A fluorescent dye, DAPI was used as the contrasting agent to stain the nuclei to demonstrate the localization of the drug. However, Dox and curcumin had inherent red and green fluorescence. In the case of Dox, the fluorescence intensity was significantly higher when loaded in the FA-GMP hydrogel compared to its bare form ($p < 0.0001$). This enhancement in fluorescence intensity indicated that hydrogel could deliver Dox more efficiently inside MCF-7 cells. Similar results were observed for curcumin, where a statistically significant increment ($p < 0.05$) in the intensity of curcumin loaded in hydrogel than its free state indicated the efficient delivery of curcumin in the cells facilitated by FA-GMP hydrogel. The folate receptors overexpressed on cancer cells interact with folates, enhancing the cellular uptake via the endocytosis mechanism, which would explain the higher cellular uptake of both Dox and curcumin when loaded in the FA-GMP hydrogel.



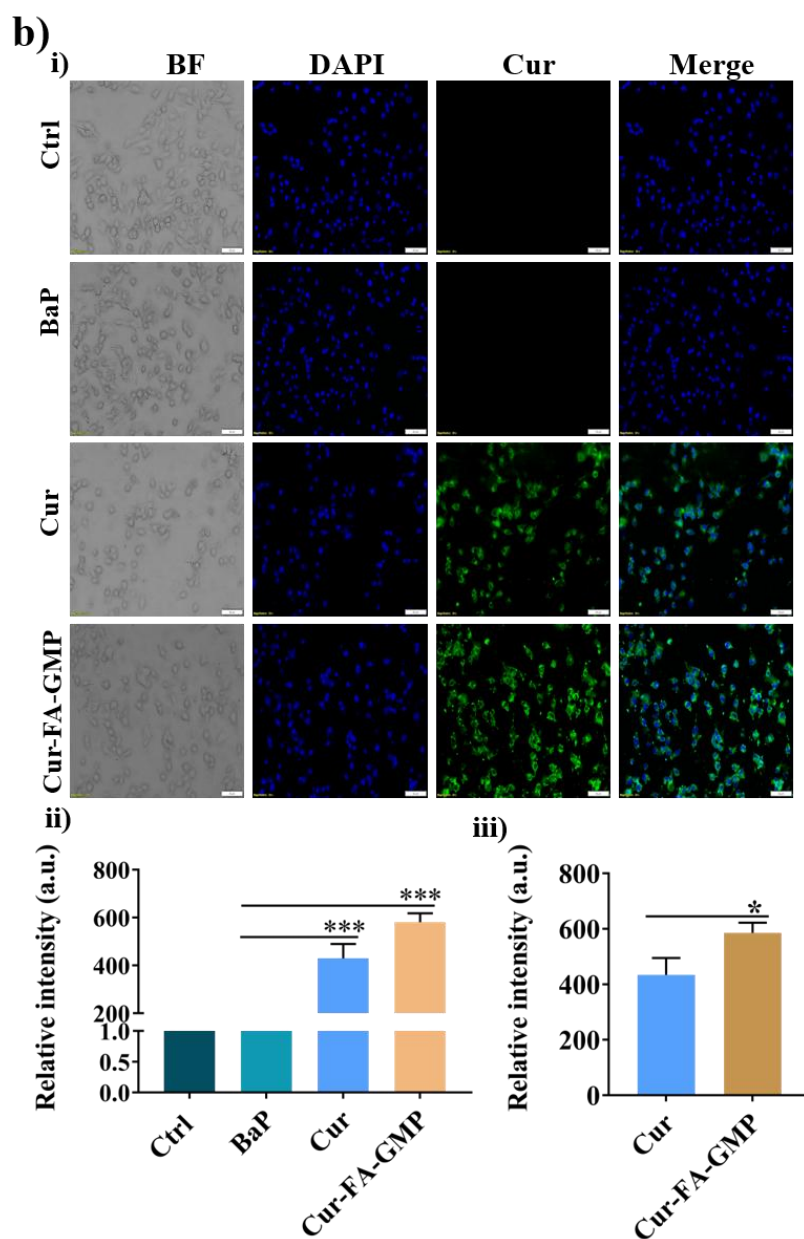


Figure 5.13. Measuring the cellular uptake for cancer cell MCF7, a) (i) CLSM images for free Dox and Dox-FA-GMP, (ii) quantification of Dox and Dox-FA-GMP intensity compared to BaP, (iii) comparison of intensity difference between Dox and Dox-FA-GMP, and b) (i) CLSM images for free Cur and Cur-FA-GMP, (ii) quantification of Cur and Cur-FA-GMP intensity compared to BaP, (iii) comparison of intensity difference between Cur and Cur-FA-GMP.

5.2.9. Anticancer properties of compounds

Quantitative real-time polymerase chain reaction (qRT-PCR) was performed on MCF-7 cells to evaluate the expression of tumor suppressor genes, apoptotic markers, and cell cycle regulators after inducing cancer-like properties with benzopyrene (Figure 5.14). Tumor suppressor genes,

including p53 and pRb, showed a statistically significant increase in expression in the Dox-FA-GMP and Cur-FA-GMP groups ($p < 0.05$) compared to the control, with superior upregulation relative to free Dox and curcumin. This indicates that drug loading in FA-GMP enhances tumor growth suppression. Further analysis revealed significant upregulation of apoptotic genes (bax, bak, bid, and caspase 9) in the Dox-FA-GMP and Cur-FA-GMP groups compared to free drugs, highlighting the hydrogel's ability to promote apoptosis more effectively. Additionally, cell cycle regulators (ccnd1, ccnb1, and cdk1) showed a significant decrease in the Dox-FA-GMP group relative to free Dox, while PCNA exhibited a greater decline in both Dox-FA-GMP and Cur-FA-GMP compared to free drugs, indicating drugs encapsulated in FA-GMP hydrogel can halt cell progression better than their bare state. These results demonstrate that the FA-GMP hydrogel system enhances the therapeutic efficacy of Dox and Cur in suppressing tumor growth, promoting apoptosis, and arresting cell cycle progression.

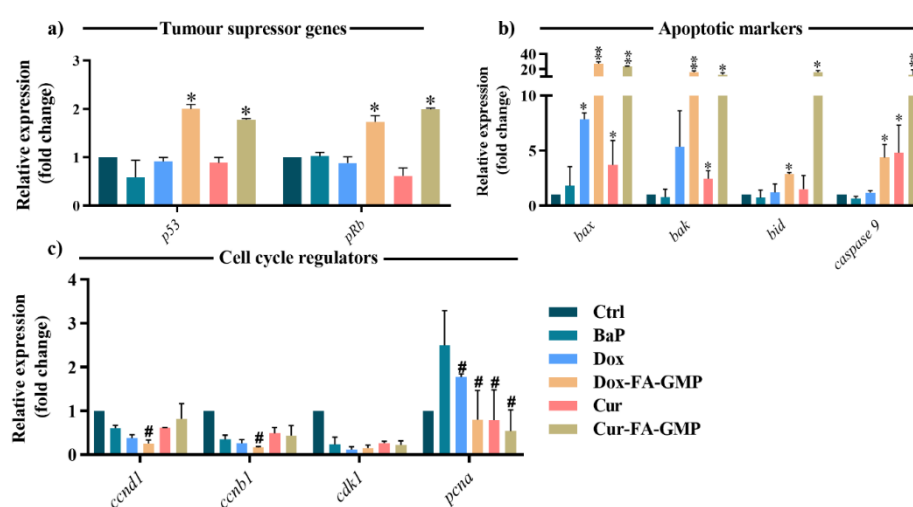


Figure 5.14. Investigating the markers related to cancer properties. **a)** Tumour suppressor genes (p53 and pRb) expression analysis after exposure to Dox, Dox-FA-GMP, Cur and Cur-FA-GMP. **b)** Changes in the mRNA expression level of apoptotic markers (bax, bak, bid, and caspase 9) compared to the BaP samples. **c)** Graph representing the amendments in the transcript level of cell cycle regulator genes (ccnd1, ccnb1, cdk1, and pcna). Given plots; x-axis, different genes; y-axis, fold change with respect to BaP exposed samples. The p-values of < 0.05 , < 0.01 , and < 0.0001 are considered statistically significant and are represented with *, **, and *** respectively. The increase and decrease are represented by * and # respectively.

Since cancer cells proliferate indefinitely due to changes in genetic makeup, we investigated the cell proliferation of MCF-7 cells when exposed to Dox, Dox-FA-GMP, Cur, and Cur-FA-GMP (Figure 5.15). The cells were stained by crystal violet basic dye which non-specifically binds to negatively charged molecules of cells such as surface molecules, extracellular matrix, proteins, polysaccharides, DNA/RNA, etc. Microscopic images in Figure 5.15a showed the lowest cell density for Dox-FA-GMP and Cur-FA-GMP indicating a more significant inhibition of cell proliferation than free drugs. On quantitatively analyzing microscopic images of crystal violet staining (Figure 5.15b), the strongest reduction in proliferation was observed for Dox-FA-GMP and Cur-FA-GMP, highlighting the superior efficacy of hydrogel as the drug carrier suppressing cell growth.

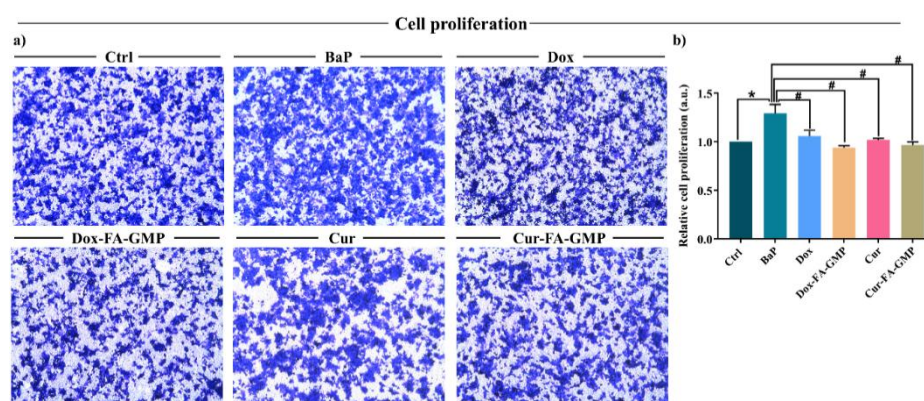


Figure 5.15. Demonstration of cell proliferation assay. a) Bright-field microscopy images of crystal violet stained cells after treatment with Dox, Dox-FA-GMP, Cur, and Cur-FA-GMP. b) Quantification of proliferating cells in Dox, Dox-FA-GMP, Cur and Cur-FA-GMP compared to the BaP. Given plot; x-axis, different samples; y-axis, relative cell proliferation with respect to BaP exposed samples. The p-values of <0.05 , <0.01 and <0.0001 are considered statistically significant and are represented with *, **, and *** respectively. The increase and decrease are represented by * and # respectively.

5.3. Conclusion

In summary, we proposed a straightforward method for preparing a folic acid hydrogel, achieved by enhancing its water solubility through self-assembly with an amphiphilic LMWG guanosine monophosphate

(GMP). The gelation process was spontaneous and the FA-GMP hydrogel was thermoreversible, injectable, thixotropic, self-healing, and self-adhesive. The hydrogel was highly biocompatible, considering precursors themselves are non-toxic and the system comprised only water solvent. The FA-GMP hydrogel was then employed as a drug carrier that could encapsulate both hydrophilic (Dox) and hydrophobic (curcumin) drugs and showed sustained release. Both the drugs showed elevated cytotoxicity and cellular uptake in the MCF-7 cancer cells when loaded in the FA-GMP hydrogel than their free form. Hydrogel-encapsulated drugs (Dox-FA-GMP and Curc-FA-GMP) demonstrated improved therapeutic efficacy compared to free drugs by significantly upregulating the expression of tumor suppressor and apoptotic genes, while also inhibiting cell proliferation markers to a greater extent than free drugs. Loading Dox and curcumin in FA-GMP hydrogel demonstrated improved targeted delivery and overall anticancer activity. Thus, the folic acid hydrogel with GMP represents a simple, economical, and biocompatible approach that can be an effective drug carrier for targeted delivery, aiding in the fight against cancer.

5.4. Experimental Section

5.4.1. Materials

Folic acid was purchased from Sigma-Aldrich. Guanosine-5'-monophosphate disodium salt hydrate ($\text{Na}_2\text{-GMP}$) and deuterium oxide (D_2O) were purchased from Sisco Research Laboratory (SRL). Curcumin was from Alfa-Aesar and doxorubicin hydrochloride was used from BLD. Milli-Q was purchased from Merck, India. All the chemicals were used as purchased with no further purification. The MCF-7 and HEK-293T cells were procured from the National Centre for Cell Science, Pune, India. The cells were cultured in Dulbecco's modified Eagle's medium DMEM; Thermo Scientific, USA) supplemented with 10% fetal bovine serum (FBS; Thermo Scientific, USA),

5.4.2. Instrumentation

UV-Vis and Circular Dichroism (CD) studies were recorded on a Perkin Elmer UV-Vis-NIR spectrophotometer (Model: Lambda 1050) and JASCO J-815 spectropolarimeter using a quartz cuvette of path length 1 mm respectively. Field emission scanning electron microscopy (FESEM) images were taken on Carl Zeiss Supra 55 instruments after Au coating. Transmission Electron microscope (TEM) images were taken from the electron microscope of model JEM-2100 at an accelerating voltage of 200 kV. Rheological studies were done using an Anton Paar Physica MCR 301 rheometer with parallel plate geometry (diameter 25 mm). A dynamic strain sweep experiment was performed using a constant frequency of 10 rad s⁻¹. The dynamic frequency sweep of the hydrogel was measured as a function of frequency in the range of 0.1–17 rad s⁻¹ with a constant strain value of 1%. The thixotropic loop test was carried out at a constant frequency of 10 rad s⁻¹, and the applied strain was changed from 0.1% to 300%. Powder X-ray diffraction patterns (PXRD) of the xerogel were recorded on a Rigaku Smartlab, Automated Multipurpose X-ray diffractometer with Cu K α source (the wavelength of the X-rays was 0.154 nm). FTIR study of xerogel was done on Bruker Alpha II Platinum ATR. ¹H, ³¹P, and ²³Na NMR spectra were recorded using a 500 MHz Bruker AV500 NMR instrument at 298 K using D₂O as solvent. The fluorescence studies were performed using the Fluoromax-4p spectrofluorometer from Horiba Jobin Yvon (FM-100). Fluorescence spectra were analyzed using OriginPro 8.1 software and the measurements were carried out at room temperature. Confocal laser scanning microscope (CLSM) was recorded on Olympus America Inc., USA.

5.4.3 Synthesis of the hydrogel

100 mM folic acid (FA) and 300 mM of guanosine monophosphate (GMP) were added to milli-Q water in a vial while kept on continuous stirring for 2-5 minutes at 65 °C. The obtained clear orange solution was allowed to rest and it formed a hydrogel in 3-5 minutes upon cooling to

room temperature.

5.4.4. Characterization

FESEM and TEM. The FA-GMP hydrogel was diluted up to 200 times in milli Q water and 10 μ l of it was drop-casted on a clean piece of glass slide and left for air drying for 24 hours. The drop-casted sample was then coated with Au and imaged under the SEM. 5 μ l of the same sample was drop-casted onto a copper grid for TEM Imaging.

UV-visible spectroscopy. UV-visible spectra of the hydrogel, FA, and GMP were recorded at a concentration of 0.025 mM each using a 1 cm path length cuvette. 100 mM of FA was first solubilized at a basic pH of 10 and then diluted to 0.025 for UV-visible studies.

NMR (1H , ^{31}P , ^{23}Na). The NMR studies were performed for FA, GMP, and FA-GMP at similar concentrations to hydrogel (GMP: 3000 mM, and FA-GMP 100:300 mM). To study the NMR of the hydrogel, it was converted to sol owing to its thermoreversible property and then transferred into the NMR tube. Folic acid was solubilized in basic pH for NMR studies.

ThT Binding Assay. A stock solution of 1 mM of ThT was prepared in ethanol and diluted to 10 μ M in water. The hydrogel was diluted up to 200 μ M with respect to folic acid in the 10 μ M solution of ThT and incubated for 2 days. The fluorescence was then checked for the ThT-FA-GMP system by exciting at 405 nm, and the emission was collected at 472 nm.

PXRD and FTIR. The hydrogel was lyophilized to obtain the xerogel. Then PXRD and FTIR were measured for the xerogel. Dry powder of FA and GMP was used for FTIR studies.

Rheological Studies. Rheological studies were performed at room temperature (25 $^{\circ}$ C) using a parallel plate (25 mm diameter). A small amount of the gel was scooped out with the help of a spatula and kept on the plate for measurement. The strain sweep measurements of the

hydrogels were carried out at a constant frequency (10 rad s^{-1}). The frequency sweep studies were performed in a $0.1\text{--}17 \text{ rad s}^{-1}$ frequency range, maintaining a constant strain of 1%. For the thixotropic loop studies, the strain was varied from 0.1% to 300% at an applied frequency of 10 rad s^{-1} . Successive low and high strains were applied at a period of 100 seconds.

5.4.5. Drug encapsulation and release

To load 0.5 mg/ml Dox in the FA-GMP hydrogel, first, a Dox solution of 0.5mg/ml concentration was prepared, then 100 mM of FA and GMP was added to it and the hydrogel was synthesized, thus in situ loading the drug in the hydrogel. In case of curcumin, 1.5 mg/ml stock of curcumin was prepared in ethanol. Hydrogel was prepared in the same concentration, but with 800 μl of water and 200 μl of the EtOH curcumin stock to make a total volume of 1 ml.

The hydrogel was rinsed with pH 7.4 PBS buffer solution to eliminate unbound drug molecules. The absorbance of the collected supernatant was analyzed using a UV-vis spectrophotometer. The encapsulated amount of vitamin or drug in the hydrogel was estimated by deducting the amount detected in the supernatant from the initial quantity, and the loading percentage was calculated using the equation below:

$$\text{Cumulative Amount Released (\%)} = \frac{M_t}{M_\infty} \times 100$$

To study the sustained release of drugs, 1 ml of drug-loaded hydrogel was taken in a vial, and 4 ml of PBS buffer was added to it. At regular time intervals, 400 μl of the buffer was taken out for UV-visible study and replenished with fresh buffer. The absorbance of the collected samples was measured at 480 and 434 nm for Dox and curcumin 480 and 434 nm respectively. The cumulative drug release was calculated as:

$$\text{Cumulative Amount Released (\%)} = M_t/M_\infty \times 100$$

where M_t and M_∞ is the amount of drugs released at time t and

the initial quantity of drugs encapsulated inside the hydrogel, respectively.

5.4.6. Cell Culture

The MCF-7 and HEK-293T cells was procured from the National Centre for Cell Science, Pune, India. The cells were cultured in Dulbecco's modified Eagle's medium DMEM; Thermo Scientific, USA) supplemented with 10% fetal bovine serum (FBS; Thermo Scientific, USA), 50 U/ml, 100 µg/ml, and 2 mM of penicillin, streptomycin, and L-Glutamine respectively. The growing cell environment was humidified with 5% CO₂ at 37 °C.

5.4.7. Cell cytotoxicity through MTT assay

For (3-(4,5-Dimethylthiazol-2-yl)-2,5-Diphenyltetrazolium Bromide) (MTT) assay, 10×10^3 HEK-293T and MCF-7 cells were seeded in a 96-well culture plate and maintained for next 24 hrs. HEK293T was treated with FA, GMP, and FA-GMP in different concentrations and meanwhile, the morphological changes were monitored using bright-field microscopy. After 24 hrs of inhibitor treatment, the cell culture media was removed and 0.5 mg/mL MTT reagent was added and incubated for the next 3 hrs at 37 °C. Then, after removing the MTT reagent, 100 µL of DMSO was added to dissolve formazan crystals by shaking for 2 hrs and absorbance was measured at 570 and 590 nm. For further experiments in MCF-7 cells, they were treated with Dox, Dox-GMP-FA, Cur, and Cur-GMP-FA at different concentrations with respect to the drug.

5.4.8. Cellular uptake

The fluorescence localization of Dox, Dox-FA-GMP was assessed in MCF-7 cells using a confocal laser scanning microscope (Olympus America Inc., USA). For the nucleus staining DAPI (0.1mg/ml: cell signaling technology). The fluorescence intensity was calculated via ImageJ software, and the graphs were plotted relative to those of the benzopyrene group.⁷⁷ For better visualization of the Dox and curcumin

fluorescence, they were loaded more into the hydrogel compared to the rest of other experiments. 1.5mg/ml of Dox and 900 µg/ml of curcumin were loaded into the hydrogel. The concentration of Dox, Dox-FA-GMP, Cur, and Cur-FA-GMP used for the experiment was 10 µg/ml with respect to the drug.

5.4.9. Quantitative real-time polymerase chain reaction

The genes involved in the cell cycle, apoptotic markers, and tumor suppressor genes profile were analyzed using qRT-PCR. A total of 0.25 million cells were seeded in a 6-well plate, after the cells' adherence the benzopyrene drug was exposed for 24 hrs followed by treatment with Dox, Dox-FA-GMP, Cur, and Cur-FA-GMP for 24 hrs. Total RNA extraction, complementary DNA preparation, and qRT-PCR were carried out as described earlier.⁷⁸ The qPCR was performed on three biological replicates and two technical replicates. Based on the MTT assay on MCF-7 cells Dox (3 µg/ml), Dox-GMP-FA (2 µg/ml with respect to Dox concentration), Cur (2 µg), and Cur-GMP-FA (2 µg/ml with respect to curcumin) was used for the experiment.

5.4.10. Cell proliferation assay

The cell proliferation assay was performed using crystal violet staining. A total of 0.25 million cells were seeded on a 6-well plate, benzopyrene exposed for 24 hrs followed by treatment with Dox, Dox-FA-GMP, Cur, and Cur-FA-GMP for 24 hrs. After that cells were fixed with 4% paraformaldehyde and stained with 0.5 g % crystal violet and images were captured under the microscope (Dmi1, Leica Microsystems). Quantification of the data was done by using Image J software (National Institutes of Health, Bethesda, MA, USA). Based on MTT assay on MCF-7 cells Dox (3 µg/ml), Dox-GMP-FA (2 µg/ml with respect to Dox concentration), Cur (2 µg), and Cur-GMP-FA (2 µg/ml with respect to curcumin) was used for the experiment.

5.4.11. Statistical analysis

Two-sample t-tests were performed to compare the mean values of the

Dox, Dox-FA-GMP, Cur, and Cur-FA-GMP samples with benzopyrene-exposed MCF-7 cells. Statistical significance was considered at the 0.05 critical level, where $p < 0.05$ at the 95% confidence interval. P values of <0.05 , <0.01 , and <0.0001 are considered statistically significant and are represented with */#, **/##, and ***/###, respectively. The upregulation and downregulation are represented by * and #, respectively.

5.5 References

1. Ferlay J., Colombet M., Soerjomataram, I., Parkin D. M. *et al.* (2021), Cancer statistics for the year 2020: An overview. *Int. J. Cancer* 149, 778–789 (DOI: 10.1002/ijc.33588).
2. Nagai H., Kim Y. H. (2017), Cancer prevention from the perspective of global cancer burden patterns. *J. Thorac. Dis.* 9 (DOI: 10.21037/jtd.2017.02.75).
3. Yin X., Yang J., Zhang M. *et al.* (2022), Serum Metabolic Fingerprints on Bowl-Shaped Submicroreactor Chip for Chemotherapy Monitoring. *ACS Nano* 16, 2852–2865 (DOI: 10.1021/acsnano.1c09864).
4. Rea F., Callegaro D., Favaretto A. *et al.* (1998), Long term results of surgery and chemotherapy in small cell lung cancer1. *Eur. J. Cardiothorac. Surg.* 14, 398–402 (DOI: 10.1016/S1010-7940(98)00203-6).
5. Rajani C., Borisa P., Karanwad T., et al. (2020). 7 - Cancer-targeted chemotherapy: Emerging role of the folate anchored dendrimer as drug delivery nanocarrier. In *Pharmaceutical Applications of Dendrimers Micro and Nano Technologies.*, A. Chauhan and H. Kulhari, eds. (Elsevier), pp. 151–198 (DOI: 10.1016/B978-0-12-814527-2.00007-X).
6. Pacheco C., Baião A., Ding T., Cui W., Sarmiento B. (2023), Recent advances in long-acting drug delivery systems for anticancer drug.

- Adv. Drug Deliv. Rev. 194, 114724 (DOI: 10.1016/j.addr.2023.114724).
7. Senapati S., Mahanta A.K., Kumar S., Maiti P. (2018), Controlled drug delivery vehicles for cancer treatment and their performance. *Signal Transduct. Target. Ther.* 3, 1–19 (DOI: 10.1038/s41392-017-0004-3).
 8. Li J., Mooney D.J. (2016), Designing hydrogels for controlled drug delivery. *Nat. Rev. Mater.* 1, 1–17 (DOI: 10.1038/natrevmats.2016.71).
 9. Thakur N., Sharma B., Bishnoi S. *et al.* (2019), Biocompatible Fe³⁺ and Ca²⁺ Dual Cross-Linked G-Quadruplex Hydrogels as Effective Drug Delivery System for pH-Responsive Sustained Zero-Order Release of Doxorubicin. *ACS Appl. Bio Mater.* 2, 3300–3311 (DOI: 10.1021/acsabm.9b00334).
 10. Gosecka M., Gosecki M., Ziemczonek P. *et al.* (2024), Selective Anticervical Cancer Injectable and Self-Healable Hydrogel Platforms Constructed of Drug-Loaded Cross-Linkable Unimolecular Micelles in a Single and Combination Therapy, *ACS Appl. Mater. Interfaces* 16, 14605–14625 (DOI: 10.1021/acsami.4c01524).
 11. Sun M., Gao M., Bi J. *et al.* (2024), Highly Efficient Hydrogel Encapsulation of Hydrophobic Drugs via an Organic Solvent-Free Process Based on Oiling-Out Crystallization and a Mechanism Study. *ACS Sustain. Chem. Eng.* 12, 4813–4824 (DOI: 10.1021/acssuschemeng.3c06018)
 12. Sun Z., Song C., Wang C., Hu Y., Wu J. (2020), Hydrogel-Based Controlled Drug Delivery for Cancer Treatment: A Review. *Mol. Pharm.* 17, 373-391 (DOI: 10.1021/acs.molpharmaceut.9b01020).
 13. Culver H. R., Clegg J. R., Peppas N. A. (2017), Analyte-Responsive Hydrogels: Intelligent Materials for Biosensing and Drug Delivery. *Acc. Chem. Res.* 50, 170–178 (DOI: 10.1021/acs.accounts.6b00533).

14. Sarma S., Thakur N., Varshney N. *et al.* (2024). Chromatin-inspired bio-condensation between biomass DNA and guanosine monophosphate produces all-nucleic hydrogel as a hydrotropic drug carrier. *Commun. Chem.* 7, 1–13 (DOI: 10.1038/s42004-024-01353-6).
15. Kariduraganavar M. Y., Heggannavar G. B., Amado S., Mitchell G. R. (2019), Chapter 6 - Protein Nanocarriers for Targeted Drug Delivery for Cancer Therapy. In *Nanocarriers for Drug Delivery Micro and Nano Technologies.*, S. S. Mohapatra, S. Ranjan, N. Dasgupta, R. K. Mishra, and S. Thomas, eds. (Elsevier), pp. 173–204 (DOI: 10.1016/B978-0-12-814033-8.00006-0).
16. Veselov V. V., Nosyrev A. E., Jicsinszky L., (2022), Targeted Delivery Methods for Anticancer Drugs. *Cancers* 14, 622 (DOI: 10.3390/cancers14030622).
17. Dharap S. S., Wang Y., Chandna P., Khandare J. J., Qiu B., *et al.* (2005), Tumor-specific targeting of an anticancer drug delivery system by LHRH peptide. *Proc. Natl. Acad. Sci.* 102, 12962–12967 (DOI: 10.1073/pnas.0504274102).
18. Rodzinski A., Guduru R., Liang P. *et al.* (2016), Targeted and controlled anticancer drug delivery and release with magnetoelectric nanoparticles. *Sci. Rep.* 6, 20867 (DOI: 10.1038/srep20867).
19. Kashkooli F. M., Soltani M., Souri M. (2020), Controlled anti-cancer drug release through advanced nano-drug delivery systems: Static and dynamic targeting strategies. *J. Controlled Release* 327, 316–349 (DOI: 10.1016/j.jconrel.2020.08.012).
20. Yu H., Ning N., Meng X., Chittasupho C., Jiang L., Zhao, Y. (2022), Sequential Drug Delivery in Targeted Cancer Therapy. *Pharmaceutics* 14, 573 (DOI: 10.3390/pharmaceutics14030573).

21. Chari R. V. J. (2008), Targeted Cancer Therapy: Conferring Specificity to Cytotoxic Drugs. *Acc. Chem. Res.* 41, 98–107 (DOI: 10.1021/ar700108g).
22. Lu Y., Sega E., Leamon C. P., Low, P. S. (2004), Folate receptor-targeted immunotherapy of cancer: mechanism and therapeutic potential. *Adv. Drug Deliv. Rev.* 56, 1161–1176 (DOI: 10.1016/j.addr.2004.01.009).
23. Siwowska K., Schmid R. M., Cohrs S., Schibli R., Müller C. (2017). Folate Receptor-Positive Gynecological Cancer Cells: In Vitro and In Vivo Characterization. *Pharmaceuticals* 10, 72 (DOI: 10.3390/ph10030072).
24. Viola-Villegas N., Rabideau A. E., Cesnavicious J., *et al.* (2008). Targeting the Folate Receptor (FR): Imaging and Cytotoxicity of Rel Conjugates in FR-Overexpressing Cancer Cells. *ChemMedChem* 3, 1387–1394 (DOI: 10.1002/cmdc.200800125).
25. Fernández M., Javaid F., Chudasama V. (2018). Advances in targeting the folate receptor in the treatment/imaging of cancers. *Chem. Sci.* 9, 790–810 (DOI: 10.1039/C7SC04004K).
26. Song W., Zhang Y., Yu D. -G. *et al.* (2021), Efficient Synthesis of Folate-Conjugated Hollow Polymeric Capsules for Accurate Drug Delivery to Cancer Cells. *Biomacromolecules* 22, 732–742 (DOI: 10.1021/acs.biomac.0c01520).
27. Parsaei M., Akhbari K. (2022), Synthesis and Application of MOF-808 Decorated with Folic Acid-Conjugated Chitosan as a Strong Nanocarrier for the Targeted Drug Delivery of Quercetin. *Inorg. Chem.* 61, 19354–19368 (DOI: 10.1021/acs.inorgchem.2c03138).
28. Bhanumathi R., Manivannan M., Thangaraj R., Kannan S. (2018), Drug-Carrying Capacity and Anticancer Effect of the Folic Acid- and Berberine-Loaded Silver Nanomaterial To Regulate the AKT-ERK

- Pathway in Breast Cancer. *ACS Omega* 3, 8317–8328 (DOI: 10.1021/acsomega.7b01347).
29. Nayak S., Lee H., Chmielewski J., Lyon L. A. (2004), Folate-Mediated Cell Targeting and Cytotoxicity Using Thermoresponsive Microgels. *J. Am. Chem. Soc.*, 126, 10258– 10259 (DOI: 10.1021/ja0474143).
30. Liu Y., Zong Y., Yang Z., *et al.* (2019), Dual-Targeted Controlled Delivery Based on Folic Acid Modified Pectin-Based Nanoparticles for Combination Therapy of Liver Cancer. *ACS Sustainable Chem. Eng.* 7, 3614– 3623 (DOI: 10.1021/acssuschemeng.8b06586).
31. Ifergan I., Assaraf Y. G. (2008), Chapter 4 Molecular Mechanisms of Adaptation to Folate Deficiency. In *Vitamins & Hormones Folic Acid and Folates*. (Academic Press), pp. 99–143 (DOI: 10.1016/S0083-6729(08)00404-4).
32. Martins I. C. B., Forte A., Diogo H. P. *et al.* (2022). A Solvent-free Strategy to Prepare Amorphous Salts of Folic Acid with Enhanced Solubility and Cell Permeability. *Chemistry–Methods* 2, e202100104 (DOI: 10.1002/cmt.202100104).
33. Hao C., Gao J., Wu Y., Wang X., Zhao R. *et al.* (2018), Design of folic acid based supramolecular hybrid gel with improved mechanical properties in NMP/H₂O for dye adsorption. *React. Funct. Polym.* 122, 140–147 (DOI: 10.1016/j.reactfunctpolym.2017.11.003).
34. Mohanta I., Sahu N., Guchhait C., Kaur L., Mandal D., Adhikari, B. (2024), Ag⁺-Induced Supramolecular Polymers of Folic Acid: Reinforced by External Kosmotropic Anions Exhibiting Salting Out. *Biomacromolecules* 25, 6203–6215 (DOI: 10.1021/acs.biomac.4c01063).
35. Xing P., Chu X., Ma M., Li S., Hao A. (2014), Supramolecular gel from folic acid with multiple responsiveness, rapid self-recovery, and

- orthogonal self-assemblies. *Phys. Chem. Chem. Phys.* 16, 8346–8359 (DOI: 10.1039/C4CP00367E).
36. Pillai J. J., Thulasidasan A. K. T., Anto R. J. *et al.* (2014). Folic acid conjugated cross-linked acrylic polymer (FA-CLAP) hydrogel for site specific delivery of hydrophobic drugs to cancer cells. *J. Nanobiotechnology* 12, 25 (DOI: 10.1186/1477-3155-12-25).
37. Li H., Gao J., Shang Y. *et al.* (2018). Folic Acid Derived Hydrogel Enhances the Survival and Promotes Therapeutic Efficacy of iPS Cells for Acute Myocardial Infarction. *ACS Appl. Mater. Interfaces* 10, 24459–24468 (DOI: 10.1021/acsami.8b08659).
38. Li X., Yang C., Zhang Z., Wu Z., *et al.* (2012), Folic acid as a versatile motif to construct molecular hydrogelators through conjugations with hydrophobic therapeutic agents. *J. Mater. Chem.* 22, 21838–21840 (DOI: 10.1039/C2JM35329F).
39. Wang H., Yang C., Wang L. *et al.* (2011). Self-assembled nanospheres as a novel delivery system for taxol: a molecular hydrogel with nanosphere morphology. *Chem. Commun.* 47, 4439–4441 (DOI: 10.1039/C1CC10506J).
40. Liu K., Zang S., Xue R. *et al.* (2018), Coordination-Triggered Hierarchical Folate/Zinc Supramolecular Hydrogels Leading to Printable Biomaterials. *ACS Appl. Mater. Interfaces* 10, 4530–4539 (DOI: 10.1021/acsami.7b18155).
41. Wu Y., Yang Z., Li X., Li T. *et al.* (2023). A self-assembled hydrogel dressing as multi-target therapeutics to promote wound healing. *Chem. Eng. J.* 477, 147145. (DOI: 10.1016/j.cej.2023.147145).
42. Wong S., Zhao J., Cao C., Wong C. K *et al.* (2019), Just add sugar for carbohydrate-induced self-assembly of curcumin. *Nat Commun.* 10, 582 (DOI: 10.1038/s41467-019-08402-y).

43. Patel A., Malinovska L., Saha S. (2017), ATP as a biological hydrotrope. *Science* 356, 753–756. (DOI: 10.1126/science.aaf6846).
44. Sarkar S., Mondal J. (2021). Mechanistic Insights on ATP's Role as a Hydrotrope. *J. Phys. Chem. B* 125, 7717–7731 (DOI: 10.1021/acs.jpcc.1c03964).
45. Pandey M. P., Sasidharan S., Raghunathan V. A., Khandelia H. (2022), Molecular Mechanism of Hydrotropic Properties of GTP and ATP. *J. Phys. Chem. B* 126, 8486–8494. (DOI: 10.1021/acs.jpcc.2c06077).
46. Mehringer J., Do T. -M., Touraud D. *et al.* (2021), Hofmeister versus Neuberger: is ATP really a biological hydrotrope? *Cell Rep. Phys. Sci.* 2, 100343 (DOI: 10.1016/j.xcrp.2021.100343).
47. Bourassa P., Tajmir-Riahi H. A. (2015), Folic acid binds DNA and RNA at different locations. *Int. J. Biol. Macromol.* 74, 337–342 (DOI: 10.1016/j.ijbiomac.2014.12.007).
48. Stefan L., Monchaud D. (2019), Applications of guanine quartets in nanotechnology and chemical biology. *Nat. Rev. Chem.* 3, 650–668 (DOI: 10.1038/s41570-019-0132-0).
49. Thakur N., Chaudhary A., Chakraborty A., Kumar R., Sarma T. K. (2021), Ion Conductive Phytic Acid-G Quadruplex Hydrogel as Electrolyte for Flexible Electrochromic Device. *ChemNanoMat* 7, 613–619 (DOI: 10.1002/cnma.202100072).
50. Loo K., Degtyareva N., Park J., *et al.* (2010), Ag⁺-Mediated Assembly of 5'-Guanosine Monophosphate. *J. Phys. Chem. B* 114, 4320–4326 (DOI: 10.1021/jp908085s).
51. Giorgi T., Lena S., Mariani P., *et al.* (2003), Supramolecular Helices via Self-Assembly of 8-Oxoguanosines. *J. Am. Chem. Soc.* 125, 14741–14749 (DOI: 10.1021/ja0364827).

52. Yoshikawa I., Li J., Sakata Y., Araki K. (2004), Design and Fabrication of a Flexible and Self-Supporting Supramolecular Film by Hierarchical Control of the Interaction between Hydrogen-Bonded Sheet Assemblies. *Angew. Chem. Int. Ed.* 43, 100–103 (DOI: 10.1002/anie.200352641).
53. Chakraborty A., Ghosh T., Sarma S., Agarwal V., Kumar R., Sarma T. K. (2024), A multi-stimuli responsive polyoxometalate-guanosine monophosphate hybrid chromogenic smart hydrogel. *J. Mater. Chem. C* 12, 13447–13456 (DOI: 10.1039/D4TC01973C).
54. Chakraborty A., Dash S., Thakur N., Agarwal V., Nayak D., Sarma T. K. (2024), Polyoxometalate-Guanosine Monophosphate Hydrogels with Haloperoxidase-like Activity for Antibacterial Performance. *Biomacromolecules* 25, 104–118 (DOI: 10.1021/acs.biomac.3c00845).
55. Magri V. R., Rocha M. A., de Matos C. S. *et al.* (2022), Folic acid and sodium folate salts: Thermal behavior and spectroscopic (IR, Raman, and solid-state ¹³C NMR) characterization. *Spectrochim. Acta. A. Mol. Biomol. Spectrosc.* 273, 120981 (DOI: 10.1016/j.saa.2022.120981).
56. Wu H., Liu G., Zhang S., Shi J. *et al.* (2011), Biocompatibility, MR imaging and targeted drug delivery of a rattle-type magnetic mesoporous silica nanosphere system conjugated with PEG and cancer-cell-specific ligands. *J. Mater. Chem.* 21, 3037–3045 (DOI: 10.1039/C0JM02863K).
57. Oh J. -M., Choi S. -J., Lee G. -E. *et al.* (2009), Inorganic Drug-Delivery Nanovehicle Conjugated with Cancer-Cell-Specific Ligand. *Adv. Funct. Mater.* 19, 1617–1624 (DOI: 10.1002/adfm.200801127).
58. Chen X., Xu X., Cao Z. (2007), Theoretical Study on the Singlet Excited State of Pterin and Its Deactivation Pathway. *J. Phys. Chem. A* 111, 9255–9262 (DOI: 10.1021/jp0727502).

59. Matias R. S. Ribeiro P. R., Sarraguça, M. C., Lopes, J. A. (2014), A UV spectrophotometric method for the determination of folic acid in pharmaceutical tablets and dissolution tests. *Anal. Methods* 6, 3065–3071 (DOI: 10.1039/C3AY41874J).
60. Gu C., Peng Y., Li J., Wang H., *et al.* (2020), Supramolecular G4 Eutectogels of Guanosine with Solvent-Induced Chiral Inversion and Excellent Electrochromic Activity. *Angew. Chem., Int. Ed.*, 59, 18768–18773 (DOI: 10.1002/anie.202009332)
61. Ida R., Kwan I. C. M., Wu G. (2007), Direct ^{23}Na NMR observation of mixed cations residing inside a G-quadruplex channel. *Chem. Commun.*, 795–797 (DOI: 10.1039/B613105K).
62. Wong A., Wu G. (2003), Selective Binding of Monovalent Cations to the Stacking G-Quartet Structure Formed by Guanosine 5'-Monophosphate: A Solid-State NMR Study. *J. Am. Chem. Soc.* 125, 13895–13905 (DOI: 10.1021/ja0302174).
63. Wong A., Fettinger J. C., Forman S. L., Davis J. T., Wu G. (2002), The Sodium Ions Inside a Lipophilic G-Quadruplex Channel as Probed by Solid-State ^{23}Na NMR. *J. Am. Chem. Soc.* 124, 742–743 (DOI: 10.1021/ja0120330).
64. Ida R., Wu G. (2008), Direct NMR Detection of Alkali Metal Ions Bound to G-Quadruplex DNA. *J. Am. Chem. Soc.* 130, 3590–3602 (DOI: 10.1021/ja709975z).
65. de la Faverie A. R., Guédin A., Bedrat A., *et al.* (2014), Thioflavin T as a fluorescence light-up probe for G4 formation. *Nucleic Acids Res.* 42, e65 (DOI: 10.1093/nar/gku111).
66. Mohanty J., Barooah N., Dhamodharan V. *et al.* (2013), Thioflavin T as an Efficient Inducer and Selective Fluorescent Sensor for the Human Telomeric G-Quadruplex DNA. *J. Am. Chem. Soc.* 135, 367–376 (DOI: 10.1021/ja309588h).

67. Qin Z., Sun Y., Jia B. *et al.* (2017), Kinetic Mechanism of Thioflavin T Binding onto the Amyloid Fibril of Hen Egg White Lysozyme. *Langmuir* 33, 5398–5405 (DOI: 10.1021/acs.langmuir.7b00221).
68. Kumar A., Khandelwal M., Gupta S. K. *et al.* (2019). Chapter 6 - Fourier transform infrared spectroscopy: Data interpretation and applications in structure elucidation and analysis of small molecules and nanostructures. In *Data Processing Handbook for Complex Biological Data Sources*, G. Misra, ed. (Academic Press), pp. 77–96 (DOI: 10.1016/B978-0-12-816548-5.00006-X).
69. Agarwal V., Varshney N., Singh S., *et al.* (2023). Cobalt-Adenosine Monophosphate Supramolecular Hydrogel with pH-Responsive Multi-Nanozymatic Activity. *ACS Appl. Bio Mater.* 6, 5018–5029 (DOI: 10.1021/acsabm.3c00719).
70. Parin F. N., Ullah S., Yildirim K. *et al.* (2021), Fabrication and Characterization of Electrospun Folic Acid/Hybrid Fibers: In Vitro Controlled Release Study and Cytocompatibility Assays. *Polymers*, 13, 3594 (DOI: 10.3390/polym13203594).
71. He Y. Y., Wang X. C., Jin P. K. *et al.* (2009), Complexation of anthracene with folic acid studied by FTIR and UV spectroscopies. *Spectrochim Acta A Mol Biomol Spectrosc.* 72, 876-879 (DOI: 10.1016/j.saa.2008.12.021).
72. Wu G., Kwan I. C. M., Yan Z., Huang Y., Ye E. (2017), On the Helical Structure of Guanosine 5'-Monophosphate Formed at pH 5: Is It Left- or Right-Handed? *J. Nucleic Acids* 2017, 6798759 (DOI: 10.1155/2017/6798759).
73. Zhang J., Li X., Sun X. *et al.* (2018). GMP-quadruplex-based hydrogels stabilized by lanthanide ions. *Sci. China Chem.* 61, 604–612. (DOI: 10.1007/s11426-017-9187-x).
74. Umesh, Sarkar S., Bera S., Moitra P., Bhattacharya S. (2023), A self-healable and injectable hydrogel for pH-responsive doxorubicin drug

- delivery *in vitro* and *in vivo* for colon cancer treatment. Mater. Today Chem. 30, 101554. (DOI: 10.1016/j.mtchem.2023.101554).
75. Gellert M., Lipsett M. N., Davies D. R. (1962), Helix formation by guanylic acid. Proc. Natl. Acad. Sci. 48, 2013–2018 (DOI: 10.1073/pnas.48.12.2013).
76. Hu S. -H., Chen S. -Y., Gao X. (2012), Multifunctional Nanocapsules for Simultaneous Encapsulation of Hydrophilic and Hydrophobic Compounds and On-Demand Release. ACS Nano 6, 2558–2565 (DOI: 10.1021/nn205023w).
77. Rani A., Jha H. C. (2024), Dissecting the Epstein-Barr virus entry pathway into astrocytes: unfolding the involvement of endosomal trafficking View supplementary material. Future Virol. 19, 381-391 (DOI: 10.1080/17460794.2024.2407729).
78. Rani A., Tanwar M., Verma T. P. *et al.* (2023), Understanding the role of membrane cholesterol upon Epstein Barr virus infection in astroglial cells. Front. Immunol. 14, 1192032 (DOI: 10.3389/fimmu.2023.1192032).

Chapter 6

Conclusion and Future Prospects

6.1 Conclusion

In this thesis, we successfully developed supramolecular hydrogel systems through physical crosslinking using guanosine monophosphate (GMP) as a low molecular weight gelator (LMWG) for various interesting applications. We proposed the right selection of crosslinkers that could self-assemble with GMP to form a hydrogel simply by one-pot mixing of the aqueous solutions of precursors under ambient conditions. This procedure keeps the inherent properties of the precursor molecules intact, making the hydrogels functional smart materials. The hydrogels were robust, thixotropic, injectable and showed stimuli-responsive properties.

We developed class I hybrid organic-inorganic hydrogels with GMP in the first three works. In the first two works, we used Keggin structured, metal oxocluster (POM) along with GMP to obtain a hydrogel for haloperoxidase-mediated antibacterial activity and to develop a chromogenic material further exploited to fabricate a simpler electrochromic device. In the third study, we created the $\text{Zn}(\text{His})_3(\text{H}_2\text{O})$ complex by combining the precursors in a 1:3 ratio, replicating the active site of the carbonic anhydrase enzyme. The complex was stabilized within the GMP self-assembled network, which mimicked the tertiary structure of a protein backbone due to its amphiphilic nature and hydrophobic pockets. This hydrogel was designed to structurally and functionally emulate carbonic anhydrase, facilitating CO_2 sequestration via the mineralization process, which was further harnessed to separate toxic metals like Pb^{2+} and Cd^{2+} . In the last work, we proposed that a small organic molecule, folic acid, which is otherwise highly water-insoluble, can form a stable hydrogel with GMP. The hydrophobic region of the G-quartet assembly co-assembles folic acid, and the hydrophilic part makes the whole system water soluble.

In this thesis, we exploited GMP as a versatile scaffold for creating nucleotide-based nanohybrid hydrogels with diverse functional capabilities. The use of a facile, derivatization-free, aqueous synthesis approach makes the system highly accessible, sustainable, and biocompatible. Furthermore, an in-depth investigation of the self-assembly mechanisms offered valuable insights into the non-covalent interactions driving fibril formation and hydrogelation, thereby enhancing our understanding of biological self-assembly in biomolecules. Overall, this work not only focused on designing functional hydrogels but also lays the foundation for future smart material development in the field of biomedical engineering, enzyme mimetics, environmental remediation, sensing, etc. These findings are expected to open new avenues in the use of nucleotide-based supramolecular systems for multifunctional and stimuli-responsive material design. These findings are expected to inspire future research on nucleotide-based nanohybrids and broaden their potential in multifunctional biomedical, environmental, and sensing applications.

6.2. Future Prospects

The findings of this thesis underscore the remarkable potential of guanosine monophosphate (GMP) as a versatile low molecular weight gelator capable of forming supramolecular hydrogels with a wide variety of components in its pristine form. The first three studies highlighted GMP's ability to co-assemble with inorganic materials to yield class I hybrid hydrogels with tunable properties. In particular, the formation of fibrillar hydrogels through GMP's interaction with inorganic metal complexes opens up a broad spectrum of future opportunities to engineer smart materials with customizable mechanical, electronic, and catalytic functions. This research paves the way for further exploration of GMP-based hybrid systems in advanced fields such as magnetism, optoelectronics, enzyme mimetics, catalysis, and photocatalysis, especially by incorporating diverse metal ions, clusters, and coordination complexes. The demonstrated ability of a GMP-polyoxometalate (POM) hydrogel to function dually as both the electrochromic layer and

electrolyte in an electrochromic device (ECD) reveals the potential of G-quadruplex hydrogels in simplifying and miniaturizing electrochemical devices. Future work may expand this concept using other electrochromic or conductive crosslinkers to design next-generation ECDs with improved efficiency and sustainability. In the fourth study, GMP was shown to encapsulate and solubilize hydrophobic molecules, demonstrating its potential to enhance the bioavailability of poorly soluble drugs and phytochemicals, an area ripe for exploration in drug delivery and pharmaceutical formulation.

The reversible, stimuli-responsive behavior of GMP hydrogels further suggests their utility in biosensing and environmental detection platforms. Their biocompatibility, ease of synthesis, and cost-effectiveness also make them attractive candidates for developing green and scalable soft materials. Moreover, the tunability of GMP hydrogel mechanics through crosslinker selection offers promising routes for biomedical applications, including tissue scaffolding, artificial joints, and 3D bioprinting. As supramolecular hydrogels based on nucleotides like GMP continue to evolve, they are poised to significantly impact multiple domains, from biomedicine and materials science to environmental technologies.

Looking forward, this work is expected to stimulate deeper investigation into the design of functional, adaptive, and sustainable hydrogel systems, ultimately contributing to the development of next-generation biomimetic materials and smart devices.

List of Publications

Thesis work:

1. **Amrita Chakraborty**, Saswati Dash, Neha Thakur, Vidhi Agarwal, Debasis Nayak*, and Tridib K Sarma*. Polyoxometalate-Guanosine Monophosphate Hydrogel with Haloperoxidase-like Activity for Antibacterial Performance, *Biomacromolecules* **2024**, 25, 104-118. DOI: 10.1021/acs.biomac.3c00845 (I.F – 5.5).
2. **Amrita Chakraborty**, Tanushree Ghosh, Suryakamal Sarma, Vidhi Agarwal, Rajesh Kumar*, and Tridib K Sarma*. A multi-stimuli responsive polyoxometalate-guanosine monophosphate hybrid chromogenic smart hydrogel. *J. Mater. Chem. C*, **2024**, 12, 13447-13456. DOI: <https://doi.org/10.1039/D4TC01973C> (I.F – 5.7).
3. **Amrita Chakraborty**, Annu Rani, Pramesh Sinha, Suryakamal Sarma, Vidhi Agarwal, Aditya Prasun, Hem Chandra Jha*, Tridib K Sarma*. Guanosine-monophosphate Induced Solubilization of Folic Acid Leading to Hydrogel Formation for Target Delivery of Hydrophilic and Hydrophobic Drugs. *ACS Appl. Mater. Interfaces*, **2025**, 17, 8, 11848–11860. DOI: 10.1021/acsami.4c21306 (I.F – 8.5)
4. **Amrita Chakraborty**, Suryakamal Sarma, Vidhi Agarwal, Aditya Prasun, Ravindra Vishwakarma, Tarun Sahu, Tridib K. Sarma*. A supramolecular approach to structurally mimic carbonic anhydrase enzyme. (*manuscript under preparation*)

Other Publications:

1. Neha Thakur, Anjali Chaudhary, **Amrita Chakraborty**, Rajesh Kumar, and Tridib K. Sarma. Ion Conductive Phytic Acid-G Quadruplex Hydrogel as Electrolyte for Flexible Electrochromic Device, *ChemNanoMat*, **2021**, 7, 613-619. DOI: 10.1002/cnma.202100072 (I.F – 2.6)
2. Siddarth Jain, **Amrita Chakraborty**, Bhagwati Sharma, Tridib K. Sarma. Cu²⁺ Ion Doping-Induced Self-Assembled ZnO-Cu_xO Nanostructures for Electrochemical Sensing of Hydrogen Peroxide and p-Nitrophenol, *ACS Appl. Nano Mater.*, **2022**, 5, 11973–11983. DOI: 10.1021/acsanm.2c03073 (I.F – 5.3)
3. Poonam Deka, **Amrita Chakraborty**, Dr. Kashyap Kumar Sarma, Dr. Rituraj Das, Dr. Sanjeev Pran Mahanta, Dr. Khaled Althubeiti, Dr. Tridib Kumar Sarma, Dr. Ranjit Thakuria. Synthesis and Characterization of pH Triggered Imine Functional Low Molecular Weight Hydrogel, *ChemistrySelect*, **2023**, 8, e202302358. DOI: 10.1002/slct.202302358 (I.F – 1.9)
4. Vidhi Agarwal, Nidhi Varshney, Surbhi Singh, Nitin Kumar, **Amrita Chakraborty**, Bhagwati Sharma, Hem Chandra Jha, Tridib K Sarma. Cobalt-Adenosine Monophosphate Supramolecular Hydrogel with pH-Responsive Multi-Nanozymatic Activity. *ACS Appl. Bio Mater.* **2023**, 6, 5018–5029. DOI: 10.1021/acsabm.3c00719 (I.F – 4.7)

